Experimental determination of Fe isotope fractionations in the diagenetic iron sulphide system

Romain Guilbaud

Doctorate of Philosophy
The University of Edinburgh
2011

Abstract

Initial published work suggested that Fe isotope fractionations recorded in sediments were a product of biological activity. Experiments and measurements of natural samples now indicate that Fe isotope fractionation can be the product of both biological and inorganic processes. Sedimentary iron sulphides provide unique information about the evolution of early life which developed under anoxic conditions. It is in these sedimentary Fe-S species and in particular in Archean and Proterozoic pyrites that the largest Fe isotope variations (up to a range of ~5‰ for $\delta^{56/54}$Fe) have been measured. Most research has focussed on potential processes responsible for the formation of a ^{56}Fe depleted Fe(II) pool from which iron sulphides would precipitate without additional fractionation, recording the light Fe isotope composition of the pool. Much less attention has been given to the possibility that the iron sulphide forming mechanisms themselves could produce significant fractionations.

The Fe-S system constitutes a diverse group of stable and metastable phases, the ultimate Fe sequestrating phase being pyrite. The aim of this study was to examine experimentally where Fe isotope fractionations occur during the abiotic formation of iron sulphides in order to assess whether or not the measured Fe isotope signatures in natural pyrite could be explained by chemical mechanisms only. Both analytical and experimental protocols were developed in order to determine the partition of Fe isotopes for each step towards diagenetic pyrite formation. $^{56/54}$Fe and $^{57/54}$Fe ratios were measured on an IsoProbe-P Micromass MC-ICP-MS, and all experiments were performed under oxygen-free N_2 atmosphere.

Supporting previously published data, the results indicate that the precipitation of the nanoparticulate iron(II) monosulphide mackinawite (FeS_m) kinetically fractionates lighter isotopes with initial fractionations of $\Delta^{56}Fe_{Fe(II)aq\text{-}FeS} = 1.17 \pm 0.16$ ‰ at 25°C and $\Delta^{56}Fe_{Fe(II)aq\text{-}FeS} = 0.98 \pm 0.16$ ‰ at 2°C. The rate of isotopic exchange between $Fe(II)_{aq}$ and FeS_m decreases as FeS_m nanoparticles grow. Fe isotope exchange kinetics are consistent with i) FeS_m nanoparticles that have a core–shell structure, in which case Fe isotope mobility is restricted to exchange between the surface shell and the solution and ii) a nanoparticle growth via an aggregation–

growth mechanism. Because of the structure of FeSm nanoparticles, the approach to isotopic equilibrium is kinetically restricted at low temperatures.

The equilibrium Fe isotope fractionation between Fe^{2+}_{aq} and FeS_m was determined using the three isotope method and is $\Delta^{56}Fe_{Fe(II)-FeS} = -0.33 \pm 0.12$ ‰ at 25°C and $\Delta^{56}Fe_{Fe(II)-FeS} = -0.52 \pm 0.16$ ‰ at 2°C. This suggests that at equilibrium, FeS_m incorporates heavier isotopes with respect to $Fe^{2+}_{aq,}$ and the isotopic composition of most naturally occurring FeS_m does not represent equilibrium.

During pyrite formation, pyrite incorporates kinetically lighter isotopes with a fractionation $\Delta^{56}Fe_{FeS-pyrite} \sim 2.2$ ‰. Because pyrite is sparingly soluble in sedimentary environments, isotope exchange is prevented and pyrite does not equilibrate with its Fe(II) source. Combined fractionation factors between Fe^{2+}_{aq}, mackinawite (FeS_m) and pyrite permit the generation of pyrite with Fe isotope signatures that encapsulate the full range of sedimentary $\delta^{56}Fe_{pyrite}$ recorded in both Archean and modern sediments. Archean Fe isotope excursions reflect various degrees of pyritisation, extent of $Fe(II)_{aq}$ utilisation, and variations in source composition rather than microbial dissimilatory Fe(III) reduction only. Our results show that sedimentary pyrite is not a passive recorder of the Fe isotope composition of the reactive Fe(II) reservoir forming pyrite. It is the formation process itself that influences pyrite Fe isotope signatures with consequent implications for the interpretation of sedimentary pyrite Fe isotope compositions throughout geological time.

Declaration

I, Romain Guilbaud, declare that the work presented in this thesis for the degree of Doctor of Philosophy is all my own except where otherwise stated. None of the work presented here has been previously submitted as a degree at this, or any other University.

Acknowledgements

I would like to thank first of all my supervisors, Ian Butler and Rob Ellam, for the constant support and enthusiasm they showed throughout this project. They have been always available for sharing their knowledge in constructive discussions. I am thankful to Kathy Keefe and Vinnie Gallagher at SUERC for their time, and particular thanks go to Terry and Margaret Donnelly for their hospitality during my stays in East Kilbride. It has been very pleasant to work within the Butler-Ngwenya labs in Edinburgh, so many thanks to Leon, Marek, Bryne, Hanna, Nimisha, Suyin, Muhua, Lisa, Kevin, Derek and Julia. Within the School of Geosciences, I also need to thank Nick Odling, Nicola Cayzer, and the work-shop crew for their help in the experimental design. Many thanks to Dave Rickard and Tony Oldroyd in Cardiff University, and to Alan Matthews, Mira Bar-Matthews and Dan Asael in the Geological Survey of Israel (Jerusalem) for their hospitality and the discussions they brought to my work.

The following work constitutes a piece of non-profit fundamental research, and has been funded by an ECOSSE PhD research grant. I do thank the people who share this communal idea that a healthy society should finance research for the sake of free knowledge, and therefore who are willing a part of the collective budget to ensure the fragile support of Universities. Knowledge entirely belongs to common good.

The past four years in Edinburgh would have not been the same without the friends around me: Leon, VFB Olli, Pula-Paula-Pascual-Lopez, Adonis, Monica, Alice, Gijs, Vera, Craig, Alegria, Rudra, Dear Nancy Burns, Claudia, James, Armando and Greer, Lorna, Sylvia, Emily, Jeong-Yon, all the members of the Thursday Club and the chemists over the road.

Je remercie aussi les copains de France, qui m'accompagnent de loin dans ma vie interminable d'étudiant – Ça y est, Eglantine, on a fini! Et puis un grand Merci à ma famille: tout d'abord toi, Ben, qui dans ton soutien permanent et ta réflexion m'offre une vie riche et très intéressante. Mes parents, qui depuis toujours m'épaulent dans mes projets et aiguisent mon goût à comprendre les choses. Et mes frères et sœurs et leurs familles qui me donnent tant de fierté et d'encouragements. Enfin, je remercie Dominique Baudart (1929-2007), qui m'a transmis son amour pour le travail de la Terre. Un travail que je poursuis, à ma manière, toujours avec la même passion!

[…] et puis tes égouts pleins de sang,
S'engouffrant dans l'Enfer comme des Orénoques,
Tes sages, tes bouffons neufs aux vieilles défroques.
Anges revêtus d'or, de pourpre et d'hyacinthe,
O vous! Soyez témoins que j'ai fait mon devoir
Comme un parfait chimiste et comme une âme sainte.

Car j'ai de chaque chose extrait la quintessence,

Tu m'as donné ta boue et j'en ai fait de l'or.

(C. Baudelaire, *Les Fleurs du Mal*.)

Table of contents

Preface

Understanding biogeochemical processes and biogeological interactions is increasingly more difficult when going backwards to the early stages of the Earth's history. For these periods, paleontological records are rare and poorly preserved, and geochemical proxies are often altered. It is well known that the evolution of biological systems and the surface of the Earth are closely related. The rise of oxygen into the atmosphere is an eloquent example; its consequences for continental erosion and the redox state of the oceans (*e.g.* Anbar *et al.*, 2007; Reinhard *et al.*, 2009) have demonstrated the impact of biological oxygenic photosynthesis upon the Earth's surface and the deposition of major geological formations such as the Banded Iron Formations (*e.g.* James, 1966; Beukes *et al.*, 1990). The concept of a biological interaction with the Earth system is not recent (*e.g.* Hutton, 1788; Vernadzky, 1929; Lovelock, 1979). In recent decades, studies have highlighted the potential role of inorganic geochemistry in the synthesis of prebiotic organic molecules (*e.g.* Wächtershäuser, 1988; Russell *et al.*, 1994). The still highly debated theory of the "iron-sulphur world" and its implications on the emergence of life, conceived by some authors as a "by-product of the Earth's convection cells" (Russell, Prebiotic chemistry workshop, Durham University, 2010) accentuate the inseparable links between biology and geology.

Major bio-geochemical processes have been assessed by traditional geochemistry using light stable isotope systems such as those of C, O, S, H and N. These systems provided successful insights into various branches of geology including planetary chemical evolution, evolution of life, environmental remediation, climate change, and the formation of ores and resources. Much less attention has been given to transition metal isotope systems. This was mainly due to analytical challenges, but also to the scientific consensus that because of their mass, heavier metal isotopes could not fractionate significantly. In the preface of *Geochemistry of Non-traditional stable isotopes (Johnson, Beard and Albarede Ed., 2004)*, James R. O'Neil wrote "Until a few years ago, I would never have imagined that a volume on the stable isotope geochemistry of elements like Mg, Fe or Cu would be written". Since the 2004 review on "non-traditional" isotopes, advances in Fe isotope research have quickly evolved and reviews dedicated to Fe isotopes have been published (Dauphas and Rouxel,

2006; Anbar and Rouxel, 2007; Johnson *et al.*, 2008a; Poitrasson, 2010). The recent development of Multi-Collector Inductively Coupled Plasma Mass Spectrometry (MC-ICP-MS) has allowed precise and accurate measurement of transition metals isotopes (Walder and Freedman, 1992; Walder *et al.*, 1993; Halliday *et al.*, 1998), and opened up an intense field of research since 1999. Measurements of the isotopic signatures of transition metals found in different natural systems have been extensively documented. Amongst the transition metals, particular focus was given to Cu, Zn, Mo, Cr, Ni and Fe, because i) their cycle is closely related those of C, S and O, and ii) these nutrients can potentially trace major biogeochemical processes. As we will discuss later, most work has been dedicated to Fe isotopes. Fe is the ninth most abundant element in the universe (Anders and Grevesse, 1989), the most abundant transition metal on Earth, and its biological importance as an organism nutrient, an electron acceptor for respiration (Vargas *et al.*, 1998), a potential key for prebiotic chemistry (Wächtershäuser, 1988) raises Fe to a central position for tracing biogeochemical processes.

In sedimentary environments, major sinks for Fe are Fe-(oxyhydr)oxides, carbonates and sulphides, but when going back in geological times, sulphides - and ultimately pyrite - become a dominant Fe sequestrating sink. Fe isotope signatures in pyrite are subjects of controversial interpretations. The main discussions arise from discrepancies between calculated fractionation factors and measured data, and without experimental insights, it has been difficult, if not impossible, to interpret these signatures successfully. The reason for this is that measuring isotopic signatures of mineral phases only tells about one end-member of the system, and equivocal assumptions have to be made for the compositions of the source or of the residue. Is pyrite a passive recorder of the isotopic composition of the Fe(II) pool? Is bacterial activity a prerequisite to produce the observed range of fractionations? Can we trace oceanic redox events from Fe isotope signatures in pyrite? The lack of experimental work on the fractionations occurring during the formation of metal-sulphides has prevented us from assessing confidently these fundamental questions.

This PhD project addresses the experimental determination of Fe isotope fractionations occurring on abiological reactions within the diagenetic Fe-S system. The ultimate Fe sequestrating phase being pyrite, our study assesses potential

fractionations between dissolved Fe(II) and solids before and during the formation of pyrite. This study firstly reviews previous work established on traditional and transition metal isotope systems, with emphasis on the genesis of metal-sulphides and their application for tracing early Earth's biogeochemical processes. We then present experimental and analytical developments that address the behaviour of Fe isotopes in a low temperature system that is oxygen sensitive and mostly comprised of metastable phases. This thesis provides fundamental answers to the mobility of Fe atoms through metastable Fe-S phases and also presents the first experimental data on Fe isotope fractionation during the formation of diagenetic pyrite.

The chapter I reviews the fundamental backgrounds of the biogeochemical evolution of the Earth's surface in order to put into context the issues raised by Fe isotopes in sedimentary sulphides. Section 1.1 illustrates the importance of iron sulphides and of the global Fe and S cycles for ancient environments in which life evolved. Indeed, iron sulphide geochemistry has been linked intimately with proposals for the onset of life on Earth (section 1.1.1) and with the global cycles of C, H and O from traditional geological and stable isotopic approaches (section 1.1.2). The mechanisms controlling the formation of iron sulphides under diagenetic conditions are presented in section 1.2. Finally, section 1.3 reviews the results and the implications of using Fe isotopes in a novel approach to assess ancient and modern biogeochemical processes.

Chapter I

The role iron sulphides in the biogeochemical evolution of the Earth's subsurface: a case for iron isotopes

1.1. The role of the Fe and S geochemical cycles in the evolution of the Earth's subsurface

The accumulation of oxygen in the Earth's atmosphere is probably the most important event in the history of the surface chemistry after the emergence of life itself. Not only did the oxygenation of the atmosphere and the oceans promote the vast diversification of weathering and geochemical processes, but it also provided O_2 as a favourable electron acceptor involved in the various metabolic pathways of subsequent aerobic organisms. None of these dramatic changes for the Earth's subsurface could have happened without the appearance of the prokaryotic cyanobacteria, an anaerobic oxygenic photoautrophic eubacteria. The oldest unquestioned fossil evidence of cyanobacteria is found in the 2.1 Ga Belcher Islands cherts, Canada (Golubic and Hofmann, 1976; see also Knoll, 2003). These fossilised colonies indicate with confidence that biological O_2 production was active in the Paleoproterozoic. Nevertheless, the presence of cyanobacterial fossils at 2.1 Ga does not provide further indications on the existence of cyanobacteria at earlier times, or about O_2 accumulation in the atmosphere. The existing models for the timing of the oxygenation of the atmosphere and the hydrosphere are still controversial (*e.g.* Ohmoto, 1996; Farquhar *et al.*, 2000; Canfield, 2005; Ohmoto *et al.*, 2006). Older microfossil records are rare and their biogenecity can be vigorously debated as is the case for the oldest putative fossil evidence for Archean life in the 3.4 Ga Apex cherts from the Warrawoona Group, Pilbara block, western Australia (*e.g.* Schopf, 1993, 2006; Hofmann *et al.*, 1999; Brasier *et al.*, 2002, 2005; Schopf *et al.*, 2007). The main reason for these controversies is the lack of preserved sediments deposited during the Proterozoic and the Archean. Garrels and Mackenzie (1971) estimated that *ca.* 90 % of the sedimentary rocks deposited during the Precambrian has gone through subsequent geological recycling. Today, the oldest sedimentary rocks found on Earth are the 3.8 Ga amphibolite-facies metasediments of the Isua Supracrustal Group in south-western Greenland. But the paucity of sedimentary geological records older than the Proterozoic Era makes the understanding of the early Earth's biogeochemistry difficult to assess.

1.1.1. The iron-sulphur world theory, the emergence of life and its evolution

Most of the early and contemporaneous theories on the emergence of life involve strong concentrations of organic compounds in the early ocean. These theories include

Darwin's "hot organic pond" (Darwin, 1888); the "hot dilute soup" proposal (*e.g.* Oparin, 1938); the Miller-Urey generation of organic molecules from a reduced atmosphere through electrical discharges (Miller, 1953) and the incorporation of replicating compounds such as RNA into organic cells (*e.g.* Dysen, 1985). As pointed out by Russell and Hall (1997), much less research has focussed on the initial geochemical conditions necessary to concentrate, and even generate the organic molecules required for life, although some authors (Bernal, 1951; Bada and Lazcano, 2002) proposed the concentration of organic molecules on hydrated clay minerals. Assuming that prebiotic organic molecules favourable for life were somehow concentrated in the early oceans, other conditions – a reducing atmosphere, and the substantial decrease of meteorite bombarding and of geological stressing - are a prerequisite for the emergence of living organisms in a clement environment. This is an issue since it is now known that the Hadean atmosphere was not reducing and the Hadean ocean was not an organic soup (Gillet, 1985). Instead, Hadean oceans were ~ 85 to 110°C and acidic (~ pH 5) due to high CO_2 atmospheric concentration (Grotzinger and Kasting, 1993). However, there is now increasing evidence supporting the early development of a continental crust at ~ 4.5 Ga (*e.g.* Harrison *et al.*, 2005), giving new prospects on the Hadean landscape, and thus, on the early formation of a potential habitat.

Strong interest has been given to the relatively low temperature Fe-S system during the last 20 years, for its potential role as a "driver" from inorganic, prebiotic geochemistry to the emergence of the first cells and the catalysis of the first organic molecules necessary for life. Thus, as opposed to the previous theories implying that the earliest life was heterotroph, this approach suggests that it was characterised by autotrophism. It constitutes the "iron sulphur world theory", first proposed by Wächterhäuser and co-workers (*e.g.* Wächtershäuser, 1988, 2006; Drobner *et al.*, 1990) and by Russell and co-workers (*e.g.* Russell *et al.*, 1994; Russell and Hall, 1997; Martin and Russell, 2003; Russell, 2007). The common observation for these two groups of research is the ubiquity of Fe-S clusters in biochemistry, as active centres of various proteins such as NADH dehydrogenase, Coenzyme Q – cytochrome C reductase, hydrogenases, and nitrogenise (for a review, see Beinert, 2000; and Johnson *et al.*, 2005a). Fe-S proteins are common in photosynthetic bacteria, plants and mitochondrial membranes as they participate in the electron transport chain, as is the case for complexes I and II of oxidative phosphorylation. Most importantly, Fe-S

clusters are present in the most ancient biological catalyst: the ferredoxins (Hall *et al.*, 1971). Thus, the Fe-S system is considered in this theory as a means to produce and catalyse small organic molecules from the initial reduction of inorganic CO_2 and CO.

Black smoker inputs provided Hadean oceans with high dissolved Fe(II) with concentrations up to 0.02 mol kg^{-1} (Von Damm, 1990) and under acidic conditions, Fe would have remained in solution and accumulated in the ocean. The degassing of high temperature, mafic to ultra mafic magmas would produce soluble volatiles such as CO, CO_2, SO_2, polyphosphates, H_2O_2. Wächtershäuser (1988) suggested that CO_2 could be reduced into organic sulphur molecules by the H_2S/FeS reducing agent. Negatively charged organic compounds can bond at the positively charged pyrite surface in a two-dimensional network. The diversity of organic compounds would have grown as such, *via* cycling C fixing chemical reactions. Experiments successfully produced organic compounds such as thiolated formic acid, CH_3SH, and CH_3COSH, a precursor for the important citrate cycle's acetyl coenzyme A (Huber and Wächtershäuser, 1997).

By contrast, Russell *et al.* (1994) proposed that C fixation occurred within three-dimensional mackinawite (iron(II) monosulphide) precipitate bubbles. They showed that the precipitation of such structures occur when alkaline fluids are injected into acidic $Fe(II)_{aq}$ rich solutions, as expected for off-ridge hydrothermal regions in Hadean oceans. Off-ridge systems result from lower temperature rock-water interactions which produce highly reduced alkaline fluids (Macleod *et al.*, 1994). In their proposal, Russell and co-workers do not consider pyrite as a catalysing mineral nor the H_2S/FeS to be an energy source for the synthesis of organic molecules. Instead, they favour other mineral species in the Fe-Ni-S sytem such as Fe_nS_n clusters, greigite (Fe_3S_4) and $FeNi_2S_4$ to act as catalytic centres. Interestingly, apart from the Fe_2S_2 cluster which displays a mackinawite-like structure, FeS clusters and greigite diplay cubane structures similar to those of ferredoxins. The binding of various nucleic acids to nanoparticulate mackinawite has been reported by Hatton and Rickard (2008). In Russell and co-workers' proposal, the geochemical pH gradient would supply energy by the protonmotive force through the FeS membrane.

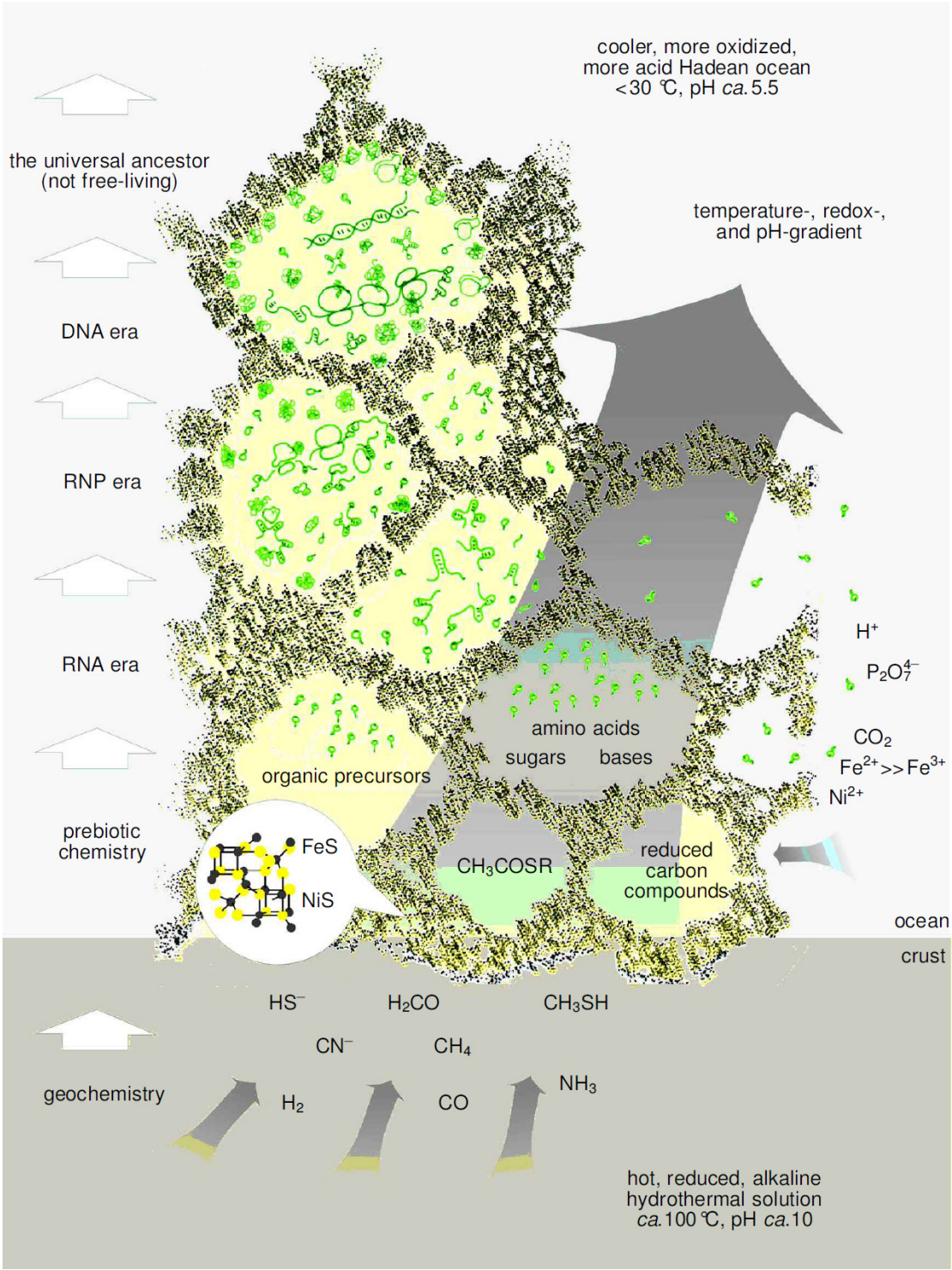

Figure 1.1: The FeS membrane protocell proposal, where FeS bubbles precipitate at the interface between an acidic $Fe(II)_{aq}$ solution and an alkaline solution. The figure is from Martin and Russell (2003). The model supports a geochemical origin of prebiotic organic molecules evolving within the 3D FeS protocells.

This FeS bubbles model has been suggested to act as a proto-cell membrane, favourable for organo-synthesis and a progressive evolution towards lipid-membrane

and cell diffraction into the two prokaryotic domains, *i.e.* the Bacteria (or eubacteria) and the Archaea (or archaeabacteria) (Martin and Russell, 2003; Fig. 1.1). However, FeS precipitates are more likely to act as a permeable barrier rather than a pH membrane (Filtness *et al.*, 2003).

An increasing number of experiments involving Fe, Ni, W and Mo have shown various pathways to produce organic molecules that are essential to biochemistry (See Cody, 2004, for a review of the transition metal pathways). However, the debate between the "iron-sulphur world theory" and the "RNA world theory" (*e.g.* de Duve, 2003; Forterre and Gribaldo, 2007) is still ongoing. Independently of the "iron-sulphur theory", the importance of the cycles of Fe and S, and therefore, of iron sulphides during the early stages of the Earth's history can be assessed by traditional geological and stable isotopic approaches.

1.1.2. Evidence from traditional approaches

1.1.2.1. The geochemical evolutions of Fe, S and O in the atmosphere-ocean system

Iron-rich sedimentary deposits known as the Banded Iron Formations or BIFs (*e.g.* James, 1966; Beukes *et al.*, 1990), mainly comprised of Fe(II)-bearing minerals such as siderite and magnetite, are remarkable demonstrations that dissolved Fe(II) accumulated, at least regionally, in early oceans until 1.8 Ga when their occurrence ceases (*e.g.* Holland, 1984). Archean seawater Fe^{2+} concentration is difficult to quantify, but an estimate of 40 to 120 μM can be made using the Phanerozoic Ca^{2+} concentration (10-30 mM, Horita *et al.*, 2002) and the siderite-calcite solubility ratio (Canfield, 2005). This compares to modern nanomolar concentrations (Wu *et al.*, 2001), and was probably amplified in hydrothermal regions as it is the case in modern systems where Douville *et al.* (2002) measured millimolar concentrations. Isley and Abbott (1999) documented the frequency and relative distribution of BIFs through geological time, and showed that BIFs are common sedimentary rocks before 2.4 Ga. The amplitude of BIFs deposition highlights that the O_2 and S(-II) concentrations in Archean seawater should be low, since Fe would otherwise be removed from the solution as oxides or sulphides without accumulating in the ocean (Holland, 1984; Canfield *et al.*, 2000).

Low seawater sulphate concentrations in the Archean until ~ 2.5 Ga are supported by S isotope systematics. Biologically mediated S isotope fractionation is recorded during dissimilatory sulphate reduction by anaerobic prokaryotic respiration, where

sulphate is used as a final electron acceptor for the oxidation of organic matter. The difference in $^{34/32}S$ isotopic compositions between reduced H_2S and sulphate, $\Delta^{34}S_{SO4\text{-}H2S}$ varies from 20 - 40 ‰ when initial sulphate concentrations are high (Thode *et al.*, 1953; Habicht and Canfield, 1997; Canfield *et al.*, 2000). By contrast, the fractionation is small when sulphate concentration is < 200 µM (Harrison and Thode, 1958; Habicht *et al.*, 2002). Cameron (1982) pointed out that for geological times older than 2.5 Ga, the recorded S isotope fractionations are small, implying that oceans were sulphate depleted compared to modern concentrations of ~ 28 mM (*e.g.* Millero, 1996). This was confirmed by Canfield *et al.* (2010) who further constrained Proterozoic sulphate concentrations to ~ 1 mM and Archean concentrations < 200µM.

The atmospheric O_2 partial pressure in the Hadean and the Archean is thought to be 10^{-5} times the present atmospheric level (*e.g.* Pavlov and Kasting, 2002; Bekker *et al.*, 2004). Low O_2 concentrations seem to be the likely explanation for low sulphate concentrations (Canfield *et al.*, 2000), limiting continental oxidative weathering of pyrite-containing rocks. Also, the preservation of redox sensitive phases such as pyrite, siderite and uraninite in detrital sediments older than 2.3 Ga (*e.g.* Roscoe, 1957; Schidlowski, 1981; Rasmussen and Buick, 1999) supports low O_2 environments. Rye and Holland (1998) reported that a large number of Precambrian paleosols older than 2.2-2.3 Ga did not show evidence for Fe oxidation. Fe oxidation profiles in paleosols usually indicates atmospheric O_2 (*e.g.* Rye and Holland, 1998; Beukes *et al.*, 2002) and the earliest paleosol supporting evidence for oxidative weathering is the 2.2 Ga Hekpoort Paleosol in the Transvaal Supergroup, South Africa (Yang and Holland, 2003). This is consistent with atmospheric O_2 accumulation during the "Great Oxidation Event", (GOE, 2.2-2.5 Ga).

Isley and Abbott (1999) showed that BIF deposition almost ceases between 2.4 and 2.0 Ga. Somehow synchronous to the GOE, it has been suggested that the O_2 level could have been high enough to oxygenate the oceans and prevent $Fe(II)_{aq}$ accumulation. However, BIFs reappearance at ~ 2.0 Ga would suggest O_2 decrease and a new $Fe(II)_{aq}$ accumulation between 2.0 and 1.8 Ga, which is supported by Cr isotopes (Frei *et al.*, 2009). Instead of a complete oxygenation of the ocean, Bjerrum and Canfield (2002) proposed that continental oxidative weathering would promote bacterial sulphate reduction (BSR) due to sulphate inputs, resulting in Fe removal from solution as sulphides. There is now an increasing collection of evidence for a progressive increase of atmospheric P_{O2} 50 to 100 Ma before the GOE, stimulating

euxinic conditions through the increase sulphate fluxes due to oxidative continental weathering (Anbar *et al.*, 2007; Kaufman *et al.*, 2007; *e.g.* Reinhard *et al.*, 2009).

After 1.8 Ga, the extent of oxygenation has been assumed by some authors (*e.g.* Holland, 2002) to reach a level at which Fe(II) could not remain dissolved in the ocean. However, large S isotope variations (Canfield, 2001) support large sulphate concentrations, which would promote the preservation of anoxic, euxinic regions in a stratified ocean (Canfield, 1998). The 0.7 Ga largest recorded $\delta^{34}S$ signatures cannot be explained by dissimilatory sulphate reduction only. Canfield and Teske (1996) proposed that those signatures could reflect the evolution of sulphur disproportionating bacteria, producing ^{34}S depleted S-bearing species such as elemental sulphur, sulphite, and thiosulphate (*e.g.* Canfield and Thamdrup, 1994). Sulphur disproportionation has also been confirmed by Parnell *et al.* (2010). It is also worthwhile noting that abiotic reduction of sulphate containing fluids can produce S isotope fractionations > 20 ‰ (Ohmoto and Goldhaber, 1997).

Recent Fe mineral speciation studies on basin scales (Raiswell and Canfield, 1998; Raiswell *et al.*, 2001; Anderson and Raiswell, 2004; Poulton *et al.*, 2004, 2010; Poulton and Canfield, 2005) have demonstrated the transition from $Fe(II)_{aq}$ rich to euxinic regions within anoxic basins. Combined Fe speciation and S isotope variations support euxinic conditions in the Mesoproterozoic (Shen *et al.*, 2001, 2003), including the transition from deep, distal ferruginous conditions to shallower, proximal sulphidic conditions in the 1.8 Ga Animikia Group, Canada (Poulton *et al.*, 2010). Unfractionated Mo isotope compositions of Proterozoic sediments have first been interpreted as widespread anoxia during the Proterozoic (Arnold *et al.*, 2004) but further research (Siebert *et al.*, 2003, 2005, 2006; Poulson *et al.*, 2006) indicates that the mechanisms responsible for Mo isotope fractionation, particularly during Mo supply to the oceans (*e.g.*Archer and Vance, 2006), are poorly known and quantification of anoxia is difficult using Mo isotopes only.

The above overview on the reconstruction of the geochemical cycles from the anoxic Archean and Proterozoic to the more recent oxygenated time demonstrates the necessity of combined geological and multi-geochemical studies to fully understand the complex chemical evolution of the Earth subsurface. Although seducing, the idea that the use of one single geochemical tool could be sufficient to describe entirely one system has not yet been demonstrated.

1.1.2.2. The records of biological oxygen production in sediments older than 2.2 Ga

The previous section described the "geochemical context" in which oxygen could start accumulating into the atmosphere. But how far back can we go in timing the start of biologic oxygen production? The first direct evidence for cyanobacterial activity are microfossils found in ~ 2.1 Ga cherts (Golubic and Hofmann, 1976). Phylogenetic studies reveal that cyanobacteria develop relatively late in the history of prokaryotes (Woese, 1987; Woese *et al.*, 1990; Pace, 1997). Before their appearance, life on the anoxic Earth was likely to have been dominated by anaerobic prokaryotes, since cyanobacteria are the only photosynthetic organisms that produce O_2 as a by-product (Blankenship, 1992), although there is evidence for some aerobic life in the early Archean, possibly before the prokaryotic differentiation into Bacteria and Archaea (Castresana and Saraste, 1995; Pereira *et al.*, 2001). These isolated aerobic organisms may have used H_2O_2 derived O_2 as an electron acceptor (see Canfield, 2005).

Research into organic geochemistry led to the discovery of molecular fossils in ancient sedimentary rocks that support evidence for cyanobacterial activity (*e.g.* Brocks *et al.*, 1999, 2005; Summons *et al.*, 2006; Eigenbrode, 2008; Eigenbrode *et al.*, 2008; Waldbauer *et al.*, 2009). These preserved organic molecules, referred as biomarkers, are derived from cellular lipids, and characterise certain organisms or particular metabolic pathways. The presence of 2α-methylhopanes in the 2.7 Ga Pilbara Craton, Australia (Brocks *et al.*, 1999) supports oxygenic photosynthesis in the late Archean as 2α-methylhopanes derive from 2-methylbacteriohopanepolyol, which is only synthesised by some cyanobacteria (Summons *et al.*, 1999). In fact, the presence of sterane in the same units has been interpreted as evidence for eukaryotes 1 Ga before the first direct eukaryote fossil record (Brocks *et al.*, 1999), although it has been argued that sterols can also be synthesised by archaeabacteria (see discussions by T. Cavalier-Smith and E. Nisbet in Martin and Russell, 2003). Jahnke and Nichols (1986) showed that molecular oxygen is required to synthesise sterols, implying that certain extents of aerobic conditions, even localised to oxygen producing zones, occurred at 2.7 Ga (Knoll, 1999, 2003). Recent research on biomarkers, although still controversial, supports oxygenic photosynthesis as a major source of organic carbon through CO_2 fixation in the Neoarchean (Brocks *et al.*, 1999; Eigenbrode *et al.*, 2008; Waldbauer *et al.*, 2009).

Another source of evidence supporting oxygenic photosynthesis (and thus the presence of cyanobacteria) comes from carbon isotopes. Biological C fixation

produces large distinct fractionations, with preferential incorporation of ^{13}C depleted inorganic carbon into organisms (Nier and Gulbransen, 1939; Murphey and Nier, 1941). The initial step is the diffusion of inorganic CO_2 into the organism's tissue, which is accompanied by small isotope fractionation (*e.g.* O'Leary, 1981). The subsequent enzymatic carboxylation step, by which CO_2 is processed into R-COOH is responsible for the larger fractionations and depends on the different pathways used by the organism to produce R-COOH. Schidlowski (2001) reviewed the major carboxylation/decarboxylation pathways and their associated C isotope fractionation. The Calvin cycle's key enzyme, the ribulose-1,5-bisophate (or Rubisco), produces a $\delta^{13}C$ ranging from – 20 ‰ to – 28 ‰ (Sirevåg *et al.*, 1977). The phosphoenolpyruvate pathway (or PEP) that produces oxaloacetate involves smaller fractionation (~ -3 ‰, Schidlowski, 2001). Organisms that use acetyl coenzyme A as a CO_2 acceptor for ferredoxin-linked carboxylation in anoxygenic photosynthesis also produce small fractionations (Sirevåg *et al.*, 1977). Carbon fixation also occurs through methane processing by methanotrophic bacteria with a $\delta^{13}C$ range form ~ -10 to -34 ‰ (Summons *et al.*, 1994) and can produce in some extreme cases $\delta^{13}C$ signatures as low as -80 ‰ (Coleman *et al.*, 1981; Freeman *et al.*, 1990). As noted by Schidlowski (2001), all these pathways are reversible and the overall range of C isotope fractionations produced by both carboxylation and decarboxylation are summarised in Fig. 1.2 Light (~ -50 to -60 ‰) $\delta^{13}C$ signatures recorded in organic carbon of the 2.7 Ga Fortescue formation (Fig. 1.2) has been interpreted as reflecting C fixation by aerobic methanotrophic bacteria (*e.g.* Hayes, 1994). This supports the presence of O_2 in levels adequate for sustaining aerobic life, even locally, and thus O_2 production.

Figure 1.2: C isotope secular fluctuations recorded in organic carbon (C_{org}) and inorganic (carbonate) carbon (C_{carb}) compared with the biologically mediated fractionations produced by: 1) C3 plants (Calvin cycle), 2) C4 plants (PEP), 3) Crassulacean acid metabolic plants, 4) eukaryotic algae, 5) cyanobacteria, 6) anoxigenic photosynthetic bacteria, 7) methanogenic bacteria and 8) methanotrophic bacteria. The figure is from Schidlowski (2001).

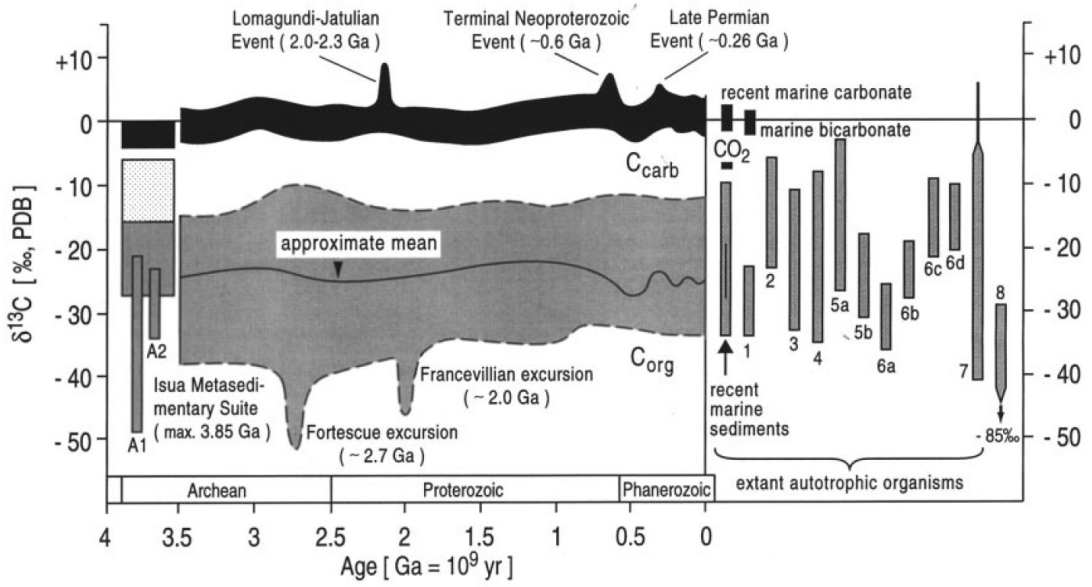

1.1.2.3. Assessing the timing of the emergence of cyanobacteria

In the paragraphs above, I discussed the largely accepted evidence supporting cyanobacterial activity at 2.7 Ga, *i.e.* 0.6 Ga before their first fossil record. The possibility for a greater cyanobacterial antiquity first emanates from geological structures: the stromatolites. Stromatolites, amongst other definitions, are referred to "accretionary sedimentary structures, commonly thinly layered, megascopic and calcareous, interpreted to have been produced by the activities of mat-building communities of mucilage-secreting micro-organisms, mainly photoautotrophic prokaryotes" (*e.g.*Schopf *et al.*, 2007). The presence of stromatolites in Archean rocks (*e.g.* Lowe, 1980; Awramik, 1992; Hofmann *et al.*, 1999) has been a promising piece of evidence for life on the early Earth and for oxygenic photosynthesis since the early Archean, although Walter *et al.* (1980) noted that non-oxygenic photosynthetic bacteria such as Chloroflexus are capable mat-builders. However, it has been demonstrated that stromatolite-like structures could be produced abiogically (Lowe, 1994; Grotzinger and Rothman, 1996) and the differences in the definition of stromatolite itself reflect the difficulty in unambiguously distinguishing between biogenic stromatolites and abiotic stromatolite-like structures. The criteria proposed by Buick *et al.* (1981) and Walter (1983) to establish the biogenecity of stromatolites focus on the presence of fossilised micro-organisms within the structure. Although the presence of these preserved microfossils itself does not prove the biologic origin of the surrounding mat structure, their abundance in Proterozoic stromatolites remove

any doubts about their biogenicity. However the presence of putative microfossils is extremely scarce in the merely Archean stromatolites. This is mainly due to the fact that, for these microscopic microbial structures to be preserved, the initial carbonate needs silica replacement in the very early stages of diagenesis, before any further fossil-destructive diagenetic or low-grade metamorphic process occurs (Schopf *et al.*, 2007). Although there has been controversial work on assessing the biogenecity of the ~ 3.465 Ga Tower Formation and Apex chert (Warawoona Group, western Australia, Schopf, 1993, 2006; Brasier *et al.*, 2002, 2005; Schopf *et al.*, 2007), improvement in Raman technology has permitted the 3D visualisation of a cylinder like structure for the putative filamentous oldest microfossil (Schopf *et al.*, 2007), refuting the abiotic graphite-like structure proposed by Brasier *et al.* (2002).

Other controversies derive from the long term record of $\delta^{13}C$ signatures of organic matter (*i.e.* the relics of living organisms) and of carbonates (which represent the inorganic counterpart). Organic matter is preserved on geological scales as kerogenous substances and their graphitic derivatives (Durand, 1980). The uniformity in $\delta^{13}C$ signatures of reduced C ($\delta^{13}C_{organic}$ ~ -25 ‰) and carbonated C ($\delta^{13}C_{organic}$ ~ 0 ‰) throughout geological times (Fig. 1.2) has been interpreted as evidence for continuous biological carboxylation since Rubisco, the dominant C fixation pathway, imposes its C isotope fractionation in modern sediments (*e.g.* Schidlowski, 1988, 2001). This signature is more or less continuous until 3.5 G, and an offset has been measured for carbonates and their graphitic counterpart in the 3.8 Ga Isua supracrustal belt, western Greenland (Schidlowski *et al.*, 1979). Schidlowski *et al.* (1979) interpreted the offset as a metamorphic effect since the sediments have suffered amphibolite facies metamorphism (Rosing *et al.*, 1996; Fedo and Whitehouse, 2002). Mojzsis *et al.* (1996) also reported biological range for $\delta^{13}C$ of graphite inclusions in apatite grains in the 3.8 Ga Akilia rocks (Greenland). In both examples, the biological origin of the graphite used as the fossilised organic carbon record has been questioned (van Zuilen *et al.*, 2002; Fedo and Whitehouse, 2002). Furthermore, it has been demonstrated that abiologic production of hydrocarbons from CO_2 and CO through Fisher-Tropsch reactions involves ^{13}C depleted hydrocarbon with $\Delta^{13}C_{organic\text{-}inorganic}$ ~ -50 ‰ (Horita and Berndt, 1999). These abiotic reactions, where inorganic carbon is reduced by H_2 (Lancet and Anders, 1970), can be produced by hydrothermal fluids. It has thus been argued that abiotic processes can reproduce similar fractionations as biologically mediated C fixation (*e.g.* Horita, 2005), and therefore that the C isotope

signatures for rocks older than 3.5 Ga are likely to reflect abiotic processes since they have been metasomatised (Fedo and Whitehouse, 2002).

1.1.2.4. Evidence for anoxigenic biological activity in the Archean

In phylogenetic models, metabolisms predating cyanobacterial oxygenic photosynthesis involve fermentation, sulphate reduction, dissimilatory iron(III) oxide reduction, anoxygenic photosynthesis and maybe methanogenesis (*e.g.* Nisbet and Sleep, 2001). The antiquity of methanogenesis (production of CH_4 as a by-product by anoxic archaeabacteria) is still debated (*e.g.* Nisbet and Sleep, 2001; Cavalier-Smith, 2002; Grassineau *et al.*, 2006), but the C isotope evidence for methanotrophs suggests that CH_4 was actively produced at 2.7 Ga (*e.g.* Schidlowski, 2001), and supports Archean methanogenesis (*e.g.* Hayes, 1994). The C isotope fractionation associated with methane production by methanogenic archaeabacteria is poorly known, but may produce a $\delta^{13}C_{methane}$ range from ~ - 5 to – 40 ‰ (Schidlowski, 2001; House *et al.*, 2003), and further methanotrophy involves lighter organic carbon $\delta^{13}C$ signatures.

The closest organisms to the last common ancestor are anaerobic sulphate reducing hyperthermophiles (*e.g.* Stetter, 1996) and therefore S reduction is considered as one of the earliest forms of microbial respiration. Archean bacterial sulphate reduction (BSR) has been suggested by Ohmoto and Felder (1987) and supported by further studies (Shen *et al.*, 2001; Londry and Des Marais, 2003; Shen and Buick, 2004). As mentioned before, large S isotope excursions start in sediments younger than 2.7 Ga (Fig. 1.3) and it is generally accepted that BSR was active at this time. Evidence for BSR for geological times older than 2.7 Ga is however more ambiguous (*e.g.* Ohmoto *et al.*, 1993; Habicht and Canfield, 1997). This is mainly because sulphates are rare in Archean sediments and therefore the S isotopic composition of seawater sulphate is not well constrained. However, convincing data were given by Shen *et al.* (2001) who presented the isotopic compositions of sulphides and related barite in 3.47 Ga sediments from the North Pole area, Western Australia. They argued that the large S isotope fractionations recorded supports evidence for early BSR. Because S isotope fractionations can also be produced abiotically (Ohmoto and Goldhaber, 1997), evidence for ancient ecosystems is given more confidence when assessed through a collection of multi-isotope or multi-disciplinary tools (*e.g.* Grassineau *et al.*, 2001, 2002, 2006; Archer and Vance, 2006; Czaja *et al.*, 2010).

Vargas *et al.* (1998) showed that Archaea and Bacteria that are the most closely related to the last common ancestor use Fe(III) reduction as a metabolic respiration pathway. In particular, even prokaryotes thought to only have a fermentation metabolism could use Fe(III) as an electron acceptor. Therefore Vargas *et al.* (1998) proposed that Fe(III) reduction was an important process on the early Earth, and might have been more likely than sulphate to be the first external electron acceptor for their respiration. The Fe isotope fractionations associated with Fe(III) reduction will be reviewed later.

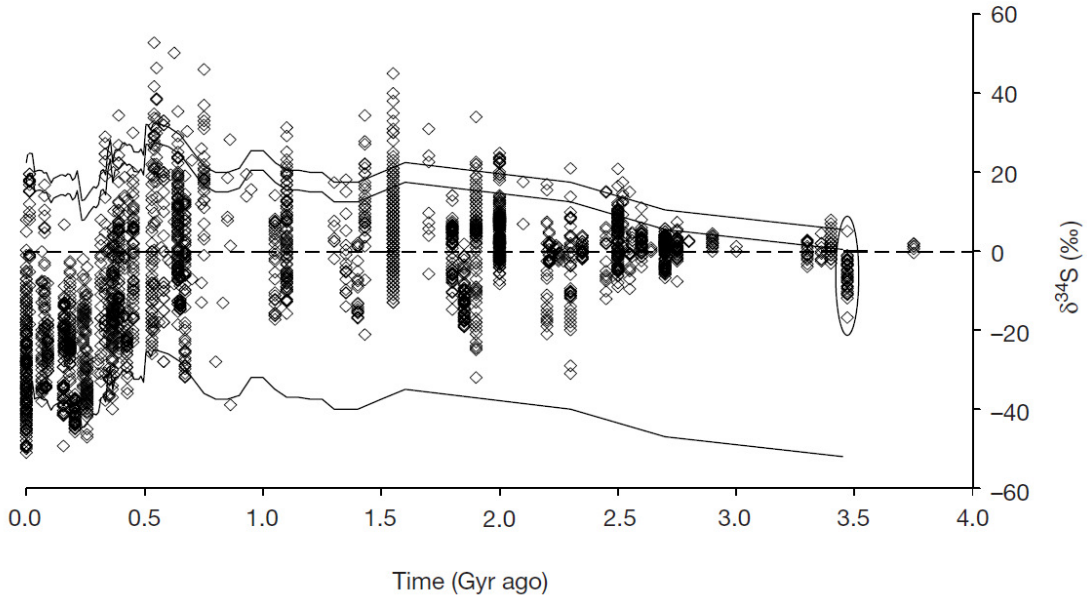

Figure 1.3: S isotope secular fluctuations recorded in sedimentary sulphides. The upper double lines represent seawater sulphate. The lower single line is a de*via*tion of 55 ‰ from seawater sulphate, enveloping the largest fractionation. Surrounded data highlight the large S isotope variations in the early Archean. The figure is from Shen *et al.* (2001).

1.1.3. Conclusions

In the previous sections, I have demonstrated that the traditional approaches to assess biogeochemical processes on the early Earth are not straight forward, and are often the source of active debate. A brief history of stable isotope geochemistry clearly demonstrates the need of multiple approaches to avoid such debates. I also showed that the acquisition of large amounts of natural data, although extremely valuable as a means to build Earth evolution models, cannot be used with certainty

without the contribution from experimental data that directly assess the foundations of those hypotheses.

The second central point is the importance of Fe and S cycles for the early Earth geochemical cycles. They both played a major role for the chemical evolution of the oceans, the atmosphere, and living metabolisms. As emphasised by Berner and Maasch (1996), Berner *et al.* (2003), Canfield (2005), the geochemical cycles of C, O, S and H are closely related as oxygen accumulates in the atmosphere as a function of the burial of organic matter and of pyrite. If oxygen respiration is in equilibrium with oxygenic photosynthesis, there should be no oxygen accumulation into the atmosphere, unless the burial of organic matter occurs. When oxygen is free to accumulate, reactions with Fe and sulphides occur. Similarly, the burial of pyrite permits oxygen accumulation since pyrite-sulphide is produced by sulphate reduction driven by organic matter production (Canfield, 2005). Isotope mass-balance models (*e.g.* Berner and Raiswell, 1983) support the idea that the burial of organic matter has been the major source of O_2 during the Phanerozoic. Canfield (2004, 2005) proposed that significant sulphate input into the oceans implied pyrite burial to be as, if not more, important than organic matter burial for O_2 production in the Proterozoic.

There is now growing interest in coupling traditional approaches with recently measurable new isotope ratios, involving transition metal isotopes and Fe in particular. But studying the behaviour of Fe in the early stages of the Earth's history, characterised by anoxia and for which Fe and S cycles are so closely related, necessitates a complete understanding of its sulphur chemistry.

1.2. The diagenetic cycles of Fe and S in anoxic environments

In ambient aqueous systems, iron sulphides constitute a diverse group of minerals with iron and sulphur atoms in different oxidation states. At low temperature, the ultimate stable phase is pyrite (also the most common sulphide mineral on the Earth's subsurface) but other metastable Fe-S phases are persistent in sediments. The formation of iron sulphides in modern diagenetic environments is closely related to biological processes, as the predominant sources of dissolved iron and sulphide in modern aqueous systems involve the biological reduction of Fe(III) (oxy)hydroxides (dissimilatory iron reduction, DIR) and of sulphate (BSR) (*e.g.* Berner, 1981; Raiswell and Berner, 1985; Canfield *et al.*, 1992).

Formation of Fe-S minerals in sediments mainly depends on the ambient pH, the concentrations in aqueous Fe(II) and S(-II), and the redox state of the system. Mineralisation and burial of organic matter determines the oxygen content in the atmosphere, thus the fixation of pyrite in sediments is directly linked to the oxygenated environment (*e.g.* Berner, 1982). $S(-II)_{aq}$ and $Fe(II)_{aq}$ can be naturally found in sedimentary pore waters and in anoxic basins (Black Sea, Cariaco Trench, fjords in Norway). Fig. 1.4 illustrates the relative oxic, suboxic and anoxic zones in porewaters, and the main geochemical redox reactions linked with sulphides and metals. It is important to distinguish the chemical terms "oxic, suboxic and anoxic" (based on the O_2 concentration) from the biological terms "aerobic, dysaerobic and anaerobic" (referring to the characteristics of organisms inhabiting specific environments). The boundaries between these zones are arbitrary and based on the detection limits of the potentiometric electrodes (in the case of sulphide) and the traditional Clark cell oxygen electrode (Luther *et al.*, 1991). The oxic zone is defined by O_2 concentrations > 10^{-6} M. The suboxic zone is defined by O_2 concentrations < 10^{-6} M and S(-II) concentrations < 10^{-6} M. This zone is a site where numerous redox reactions occur resulting in changes of speciation of many elements such as Fe and Mn (Murray *et al.*, 1989). The anoxic zone is defined by S(-II) concentrations > 10^{-6} M. In near shore environments, the oxic zone represents 1-2 mm (Revsbech *et al.*, 1981). In the deep ocean, O_2 is depleted after several centimetres (Revsbech *et al.*, 1986). The thickness of the suboxic zone can vary from a few millimetres or centimetres (Skei, 1988) to several metres (Murray *et al.*, 1989). These diagenetic zones can be stretched by physical forcing (seasonal weather, storms, bioturbations) and chemical contents (*e.g.* the availability of organic matter and of electron acceptors for redox reactions).

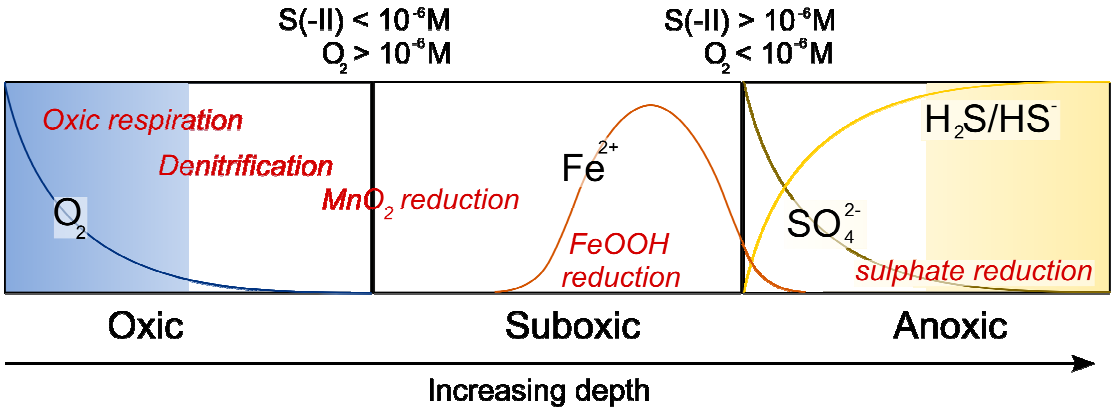

Figure 1.4: Schematic diagram showing the biogeochemical reactions in a sediment profile, from oxic porewaters to anoxic porewaters. The oxic, suboxic and anoxic zones are defined by O_2 and S(-II) contents. Microbial reducing reactions are shown in red.

1.2.1. The aqueous geochemical cycles of S and Fe

1.2.1.1. Sulphur chemistry in subsurface environments

The average oceanic sulphate concentration is 0.028 M (Millero, 1996). Before the discovery of hydrothermal vents, it was thought that sulphides in low temperature aqueous environments were a result of the microbial reduction of sulphate. This assumption was supported by the fact that sulphate is far more soluble than dioxygen in water, and thus sulphate is a more abundant electron acceptor for microbial respiration. Respiration *via* microbial sulphate reduction is the most important pathway for mineralisation of organic matter in marine sediments (Bottrell and Newton, 2006). In contrast, abiotic sulphate reduction at low temperatures is kinetically extremely slow (see Rickard and Luther, 2007). Although the microbial reduction of sulphate is a large and widespread process, it cannot solely explain the actual sulphur budget, which is solved by hydrothermal activity and other processes linked to burial diagenesis of methane and organic sulphur (*e.g.* Raiswell *et al.*, 1993).

In aqueous solutions, dissolved S(-II) exists mainly in the forms H_2S and HS^-. Contributions of S^{2-} are minor or non existent. Fig. 1.5 illustrates the activities of the main sulphide species as a function of the pH. The $pK_1(H_2S)$ is 6.99 ± 0.03 at 25°C and 1 bar (Suleimenov and Seward, 1997). It means that acidic pH systems will be dominated by H_2S whereas neutral to basic pH systems (and therefore in modern natural marine systems) will be dominated by HS^-. The $pK_2(H_2S)$ is less precisely constrained (mainly because of polysulphide contamination in experimental measurements), but estimated to be > 17 (Giggenbach, 1971; Schoonen and Barnes, 1988; Migdisov *et al.*, 2002). This means that S^{2-} has no significant activity in natural or most ambient temperature experimental systems. Polysulphide ions act as minor species in basic pH. They consist of chains of sulphur atoms that have never been individually isolated in aqueous solutions, but the sodium salts can be readily synthesised at high temperature (Rosen and Tegman, 1971). The evidence for their existence is based on an arithmetic analysis of spectroscopic data. They can also be identified using X-ray diffraction and fast scan voltammetry (*e.g.* Luther *et al.*, 2001). Polysulphide species are present at the oxic/anoxic interface, and H_2S/HS^-_{aq} and

dissolved FeS clusters dominate in reduced environments below the oxic/anoxic interface (Luther *et al.*, 2003). Models for the geometry of polysulphide species have been reported by Muller and Diemann (1987). As the Lowest Unoccupied Molecular Orbital (LUMO) of HS^- is at a very high energy state, HS^- is unlikely to be an electron acceptor. The Highest Occupied Molecular Orbital of HS^- (HOMO) is also higher than that of H_2S, making HS^- more susceptible to be an electron donor than H_2S. Consequently, HS^- acts as a Lewis base in aqueous solutions. H_2S can be an excellent electron acceptor but a poor electron donor due to the HOMO being at a very stable energy level. Thus H_2S can act as both a Lewis base or a Lewis acid in aqueous solutions.

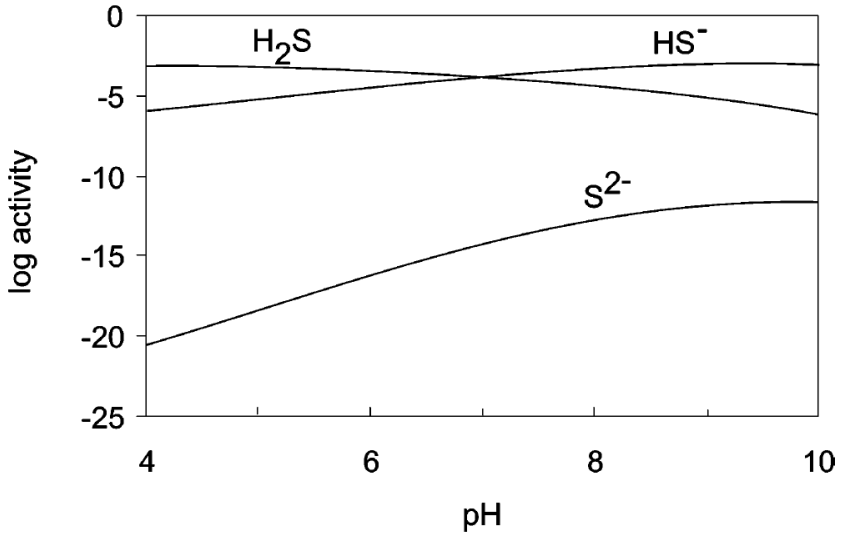

Figure 1.5: $S(-II)_{aq}$ speciation for $\Sigma\{S(-II)\} = 10^{-3}$ M. H_2S_{aq} dominates the S(-II) speciation for acidic pH. HS^- dominates the S(-II) speciation for near neutral to alkaline pH. The figure is from Rickard and Luther (2007).

1.2.1.2. Iron chemistry in subsurface environments

Iron is a trace metal in the present day upper ocean (Wu *et al.*, 2001) recognised as a limiting nutrient in large regions of the oceanosphere and in certain coastal areas (*e.g.* Johnson *et al.*, 1997). The upper ocean has nanomolar total Fe concentrations and some modern marginal environments display micromolar concentrations. The main sources for dissolved Fe are the input from the atmosphere (aerosols), the continental detrital input (*via* fluvial systems) and hydrothermal systems. Since Fe has a very short residence time in seawater, highest Fe concentrations are found near the sources *i.e.* in coastal and ridge areas.

In normal seawater, the dominant Fe-bearing aqueous species are Fe(III) hydroxyl complexes (*e.g.* $FeOH^{2+}$, $Fe(OH)_2^+$, $Fe(OH)_3$) and Fe^{2+}_{aq} (Turner *et al.*, 1981). The ferrous ion in aqueous solution is usually written as Fe^{2+}_{aq}, but essentially consists of the hexaqua complex $[Fe(H_2O)_6]^{2+}_{aq}$. The complex shows a coordination number of 6 and thus has an octahedral geometry. The cavity produced has the appropriate size to allow Fe^{2+} to be contained while providing enough space for significant Fe-OH_2 bonding interactions. The value for $\Delta G^o_f(Fe^{2+}_{aq})$ has been largely discussed (*e.g.* Randall and Frandsen, 1932; Patrick and Thompson, 1953; Sweeton and Baes, 1970; Whittermore and Langmuir, 1972; Cobble and Murray, 1978; Tremaine and LeBlanc, 1980). The value now commonly accepted is the modern IUPAC value of -90.53 ± 1 $kJ.mol^{-1}$ (Parker and Khodakovskii, 1995), although many published models have used the incorrect $\Delta G^o_f(Fe^{2+}_{aq})$ even recently (for review, see Rickard and Luther, 2007).

In oxic waters, dissolved Fe precipitates quantitatively as solid oxides at marine pH (Fig. 1.6). Although the stable Fe-oxides in the Fe-H_2O system are hematite (Fe_2O_3), magnetite (Fe_3O_4) and wüstite (FeO), the major observed phase is nanoparticulate goethite (FeOOH) and other oxy(hydr)oxides because the formation of more stable phases at ambient temperatures is kinetically hindered (van der Zee *et al.*, 2003).

Fe^{2+}_{aq} is much more soluble than $Fe(III)_{aq}$ species and Fe can remain dissolved in reduced anoxic environments (Fig. 1.6) for large spatial and temporal scales (Morse and Rickard, 2004). Fe in mantle and crustal rocks is mainly ferrous, so their weathering through hydrothermal vents produces Fe^{2+}_{aq} inputs to the ocean. Fe^{2+}_{aq} oxidation is thermodynamically favoured in oxic waters (Fig. 1.6), but other mechanisms responsible for the oxidation of hydrothermal Fe^{2+}_{aq} include abiotic photo-oxidation (Braterman *et al.*, 1984), O_2 oxidation from oxygenic cyanobacterial photosynthesis, anaerobic phototrophic Fe(II) oxidation by purple and green bacteria (*e.g.* Widdel *et al.*, 1993), nitrate reduction coupled Fe oxidation (*e.g.* Benz *et al.*, 1998) and O_2 reduction (*e.g.* Edwards *et al.*, 2000). Microbial Fe(II) oxidation is usually restricted to anoxic environments since the presence of O_2 would oxidise Fe(II) at a faster rate than microbial oxidation. Fe(II) acts as an electron donor for energy generation and/or carbon fixation (*e.g.* Emerson, 2000; Straub *et al.*, 2001). Photosynthetic Fe(II) oxidation may have played a major role in the early Earth history since oxygen contents in the atmosphere were very low.

All these mechanisms produce Fe(III) oxy(hydr)oxides or $Fe(III)_{aq}$ species that quickly precipitate as Fe(III) oxy(hydr)oxides. Further reduction of Fe(III) oxy(hydr)oxides and oxides involves DIR (*e.g.* Wells *et al.*, 1995; Lovley, 2006) or sulphidation mechanisms (*e.g.* Rickard, 1974; Pyzik and Sommer, 1981; Dos Santos Afonso and Stumm, 1992; Wei and Osseo-Asare, 1996) where H_2S_{aq} reduces Fe(III) into $Fe(II)_{aq}$ and Fe-S species as well as S(0). In dissimilatory Fe(III) reduction, Fe(III) acts as an electron acceptor required for bacterial respiration (*e.g.* Nealson and Saffarini, 1994). Fe(III) is reduced from Fe(III) oxides such as hematite, goethite and ferrihydrite and products are, in addition of $Fe(II)_{aq}$, FeOOH, siderite and ankerite under anaerobic conditions. In sedimentary basins, Fe^{2+}_{aq} mainly emanates from the bacterial reduction of Fe(III) minerals rather than from hydrothermal inputs. Note that the reduction of Fe(III) by bacterial activity occurs before sulphate reduction, near the suboxic-anoxic interface (Fig. 1.4).

Dissolved Fe is also involved in biogeochemical processes as a nutrient. Assimilatory Fe metabolism is the stepwise uptake and incorporation of Fe into the organisms, and the reaction products are Fe biomolecules (*e.g.* Lowenstam, 1981).

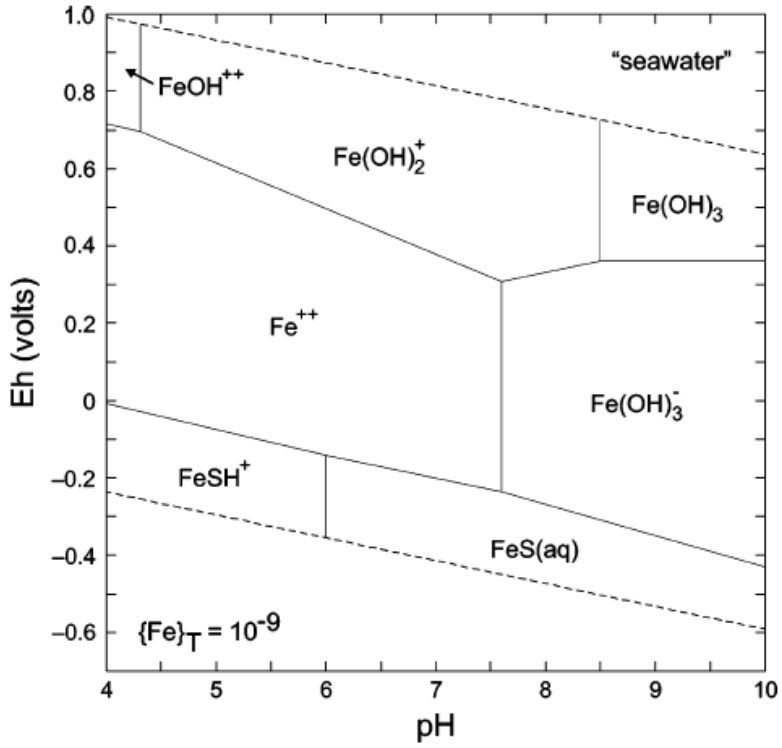

Figure 1.6: Eh-pH diagram illustrating the stability fields of dissolved Fe(III) and Fe(II) species in equilibrium with SO_4^{2-} for average seawater composition. The figure is from Rickard and Luther (2007).

1.2.2. Fe-S mineralogy: from complexes to minerals

Although a large variety of Fe-S minerals could form in aqueous systems, some of them have never been observed (or very rarely) in actual marine sediments. This is the case of cubic iron monosulphide, troilite, pyrrhotite, smythite and marcasite which are only rarely found in modern marine sediments. In contrast, the stable phase pyrite and the metastable phases mackinawite (FeS_m) and greigite (which have been however rarely clearly identified or assimilated to Acid Volatile Sulphides, or AVS) have been reported in natural sediments and play, along with dissolved FeS species and clusters, a major role for the global Fe-S biogeosystem. The Fe-S system has been investigated for about 160 years; however, as discussed below, some of the mechanisms involved in mineral forming reactions are still subject of debate.

1.2.2.1. Complexes and clusters in the Fe-S system

In marine environments, Fe complexes are present in many forms including $[Fe(H_2O)_6]^{2+}$, $[Fe(H_2O)_6]^{3+}$, $[FeHCO_3]^+$, $[Fe(OH)_3]^-$ and $[Fe(SH)]^+$. FeS clusters, referred here to FeS^0_{aq}, are defined as multinuclear iron sulphide complexes that develop to form the first nanoparticulate iron sulphide condensed phase. Solubility and voltammetric approaches are generally used to report the iron sulphide complexes and clusters (*e.g.* Chadwell *et al.*, 1999, 2001; Wincott and Vaughan, 2006). Although FeS clusters are well-known in biochemistry as they are essential components of FeS proteins, they were first measured in aqueous environments only in 1988 (Buffle *et al.*, 1988). FeS^0_{aq} as a dominant species has been widely observed in environments with greater than micromolar total dissolved S(-II) concentration (Rickard *et al.*, 2006) at marine pH range. The FeS^0_{aq} cluster stoichiometry could range from Fe_2S_2 to $Fe_{150}S_{150}$ (Rickard and Luther, 2007), where the first condensed phase of mackinawite appears with a 2 nm size (Wolthers *et al.*, 2003, 2005; Ohfuji and Rickard, 2006). As discussed below, FeS^0_{aq} clusters are very central components in the Fe-S reaction pathways and play an essential role in both mackinawite and pyrite formations, since they act as a dissolved intermediate phase. Clusters are also structural components of mackinawite, and molecular models for the smaller clusters (Rickard and Luther, 2007) have a similar structure as found in proteins. FeS^0_{aq} could be a link between the organic and the inorganic worlds in the iron sulphide system.

Metal sulphide complexes and clusters enhance the solubility of metal sulphide minerals in natural aqueous systems (Rickard and Luther, 2006). Many of the stability

constants in inorganic systems for metal sulphide complexes are very uncertain because of the lack of independent evidence for their existence. The formation of metal sulphide complexes involves a ligand substitution reaction, where the sulphide species replaces the water in the first coordination sphere of the free metal ion. As discussed above, both HS^- and H_2S are likely to interact with Fe(II) as electron donors because the LUMO of Fe(II) is more stable than the HOMO of both HS^- and H_2S. The octahedral geometry in hexaqua Fe(II) produces a cavity such that the metal ion can be contained whilst providing enough space for significant metal-OH_2 bonding interaction.

1.2.2.2. Mackinawite (FeS_m): the aqueous iron(II) monosulphide

The first condensed phase that occurs during the reaction between aqueous Fe(II) and S(-II) is the iron(II) monosulphide mackinawite, FeS_m (Wolthers *et al.*, 2005; Ohfuji and Rickard, 2006). Lennie *et al.* (1995) showed that crystallographic data support stoichiometric tetragonal FeS, but the stoichiometry of mackinawite remained uncertain until Rickard *et al.* (2006) showed that mackinawite is stoichiometric FeS. This material was previously described as amorphous FeS_{am} but structural analyses have demonstrated that the FeS_m phase is in fact tetragonal (Berner, 1962; Lennie *et al.*, 1995; Rickard, 1995; Wolthers *et al.*, 2005). The reason for these long-standing confusions emanated from analytical challenges to quantitatively assess nanomaterials. FeS_m is readily formed in aqueous solutions as a nanoparticulate precipitate (Wolthers *et al.*, 2003; Ohfuji and Rickard, 2006; Rickard *et al.*, 2006; Jeong *et al.*, 2008) and the first FeS_m nanoparticles precipitate with a 2 μm mean diameter (Wolthers *et al.*, 2003). Size determinations were reviewed by Ohfuji and Rickard (2006) and Jeong *et al.* (2008). Mackinawite nanocrystals have a platy shape (Fig. 1.7, *e.g.* Wolthers *et al.*, 2003) and Guilbaud *et al.* (2010) (chapter IV) suggested that FeS_m nanoparticles have a core-shell structure similar to those described for TiO_2, ZnS and NiS nanoparticles (Banfield and Zhang, 2001; Zhang *et al.*, 2003; Huang *et al.*, 2009). Such disordered-shell structures are favourable for aggregation growth (*e.g.* Zhang *et al.*, 2003) and Guilbaud *et al.* (2010a) showed that FeS_m nanoparticles are likely to grow *via* aggregation growth rather than Ostwald-ripening mechanism (chapter IV).

Investigations into the solubility of FeS_m (Rickard, 2006) are illustrated in Fig. 1.8 and show two distinct pH-areas. For acidic pH, the solubility of FeS_m is pH dependent

with a slope of -2. For neutral to alkaline regions, the solubility of FeS_m does not show a dependence on pH. This feature provides evidence for two competing reactions, depending on the pH and the total S(-II) concentration. In acidic solutions, log Σ[Fe(II)] is inversely proportional to pH, which is consistent with the dominance of H_2S for acidic pH, following Eq. 1.1:

$$FeS_m + 2H^+ = Fe^{2+} + H_2S \qquad (1.1)$$

$$\log K_{1,sp}(FeS_m) = \log\{Fe^{2+}\} + \log\{H_2S\} + 2pH \qquad (1.2)$$

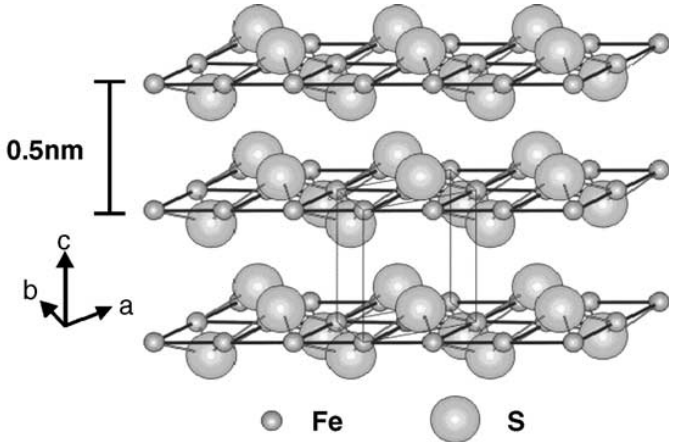

Figure 1.7: Illustration of the layered mackinawite stracture, from Ohfuji and Rickard (2006).

Rickard (2006) found a value for log $K_{1,sp}$ = 3.5 ± 0.25, consistent with the equilibrium shown in Eq. 1.2. Voltammetric titration has given evidence that the dissolved Fe(II) product in those acidic solutions is only Fe^{2+}. In alkaline solutions, log Σ[Fe(II)] is independent of the pH. Rickard (2006) showed that in this pH-independent area the dominant dissolved Fe(II) species is FeS^0_{aq}, and the solubility of FeS_m is given by Eq. 1.3:

$$FeS_m = FeS^0_{aq} \qquad (1.3)$$

for which log $K_0(FeS_m)$ = -5.7. Such pH-independent behaviour had been observed in 1999 (Davison *et al.*, 1999), but the complex $FeSH_2$, rather than the clusters FeS^0_{aq}, was supposed to be involved. The solubility constant $K_0(FeS_m)$ indicates that for a total sulphide concentration of $[S(-II)]_T < 10^{-5.7}$, FeS_m dissolves to form Fe^{2+}. FeS^0_{aq} as a dominant species is limited to environments with $[S(-II)]_T > 10^{-6}$ M.

The kinetics and mechanisms of FeS_m formation from aqueous solutions have been reported (Rickard, 1995) and involve two different pathways: the H_2S path

reaction (Eq. 1.4) and the HS^- path reaction (Eq. 1.5), as shown by the equations (4) and (5):

$$Fe^{2+}_{(aq)} + H_2S_{(aq)} = FeS_m + 2H^+_{(aq)} \qquad (1.4)$$

$$Fe^{2+}_{(aq)} + HS^-_{(aq)} = FeS_m + H^+_{(aq)} \qquad (1.5)$$

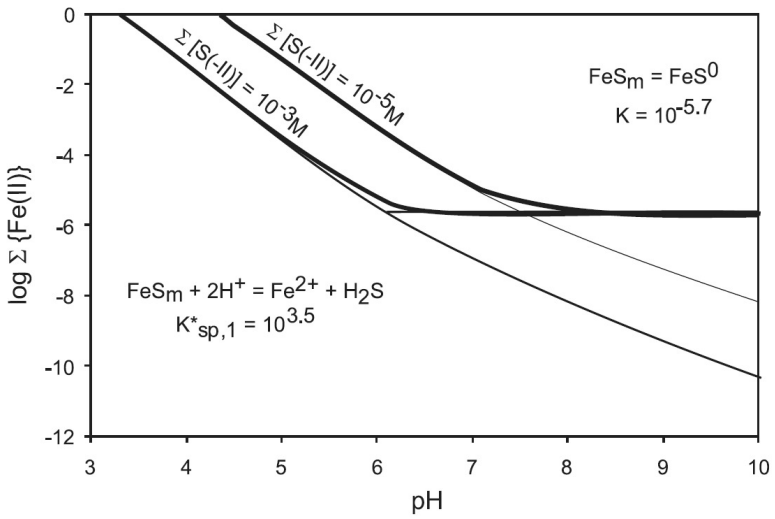

Figure 1.8: Solubility diagram for FeS_m, from Rickard (2006).

Both FeS_m forming reactions are non-redox (*i.e.* Fe and S remain in the same oxidation states) and proceed *via* the exchange of H_2O with either H_2S or HS^- followed by the release of protons after the formation of a charged inner sphere complex. Ligand exchange occurs between the outer-sphere sulphide and the inner-sphere water in the hexaqua Fe(II) to form $FeH_2S.(H_2O)_5^{2+}{}_{(aq)}$ (with $H_2S_{(aq)}$) or $Fe(HS).(H_2O)^{5+}{}_{(aq)}$ (with HS^-). The subsequent nucleation of FeS_m is fast. The reaction with HS^- involves cluster formation, as suggested by the solubility studies where $FeS^0{}_{aq}$ as a dominant species was found under alkaline conditions, in which HS^- is the dominant sulphide species. The rate laws for both reactions forming mackinawite are pH dependent and consistent with Eigen-Wilkins mechanisms (Eigen and Wilkins, 1965), in which the rate of reaction for most transition metals is determined by the rate of water exchange between the aqua-ion and the solvent. The rates of FeS_m formation are fast ($>10^7$ M^{-1} s^{-1}) and can be written as Eq. 1.6 for the reaction involving H_2S, where k_1 is the first order rate constant (s^{-1}):

$$\partial c_{FeS_m} / \partial t = k_1 \{Fe^{2+}\}\{H_2S\} \qquad (1.6)$$

For the reaction 1.5, the rate is more difficult to estimate because the HS^- consuming process is so fast. In sulphide rich systems, the rate of FeS_m precipitation is greater in neutral to alkaline solutions. By contrast in sulphide poor systems, the rate is greater in neutral to acid conditions.

1.2.2.3. Greigite (Fe_3S_4): the iron(II)-iron(III) thiospinel

Greigite is the sulphur analogue species to the iron oxide magnetite Fe_3O_4. Similarly to magnetite, Fe atoms in greigite occur in both ferric and ferrous states as $Fe^{II}Fe^{III}{}_2S_4$, where Fe^{II} atoms occur in tetrahedral sites and Fe^{III} atoms occur in octahedral sites. The cubic structure of Greigite shows homology with the structure of mackinawite, as pointed as by Yamaguchi and Katsurai (1960).

The solubility of greigite is poorly constrained and has only been measured once (Berner, 1967). This is due to the fact that the synthesis of pure greigite without residual FeS_m is hard to achieve (*e.g.* Benning *et al.*, 2000). The stability of greigite at total Fe concentrations lower than micromolar concentrations is insignificant. This is supported by field observations which suggest that greigite occurs scarcely in natural sediments.

Experiments carried out on greigite formation have shown that greigite forms from Fe-S species such as FeS_m after its partial oxidation. This could be reached by direct O_2 oxidation when FeS_m is shortly exposed to the open air (Lennie *et al.*, 1995). However in solution, the oxidation reaction involving H_2O produces H_2, which has not been seen experimentally (Butler, *pers. comm.*). Thus, under marine conditions, greigite formation was thought to be a solid state transformation that involves FeS_m plus sulphur which acts as an electron acceptor for FeS_m-Fe partial oxidation (Eq. 1.7):

$$3FeS_m + S^0 = Fe_3S_{4\,gr} \qquad (1.7)$$

Eq. 1.7 does not describe a mechanism, but only represents a net reaction, and as S(0) is found in nature as S_8, it makes it an improbable reaction step. Lennie *et al.* (1997) showed that greigite can form *via* solid diffusion of Fe(II) to octahedral and tetrahedral sites without changing the S lattice. The question of the electron acceptor remains in this case unsolved as there is no evidence for Fe(0) formation. Thus, greigite chemistry remains contentious, particularly for its role during pyrite

formation (Wilkin and Barnes, 1996, 1997; Benning *et al.*, 2000; Butler and Rickard, 2000; Rickard *et al.*, 2001).

1.2.2.4. Pyrite (FeS_2)

Pyrite is the most common sulphide ore on the Earth's surface. The structure of pyrite is a NaCl type structure, where the S_2 groups are situated at the cube centre and at the midpoints of the cube edges and the low-spin Fe^{II} atoms are situated at the corners and face centres (Fig. 1.9).

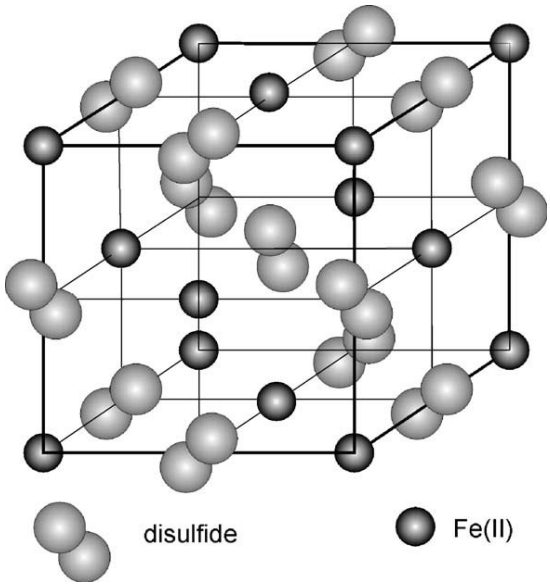

Figure 1.9: Pyrite structure with Fe atoms in dark grey and bisulphide groups in bright grey. The figure is from Rickard and Morse (2005).

Pyrite is an extremely sparingly soluble mineral and its solubility in ambient temperature solutions is too low to be measurable. In terms of $\{Fe^{2+}\}\{H_2S\}$ and at pH 7, the solubility of pyrite is given as $10^{-21.2}$ (for discussion, see Rickard and Luther, 2007). Mackinawite has been described as a precursor mineral in the literature (*e.g.* Rickard, 1969; Berner, 1970; Sweeney and Kaplan, 1973; Schoonen and Barnes, 1991; Canfield *et al.*, 1992; Wilkin and Barnes, 1996). However, it is not necessary reactant for pyrite formation. Mechanistically, it has been demonstrated that the formation of pyrite is not a solid state transformation and requires the formation of a dissolved Fe-S transition intermediate (*e.g.* Luther, 1991; Rickard and Luther, 1997). This means that any other Fe bearing mineral can be used as a reactant. Experimentally, pyrite has been synthesised using troilite, mackinawite, greigite, Fe oxy(hydr)oxides, Fe salts and Fe carbonates as reagents (for a review, see Rickard and

Luther, 2007). Naturally, pyrite is associated to mackinawite and greigite. Wilkin and Barnes (1996) suggested that greigite was a necessary prerequisite for the formation of framboidal pyrite, which was disproved by Butler and Rickard (2000). Experimentally, FeS_m has been the mineral the most often used for pyrite formation because in the highly supersaturated conditions required for pyrite nucleation, the system will tend to be saturated with respect to FeS_m. Batch pyrite synthesis requires a supersaturation level, whose reactants concentrations are much greater than natural concentrations. However, Harmandas *et al.* (1998) performed pyrite precipitation from undersaturation using a chemostatic continuous flow reactor.

Pyrite formation involves two distinct physical processes: nucleation and crystal growth. The relative rates of pyrite nucleation and crystal growth have been discussed in Rickard and Luther (2007), and once pyrite starts nucleating, the rate of pyrite formation is controlled by the rate of pyrite crystal growth. Therefore, it is crystal growth that is responsible for bulk pyrite formation in sediments. The stoichiometry and rates of pyrite formation have been described for two mechanisms: the polysulphide pathway and the H_2S pathway (*e.g.* Rickard, 1975, 1997; Luther, 1991; Rickard and Luther, 1997). The other pathways actually result from these two reactions, as noted by Butler *et al.* (2004) for the so-called "iron loss pathway", or involve solid state transformations which are inconsistent with experimental and natural observations. As $S(-II)_{aq}$ speciation strongly depends on pH (section 1.2.1.1 of this chapter), both mechanisms depend themselves on the reaction pH. Voltammetric evidence (Luther, 1991; Rickard, 1997) support that the dissolved Fe(II) species FeS^0_{aq} is involved in both reactions, and Rickard *et al.* (2001) observed that FeS^0_{aq} suppression inhibits subsequent pyrite formation. The rates of both of the pathways have been determined by Rickard (1995, 1997). The polysulphide mechanism has been confirmed by Luther (1991). The rate of pyrite formation is first order with respect to polysulphide and second order with respect to FeS_m surface area.

At pH 7, pyrite forms at a rate of ~ 8 x 10^{-11} M L^{-1} s^{-1} *via* the polysulphide pathway when FeS_m is present (Eq. 1.8)

$$FeS_m \rightarrow FeS^0_{aq} + S^{2-}_n = FeS_2 + S^{2-}_{n-1} \qquad (1.8)$$

The reaction with H_2S forms pyrite at a rate of ~ 2 x 10^{-8} M L^{-1} s^{-1} at pH 7 when FeS_m is present (Eq. 1.9):

$$FeS_m \rightarrow FeS^0_{aq} + H_2S_{(aq)} = FeS_2 + H_2 \qquad (1.9)$$

The persistence of metastable FeS_m with H_2S is well known (*e.g.* Benning and Barnes, 1998; Benning *et al.*, 1999, 2000) and is due the inhibition of pyrite nucleation. According to the pH speciation of the sulphide components, the polysulphide pathway should be initially rate limiting under alkaline conditions, and might reflect the rate of pyrite nucleation. As the system becomes more and more reduced and acidic, the H_2S pathway should become rate limiting. Rickard and Morse (2005) suggested a global rate equation for pyrite formation including both pathways (Eq. 1.10):

$$\partial[FeS_{2p}]/\partial t = k_{H_2S}[FeS_m][H_2S] = k_{S_n(-II)}[FeS_m]^2[S(0)][S(-II)]_T[H^+] \quad (1.10)$$

where k are the rate constants for H_2S and polysulphide reactions (s^{-1}). In alkaline sulphidic environments, the H_2S concentration approaches 0 and the rate is only dependent on S(0), S(-II) and pH.

In the H_2S pathway, sulphur present in the product pyrite is derived from the FeS_m and H_2S reservoirs. Thus, the sulphur isotopic composition of pyrite should represent the input of both the FeS_m and H_2S reservoirs. In the polysulphide pathway, Butler *et al.* (2004) have suggested that pyrite inherits the sulphur from the polysulphide. However, they have shown that the synthetic pyrite sulphur signature is more complex than predicted, due to small isotopic exchange with the sulphide reservoir. This isotopic study supports the predicted mechanisms for pyrite formation.

Fig. 1.10 illustrates the computed Eh-pH stability field diagram for the Fe-S-H_2O system at 25°C. Pyrite is the stable phase in any reduced anoxic environment for total Fe(II) and S(-II) activities > 10^{-3} M (light grey) but not for low total Fe(II) and S(-II) activities (dark grey). The pyrite supersaturation is very sensitive to pH and Eh near the upper redox boundary, possibly impacting upon the subsequent pyrite textures, as the supersaturation condition, and therefore the nucleation rates are changing. The diagram (Fig. 1.10) illustrates that pyrite is present at the oxidised boundary of dissolved sulphides or iron monosulphides. Indeed both pyrite forming mechanisms involve the oxidation of S, from S(-II) to S(-I) concerning the H_2S pathway, and from mixed valence S(-II) and S(0) to S(-I) concerning the S_n^{2-} pathway. Even from highly supersaturated conditions with respect to FeS_m, this oxidation step is not facile in the strict absence of S(0) or O_2, making pyrite nucleation difficult. Similarly, pyrite crystal growth is also an oxidation reaction rather than simple accretion of Fe and S atoms at the crystal surface.

Figure 1.10: Eh-pH diagram for the Fe-S-H_2O system at 25°C. Pyrite stability field is illustrated by the grey areas. The darkest grey represents the pyrite stability field for $\Sigma\{Fe(II)\} = 10^{-6}$ M. The lightest grey represents the pyrite stability field for $\Sigma\{Fe(II)\} = 10^{-3}$ M. Increasing total {Fe(II)} and {S(-II)} from micro- to millimolar concentrations induces the extension of the FeS_2 stability field (illustrated by the grey gradient). The figure is from Morse and Rickard (2004), modified after Butler and Rickard (2000).

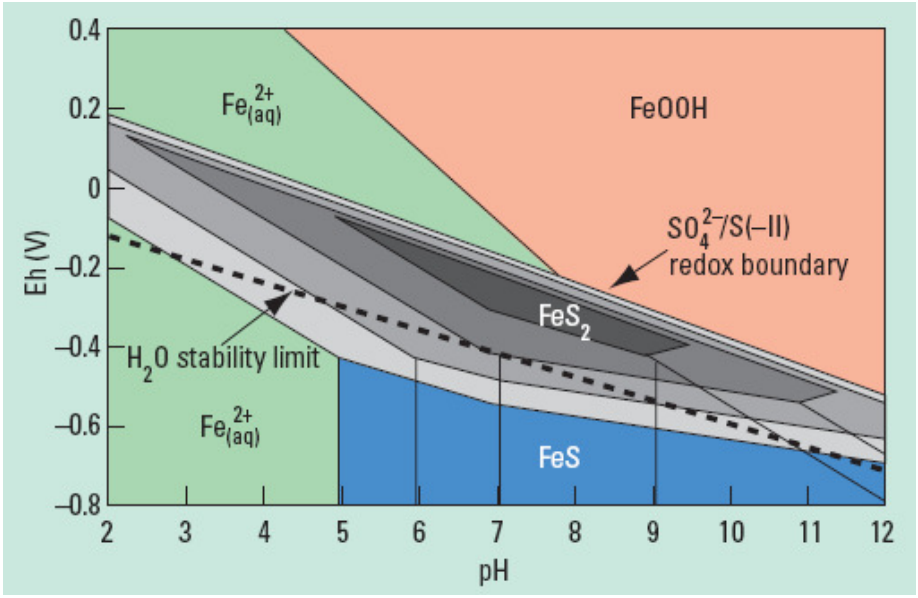

1.2.2.5. A brief overview on other iron sulphides

Cubic FeS_c has never been found in nature, but is a metastable corrosion product of the reaction between H_2S and metallic Fe (Murowchick and Barnes, 1986). The pyrrhotite group and troilite FeS_t have been observed extremely rarely in sediments. Pyrrhotite commonly occurs naturally at higher temperatures, in igneous and metamorphic rocks or hydrothermal veins, and is therefore the most common iron sulphide in the solar system (see Rickard and Luther, 2007). Smythite, Fe_9S_{11s}, occurs naturally in brackish sediments, *via* sulphidation of siderite (Furukawa and Barnes, 1996). Marcasite, orthorhombic FeS_2, is a common mineral forming in hydrothermal vents. Marcasite precipitation requires acid conditions (*e.g.* Schoonen and Barnes, 1991), avoiding its formation in normal marine environments.

1.2.3. Summary: reaction pathways in the diagenetic Fe-S system

Fig. 1.11 is a simplified overview of the Fe-S system under diagenetic conditions. Mackinawite can precipitate from normal seawater in the presence of millimolar S(-II) concentrations in the water column. The HS^- pathway is likely to be the main

mechanism for mackinawite formation in natural anoxic sedimentary environments, involving FeS^0_{aq} intermediates. It is also possible that FeS_m forms *via* sulphidation of Fe(III) minerals such as goethite, (*e.g.* Rickard, 1974; Pyzik and Sommer, 1981; Wei and Osseo-Asare, 1996), where the mineral surface is reduced by HS^- to produce sulphur S^0 and Fe(II) hydroxides which dissolves and react to precipitate FeS_m. For nanomolar Fe concentrations, FeS_m does not precipitate for pH < 8. FeS_m has a significant stability for pH>6 and micromolar Fe concentration. This means that in marine sediments (pH ~8-8.5), FeS_m is not likely to precipitate if Fe concentration is less than micromolar. FeS^0_{aq} will be however the dominant aqueous species, since the total sulphide concentration is > 1 μM.

Pyrite is the ultimate Fe sequestering phase. Pyrite can form diagenetically in sediments overlain by oxic waters (normal marine conditions) or directly in the water column when H_2S is present in the overlying water. Both pathways have been reported for pyrite formation in the Black Sea (Rickard and Luther, 2007 and references therein). In anoxic environments, H_2S and HS^- are the predominant forms of sulphide species, favouring the H_2S pathway as the main reaction for pyrite formation. At the oxic/anoxic interface and pH>7.5, however, the polysulphide reaction becomes predominant in alkaline solutions since H_2S becomes a minor species. Polysulphides may form at the Fe(III) minerals surface when sulphur is produced by sulphidation of Fe(III) by H_2S.

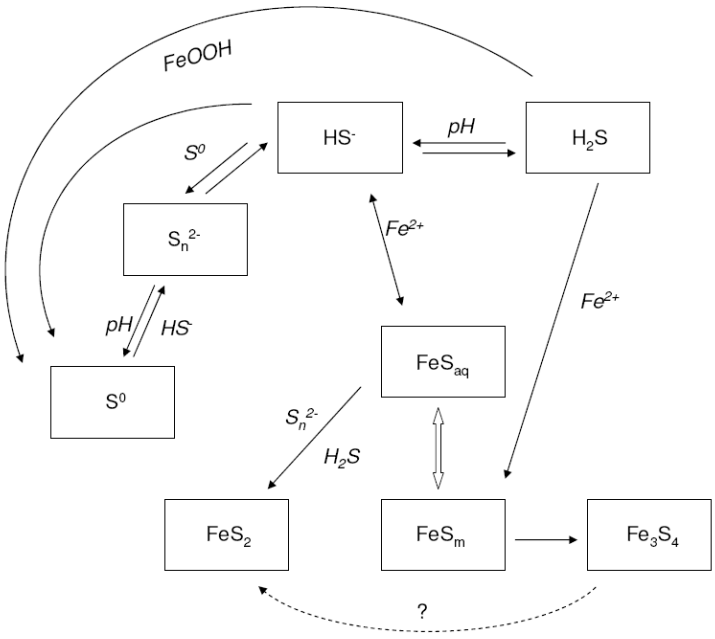

Figure 1.11: Scheme of the diagenetic Fe-S pathways under anoxic conditions.

1.3. A "non-traditional" approach: Fe isotope geochemistry

The recent development in analytical capability opened up an entire field of research into transition metal isotope geochemistry. The importance of Fe and S in the bulk terrestrial cycles highlights the potential role for Fe isotope as a tool for tracing biogeochemical processes. After the first measurements in 1999 (*e.g.* Beard *et al.*, 1999), an exponentially increasing collection of natural and experimental data have been published. Table 1.1 summarises the natural variations of some transition metal isotopes. As briefly mentioned above, Fe isotopes received particular attention with respect to other transition metals.

1.3.1. General concepts and nomenclature

The relative atomic mass of an element is determined by the abundance of each isotope of the element. As an example, Fe has an atomic mass of 55.845, which results from the mixture of 5.81 wt% ^{54}Fe, 91.723 wt% ^{56}Fe, 2.21 wt% ^{57}Fe and 0.281 wt% ^{58}Fe (Taylor *et al.*, 1992). In a natural sample any deviation from this distribution, *i.e.* the preferential concentration of some isotopes with respect to the others, is called isotope fractionation. When measuring isotope ratios, these deviations from the relative abundances can be so small that they only affect the fourth or fifth decimal place of the ratio. For this reason, depending on the order of magnitude of the deviation, isotope compositions are usually reported with conventional δ or ε notations expressed by Eqs. 1.11 and 1.12:

$$\delta = \left(\frac{R_{sample}}{R_{std}} - 1 \right) \times 1000 \qquad (1.11)$$

$$\varepsilon = \left(\frac{R_{sample}}{R_{std}} - 1 \right) \times 10000 \qquad (1.12)$$

where R stands for the isotope ratio in the sample and in the standard (*std*).

The magnitude of isotope fractionations is usually inversely proportional to the mass and proportional to the isotope mass difference (*e.g.* Criss, 1999). Larger isotope fractionations thus occur for lighter elements and follow the $(m_{heavy}\text{-}m_{light})/(m_{heavy} \times m_{light})$ ratio, m referring to the mass of the isotope. For iron isotopes, the relative isotope mass differences are small and measured variations in R_{sample}/R_{std} concern the third or the fourth decimal place. Hence, the commonly adopted notation for the isotopic composition in iron is given by the δ value (Eqs. 1.13 & 1.14):

$$\delta^{56}Fe = \left(\frac{(^{56}Fe/^{54}Fe)sample}{(^{56}Fe/^{54}Fe)std} - 1 \right) \times 10^3 \qquad (1.13)$$

$$\delta^{57}Fe = \left(\frac{(^{57}Fe/^{54}Fe)sample}{(^{57}Fe/^{54}Fe)std} - 1 \right) \times 10^3 \qquad (1.14)$$

The reason why isotopes fractionate between molecules is energy related. Two identical molecules with different isotopes have a different zero point energy (Fig. 1.12, Urey, 1947). Zero point energies are mass-dependent because they are functions of the vibrational frequencies of the inter-atomic bonds, which themselves depend on the mass of the atoms. The vibrational frequency being inversely proportional to the mass, heavier isotopes make stronger bonds with respect to lighter isotopes. Thus, two similar molecules made from different isotopes have a slightly different strength in bonds which is responsible for the occurrence of isotope fractionation between these two molecules. Any mechanism or parameter that may affect the bond environment of the molecule will contribute in some extent to the isotopic fractionation. These mechanisms can involve metabolic reactions (mass preferential uptake from organisms), changes in the redox state, in the coordination geometry, in the quantum properties of the molecule and in the nature of the ligands.

At equilibrium, heavier isotopes tend to concentrate in the species with the shortest, strongest bond, and thus they generally concentrate in species i) with the higher oxidation state, ii) involving the most covalent bonds, iii) involving low coordination numbers and iv) involving low spin configuration for transition metals (Schauble, 2004). These general trends are qualitative and must be treated with care. The $Fe(III)_{aq}$-$Fe(II)_{aq}$ couple, in which heavier isotopes concentrate in the ferric species (*e.g.* Johnson *et al.*, 2002) is in good agreement with these qualitative rules. But in the case of pyrite, in which Fe is in its ferrous state, calculations predict the concentration of heavy Fe isotopes in the mineral. Note that in pyrite, Fe(II) is low spin (Rickard and Luther, 2007) and involves covalent bonds. Criss (1999) reviewed in detail the fundamentals of stable isotope fractionation and Schauble (2004) reviewed these fundamentals focussing on "non-traditional" isotope systems.

Figure 1.12: Diagram illustrating the small difference in zero point energy between the same molecule AB with difference isotope x and y (x being heavier than y). The figure is from Anbar and Rouxel (2007).

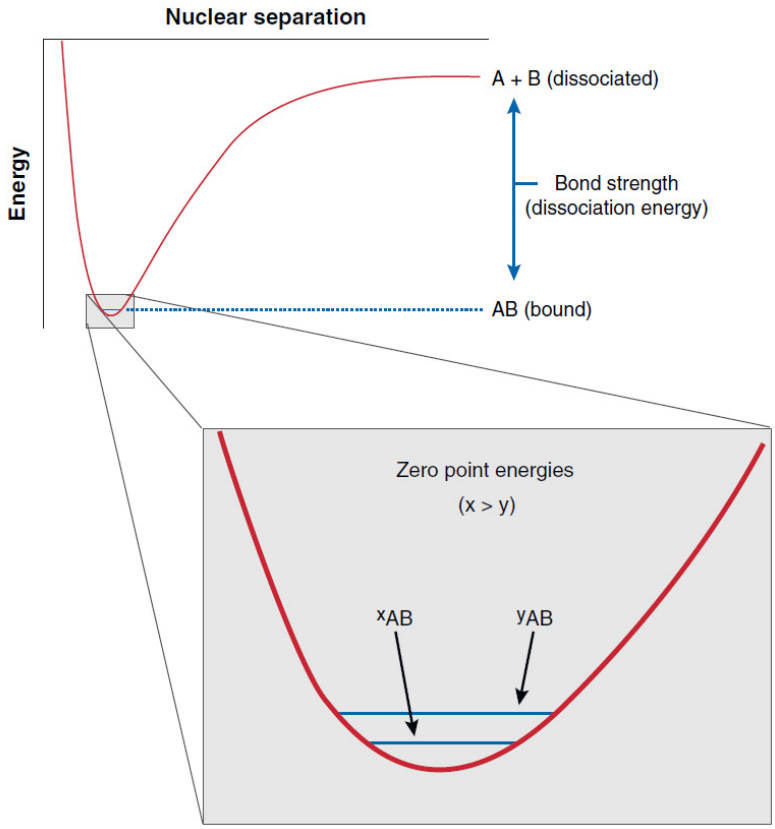

1.3.1.1. Kinetic and equilibrium isotope fractionations

Marcus' theory (Marcus, 1964) showed the dependence between the change in free energy and the kinetics of electron transfer. Kavner *et al.* (2005) extended this theory to isotope fractionation and suggested that electron transfer should result in kinetic isotope fractionation. Kinetic isotope fractionation is a common natural phenomenon that occurs during unidirectional or incomplete reaction. Since lighter isotopes participate more quickly in reactions than do heavier isotopes, the first reaction products will typically be characterised by depletion in heavy isotopes, *i.e.* enrichment in lighter isotopes. Chemical equilibria are often dynamic, and atoms exchange between the different phases in a 1:1 ratio. Thus, a system in isotopic equilibrium reflects true chemical equilibrium (thermodynamic equilibrium), which is reached when the atomic exchange between the species makes no difference in their energy state, *i.e.* in their isotopic signature. Equilibrium isotopic fractionation is the signature of an isotopic exchange towards the energetically most stable state. Both equilibrium and kinetic mass fractionation of stable isotopes are expected to become smaller with the decrease of the relative mass difference between the isotopes (*e.g.* Urey, 1947; Criss, 1999).

Natural samples	Cu	Zn	Mo	Fe	Ni	Cr
meteorites	1,2,3	1, 3		3,29,30,31,32	3,5,6,7,8,10	10,11
igneous rocks	24,25	24	13	27,28,33,36	5,6	4
sediments	22,26	26	13,14,15,16,17,18,19,20	37,38,39,40,41,42,43	5	
hydrothermal fluids and ores	21,22, 24, 25,26	24,26	12	21,35,37		
biological products	23,26	23,26		23,44		
ground/sea water	9	9	12, 13	34,43		4

1 Luck et al., 2005
2 Luck et al., 2003
3 Moynier et al., 2007
4 Ellis et al., 2002
5 Cameron et al., 2009
6 Cook, et al., 2008
7 Quitte, et al., 2008
8 Shimamura et al., 1983
9 Bermin et al., 2006
10 Birck & Lugmair, 1988
11 Rotaru et al., 1992
12 McManus et al., 2002
13 Siebert et al., 2003
14 Poulson et al., 2006
15 Siebert et al., 2005
16 Nagler et al., 2005
17 Arnold et al., 2004
18 Siebert et al., 2006
19 Wille et al., 2007
20 Pearce et al., 2008
21 Graham et al., 2004
22 Zhu et al., 2000
23 Becker et al., 2005
24 Mason et al., 2005
25 Larson et al., 2003
26 Marechal et al., 1999
27 Beard et al., 2003
28 Wiesli et al., 2003
29 Zhu et al., 2001
30 Mullane et al., 2002
31 Kehm et al., 2003
32 Poitrasson et al., 2005
33 Poitrasson & Freydier, 2005
34 Zhu et al., 2000b
35 Sharma et al., 2001
36 Beard & Johson, 2004
37 Beard et al., 2003b
38 Yamagushi et al., 2004
39 Matthews et al., 2004
40 Johnson et al., 2003
41 Rouxel et al., 2005
42 Archer and Vance 2006
43 Severmann et al., 2006
44 Walczyk & von Blanckenburg, 2002

Table 1.1: A non exhaustive list of the measurement of some transition metal isotopes in natural samples.

Although necessary for interpreting natural data, it is often difficult to establish if measured compositions reflect kinetic or true equilibrium effects because they can both act simultaneously (*e.g.* Welch *et al.*, 2003). Of course natural systems are often characterised by kinetic fractionations because the kinetics of geochemical reactions can be slow and thus incomplete. Equilibrium fractionations reflect the very end of a process, but systems can stay in metastable disequilibrium for large temporal scales as will be discussed in chapters IV and V.

1.3.1.2. High and low temperature processes

The fractionation $\Delta^{i/j}_{A\text{-}B}$ for the isotope ratio *i/j* between two phases *A* and *B*, is the difference in their respective isotopic composition $\delta^{i/j}_{A}$ and $\delta^{i/j}_{B}$ (Eq. 1.15):

$$\Delta^{i/j}_{A-B} = \delta^{i/j}_{A} - \delta^{i/j}_{B} \qquad (1.15)$$

Similarly, the isotope equilibrium fractionation factor, α, is given by Eq. 1.16:

$$\alpha^{i/j}_{A-B} = \frac{\delta^{i/j}_{A} + 1000}{\delta^{i/j}_{A} + 1000} \qquad (1.16)$$

Because α is very close to unity, Eq. 1.16 can be approximated into Eq. 1.17:

$$10^3 \ln \alpha^{i/j}_{A-B} \approx \Delta^{i/j}_{A-B} \qquad (1.17)$$

Kinetic and equilibrium isotope fractionations decrease with increasing temperature, usually as a linear function of $1/T$ or $1/T^2$, where T is the temperature in K (*e.g.* Urey, 1947). Indeed, the higher the temperature, the more energy provided to the system to permit isotope homogenisation, annihilating any fractionation. It can be thus assumed that at very high temperature, the fractionation approaches zero. Some isotope systems, for their temperature dependence, can be used as geothermometers. As an example, Bottinga and Javoy (1973) showed that for temperatures < 500°C, O isotope fractionation is described by $10^3 \ln\alpha = X/T^2 + Y$, whereas for temperatures > 500°C, it is described by $10^3 \ln\alpha = X/T^2$, where X and Y are equilibrium constants.

High temperature processes include evaporation, condensation, diffusion and phase partitioning. Equilibrium fractionations are often biased by larger kinetic effects during evaporation and condensation, whilst both equilibrium and kinetic fractionations compete in high temperature diffusion and phase partitioning. Dauphas

and Rouxel (2006) reviewed the theoretical work established for high temperature processes.

1.3.2. Theoretically computed Fe fractionation factors

Equilibrium fractionation factors between two species A and B can be calculated from the partition factors, or β-factors, of A and B as described by Eq. 1.18:

$$10^3 \ln \alpha_{A-B}^{i/j} = 10^3 \ln \beta_A^{i/j} - 10^3 \ln \beta_B^{i/j} \qquad (1.18)$$

where α stands for the fractionation factor between *A* and *B* for the isotope ratio *i/j* and β for the partition factor of *A* and *B* for the isotope ratio *i/j*. Calculated equilibrium fractionation factors are useful as they anticipate the fractionation that may occur in nature, often inaccessible by experiments. In the Fe isotope system, the β-factors have been typically estimated from vibrational data and empirical force field model (the Modified Urey-Bradley Force Field model, MUBFF, Schauble *et al.* (2001)), from Density Function Theory (Jarzecki *et al.*, 2004; DFT, *e.g.* Anbar *et al.*, 2005), or from Mössbauer and inelastic nuclear resonant X-ray scattering (INRXS) data (*e.g.* Polyakov and Mineev, 2000; Polyakov *et al.*, 2007). Thus, theoretical computations rely on various methods that all result from quantum mechanics of molecular vibrational modes and rotation (*e.g.* Urey, 1947; Schauble, 2004).

β-factors have been estimated for metal Fe (Polyakov, 1997; Polyakov and Mineev, 2000; Schauble *et al.*, 2001; Polyakov *et al.*, 2007) hexaqua Fe(II) (Schauble *et al.*, 2001; Jarzecki *et al.*, 2004; Anbar *et al.*, 2005; Domagal-Goldman and Kubicki, 2008; Ottonello and Zuccolini, 2009); hexaqua Fe(III) (Schauble *et al.*, 2001; Jarzecki *et al.*, 2004; Anbar *et al.*, 2005; Hill and Schauble, 2008; Domagal-Goldman and Kubicki, 2008; Hill *et al.*, 2009; Ottonello and Zuccolini, 2009); numerous ferrous and ferric complexes including chloro- and bromo- complexes (Schauble *et al.*, 2001; Hill and Schauble, 2008; Hill *et al.*, 2009); goethite and various FeOOH species (Polyakov and Mineev, 2000); magnetite (Polyakov and Mineev, 2000; Polyakov *et al.*, 2007); hematite (Polyakov and Mineev, 2000; Polyakov *et al.*, 2007; Blanchard *et al.*, 2009); siderite (Polyakov and Mineev, 2000; Polyakov *et al.*, 2007; Blanchard *et al.*, 2009); clino- and orthopyroxenes (Polyakov and Mineev, 2000); olivine (Polyakov and Mineev, 2000); pyrite (Polyakov and Mineev, 2000; Polyakov *et al.*, 2007; Blanchard *et al.*, 2009); and other sulphide minerals such as troilite, marcassite and Fe_3S (Polyakov *et al.*, 2007).

1.3.2.1. High temperature predictions

Theoretical computations suggest that terrestrial high temperature processes should record measurable Fe isotope fractionations, *i.e.* > 0.1 ‰ (Polyakov and Mineev, 2000). Geologically important systems involve metal-silicate fractionations to assess Fe isotope fractionations associated with the core-mantle differentiation. I compare the theoretical predictions with experimentally determined fractionation factors and measured natural data later.

1.3.2.2. Example of a low temperature process: the aqueous Fe^{3+}/Fe^{2+} couple

Redox processes contribute to isotope fractionation because they involve changes in the electronic configuration of the transition metal. Thus, they are directly linked to the bond strength of a molecule. For instance, Anbar *et al.* (2005) investigated the bond strengths and vibrational frequences of $[Fe(H_2O)_6]^{2+}$ and $[Fe(H_2O)_6]^{3+}$. Fe(III) has a d^5 configuration unlike Fe(II) which has a d^6 configuration. Consequently, the metal-ligand bond in the Fe(III) species is shorter and stronger than in the Fe(II) species. According to the equilibrium fractionation theory, heavier isotopes make the stronger bonds and will have the tendency to concentrate into $[Fe(H_2O)_6]^{3+}$. As shown by Fig. 1.13, stronger bonds display shorter length. Anbar *et al.* (2005) reported from their models equal Fe-O bonds of 2.039 Å for $[Fe(H_2O)_6]^{3+}$ whereas in $[Fe(H_2O)_6]^{2+}$, the four equatorial bond lengths are 2.11 Å and the two axial lengths are 2.14 Å. According to the kinetic fractionation theory, lighter isotopes will participate more quickly in chemical reactions because the Fe-ligand bond will be broken more readily.

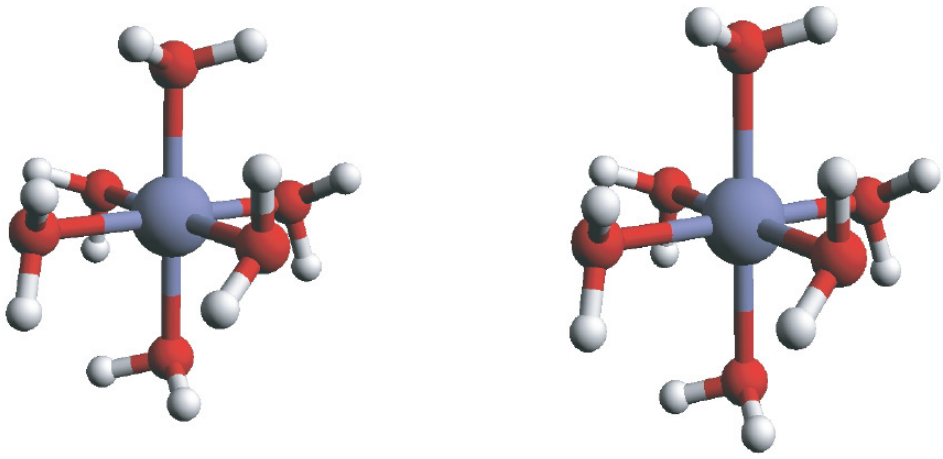

Figure 1.13: Molecular models for $[Fe(H_2O)_6]^{3+}$ (left) and $[Fe(H_2O)_6]^{2+}$ (right), drawn with ArgusLab©. Data are from Anbar *et al.* (2005). The Fe(II) species displays larger axial bonds than the Fe(III) species.

1.3.2.3. Issues for unidirectional or incomplete chemical reactions

Theoretical computations are limited to the determination of equilibrium fractionation factors. When possible, it is thus extremely convenient to compare calculated predictions with experimentally derived data, which can provide both kinetic and equilibrium fractionation factors. As Beard *et al.* (2010) pointed out, it is generally the case that good agreement between computationally and experimentally derived fractionation factors are obtained for fluid-fluid (*e.g.* Johnson *et al.*, 2002; Hill *et al.*, 2009) or mineral-mineral fractionations (*e.g.* Shahar *et al.*, 2008), and that fluid-mineral systems are usually less consistent (*e.g.* Johnson *et al.*, 2005b; Beard *et al.*, 2010). Natural data are controlled by geological processes, which are themselves often characterised by unidirectional, metastable, or incomplete reactions, which are likely to record kinetic fractionations. Discrepancies between natural samples and calculated equilibrium predictions can be source of controversy (*e.g.* Rouxel *et al.*, 2005; Archer and Vance, 2006, chapter VI).

1.3.3. Improvement of analytical capability for the measurement of experimental and natural Fe isotope data

As mentioned above, typical Fe isotope fractionations in natural samples are relatively small (less than 5 ‰, and often clustered at ~ 1 ‰). It is, for comparison, at least one order of magnitude less than the fractionations occurring within more traditional C-O-S isotope systems. The observation of any fractionation with acceptable precision in the Fe isotope system therefore presented major analytical challenges. The first measurements of Fe isotope ratios were performed in the late 40s (Valley and Anderson, 1947). Since the 80s, thermal ionisation mass spectrometry permitted the analysis of $^{56/54}$Fe and $^{57/54}$Fe ratios with a precision of ± 0.6 ‰ at the 2σ level (Gotz and Heumann, 1988; Walczyk, 1997; Bullen and McMahon, 1998). It was the development of inductively-coupled plasma mass spectrometry (Walder and Freedman, 1992; Walder *et al.*, 1993; Halliday *et al.*, 1998) that permitted precise and accurate measurement of Fe isotope ratios with precision as low as ± 0.05 ‰

(Guilbaud *et al.*, 2010b). Detailed descriptions of the instrumental development and the analytical protocols are given in chapters II and III.

The major challenge for high precision measurements of Fe isotopes with MC-ICP-MS is the removal of polyatomic and atomic isobaric interferences produced in the Ar plasma. Additional interferences can be due to sample matrix. Isobaric interferences for Fe isotopes are typically $^{40}Ar^{14}N^+$ and $^{54}Cr^+$ on $^{54}Fe^+$, $^{40}Ar^{16}O^+$ on $^{56}Fe^+$, $^{40}Ca^{16}OH^+$ and $^{40}Ar^{16}OH^+$ on $^{57}Fe^+$, and $^{40}Ar^{18}O^+$ and $^{58}Ni^+$ on $^{58}Fe^+$. Column chemistry is inevitable to remove Ca, Cr and Ni inputs from natural samples. Various strategies have been developed to reduce, eliminate, or resolve the interferences due to atmospheric elements such as H, N, O created in the Ar plasma: i) sample desolvation (Anbar *et al.*, 2000; Belshaw *et al.*, 2000; Sharma *et al.*, 2001; Roe *et al.*, 2003), ii) cold plasma (Walczyk and von Blanckenburg, 2002; Kehm *et al.*, 2003), iii) high resolution multi-collection (Malinovsky *et al.*, 2003; Weyer and Schwieters, 2003) and iv) collision cell technology (Beard and Johnson, 1999; Mullane *et al.*, 2003; Rouxel *et al.*, 2003; Dauphas *et al.*, 2004a). Chromium and nickel interferences can be monitored and corrected if present (*e.g.* Vogl *et al.*, 2003; Dauphas *et al.*, 2004a). Some authors (*e.g.* Belshaw *et al.*, 2000) used HCl matrix instead of HNO_3^- to minimise the formation of ArN^+, and high concentrations of Fe (up to 10 ppm) in order to increase the signal-to-background ratio. The use of cold plasma has been only investigated by a few studies (Walczyk and von Blanckenburg, 2002; Kehm *et al.*, 2003). The plasma power is reduced to 600 W instead of ~1500 W in order to reduce significantly the $^{40}Ar^{14}N^+$ and $^{40}Ar^{16}O^+$ intensities relative to the Fe signal (sensitivity). However, the ionisation efficiency also decreases, reducing considerably the sensitivity. Cold plasma also does not remove the $^{40}Ar^{16}OH^+$ interferences on $^{57}Fe^+$. High mass resolution is the most robust method to solve the interference issue. The resolving power is a dimensionless mass ratio that reflects the ability to separate the interference peak from the Fe peak. Fe peaks can be separated from molecular interference peaks with a resolving power of ~3000 (Vogl *et al.*, 2003) and flat peaks can be preserved with resolving power of ~9000 (Weyer and Schwieters, 2003).

The incorporation of a hexapole reaction cell into the standard MC-ICP-MS instrumentation can lead to the removal of $^{40}Ar^{14}N^+$ and $^{40}Ar^{16}O^+$ interferences and the decrease of $^{40}Ar^{16}OH^+$ interferences. The introduction of collision gases (Ar, H_2 or He) into the hexapole induces a series of ion-molecule reactions leading to the decrease of argides, oxides and hydrides in the ion beam. These reactions and

collisions involve either the neutralisation of the charge of the interference, or the significant decrease of their energy. In both cases, interferences are not transmitted into the analyser. Generally, it has been shown that the interferences on mass 54 mass 56 can be totally removed, but $^{40}Ar^{16}OH^{+}$ remains the most difficult interference to handle (*e.g.* Beard *et al.*, 2003a; Rouxel *et al.*, 2003; Vogl *et al.*, 2003; Dauphas *et al.*, 2004a).

ICP technology is characterised by a large but very stable instrumental bias through time. Mass bias correction for Fe isotope analysis can involve elemental doping with Cu or Ni (Anbar *et al.*, 2000; Belshaw *et al.*, 2000; Beard *et al.*, 2003a), double spike correction (Dideriksen *et al.*, 2006) and, most commonly sample-standard bracketing (*e.g.* Belshaw *et al.*, 2000; Dauphas *et al.*, 2004a; Schoenberg and von Blanckenburg, 2005; Guilbaud, 2010b). This method relies on interpolating the mass bias of a known standard to the standard-bracketed sample analyte. The corrected isotope ratio of the sample is given by equation Eq. 1.19:

$$R_{sample} = R_{s\tan dard} \frac{r_{sample}}{\sqrt{r^{1}_{s\tan dard} \times r^{2}_{s\tan dard}}} \qquad (1.19)$$

where R stands for the true isotope ratios of the sample and the standard and r for the measured isotope ratios of the sample and the bracketing standards (the superscripts ^{1} and ^{2} stand for the first standard and the second standard, respectively).

The choice of the standard has been debated. Some authors (*e.g.* Beard and co-workers) have proposed the use of the bulk composition of the Earth-Moon system (Beard *et al.*, 2003a) as a reference for geochemical processes. Other authors (*e.g.* Poitrasson *et al.*, 2004; Dauphas and Rouxel, 2006) favour the use of the certified IRMM-14 standard (IRMM™) because heterogeneities exist within the Earth-Moon system (Poitrasson *et al.*, 2004), and argue that the IRMM-14 standard has a composition very close to those of bulk chondrites (Schoenberg and von Blanckenburg, 2006). The standard used throughout this work is the certified IRMM-014. The isotopic concentrations of IRMM-14 are in percent (at the 2σ level), 5.845 ± 0.023 for ^{54}Fe, 91.754 ± 0.024 for ^{56}Fe, 2.1192 ± 0.0065 for ^{57}Fe, and 0.2818 ± 0.0027 for ^{58}Fe.

Correction for accurate Fe isotope ratios is made by the analysis of geostandards of known isotopic composition such as BCR-1 basalt (*e.g.* Beard *et al.*, 2003a; Poitrasson *et al.*, 2004; Butler *et al.*, 2005) or the Orgueil carbonaceous chondrite

(Zhu *et al.*, 2001; Kehm *et al.*, 2003; Dauphas *et al.*, 2004a,b). The use of geostandards is crucial when measuring isotope ratios of natural material. However, the very useful δ notation (Eq. 1.13) which is essentially the ratio of two ratios is a way to avoid the analysis of geostandards since the precision only, rather than accuracy is then required.

1.3.4. Experimentally derived fractionation factors

Experiments conducted to determine transition metal isotope fractionations are listed in Table 1.2. As for the measurement of natural samples, most of the literature concerns Fe isotope fractionation factors, which are deliberately not shown in the table since the work is detailed below. As explained above, it is crucial to distinguish between equilibrium and kinetic fractionations in order to understand natural data. Theoretically derived fractionations represent isotopic equilibrium. Experimentally, the use of the three isotope method (*e.g.* Matsuhisa *et al.*, 1978; Matthews *et al.*, 1983; Shahar *et al.*, 2008; Beard *et al.*, 2010) is the most robust experimental method to determine equilibrium fractionations. By deduction, any other fractionations measured within the same system are kinetic. The kinetics and extent of isotopic exchange have also been determined using an isotope tracer (*e.g.* Johnson *et al.*, 2002) or sampling kinetic reactions (*e.g.* Poulson *et al.*, 2005; Guilbaud, 2010a).

Experiments	Cu	Zn	Mo	Ni	Cr
mineral leaching	1,12	1	14		
adsobtion on mineral surface	4,5	5, 13	3		8
mineral replacement	6				
precipitation	2,15	15			
reduction					7
microbiology	10	10		9	
soil/weathering mobility	11				

1 Fernandez & Borrok, 2009
2 Ehrlich et al., 2004
3 Barling & Anbar 20074
4 Clayton et al., 2005
5 Balistrieri et al., 2008
6 Pekala et al., submitted
7 Ellis et al., 2002
8 Ellis et al., 2004
9 Cameron et al., 2009
10 Becker et al., 2005
11 Nolan et al., 2004
12 Mathur et al., 2005
13 Pokrovsky et al., 2005
14 Siebert et al., 2003
15 Archer, 2007

Table 1.2: Experiment conducted for some transition metal isotopes.

1.3.4.1. High temperature processes

Fe isotope diffusion in molten oxides, basalts and rhyolites has been experimentally determined (Richter *et al.*, 2003, 2009). Evaporation and condensation effects have also been assessed (Dauphas *et al.*, 2004a; Richter *et al.*, 2009).

Schuessler *et al.* (2007) showed that lighter isotopes incorporate into pyrrhotite melts in equilibrium with silicate melts with fractionation factors similar to those predicted (Polyakov and Mineev, 2000).

Fe isotope fractionation during metal segregation from silicate melts is significant (Roskosz *et al.*, 2006) and Roskosz *et al.* (2006) reported that kinetic fractionation during melt segregation favours the formation of a ^{56}Fe depleted metal phase with respect to the residual silicate. By contrast, Shahar *et al.* (2008) determined the equilibrium Fe isotope fractionation between magnetite and fayalite, and they showed that this system favours ^{56}Fe enrichment into the oxide phase with respect to the silicate. Shahar *et al.* (2008) proposed that this system can be used as a thermometer

since the equilibrium fractionation is temperature dependent. The results are consistent with predicted fractionation factors (Polyakov *et al.*, 2007).

1.3.4.2. Low temperature processes

Experimental data on aqueous Fe species, Fe-oxides and Fe-carbonates have been documented and demonstrate that the largest Fe isotope fractionations are produced during redox reactions in both biologically mediated (Beard *et al.*, 1999; Brantley *et al.*, 2001, 2004; Beard *et al.*, 2003a; Anbar, 2004; Croal *et al.*, 2004; Icopini *et al.*, 2004; Johnson *et al.*, 2004; Teutsch *et al.*, 2005) and abiotic systems (Anbar *et al.*, 2000; Bullen *et al.*, 2001; Matthews *et al.*, 2001; Skulan *et al.*, 2002; Welch *et al.*, 2003; Brantley *et al.*, 2004; Jang *et al.*, 2008; Handler *et al.*, 2009; McAnena *et al.*, 2009; Hill *et al.*, 2009; Beard *et al.*, 2010). Smaller, but significant fractionations have been seen in abiotic non-redox reactions (Wiesli *et al.*, 2004), including the ligand-exchange process involved in FeS_m formation (Butler *et al.*, 2005).

1.3.4.2.1. Biologically mediated reactions

Fe isotope fractionations involved during assimilatory Fe metabolism are poorly constrained. Mandernack *et al.* (1999) reported that there is no significant fractionation associated with Fe assimilation by magnetotactic bacteria, which mineralise Fe as magnetite and mackinawite (or greigite) for their metabolism. Fe being a limiting nutrient, this suggests that isotopic segregation by organisms is negligible.

Biologically mediated Fe isotope fractionations have been documented for redox mechanisms involving Fe(II)-oxidation by photoautrophic bacteria (Croal *et al.*, 2004) and DIR between Fe(III) oxides and $Fe(II)_{aq}$ (Beard *et al.*, 1999; Beard *et al.*, 2003b; Crosby *et al.*, 2005, 2007; Johnson *et al.*, 2005c). The Fe isotope fractionation occurring during partial dissolution of silicate and goethite has also been reported (Brantley *et al.*, 2001, 2004). Photoautrophic Fe(II)-oxidation produces ^{56}Fe enriched $Fe(II)_{aq}$ (Croal *et al.*, 2004), but the ~ -1.5 ‰ fractionation between $Fe(II)_{aq}$ and the ferrihydrite precipitate is lower than predicted equilibrium (Anbar *et al.*, 2005). This suggests that the measured fractionation reflects kinetic rather than equilibrium fractionation. Balci *et al.* (2006) suggested that the observed fractionation during biologically mediated Fe(II) oxidation is principally due to abiotic processes.

Partial dissolution of hornblende and goethite in the presence of siderophore producing bacteria and other organic ligands is accompanied by large isotope fractionations (Brantley *et al.*, 2001, 2004) (Table 1.3) producing ^{56}Fe depleted $Fe(II)_{aq}$. The magnitude of the fractionation is consistent with the strength of the ligands and of the mineral bonds.

Fe(II) oxidation	$\Delta^{56}Fe$ (‰)	References
Fe(II)aq-Fe(III)aq	-2.9	Balci et al., 2006
Fe(II)aq-Fe(III) (hydr)oxide	-1.5 ± 0.2	Croal et al., 2004
Mineral dissolution by siderophore bacteria		
Fe(aq)-hornblende	-0.56 ± 0.19	Brantley et al., 2001; 2004
Fe(aq)-goethite	-1.44 ± 0.16	Brantley et al., 2001; 2004
Dissimilatory iron reduction		
Fe(II)aq-Fe(III) (hydr)oxide	-2.3 to ***-1.3***	Beard et al., 1999,2003; Johnson et al., 2005
Fe(II)aq-Fe(II) surface of oxide	-2.1 to ***0***	Icopini et al., 2004; Crosby et al., 2007
Fe(II)aq-Fe(III) surface of oxide	~ -2.9	Crosby et al., 2005; Crosby et al., 2007
Fe(II)aq-Fe(II)sorb at oxide surface	-0.9 to -0.4	Crosby et al., 2005
Fe(II)aq-magnetite	***-1.3*** ± 0.1	Johnson et al., 2005
Fe(II)aq-siderite	1.2 to ***0***	Johnson et al., 2005
Fe(II)aq-Ca-Fe carbonate	2.2 to ***0.9***	Johnson et al., 2005

Table 1.3: Summary of the experimentally determined Fe isotope fractionations for biologically mediated reactions. Values in bold italic represent equilibrium fractionations. Other data reflect kinetic fractionations.

It is widely recognised that large amounts of ^{56}Fe depleted $Fe(II)_{aq}$ are produced during DIR (*e.g.* Johnson *et al.*, 2008a). The first evidence was the production of $Fe(II)_{aq}$ ~ 1.3 ‰ lighter than the ferrihydrite mineral (Beard *et al.*, 1999). Further research supported the initial results and indicated that DIR can produce a large range of isotopic compositions depending on the experimental set up (Beard *et al.*, 2003a; Icopini *et al.*, 2004; Crosby *et al.*, 2005; Johnson *et al.*, 2005b). Icopini *et al.* (2004) and Crosby *et al.* (2005) put emphasis on the potential effects of Fe(II) adsorption at the mineral surface to explain the range of measured fractionations. In particular, they questioned the mechanism that is responsible for the observed fractionation between the goethite surface and $Fe(II)_{aq}$, opening up recent research in abiotic experiments. Crosby *et al.* (2007) suggested that the fractionation between $Fe(II)_{aq}$ and $Fe(II)_{sorb}$ at the mineral surface is smaller than between $Fe(II)_{aq}$ and the Fe(III) mineral surface. They noted that $Fe(II)_{sorb}$ depends on the nature of the substrate, whereas there is no

difference between the fractionations produced with magnetite, hematite and goethite, implying that the nature of the Fe(III) substrate is irrelevant.

1.3.4.2.2. Abiotic Fe isotope fractionations

Experiments involving abiotic Fe isotope fractionations are listed in Table 1.4. Fe isotope exchange between $Fe(II)_{aq}$ and the surface of Fe(III) oxy(hydr)oxide has attracted attention in order to assess exchange effects on the abiotic redox reaction (*e.g.* Icopini *et al.*, 2004; Crosby *et al.*, 2005, 2007; Teutsch *et al.*, 2005; Jang *et al.*, 2008; Handler *et al.*, 2009; Beard *et al.*, 2010). Results are consistent with the abiotic redox reaction between $Fe(II)_{aq}$ and Fe(III) oxides (Bullen *et al.*, 2001) which is characterised by the precipitation of ^{56}Fe enriched Fe(III) oxides with respect to residual $Fe(II)_{aq}$. Abiotic fractionation between $Fe(II)_{aq}$ and $Fe(III)_{aq}$ is ~ -2.9 ‰ (Johnson *et al.*, 2002; Welch *et al.*, 2003), which is consistent with abiotic Fe(II) photo-oxidation (Staton, 2006) and the theoretically derived calculations (Anbar *et al.*, 2005).

Other abiotic redox reactions involving aqueous organic complexes have shown the largest kinetic Fe isotope fractionations recorded (up to -11.7 ‰, Matthews *et al.*, 2001). Ligand controlled dissolution of goethite and hornblende also record significant Fe isotope fractionations, but systematically of a higher magnitude for dissolutions involving a redox change (Brantley *et al.*, 2004; Wiederhold *et al.*, 2006).

I discussed above the formation of FeS_m by sulphidation of Fe(III)oxides. The sulphidation occurs first by conversion of the Fe(III) mineral surface into Fe(II)hydroxides and then the Fe(II) phase dissolves to form FeS_m. The sulphidation of goethite should thus produce maximum kinetic Fe fractionation since the Fe(II) phase will concentrate light isotopes (Brantley *et al.*, 2004; Johnson *et al.*, 2004). McAnena *et al.* (2009) showed that the Fe isotope fractionation recorded during sulphidation of Fe(III) minerals is correlated to the bond strength in the mineral substrate.

Smaller but significant fractionations have been documented for non-redox reactions including aqueous ferric chloro-complexes (Hill *et al.*, 2009); carbonate precipitation (Wiesli *et al.*, 2004), hematite precipitation (Skulan *et al.*, 2002), and mackinawite precipitation (Butler *et al.*, 2005). Butler *et al.* (2005) reported a kinetic fractionation $\Delta^{56}Fe_{Fe(II)\text{-}FeS}$ ranging from + 0.9 to +0.3 ‰. They suggested that the isotopic fractionation of Fe occurs during the inner sphere ligand exchange, during the

formation of FeS^{2+}, and before the development of the condensed phase FeS_m. During ligand exchange reactions, lighter Fe isotopes participate at a faster rate than heavier ones. Apart from Fe isotopes, only the behaviour of Cu and Zn for transition metal sulphides has been studied. CuS precipitates from $Cu(II)_{aq}$ with $\Delta^{65}Cu_{Cu(II)aq\text{-}CuS} = 3.06 \pm 0.14$ ‰ (Ehrlich *et al.*, 2004). Ehrlich *et al.* (2004) interpreted this result as a redox effect, since the precipitate is reduced to Cu(I)S from the aqueous Cu(II). Like FeS and CuS, (Archer, 2007) showed that ZnS precipitates from $Zn(II)_{aq}$ with depletion in heavy isotopes ($\Delta^{66}Zn_{Zn(II)aq\text{-}ZnS} \sim 0.4$ ‰). However, both Ehrlich *et al.* (2004) and Archer (2007) argued that their values were likely to be kinetic fractionations, CuS and ZnS being significantly less soluble than FeS_m ($Ksp_{FeS} = 3.5$, (Rickard, 2006); $Ksp_{CuS} = 22.2$, (Smith and Martell, 1976); $Ksp_{sphalerite} = 10.93$, (Dyrssen and Kremling, 1990); where *K*sp values given here are for free hexaqua species and the minerals).

Redox reactions	**Δ^{56}Fe (‰)**	**References**
Fe(II)aq-Fe(III)aq	***-2.8 ± 0.2***	Johnson et al., 2002; Welch et al., 2003
Fe(II)aq-hematite	***-2.9 ± 0.2***	Johnson et al., 2002; Skulan et al., 2002; Welch et al., 2003
Fe(II)aq-goethite	-0.5 to -1	Icopini et al., 2004
Fe(II)aq-goethite	***-1.05 ± 0.08***	Beard et al., 2010
Fe(II)aq-Fe(III) goethite surface	-2.1	Beard et al., 2010
Fe(II)aq-ferrihydrite	-0.9 ± 0.2	Bullen et al., 2001
Fe(II)-Fe(III) bipyridine complexes	1.7 to 11.7	Matthews et al., 2001
Ligand controlled mineral dissolution		
Fe(aq)-hornblende	-0.4 to -1.2	Brantley et al., 2004
Fe(aq)-goethite	~ 0 to -1.7	Brantley et al., 2004; Wiederhold et al., 2006
Non-redox reactions		
Fe(III)aq-hematite	1.32 to ***-0.1*** ± 0.2	Skulan et al., 2002
Fe(III)aq-Fe(III)ether chlorocomplexes	***0.8 to 0***	Hill et al., 2009
Fe(II)aq-Fe(II)sorb on hematite	-0.49 ± 0.15	Wu et al., 2010
Fe(II)aq-Fe(II)sorb on goethite	***-1.24*** ± 0.24	Beard et al., 2010
Fe(II)aq-Fe(II)sorb on goethite	-2.7 to -3.7	Icopini et al., 2004
Fe(II)aq-Fe(II)sorb on ferrihydrite	-2.7	Teutsch et al., 2005
Fe(II)aq-siderite	***0.4 to 0.6***	Wiesli et al., 2004
Fe(II)aq-mackinawite	0.9 to 0.2	Butler et al., 2005; Guilbaud et al., 2010a
Fe(II)aq-mackinawite	***equilibrium - chapter V***	
FeS(0)aq-pyrite	kinetic - chapter VI	

Table 1.4: Abiotically conducted experiments for the determination of Fe isotope fractionations. Equilibrium data are in bold italic, other data represent kinetic fractionations.

1.3.5. Natural Fe isotope variations in terrestrial and planetary materials

1.3.5.1. High temperature processes

As mentioned above, both kinetic and equilibrium isotope fractionations decrease with increasing temperature, and the Fe isotope analysis of natural high temperature rocks has shown little (but measurable) variation. Bulk chondrite Fe isotope

compositions are very homogeneous (mean $\delta^{56}Fe$ = - 0.015 ± 0.020 ‰ with respect to IRMM-14, Schoenberg and von Blanckenburg, 2006) and approximate the IRMM-14 value. However, the analysis of single chondrules displays a range of compositions varying from – 1.85 to 0.68 ‰ (Zhu *et al.*, 2001; Kehm *et al.*, 2003; Mullane *et al.*, 2003). These intra-chondrite variations are likely to reflect evaporation kinetic fractionations during chondrule formation or secondary chondrite alteration. Schoenberg and von Blanckenburg (2006) suggested that the chondrite homogeneity supports the existence of a chondrite uniform reservoir (CHUR).

Early analyses of lunar and terrestrial bulk igneous rocks (Beard and Johnson, 1999; Beard *et al.*, 2003b) showed very homogeneous Fe isotope compositions of +0.09 ± 0.05 ‰ with respect to the IRMM-14 reference. Beard *et al.* (2003b) thus proposed that Fe isotopic compositions should be given in respect with the bulk Earth-Moon system, rather than with the IRMM-14 reference which has less geological significance. However, Poitrasson *et al.* (2004) highlighted differences between the Fe isotope compositions of the "mean mafic Earth" (0.07 ± 0.03 ‰), the Moon (0.140 ± 0.029 ‰) and other planetary bodies such as Mars (0.002 ± 0.018 ‰) and Vesta (0.021 ± 0.028 ‰) and detailed studies on various terrestrial igneous rocks (Poitrasson and Freydier, 2005; Schoenberg and von Blanckenburg, 2006) pointed out heterogeneities between the Fe isotope signatures of the mean mafic Earth and those of SiO_2 > 71 wt% terrestrial granites (with $\delta^{56}Fe$ as high as 0.4 ‰). Also, the Fe isotope composition of mantle xenoliths is lighter than terrestrial basalts (Weyer *et al.*, 2005; Schoenberg and von Blanckenburg, 2006). For this reason it was proposed that Fe isotope fractionation could occur during planetary differentiation and crust formation (Weyer *et al.*, 2005; Weyer, 2008). However, Poitrasson (2007) argued that the fact that the signatures of eucritic and basaltic rocks from other planetary bodies are indistinguishable, along with the chondritic homogeneity, disprove the role of planetary differentiation in Fe isotope fractionation. Similar conclusions were raised for the core-mantle differentiation (Poitrasson *et al.*, 2005).

The reason why planetary bodies have relatively homogeneous Fe isotope compositions but display variations at a planetary scale (comparing one body to another one) is unclear. Poitrasson *et al.* (2004) proposed that the terrestrial and lunar enrichment in heavier isotopes compared to other solar system bodies supports the Moon-Earth formation impact model, in which kinetic Fe isotope fractionation would occur during evaporative Fe loss.

1.3.5.2. Low temperature processes

Measuring Fe isotope signatures in the sedimentary and aqueous Fe budget has shown the largest variations in δ^{56}Fe in both modern and ancient rocks including black shales, BIFs, and Fe-Mn modules. These signatures have been first interpreted as evidence for biological activity (Beard and Johnson, 1999; Beard *et al.*, 1999), opening up a vast research potential into the microbial fingerprints in Fe isotope signatures (*e.g.* Beard *et al.*, 2003a; Johnson and Beard, 2004; Johnson *et al.*, 2008a). However, non-biological Fe isotope fractionation was quickly discovered during abiotic chromatographic experiments (Anbar *et al.*, 2000), showing that both biologically mediated and abiotic Fe isotope fractionations occur in nature. Fig. 1.14 summarises the Fe isotope variations recorded in major sedimentary environments.

1.3.5.2.1. Modern sedimentary environments

Anbar and Rouxel (2007) noted that the controls on isotopic records of dissolved and particulate Fe in seawater remain poorly explored. As we discussed above, the total Fe budget in the oceans is a combination between atmospheric input as aerosols, continental fluxes and weathering based processes, hydrothermal inputs, and dissolution of reactive Fe in early diagenesis through sulphidation or DIR. Thus, the isotopic composition of sedimentary Fe is a product of the different sources, the precipitation into various Fe-bearing phases and the extent of equilibration between seawater Fe, porewater Fe, and solid Fe.

Figure 1.14: Summary of the Fe isotope signatures of major low temperature processes including modern and ancient sedimentary rocks. Largest variations are recorded in Precambrian sulphidic rocks. Bulk silicate Earth is illustrated by the grey band clustering at ~ 0 ‰. The figure is from Dauphas and Rouxel (2006).

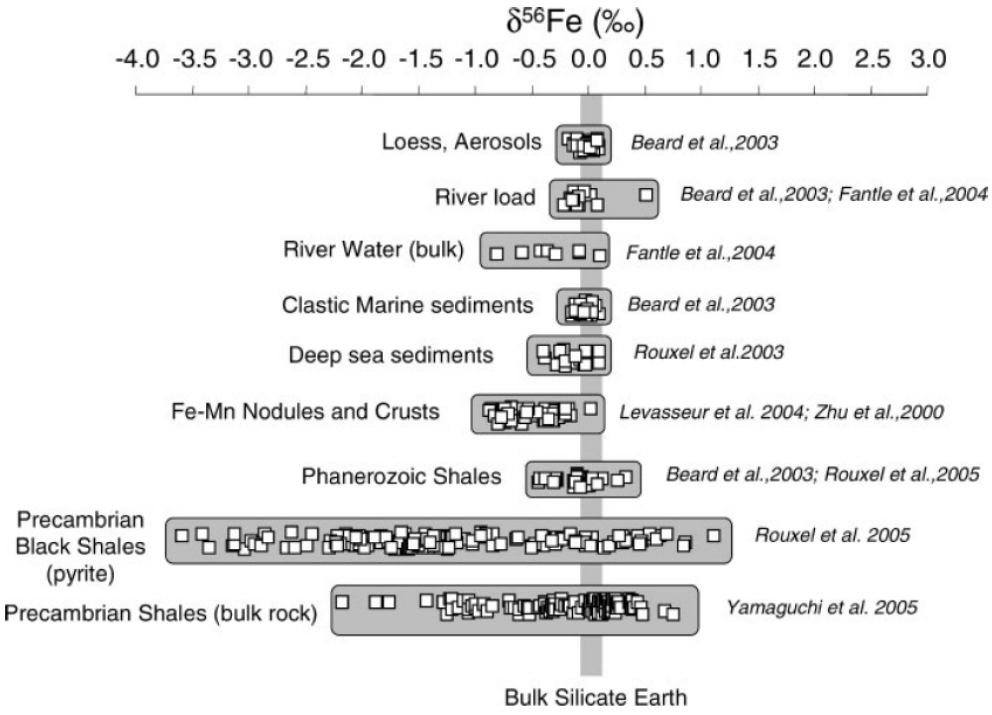

1.3.5.2.1.1. Atmospheric inputs and continental weathering

Modern marine sediments such as deep sea clays, terrigenous sediments, turbidite clays and volcanoclastites have Fe isotopic compositions clustered around the igneous values (Beard *et al.*, 2003a; Rouxel *et al.*, 2003; Fantle and DePaolo, 2004). This is consistent with loess, aerosol and suspended river load values, suggesting that the transport of eroded particulate Fe does not modify significantly the Fe isotope composition in the solid phase. It seems that continental variations pointed out by Poitrasson and Freydier (2005) are not recorded in the river load fraction. By contrast, differences in weathering regime should produce a range of fractionations. Dissolved Fe in rivers displays lighter isotopic compositions than those of igneous rocks (Fantle and DePaolo, 2004), suggesting that dissolution weathering kinetically fractionates Fe isotopes. Bergquist and Boyle (2006) also observed ^{56}Fe depleted dissolved Fe with respect to igneous rocks, however they noted that dissolved Fe and the river load had similar signatures for high weathering regimes (*i.e.* the Amazon river). The presence of ^{56}Fe depleted chelated and particulate Fe in soils is consistent with the experiments conducted by Brantley *et al.* (2001, 2004) and Wiederhold *et al.* (2007). Emmanuel *et al.* (2005) showed that Fe cycling during soil forming processes can be quantified by Fe isotopes, which is supported by Wiederhold *et al.* (2007) who showed that Fe mobilisation during mineral leaching and soil formation is accompanied by significant

Fe isotope fractionation. Soil erosion might thus participate to a wider isotopic range for particulate Fe in river loads.

1.3.5.2.1.2. Hydrothermal systems

Hydrothermal fluids have δ^{56}Fe values from – 0.21 to – 0.69 ‰ lower than those of igneous rocks (Sharma *et al.*, 2001; Beard *et al.*, 2003b; Severmann *et al.*, 2004; Bennett *et al.*, 2009). Sharma *et al.* (2001) suggested that the low δ^{56}Fe values are due to 1) basalt leaching by fluids, 2) precipitation of sulphides and oxyhydroxides from vent fluids and 3) phase separation between vapour and brine. Beard *et al.* (2003b) suggested that there is no Fe isotope fractionation during phase separation since vapour and brines have the same isotopic composition. Bennett *et al.* (2009) proposed that all dissolved Fe phases are isotopically heavier than the primary fluid after precipitation of depleted sulphides (~ -0.89 ‰) and oxyhydroxides (~ -0.19 ‰). Rouxel *et al.* (2003, 2004, 2008A) found isotopic composition variations between different sulphide minerals with lower δ^{56}Fe values for pyrite and marcasite and higher δ^{56}Fe values for chalcopyrite. Chalcopyrite is a high temperature sulphide precipitating first from the vent fluids, depleting the residual fluid in heavier Fe. By contrast, Markl *et al.* (2006) found no difference in δ^{56}Fe values for primary pyrite and chalcopyrite from hydrothermal veins.

Rouxel *et al.* (2003) found that δ^{56}Fe values in the oceanic crust increase with increasing degrees of Fe leaching. They suggested that these variations are related to kinetic effects producing lighter fluids or, alternatively, the formation of δ^{56}Fe enriched clays. This suggestion was supported by the fact that celadonite veins were found with δ^{56}Fe value of +1.1‰ which is consistent with the predictions of Polyakov and Mineev (2000).

1.3.5.2.1.3. Early diagenetic processes

Von Blanckenburg *et al.* (2008) reported the Fe isotopic compositions of modern microbial carbonates, ranging from ~ -0.12 to +0.15 ‰. They argued that the diagenetic processes that occurred to these stromatilitic features, including dolomitisation, did not alter their original isotope signature. Some authors also proposed that Fe(II) incorporation into carbonates could reflect the composition of the dissolved Fe(II) pool (Dideriksen *et al.*, 2006).

Fe isotopic composition of diagenetic fluids including marine suboxic and anoxic porewaters (Severmann *et al.*, 2006; Staubwasser *et al.*, 2006; Homoky *et al.*, 2009), benthic fluxes (Rouxel and Auro, 2010; Severmann *et al.*, 2010), and estuarine water (Fantle and DePaolo, 2004; Rouxel *et al.*, 2008b) record δ^{56}Fe signatures down to –3 ‰, with some extremes at –5 ‰. Because DIR is a dominant pathway for the oxidation of organic matter in sedimentary environments (*e.g.* Berner, 1982) that produces isotopically light fluids (Table 1.3), such low values in diagenetic fluids have been interpreted by some authors as an evidence for microbial iron reduction (Severmann *et al.*, 2006; Johnson *et al.*, 2008a). Others proposed that abiotic precipitation of ^{56}Fe enriched Fe oxy(hydr)oxides characterising the short Fe residence time in seawater was responsible for such low values (Rouxel *et al.*, 2008b; Homoky *et al.*, 2009).

Fe isotope composition of reactive Fe(III) (ferrihydrite, goethite, hematite) and Fe(II) (mackinawite, pyrite) in suboxic to anoxic environments was measured (Severmann *et al.*, 2006; Staubwasser *et al.*, 2006). Results show that Fe oxyhydroxides are systematically ^{56}Fe enriched with respect to porewater Fe. HCl extractable Fe-S phases vary from -0.4 to +0.4 ‰, whereas pyrite displays a more ^{56}Fe depleted range from -0.5 to -1‰ (Severmann *et al.*, 2006). These observations were interpreted as supporting the production of isotopically light Fe fluids during diagenetic reduction and dissolution of inherited oxy(hydr)oxides, and the incorporation of lighter isotopes during subsequent formation of authigenic iron sulphides.

Marine sediments associated with ferromanganese precipitates are characterised by negative values down to –0.8‰ (Zhu, O'Nions, *et al.*, 2000; Rouxel *et al.*, 2003; Levasseur *et al.*, 2004; Chu *et al.*, 2006). Beard *et al.* (2003b) proposed that these signatures could derive from relative mixing between aerosols and hydrothermal fluids. Others suggested that they are likely to reflect diagenetic remobilisation of Fe during Fe-Mn crust formation (Dauphas and Rouxel, 2006).

1.3.5.2.2. Ancient sedimentary rocks

Amongst ancient sedimentary rocks, Cainozoic Fe-Mn crusts, Archean stromatolites, BIFs and Precambrian sulphides have been suggested as potential new palaeoproxies. Cainozoic Fe-Mn crusts were suggested (*e.g.* Zhu *et al.*, 2002) to trace changes in Fe fluxes in the marine system but diagenetic remobilisation is questioned

(see above). Large negative $\delta^{56}Fe$ values down to -2 ‰ recorded in Archean stromatolites contrast with modern data, and Von Blanckenburg *et al.* (2008) suggested that microbial formations may trace redox changes from Archean ferrous Fe to modern ferric Fe. The two major ancient sedimentary formations that have attracted enthusiasm as potential paleorecords involve BIFs and sulphidic black shales (Fig. 1.15).

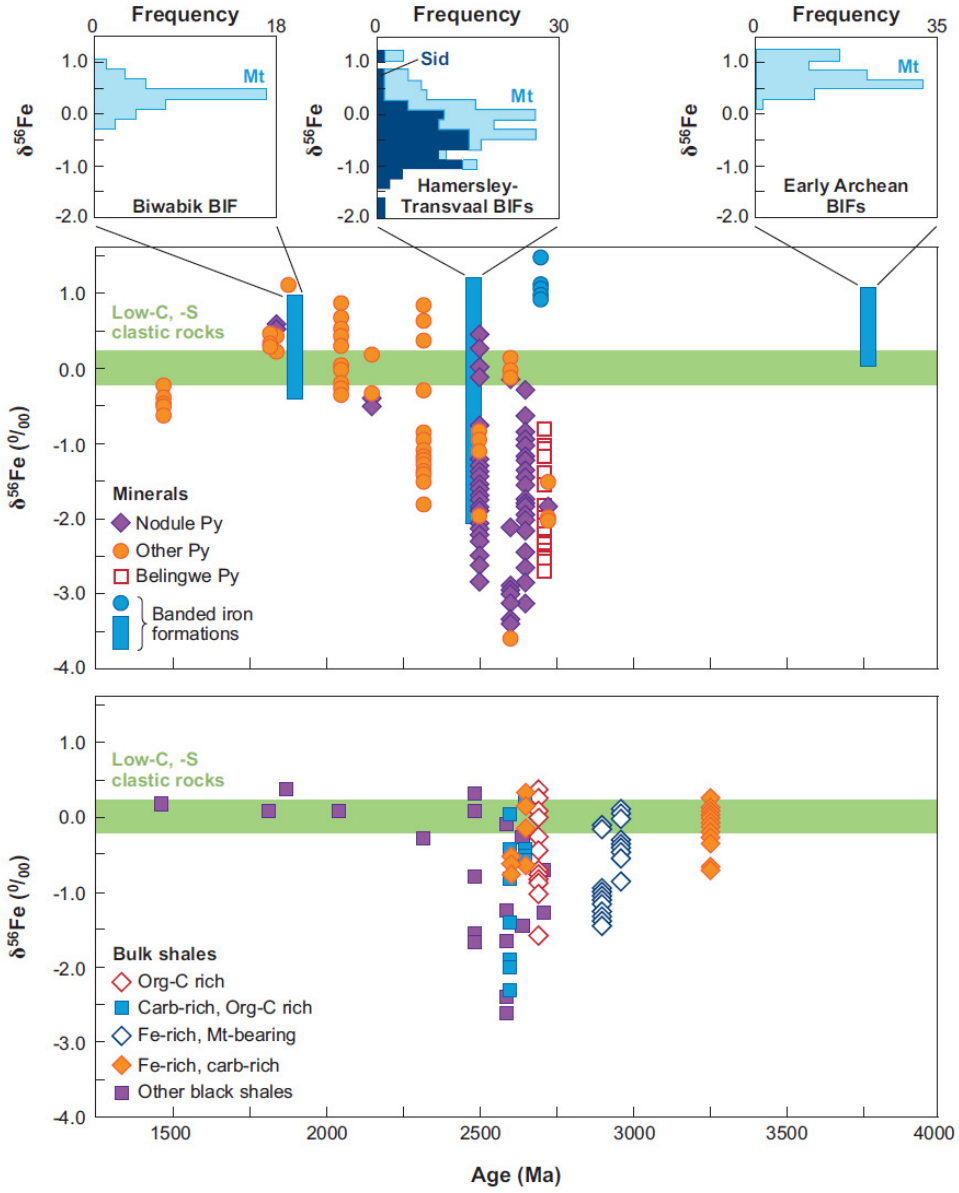

Figure 1.15: Temporal variations and isotopic distribution of $\delta^{56}Fe$ measured in Archean and Proterozoic BIFs, sulphidic shales and pyrite, from Johnson *et al.* (2008a). Data are from Beard *et al.*, (2003b); Dauphas *et al.*, (2004b); Rouxel *et al.*, (2005); Yamaguchi *et al.*, (2005); Whitehouse and Fedo, (2007); Johnson *et al.*, (2008b).

1.3.5.2.2.1. Fe isotope signatures recorded in BIFs

The Banded Iron Formations record a large degree of Fe cycling on the early Earth. Common mineral phases are magnetite, siderite and hematite, which emphasises a certain degree of oxidation since Fe inputs in the Archean and the Proterozoic consists of solid and dissolved Fe(II) species. Possible scenarios for Fe oxidation have been discussed above (section 2.1.2) and result in the precipitation of ferrihydrite and Fe oxy(hydr)oxide BIFs precursor phases. Both biologically mediated and abiotic oxidation of $Fe(II)_{aq}$ produce ^{56}Fe enriched precipitates (*e.g.* Croal *et al.*, 2004; Teutsch *et al.*, 2005) and the positive $\delta^{56}Fe$ excursions up to +2 ‰ recorded in the > 3.7 Ga Isua Greenstone Belt (Greenland) BIFs (Dauphas *et al.*, 2004b; Whitehouse and Fedo, 2007) were interpreted as reflecting Fe(II) oxidation (also see Dauphas and Rouxel, 2006). Whitehouse and Fedo (2007) noted that the highest measured values were consistent with the fractionation between $Fe(II)_{aq}$ and $Fe(III)_{aq}$ (*e.g.* Welch *et al.*, 2003) assuming seawater $\delta^{56}Fe_{Fe(II)aq}$ ranging from -0.5 to 0 ‰. The positive $\delta^{56}Fe$ recorded in hematite and magnetite grains from the 1.8 Ga Biwabik BIFs suggest the quantitative removal of Fe in an oxidised ^{56}Fe enriched ocean (Rouxel *et al.*, 2005).

Magnetite and siderite are the dominant Fe bearing minerals in BIFs (*e.g.* Johnson *et al.*, 2008b) and both display Fe (at least partly) in its ferrous state. Siderite precipitates as authigenic cements in anoxic environments and is a common early diagenetic phase. Johnson *et al.* (2008b) showed that in the 2.5 Ga Hamersley-Transvaal BIFs, the mean $\delta^{56}Fe$ value for siderite is ~ -0.5 ‰, implying that it formed in isotopic equilibrium with seawater (Wiesli *et al.*, 2004). By contrast, the isotopic compositions of siderite and magnetite are not consistent with the predicted equilibrium fractionation between siderite and magnetite (Johnson *et al.*, 2005b). Johnson *et al.* (2008b) emphasised that BIF diagenesis requires a certain extent of Fe(III) reduction from Fe(III) precursors to Fe(II) bearing minerals. Because the earliest forms of microbial respiration involve sulphate (Shen *et al.*, 2001) and Fe(III) (Vargas *et al.*, 1998) reduction and DIR produces ^{56}Fe depleted $Fe(II)_{aq}$ (*e.g.* Beard *et al.*, 1999; Beard *et al.*, 2003a), it was proposed that the large variability and negative excursions in $\delta^{56}Fe_{magnetite}$ recorded in the 2.5 Ga BIFs reflected intense DIR in the Archean (Johnson *et al.*, 2008a,b).

1.3.5.2.2.2. Fe isotope signatures of ancient sedimentary sulphides

Ancient sedimentary sulphides and black shales, in which pyrite is the dominant Fe bearing mineral, display $\delta^{56}Fe$ signatures significantly different to those recorded in modern sediments (Severmann *et al.*, 2006). $\delta^{56}Fe_{pyrite}$ ranges from ~ +0.2 to -1 ‰ in the Phanerozoic and the Mesoproterozoic (Matthews *et al.*, 2004; Rouxel *et al.*, 2005; Anbar and Rouxel, 2007). The late Paleoproterozoic (2.3 Ga to 1.7 Ga) is characterised by more positive $\delta^{56}Fe_{pyrite}$ and a range comprised between ~ +1.2 to -0.5 ‰ (Yamaguchi *et al.*, 2004, 2005; Rouxel *et al.*, 2005). Early Paleoproterozoic and Archean sedimentary pyrites are characterised by the appearance of very negative $\delta^{56}Fe_{pyrite}$ with a range comprised between ~ +0.5 to -3.5 ‰ (Rouxel *et al.*, 2005; Archer and Vance, 2006; Czaja *et al.*, 2010). Because the kinetic fractionation between $Fe(II)_{aq}$ and FeS_m was the only published experimental data for iron sulphides (Butler *et al.*, 2005), it has been generally assumed that abiotic pyrite formation should record a fractionation of a similar magnitude to those occurring during FeS_m precipitation (Matthews *et al.*, 2004; Rouxel *et al.*, 2005; Yamaguchi *et al.*, 2005; Archer and Vance, 2006; Severmann *et al.*, 2006; Czaja *et al.*, 2010; Nishizawa *et al.*, 2010). Thus, workers have focussed on determining which processes could contribute to the formation of a ^{56}Fe depleted reservoir, from which pyrite could form. Similarly to the Fe isotope signatures of BIFs, it was suggested that DIR may be responsible for such a reservoir (Archer and Vance, 2006; Johnson *et al.*, 2008a; Czaja *et al.*, 2010; Nishizawa *et al.*, 2010). In contrast, others proposed that pyrite formed from ^{56}Fe depleted fluids produced by previous precipitation of enriched Fe oxy(hydr)oxides (*e.g.* Rouxel *et al.*, 2005; Anbar and Rouxel, 2007). In the absence of measured or calculated fractionation factors for sedimentary pyrite formation, these divergent interpretations remain difficult or impossible to test. Theoretical computations predict ^{56}Fe enriched pyrite up to ~ +1 ‰ with $\Delta^{56}Fe_{Fe(II)\text{-}pyrite}$ varying from ~ -2.5 to -4.5 ‰ at 20°C (Polyakov *et al.*, 2007; Blanchard *et al.*, 2009). Such data indicate that sedimentary pyrite does not reflect isotope equilibrium. However, it does not explain what mechanisms are responsible for the measured isotope fractionations.

1.4. Conclusions

The field of transition metal geochemistry has expanded in the last decade, particularly in the case of Fe isotopes. This is because of the close relationship existing between Fe, life, and the global cycles of C, H and O.

Fe isotopes have been proven to be a powerful tool for tracing biogeochemical processes. Various biologically mediated and abiotic processes have been studied for their effects on Fe isotope fractionations. A prerequisite to succesfully interpret natural data is the knowledge of all potential mechanisms that are responsible for the measured fractionations. Although the Fe-O system has been quite thoroughly inspected, the lack of experimental data in the Fe-S system makes natural pyrite data a source of continuous debate. To my knowledge Fe isotopes have never been used to explore experimentally the iron-sulphur theory for the onset of life on Earth. The collection of experimental data on Fe isotope fractionations within the Fe-S system is meagre, since until 2010, the study on mackinawite precipitation (Butler *et al.*, 2005) was the only Fe isotope published study on iron sulphides. However knowing the mechanisms that can fractionate Fe isotopes in the Fe-S system is necessary for a full understanding the Fe isotope cycle throughout the Earth's history, and the potential tracing of prokaryotic life in the early Archean.

In this project, the abiotic Fe isotope fractionations occurring during the diagenesis of pyrite have been assessed. Chapter II presents the experimental and analytical methods for the determination of Fe isotope fractionations in the Fe-S system. Chapter III details the recent development and improvement of analytical protocols for precise analysis of $^{56/54}$Fe and $^{57/54}$Fe isotope ratios. In chapter IV I report the mechanisms for isotopic exchange between nanoparticulate FeS_m and $Fe(II)_{aq}$ during nanoparticle growth. The equilibrium Fe isotope fractionation is documented in chapter V. In chapter VI I present the first experimental data on the Fe isotope fractionation occurring during the formation of sedimentary pyrite. Finally, I report in chapter VII preliminary results for a new chemostat experimental set up.

1.5. References

Anbar, A., 2004. Iron stable isotopes: beyond biosignatures. Earth and Planetary Science Letters 217, 223-236.

Anbar, A., Jarzecki, A., Spiro, T., 2005. Theoretical investigation of iron isotope fractionation between Fe(H2O)63+ and Fe(H2O)62+: Implication for iron stable isotope geochemistry. Geochim. Cosmochim. Acta 69, 825-837.

Anbar, A., Roe, J., Barling, J., Nealson, K., 2000. Nonbiological fractionation of iron isotopes. Science 288, 126-128.

Anbar, A., Rouxel, O., 2007. Metal Stable Isotopes in Paleoceanography. Annu. Rev.

Earth Planet. Sci. 35, 717–746.

Anbar, A.D., Duan, Y., Lyons, T.W., Arnold, G.L., Kendall, B., Creaser, R.A., Kaufman, A.J., Gordon, G.W., Scott, C., Garvin, J., Buick, R., 2007. A Whiff of Oxygen Before the Great Oxidation Event? Science 317, 1903-1906.

Anders, E., Grevesse, N., 1989. Abundances of the elements: Meteoritic and solar. Geochim. Cosmochim. Acta 53, 197-214.

Anderson, T., Raiswell, R., 2004. Sources and mechanisms for the enrichment of highly reactive iron in euxinic Black Sea sediments. American Journal of Science 304, 203.

Archer, C., 2007. The application of transition metal isotope systems to biogeochemical studies of the early Earth.

Archer, C., Vance, D., 2006. Coupled Fe and S isotope evidence for Archean microbial Fe(III) and sulfate reduction. Geology 34, 153-156.

Arnold, G., Anbar, A., Barling, J., Lyons, T., 2004. Molybdenum Isotope Evidence for Widespread Anoxia in Mid-Proterozoic Oceans. Science 304, 87-90.

Awramik, S.M., 1992. The oldest records of photosynthesis. Photosynthesis Research 33, 75-89.

Bada, J.L., Lazcano, A., 2002. Origin of Life: Some Like It Hot, But Not the First Biomolecules. Science 296, 1982-1983.

Balci, N., Bullen, T.D., Witte-Lien, K., Shanks, W.C., Motelica, M., Mandernack, K.W., 2006. Iron isotope fractionation during microbially stimulated Fe(II) oxidation and Fe(III) precipitation. Geochimica et Cosmochimica Acta 70, 622-639.

Balistrieri, L., Borrok, D., Wanty, R., Ridley, W., 2008. Fractionation of Cu and Zn isotopes during adsorption onto amorphous Fe(III) oxyhydroxide: Experimental mixing of acid rock drainage and ambient river water. Geochimica et Cosmochimica Acta 72, 311-328.

Banfield, J., Zhang, H., 2001. Nanoparticles in the environment. Reviews in Mineralogy & Geochemistry 44, 1-58.

Barling, J., Anbar, A., 2004. Molybdenum isotope fractionation during adsorption by manganese oxides. Earth and Planetary Science Letters 217, 315-329.

Beard, B., Johnson, C., 2004. Fe Isotope Variations in the Modern and Ancient Earth and Other Planetary Bodies. Reviews in Mineralogy & Geochemistry 55, 319-357.

Beard, B., Johnson, C., 1999. High precision iron isotope measurements of terrestrial and lunar materials. Geochim. Cosmochim. Acta 63, 1653-1660.

Beard, B., Handler, R., Scherer, M., Wu, L., Czaja, A., Heimann, A., Johnson, C., 2010. Iron isotope fractionation between aqueous ferrous iron and goethite. Earth and Planetary Science Letters 295, 241-250.

Beard, B., Johnson, C., Skulan, J., Nealson, K., Cox, L., Sun, H., 2003a. Application of Fe isotopes to tracing the geochemical and biological cycling of Fe. Chem. Geol. 195, 87-117.

Beard, B.L., Johnson, C.M., Von Damm, K.L., Poulson, R.L., 2003b. Iron isotope constraints on Fe cycling and mass balance in oxygenated Earth oceans. Geology 31, 629 -632.

Beard, B., Johnson, C., Cox, L., Nealson, K., Aguilar, C., 1999. Iron isotope biosignatures. Science 285, 1889-1892.

Becker, J., Zoriy, M., Pickhardt, C., Przybylski, M., Becker, J., 2005. Investigation of Cu-, Zn- and Fe-containing human brain proteins using isotopic-enriched tracers by LA-ICP-MS and MALDI-FT-ICR-MS. International Journal of Mass Spectrometry 242, 135-144.

Beinert, H., 2000. Iron-sulfur proteins: ancient structures, still full of surprises. Journal of Biological Inorganic Chemistry 5, 2-15-15.

Bekker, A., Holland, H., Wang, P., Rumble, D., Stein, H., Hannah, J., Coetzee, L., Beukes, N., 2004. Dating the rise of atmospheric oxygen. Nature 427, 117-120.

Belshaw, N., Zhu, X., Guo, Y., O'Nions, R., 2000. High precision measurement of iron isotopes by plasma source mass spectrometry. Int. J. Mass Spectrom 197, 191-195.

Bennett, S.A., Rouxel, O., Schmidt, K., Garbe-Schoenberg, D., Statham, P.J., German, C.R., 2009. Iron isotope fractionation in a buoyant hydrothermal plume, 5°S Mid-Atlantic Ridge. Geochimica et Cosmochimica Acta 73, 5619-5634.

Benning, L., Barnes, H., 1998. In situ determination of the stability of iron monosulphide and kinetics of pyrite formation. Mineralogical Magazine 62A, 151-152.

Benning, L., Wilkin, R., Barnes, H., 2000. Reaction pathways in the Fe–S system

below 1008C. Chem. Geol. 167, 25-51.

Benning, L., Wilkin, R., Konhauser, K., 1999. Iron monosulphide stability: experiments with sulphate-reducing bacteria. Proceedings of the International Symposium on the Geochemistry of Earth's Surface 5, 429-432.

Benz, M., Brune, A., Schink, B., 1998. Anaerobic and aerobic oxidation of ferrous iron at neutral pH by chemoheterotrophic nitrate-reducing bacteria. Archives of Microbiology 169, 159-165-165.

Bergquist, B., Boyle, E., 2006. Iron isotopes in the Amazon River system: Weathering and transport signatures. Earth and Planetary Science Letters 248, 54-68.

Bermin, J., Vance, D., Archer, C., Statham, P., 2006. The determination of the isotopic composition of Cu and Zn in seawater. Chemical Geology 226, 280-297.

Bernal, J., 1951. The Physical Basis of Life. Routledge and Kegan Paul, London.

Berner, R., 1962. Tetragonal iron sulfide. Science 137, 669.

Berner, R., 1967. Thermodynamic stability of sedimentary iron sulfides. American Journal of Science 265, 773-785.

Berner, R., 1970. Sedimentary pyrite formation. Am. J. Sci. 268, 1-23.

Berner, R., 1981. A New Geochemical Classification of Sedimentary Environments. J. Sediment. Research 51, 117-135.

Berner, R., 1982. Burial of organic carbon and pyrite sulfur in the modern ocean; its geochemical and environmental significance. Am. J. Sci. 282, 451-473.

Berner, R., Maasch, K., 1996. Chemical weathering and controls on atmospheric O2 andCO2: Fundamental principles were enunciated by J.J. Ebelman in 1845. Geochim. Cosmochim. Acta 60, 1633–1637.

Berner, R.A., Raiswell, R., 1983. Burial of organic carbon and pyrite sulfur in sediments over phanerozoic time: a new theory. Geochimica et Cosmochimica Acta 47, 855-862.

Berner, R.A., Beerling, D.J., Dudley, R., Robinson, J.M., Wildman, R.A., 2003. Phanerozoic Atmospheric Oxygen. Annu. Rev. Earth Planet. Sci. 31, 105-134.

Beukes, N., Klein, C., Kaufman, A., Hayes, J.M., 1990. Carbonate petrography, kerogen distribution, and carbon and oxygen isotope variations in an early Proterozoic transition from limestone to iron-formation deposition, Transvaal Supergroup, South Africa. Econ. Geol. 85, 663-690.

Beukes, N.J., Dorland, H., Gutzmer, J., Nedachi, M., Ohmoto, H., 2002. Tropical

laterites, life on land, and the history of atmospheric oxygen in the Paleoproterozoic. Geology 30, 491 -494.

Birck, J., Lugmair, G., 1988. Nickel and Chromium isotopes in Allende inclusions. Earth and Planet. Science Letters 90, 131-143.

Bjerrum, C.J., Canfield, D.E., 2002. Ocean productivity before about 1.9[thinsp]Gyr ago limited by phosphorus adsorption onto iron oxides. Nature 417, 159-162.

Blanchard, M., Poitrasson, F., Méheut, M., Lazzeri, M., Mauri, F., Balan, E., 2009. Iron isotope fractionation between pyrite (FeS2), hematite (Fe2O3) and siderite (FeCO3): A first-principles density functional theory study. Geochimica et Cosmochimica Acta 73, 6565-6578.

von Blanckenburg, F., Mamberti, M., Schoenberg, R., Kamber, B.S., Webb, G.E., 2008. The iron isotope composition of microbial carbonate. Chemical Geology 249, 113-128.

Blankenship, R.E., 1992. Origin and early evolution of photosynthesis. Photosynthesis Research 33, 91-111-111.

Bottinga, Y., Javoy, M., 1973. Comments on oxygen isotope geothermometry. Earth and Planetary Science Letters 20, 250-265.

Bottrell, S., Newton, R., 2006. Reconstruction of changes in global sulfur cycling from marine sulfate isotopes. Earth Sci. Rev. 75, 59-83.

Brantley, S., Liermann, L., Bullen, T., 2001. Fractionation of Fe isotopes by soil microbes and organic acids. Geology 29, 535-538.

Brantley, S., Liermann, L., Guynn, R., Anbar, A., Icopini, G., Barling, J., 2004. Fe isotopic fractionation during mineral dissolution with and without bacteria. Geochimica. Cosmochim. Acta 68, 3189–3204.

Brasier, M.D., Green, O.R., Jephcoat, A.P., Kleppe, A.K., Van Kranendonk, M.J., Lindsay, J.F., Steele, A., Grassineau, N.V., 2002. Questioning the evidence for Earth's oldest fossils. Nature 416, 76-81.

Brasier, M.D., Green, O.R., Lindsay, J.F., McLoughlin, N., Steele, A., Stoakes, C., 2005. Critical testing of Earth's oldest putative fossil assemblage from the ~3.5 Ga Apex chert, Chinaman Creek, Western Australia. Precambrian Research 140, 55-102.

Braterman, P.S., Cairns-Smith, A.G., Sloper, R.W., Truscott, T.G., Craw, M., 1984. Photo-oxidation of iron(II) in water between pH 7.5 and 4.0. J. Chem. Soc., Dalton Trans. 1441-1445.

Brocks, J.J., Logan, G.A., Buick, R., Summons, R.E., 1999. Archean Molecular Fossils and the Early Rise of Eukaryotes. Science 285, 1033-1036.

Brocks, J.J., Love, G.D., Summons, R.E., Knoll, A.H., Logan, G.A., Bowden, S.A., 2005. Biomarker evidence for green and purple sulphur bacteria in a stratified Palaeoproterozoic sea. Nature 437, 866-870.

Buffle, J., de Vitre, R., Perret, D., Leppard, G., 1988. Combining field measurements for speciation in non perturbable waters, in: Metal Speciation: Theory, Analysis and Application. Lewis Publishers Inc., London, pp. 99-124.

Buick, R., Dunlop, J., Groves, D., 1981. Stromatolite recognition in ancient rocks: an appraisal of irregular laminated structures in an early Archean chert–barite unit from North Pole,Western Australia. Alcheringa 5, 161-181.

Bullen, T., McMahon, P., 1998. Using stable Fe isotopes to assess microbially-mediated Fe3+ reduction in a jet-fuel contaminated aquifer. Mineral. Mag. 62A, 255-256.

Bullen, T., White, A., Childs, C., Vivit, D., Schulz, M., 2001. Demonstration of significant abiotic ion isotope fractionation. Geology 29, 699-702.

Butler, I., Archer, C., Vance, D., Oldroyd, A., Rickard, D., 2005. Fe isotope fractionation on FeS formation in ambient aqueous solution. Earth and Planet. Science Letters 236.

Butler, I., Bottcher, M., Rickard, D., Oldroyd, A., 2004. Sulfur isotope partitioning during experimental formation of pyrite via the polysulfide and hydrogen sulfide pathways: implications for the interpretation of sedimentary and hydrothermal pyrite isotope records. Earth and Planet. Science Letters 228, 495-509.

Butler, I., Rickard, D., 2000. Framboidal pyrite formation via the oxidation of iron (II) monosulfide by hydrogen sulphide. Geochim Cosmochim Acta 64, 2665–2672.

Cameron, E.M., 1982. Sulphate and sulphate reduction in early Precambrian oceans. Nature 296, 145-148.

Cameron, V., Vance, D., Archer, C., House, C., 2009. A biomarker based on the stable isotopes of nickel. Proceedings of the National Academy of Sciences 106, 10944-10948.

Canfield, D.E., 1998. A new model for Proterozoic ocean chemistry. Nature 396, 450-453.

Canfield, D.E., 2001. Biogeochemistry of Sulfur Isotopes. Reviews in Mineralogy and Geochemistry 43, 607-636.

Canfield, D.E., 2004. The evolution of the Earth surface sulfur reservoir. Am J Sci 304, 839-861.

Canfield, D., 2005. The early history of atmospheric oxygen: Homage to Robert M. Garrels. Annual Review of Earth and Planetary Sciences 33, 1-36.

Canfield, D., Habicht, K., Thamdrup, B., 2000. The Archean Sulfur Cycle and the Early History of Atmospheric Oxygen. Science 288, 658-661.

Canfield, D., Raiswell, R., Bottrell, S., 1992. The reactivity of sedimentary iron minerals toward sulfide. American Journal of Science 292, 659-683.

Canfield, D., Teske, A., 1996. Late Proterozoic rise in atmospheric oxygen concentration inferred from phylogenetic and sulphurisotope studies. Nature 382, 127-132.

Canfield, D., Thamdrup, B., 1994. The production of 34S-depleted sulfide during bacterial disproportionation of elemental sulfur. Science 266, 1973 -1975.

Canfield, D.E., Farquhar, J., Zerkle, A.L., 2010. High isotope fractionations during sulfate reduction in a low-sulfate euxinic ocean analog. Geology 38, 415-418.

Castresana, J., Saraste, M., 1995. Evolution of energetic metabolism: the respiration-early hypothesis. Trends in Biochemical Sciences 20, 443-448.

Cavalier-Smith, T., 2002. The neomuran origin of archaebacteria, the negibacterial root of the universal tree and bacterial megaclassification. Int J Syst Evol Microbiol 52, 7-76.

Chadwell, S., Rickard, D., Luther, G., 1999. Electrochemical Evidence for Pentasulfide Complexes with Mn2+, Fe2+, Co2+, Ni2+, Cu2+ and Zn2+. Aquat. Geochem. 5, 29-57.

Chadwell, S., Rickard, D., Luther, G., 2001. Electrochemical Evidence for Metal Polysulfide Complexes: Tetrasulfide (S2-4) Reactions with Mn2+, Fe2+, Co2+, Ni2+, Cu2+, and Zn2+. Electroanalysis 13, 21-29.

Chu, N., Johnson, C., Beard, B., German, C., Nesbitt, R., Frank, M., Bohn, M., Kubik, P., Usui, A., Graham, I., 2006. Evidence for hydrothermal venting in Fe isotope compositions of the deep Pacific Ocean through time. Earth and Planetary Science Letters 245, 202-217.

Clayton, R., Hudson-Edwards, K.A., Houghton, S.L., 2005. Isotopic effects during Cu adsorption onto goethite. Geochimica et Cosmochimica Acta 69, A216.

Cobble, J., Murray, R., 1978. Unusual ion solvation energies in high temperature water. Faraday Discussions of the Chemical Society 64, 144-149.

Cody, G.D., 2004. TRANSITION METAL SULFIDES AND THE ORIGINS OF METABOLISM. Annual Review of Earth and Planetary Sciences 32, 569-599.

Coleman, D.D., Risatti, J., Schoell, M., 1981. Fractionation of carbon and hydrogen isotopes by methane-oxidizing bacteria. Geochimica et Cosmochimica Acta 45, 1033-1037.

Cook, D., Clayton, R., Wadhwa, M., Janney, P., Davis, A., 2008. Nickel isotopic anomalies in troilite from iron meteorites. Geophys. Res. Lett. 35, L01203.

Criss, R., 1999. Principles of stable isotope distribution. Oxford University Press, New York 244pp.

Croal, L., Johnson, C., Beard, B., Newman, D., 2004. Iron isotope fractionation by Fe(II)-oxidizing photoautotrophic bacteria. Geochim Cosmochim Acta 68, 1127-1242.

Crosby, H., Johnson, C., Roden, E., Beard, B., 2005. Coupled Fe(II)-Fe(III) electron and atom exchange as a mechanism for Fe isotope fractionation during dissimilatory iron oxide reduction. Environ. Sci. Technol. 39, 6698-6704.

Crosby, H., Roden, E., Johnson, C., Beard, B., 2007. The mechanisms of iron isotope fractionation produced during dissimilatory Fe(III) reduction by Shewanella putrefaciens and Geobacter sulfurreducens. Geobiology 5, 169-189.

Czaja, A., Johnson, C., Beard, B., Eigenbrode, J., Freeman, K., Yamaguchi, K., 2010. Iron and carbon isotope evidence for ecosystem and environmental diversity in the ~ 2.7 to 2.5 Ga Hamersley Province, Western Australia. Earth and Planetary Science Letters 292, 170-180.

Darwin, F., 1888. The Life and Letters of Charles Darwin. John Murray, London.

Dauphas, N., Janney, P., Mendybaev, R., Wadhwa, M., Richter, F., Davis, A., van Zuilen, M., Hines, R., Foley, C., 2004a. Chromatographic separation and multicollection-ICPMS analysis of iron. Investigating mass dependent and -independent isotope effects. Anal. Chem. 76, 5855-5863.

Dauphas, N., van Zuilen, M., Wadhwa, M., Davis, A., Marty, B., Janney, P., 2004b. Clues from Fe Isotope Variations on the Origin of Early Archean BIFs from Greenland. Science 306, 2077-2080.

Dauphas, N., Rouxel, O., 2006. Mass Spectrometry and natural variations of iron

isotopes. Mass Spectrometry Reviews 25, 515-550.

Davison, W., Phillips, N., Tabner, B.J., 1999. Soluble iron sulfide species in natural waters: Reappraisal of their stoichiometry and stability constants. Aquatic Sciences - Research Across Boundaries 61, 23-43-43.

Dideriksen, K., Baker, J., Stipp, S., 2006. Iron isotopes in natural carbonate minerals determined by MC-ICP-MS with a 58Fe-54Fe double spike. Geochimica et Cosmochimica Acta 70, 118-132.

Domagal-Goldman, S.D., Kubicki, J.D., 2008. Density functional theory predictions of equilibrium isotope fractionation of iron due to redox changes and organic complexation. Geochimica et Cosmochimica Acta 72, 5201-5216.

Douville, E., Charlou, J.L., Oelkers, E.H., Bienvenu, P., Jove Colon, C.F., Donval, J.P., Fouquet, Y., Prieur, D., Appriou, P., 2002. The rainbow vent fluids (36°14'N, MAR): the influence of ultramafic rocks and phase separation on trace metal content in Mid-Atlantic Ridge hydrothermal fluids. Chemical Geology 184, 37-48.

Dos Santos Afonso, M., Stumm, W., 1992. Reductive dissolution of Fe(III) (hydr)oxides by hydrogen sulfide. Langmuir, 8, 1671-1675.

Drobner, E., Huber, H., Wächtershäuser, G., Rose, D., Stetter, K., 1990. Pyrite formation linked with hydrogen evolution under anaerobic conditions. Nature 346, 742-744.

Durand, B., 1980. Kerogen - Insoluble Organic Matter from Sedimentary Rocks, Edition Technip. ed. Paris.

de Duve, C., 2003. A Research Proposal on the Origin Of Life. Closing Lecture given at the ISSOL Congress in Oaxaca, Mexico, on July 4, 2002. Origins of Life and Evolution of Biospheres 33, 559-574.

Dyrssen, D., Kremling, K., 1990. Increasing hydrogen sulphide concentration and race metal behaviour in the anoxic Baltic waters. Marine Chemistry 30, 193-204.

Dysen, F., 1985. The Origin of Life. Cambridge University Press, Cambridge.

Edwards, K.J., Bond, P.L., Gihring, T.M., Banfield, J.F., 2000. An Archaeal Iron-Oxidizing Extreme Acidophile Important in Acid Mine Drainage. Science 287, 1796 -1799.

Ehrlich, S., Butler, I., Halicz, L., Rickard, D., Oldroyd, A., Matthews, A., 2004.

Experimental study of the copper isotope fractionation between aqueous Cu(II) and covellite, CuS. Chemical Geology 209, 259-269.

Eigen, M., Wilkins, R., 1965. The kinetics and mechanism of formation of metal complexes. Mechanisms of Inorganic Reactions, ACS Symposium Series 49, 55-80.

Eigenbrode, J.L., 2008. Fossil Lipids for Life-Detection: A Case Study from the Early Earth Record, in: Strategies of Life Detection, Space Sciences Series of ISSI. Springer US, pp. 161-185-185.

Eigenbrode, J.L., Freeman, K.H., Summons, R.E., 2008. Methylhopane biomarker hydrocarbons in Hamersley Province sediments provide evidence for Neoarchean aerobiosis. Earth and Planetary Science Letters 273, 323-331.

Ellis, A.S., Johnson, T.M., Bullen, T.D., 2002. Chromium Isotopes and the Fate of Hexavalent Chromium in the Environment. Science 295, 2060 -2062.

Ellis, A.S., Johnson, T.M., Bullen, T.D., 2004. Using Chromium Stable Isotope Ratios To Quantify Cr(VI) Reduction:□ Lack of Sorption Effects. Environmental Science & Technology 38, 3604-3607.

Emerson, D., 2000. Microbial Oxidation of Fe (II) and Mn (II) at Circumneutral pH. In: Environmental Microbe-Metal Interactions. Editor: Derek R. Lovley. 31-52.

Emmanuel, S., Erel, Y., Matthews, A., Teutsch, N., 2005. A preliminary mixing model for Fe isotopes in soils. Chemical Geology 222, 23-34.

Fantle, M., DePaolo, D., 2004. Iron isotopic fractionation during continental weathering. Earth and Planet. Science Letters 228, 547-562.

Farquhar, J., Bao, H., Thiemens, M., 2000. Atmospheric Influence of Earth's Earliest Sulfur Cycle. Science 289, 756-758.

Fedo, C.M., Whitehouse, M.J., 2002. Metasomatic Origin of Quartz-Pyroxene Rock, Akilia, Greenland, and Implications for Earth's Earliest Life. Science 296, 1448-1452.

Fernandez, A., Borrok, D., 2009. Fractionation of Cu, Fe, and Zn isotopes during the oxidative weathering of sulfide-rich rocks. Chemical Geology 264, 1-12.

Filtness, M., Butler, I., Rickard, D., 2003. The Origin of Life: The Properties of Iron Sulphide Membranes. Applied Earth Science (Trans. Inst. Min. Metall.) 112B, 171-172.

Forterre, P., Gribaldo, S., 2007. The origin of modern terrestrial life. HFSP J. 1, 156-

168.

Frei, R., Gaucher, C., Poulton, S.W., Canfield, D.E., 2009. Fluctuations in Precambrian atmospheric oxygenation recorded by chromium isotopes. Nature, 461, 250-254.

Freeman, K.H., Hayes, J.M., Trendel, J., Albrecht, P., 1990. Evidence from carbon isotope measurements for diverse origins of sedimentary hydrocarbons. Nature 343, 254-256.

Furukawa, Y., Barnes, H.L., 1996. Reactions forming smythite, Fe9S11. Geochimica et Cosmochimica Acta 60, 3581-3591.

Garrels, R., Mackenzie, F., 1971. Evolution of Sedimentary Rocks. Norton, New York.

Giggenbach, W., 1971. Optical Spectra of Highly Alkaline Sulfide Solutions and the Second Dissociation Constant of Hydrogen Sulfide. Inorg. Chem. 10, 1333.

Gillet, S., 1985. The rise and fall of the early reducing atmosphere. Astronomy 13, 66-71.

Golubic, S., Hofmann, H., 1976. Comparison of Holocene and mid-Precambrian Entophysalidaceae (Cyanophyta) in stromatolitic algal mats: cell division and degradation. Jounal of Paleontology 50, 1074-1082.

Gotz, A., Heumann, K., 1988. Iron isotope ratio measurements with the thermal ionization technique using a compact quadrupole mass-spectrometer. int. J. Mass Spectrom. Ion Proc. 83, 319-330.

Graham, S., Pearson, N., Jackson, S., Griffin, W., O'Reilly, S., 2004. Tracing Cu and Fe from source to porphyry: in situ determination of Cu and Fe isotope ratios in sulfides from the Grasberg Cu-Au deposit. Chemical Geology 207, 147-169.

Grassineau, N.V., Nisbet, *E.G.*, Bickle, M.J., Fowler, C.M.R., Lowry, D., Mattey, D.P., Abell, P., Martin, A., 2001. Antiquity of the biological sulphur cycle: evidence from sulphur and carbon isotopes in 2700 million–year–old rocks of the Belingwe Belt, Zimbabwe. Proceedings of the Royal Society of London. Series B: Biological Sciences 268, 113 -119.

Grassineau, N.V., Nisbet, *E.G.*, Fowler, C.M.R., Bickle, M.J., Lowry, D., Chapman, H.J., Mattey, D.P., Abell, P., Yong, J., Martin, A., 2002. Stable isotopes in the Archaean Belingwe belt, Zimbabwe: evidence for a diverse microbial mat ecology. Geological Society, London, Special Publications 199, 309-328.

Grassineau, N., Abell, P., Appel, P., Lowry, D., Nisbet, E., 2006. Early life signatures in sulphur and carbon isotopes from Isua, Barberton, Wabigoon (Steep Rock) and Belingwe Greenstone belts, in: Evolution of Early Earth's Atmosphere, Hydrosphere and Biosphere – Constraints from Ore Deposits. Geological Society of America, Special Publication, pp. 33–52.

Grotzinger, J., Kasting, J., 1993. New constaints on Precambrian ocean composition. J. Geol. 101, 235-243.

Grotzinger, J.P., Rothman, D.H., 1996. An abiotic model for stromatolite morphogenesis. Nature 383, 423-425.

Guilbaud, R., Butler, I.B., Ellam, R.M., Rickard, D., 2010a. Fe isotope exchange between Fe(II)aq and nanoparticulate mackinawite (FeSm) during nanoparticle growth. Earth and Planetary Science Letters 300, 174-183.

Guilbaud, R., Ellam, R., Butler, I., Gallagher, V., Keefe, K., 2010b. A procedural development for the analysis of 56/54Fe and 57/54Fe isotope ratios with new generation IsoProbe MC-ICP-MS. J. Anal. At. Spectrom 25, 1598-1604.

Habicht, K.S., Canfield, D.E., 1997. Sulfur isotope fractionation during bacterial sulfate reduction in organic-rich sediments. Geochimica et Cosmochimica Acta 61, 5351-5361.

Habicht, K.S., Gade, M., Thamdrup, B., Berg, P., Canfield, D.E., 2002. Calibration of Sulfate Levels in the Archean Ocean. Science 298, 2372 -2374.

Hall, D.O., Cammack, R., Rao, K.K., 1971. Role for Ferredoxins in the Origin of Life and Biological Evolution. Nature 233, 136-138.

Halliday, A., Lee, D., Christensen, J., Rehkamper, M., Li, W., Luo, X., Hall, C., Ballentine, C., Pettlee, T., Stirling, C., 1998. Applications of multiple collector ICPMS to cosmochemistry, geochemistry and paleoceanography. Geochim. Cosmochim. Acta 62, 919-940.

Handler, R., Beard, B., Johnson, C., Scherer, M., 2009. Atom Exchange between Aqueous Fe(II) and Goethite: An Fe Isotope Tracer Study. Environmental Science & Technology 43, 1102-1107.

Harmandas, N., Navarro Fernandez, E., Koutsoukos, P., 1998. Crystal Growth of Pyrite in Aqueous Solutions. Inhibition by Organophosphorus Compounds. Langmuir, American Chemical Society 14, 1250-1255.

Harrison, A., Thode, H.G., 1958. Mechanisms of the bacterial reduction of sulfate from isotope fractionation studies. Faraday Soc. Trans. 53, 84-92.

Harrison, T.M., Blichert-Toft, J., Muller, W., Albarede, F., Holden, P., Mojzsis, S.J., 2005. Heterogeneous Hadean Hafnium: Evidence of Continental Crust at 4.4 to 4.5 Ga. Science 310, 1947-1950.

Hatton, B., Rickard, D., 2008. Nucleic Acids Bind to Nanoparticulate iron (II) Monosulphide in Aqueous Solutions. Origins of Life and Evolution of Biospheres 38, 257-270.

Hayes, J., 1994. Global methanotrophy ath the Archean-Proterozoic transition., in: Bengston, S. (Ed.), Early Life on Earth (Nobel Symposium 84). pp. 220-236.

Hill, P., Schauble, E., 2008. Modeling the effects of bond environment on equilibrium iron isotope fractionation in ferric aquo-chloro complexes. Geochimica et Cosmochimica Acta 72, 1939-1958.

Hill, P.S., Schauble, E.A., Shahar, A., Tonui, E., Young, E.D., 2009. Experimental studies of equilibrium iron isotope fractionation in ferric aquo-chloro complexes. Geochimica et Cosmochimica Acta 73, 2366-2381.

Hofmann, H.J., Grey, K., Hickman, A.H., Thorpe, R.I., 1999. Origin of 3.45 Ga coniform stromatolites in Warrawoona Group, Western Australia. Geological Society of America Bulletin 111, 1256 -1262.

Holland, H., 1984. The chemical evolution of the atmosphere and oceans. New York: Princeton University Press.

Holland, H.D., 2002. Volcanic gases, black smokers, and the great oxidation event. Geochimica et Cosmochimica Acta 66, 3811-3826.

Homoky, W., Severmann, S., Mills, R., Statham, P., Fones, G., 2009. Pore-fluid Fe isotopes reflect the extent of benthic Fe redox recycling: Evidence from continental shelf and deep-sea sediments. Geology 37, 751-754.

Horita, J., 2005. Some perspectives on isotope biosignatures for early life. Chemical Geology 218, 171-186.

Horita, J., Berndt, M.E., 1999. Abiogenic Methane Formation and Isotopic Fractionation Under Hydrothermal Conditions. Science 285, 1055 -1057.

Horita, J., Zimmermann, H., Holland, H.D., 2002. Chemical evolution of seawater during the Phanerozoic: Implications from the record of marine evaporites. Geochimica et Cosmochimica Acta 66, 3733-3756.

House, C.H., Schopf, J.W., Stetter, K.O., 2003. Carbon isotopic fractionation by Archaeans and other thermophilic prokaryotes. Organic Geochemistry 34, 345-356.

Huang, S., Harris, K., Lopez-Capel, E., Manning, D., Rickard, D., 2009. "Amorphous Nickel Sulfide" Is Hydrated Nanocrystalline NiS with a Core-Shell Structure. Inorganic Chemistry 48, 11486-11488.

Huber, C., Wächtershäuser, G., 1997. “Activated acetic acid by carbon fixation on (Fe, Ni)s under primordial conditions.”. Science 276, 245 – 247.

Hutton, J., 1788. Theory of the Earth; or an investigation of the laws observable in the composition, dissolution, and restoration of land upon the globe. R Soc Edinb Trans 1, 209-304.

Icopini, G., Anbar, A., Ruebush, S., Tien, M., Brantley, S., 2004. Iron isotope fractionation during microbial reduction of iron: The importance of adsorption. Geology 32, 205-208.

Isley, A., Abbott, D., 1999. Plume-related mafic volcanism and the deposition of banded iron formation. J. Geophys. Res. 104, 15461-15477.

Jahnke, L.L., Nichols, P.D., 1986. Methyl sterol and cyclopropane fatty acid composition of Methylococcus capsulatus grown at low oxygen tensions. J. Bacteriol. 167, 238-242.

James, H., 1966. Chemistry of the iron-rich sedimentary rocks, U.S. Geol. Surv. Prof. Pap. ed.

Jang, J., Mathur, R., Liermann, L., Ruebush, S., Brantley, S., 2008. An iron isotope signature related to electron transfer between aqueous ferrous iron and goethite. Chemical Geology 250, 40-48.

Jarzecki, A., Anbar, A., Spiro, T., 2004. DFT Analysis of Fe(H2O)63+ and Fe(H2O)62+ Structure and Vibrations; Implication for Isotope Fractionation. J. Phys. Chem. A. 108, 2726-2732.

Jeong, H., Lee, J., Hayes, K., 2008. Characterization of synthetic nanocrystalline mackinawite: Crystal structure, particle size, and specific surface area. Geochimica et Cosmochimica Acta 72, 493-505.

Johnson, C., Beard, B., 2004. Isotopic Constraints on Biogeochemical Cycling of Fe. Reviews in Mineralogy and Geochemistry 55, 359-408.

Johnson, C., Beard, B., Roden, E., 2008a. The Iron Isotope Fingerprints of Redox and Biogeochemical Cycling in Modern and Ancient Earth. Annual Review of Earth and Planetary Sciences 36, 457-493.

Johnson, C., Beard, B., Klein, C., Beukes, N., Roden, E., 2008b. Iron isotopes constrain biologic and abiologic processes in banded iron formation genesis.

Geochim Cosmochim Acta 72, 151-169.

Johnson, D.C., Dean, D.R., Smith, A.D., Johnson, M.K., 2005a. Structure, function, and formation of biological iron-sulfur clusters. Annu. Rev. Biochem. 74, 247-281.

Johnson, C., Roden, E.E., Welch, S.A., Beard, B.L., 2005b. Experimental constraints on Fe isotope fractionation during magnetite and Fe carbonate formation coupled to dissimilatory hydrous ferric oxide reduction. Geochimica et Cosmochimica Acta 69, 963-993.

Johnson, C., Beard, B., Welch, S., Croal, L., Newman, D., Nealson, K., 2005c. Experimental constraints on Fe isotope fractionations during biogeochemical cycling of Fe. Geochim. Cosmochim. Acta 66, A371.

Johnson, C., Beard, B., Roden, E., Newman, D., Nealson, K., 2004. Isotopic Constraints on Biochemical Cycling of Fe. Reviews in Mineralogy & Geochemistry 55, 359-408.

Johnson, C., Beard, B., Beukes, N., Klein, C., O'Leary, J., 2003. Ancient geochemical cycling in the Earth as inferred from Fe isotope studies of banded iron formations from the Transvaal Craton. Contributions to Mineralogy and Petrology 523-547.

Johnson, C., Skulan, J., Beard, B., Sun, H., Nealson, K., Braterman, P., 2002. Isotopic fractionation between Fe(III) and Fe(II) in aqueous solutions. Earth and Planetary Science Letters 195, 141-153.

Johnson, K., Gordon, R., Coale, K., 1997. What controls dissolved iron concentrations in the world ocean? Marine Chemistry 57, 137-161.

Kaufman, A., Johnston, D., Farquhar, J., Masterson, A., Lyons, T., Bates, S., Anbar, A., Arnold, G., Garvin, J., Buick, R., 2007. Late Archean Biospheric Oxygenation and Atmospheric Evolution. Science 317, 1900-1903.

Kavner, A., Bonet, F., Shahar, A., Simon, J., Young, E., 2005. The isotopic effects of electron transfer: An explanation for Fe isotope fractionation in nature. Geochim Cosmochim Acta 69, 2971–2979.

Kehm, K., Hauri, E., Alexander, C., Carlson, R., 2003. High precision iron isotope measurements of meteoritic material by cold plasma ICPMS. Geochim Cosmochim Acta 67.

Knoll, A.H., 1999. A New Molecular Window on Early Life. Science 285, 1025 - 1026.

Knoll, A.H., 2003. The geological consequences of evolution. Geobiology 1, 3-14.

Lancet, M.S., Anders, E., 1970. Carbon Isotope Fractionation in the Fischer-Tropsch Synthesis and in Meteorites. Science 170, 980 -982.

Larson, P., Maher, K., Ramos, F., Chang, Z., Gaspar, M., Meinert, L., 2003. Copper isotope ratios in magmatic and hydrothermal ore-forming environments. Chemical Geology 201, 337-350.

Lennie, A., Redfern, S., Champness, P., Stoddart, C., Schofield, P., Vaughan, D., 1997. Transformation of mackinawite to greigite: An in situ X-ray powder diffraction and transmission electron microscope study. American Mineralogist 82, 302–309.

Lennie, A., Redfern, S., Schofield, P., Vaughan, D., 1995. Synthesis and Rietveld crystal structure refinement of mackinawite, tetragonal FeS. Min. Mag. 59, 677– 683.

Levasseur, S., Frank, M., Hein, J., Halliday, A., 2004. The global variation in the iron isotope composition of marine hydrogenetic ferromanganese deposits: implications for seawater chemistry? Earth and Planetary Science Letters 224, 91-105.

Londry, K.L., Des Marais, D.J., 2003. Stable Carbon Isotope Fractionation by Sulfate-Reducing Bacteria. Appl. Environ. Microbiol. 69, 2942-2949.

Lovelock, J., 1979. Gaia: A New Look at Life on Earth, Oxford University Press. ed. Oxford.

Lovley, D., 2006. Dissimilatory Fe(III)- and Mn(IV)-Reducing Prokaryotes, in: The Prokaryotes. Springer New York, pp. 635-658-658.

Lowe, D.R., 1980. Stromatolites 3,400-Myr old from the Archean of Western Australia. Nature 284, 441-443.

Lowe, D.R., 1994. Abiological origin of described stromatolites older than 3.2 Ga. Geology 22, 387-390.

Lowenstam, H., 1981. Minerals formed by organisms. Science 211, 1126-1131.

Luck, J., Othman, D., Barrat, J., Albarède, F., 2003. Coupled 63Cu and 16O excesses in chondrites. Geochimica et Cosmochimica Acta 67, 143-151.

Luck, J., Othman, D., Albarède, F., 2005. Zn and Cu isotopic variations in chondrites and iron meteorites: Early solar nebula reservoirs and parent-body processes. Geochimica et Cosmochimica Acta 69, 5351-5363.

Luther, G., 1991. Pyrite synthesis via polysulfide compounds. Geochim. Cosmochim.

Acta 55, 2839– 2849.

Luther, G., Church, T., Powell, D., 1991. Sulfur Speciation and Sulfide Oxidation in the Water Column of the Black Sea. Deep-Sea Research DESRAY 38, 1121-1137.

Luther, G., Rozan, T., Taillefert, M., Nuzzio, D., Di Meo, C., Shank, T., Lutz, R., Craig Cary, S., 2001. Chemical speciation drives hydrothermal vent ecology. Nature 410, 813–816.

Luther, G., Taillefert, M., Rozan, T., Rickard, D., 2003. Geochemical implications of the polysulfide vs. sulfide pyrite formation reactions based on real time measurements of soluble reactants. Abstr. Pap. - Am. Chem. Soc. GEOC9.

Macleod, G., McKeown, C., Hall, A.J., Russell, M.J., 1994. Hydrothermal and oceanic pH conditions of possible relevance to the origin of life. Origins of Life and Evolution of Biospheres 24, 19-41-41.

Malinovsky, D., Stenberg, A., Rodushkin, I., Andren, H., Ingri, J., Ohlander, B., Baxter, D.C., 2003. Performance of high resolution MC-ICP-MS for Fe isotope ratio measurements in sedimentary geological materials. J. Anal. At. Spectrom. 18, 687-695.

Mandernack, K.W., Bazylinski, D.A., Shanks, W.C., III, Bullen, T.D., 1999. Oxygen and Iron Isotope Studies of Magnetite Produced by Magnetotactic Bacteria. Science 285, 1892 -1896.

Marcus, R.A., 1964. Chemical and Electrochemical Electron-Transfer Theory. Annu. Rev. Phys. Chem. 15, 155-196.

Marechal, C., Telouk, P., Albarede, F., 1999. Precise analysis of copper and zinc isotopic compositions by plasmasource mass spectrometry. Chem. Geol. 156, 251-273.

Markl, G., von Blanckenburg, F., Wagner, T., 2006. Iron isotope fractionation during hydrothermal ore deposition and alteration. Geochimica et Cosmochimica Acta 70, 3011-3030.

Martin, W., Russell, M., 2003. On the origins of cells: a hypothesis for the evolutionary transitions from abiotic geochemistry to chemoautotrophic prokaryotes, and from prokaryotes to nucleated cells. Philosophical Transactions of the Royal Society of London. Series B: Biological Sciences 358, 59-85.

Mason, T., Weiss, D., Chapman, J., Wilkinson, J., Tessalina, S., Spiro, B.,

Horstwood, M., Spratt, J., Coles, B., 2005. Zn and Cu isotopic variability in the Alexandrinka volcanic-hosted massive sulphide (VHMS) ore deposit, Urals, Russia. Chemical Geology 221, 170-187.

Mathur, R., Ruiz, J., Titley, S., Liermann, L., Buss, H., Brantley, S., 2005. Cu isotopic fractionation in the supergene environment with and without bacteria. Geochimica et Cosmochimica Acta 69, 5233-5246.

Matsuhisa, Y., Goldsmith, J., Clayton, R., 1978. Mechanisms of hydrothermal crystallization of quartz at 250°C and 15 kbar. Geochimica et Cosmochimica Acta 42, 173-182.

Matthews, A., Goldsmith, J., Clayton, R., 1983. On the mechanisms and kinetics of oxygen isotope exchange in quartz and feldspars at elevated temperatures and pressures. Geol. Soc. Am. Bul. 94, 396-412.

Matthews, A., Morgans-Bell, H., Emmanuel, S., Jenkyns, H., Erel, Y., Halicz, L., 2004. Controls on iron-isotope fractionation in organic-rich sediments (Kimmeridge Clay, Upper Jurassic, Southern England). Geochimica et Cosmochimica Acta 68, 3107-3123.

Matthews, A., Zhu, X., O'Nions, K., 2001. Kinetic iron stable isotope fractionation between iron (-II) and (-III) complexes in solution. Earth and Planet. Science Letters 192.

McAnena, A., Severmann, S., Poulton, S., 2009. Abiotic Fe isotope fractionation during sulfide mediated reductive dissolution of Fe oxide minerals. Goldschmidt Conference Abstracts.

McManus, J., Nagler, T., Siebert, C., Wheat, C., Hammond, D., 2002. Oceanic molybdenum isotope fractionation: Diagenesis and hydrothermal ridge-flank alteration. Geochem. Gephys. Geosys. 3.

Migdisov, A.A., Williams-Jones, A.E., Lakshtanov, L.Z., Alekhin, Y.V., 2002. Estimates of the second dissociation constant of H2S from the surface sulfidation of crystalline sulfur. Geochimica et Cosmochimica Acta 66, 1713-1725.

Miller, S., 1953. A production of amino acids under possible primitive Earth conditions. Science 117, 528-529.

Millero, F., 1996. Chemical Oceanography. CRC Press: Boca Raton, FL.

Mojzsis, S., Arrhenius, G., McKeegan, K., Harrison, T., Nutman, A., Friend, C., 1996. Evidence for life on Earth before 3,800 million years ago. Nature 384,

55-59.

Morse, J.W., Rickard, D., 2004. Peer Reviewed: Chemical Dynamics of Sedimentary Acid Volatile Sulfide. Environmental Science & Technology 38, 131A-136A.

Moynier, F., Blichert-Toft, J., Telouk, P., Luck, J., Albarède, F., 2007. Comparative stable isotope geochemistry of Ni, Cu, Zn, and Fe in chondrites and iron meteorites. Geochimica et Cosmochimica Acta 71, 4365-4379.

Mullane, E., Russell, S., Gounelle, M., Mason, T., Din, V., Weiss, D., Coles, B., 2003. Precise and accurate determination of iron isotopes by multi-collector inductively coupled plasma mass spectrometry. In plasma source mass spectrometry: Applications and emerging technologies. London: The Royal Society of Chemistry. 351-361.

Muller, A., Diemann, E., 1987. Polysulphide complexes of metals. Adv. Inorg. Chem. 31, 89-122.

Murowchick, J.B., Barnes, H.L., 1986. Formation of cubic FeS. American Mineralogist 71, 1243-1246.

Murphey, B., Nier, A., 1941. Variations in the Relative Abundance of the Carbon Isotopes. Physical reviews 59, 771-772.

Murray, J., Jannasch, H., Honjo, S., Anderson, R., Reeburgh, W., Top, Z., Friederich, G., Codispoti, L., Izdar, E., 1989. Unexpected changes in the oxic/anoxic interface in the Black Sea. Nature 338, 411 - 413.

Nägler, T., Siebert, C., Lüschen, H., Böttcher, M., 2005. Sedimentary Mo isotope record across the Holocene fresh-brackish water transition of the Black Sea. Chemical Geology 219, 283-295.

Nealson, K., Saffarini, D., 1994. Iron and Manganese in Anaerobic Respiration: Environmental Significance, Physiology, and Regulation. Annual Review of Microbiology 48, 311-343.

Nier, A.O., Gulbransen, E.A., 1939. Variations in the Relative Abundance of the Carbon Isotopes. Journal of the American Chemical Society 61, 697-698.

Nisbet, *E.G.*, Sleep, N.H., 2001. The habitat and nature of early life. Nature 409, 1083-1091.

Nishizawa, M., Yamamoto, H., Ueno, Y., Tsuruoka, S., Shibuya, T., Sawaki, Y., Yamamoto, S., Kon, Y., Kitajima, K., Komiya, T., Maruyama, S., Hirata, T., 2010. Grain-scale iron isotopic distribution of pyrite from Precambrian shallow marine carbonate revealed by a femtosecond laser ablation

multicollector ICP-MS technique: Possible proxy for the redox state of ancient seawater. Geochimica et Cosmochimica Acta 74, 2760-2778.

Nolan, A.L., Ma, Y., Lombi, E., McLaughlin, M.J., 2004. Measurement of labile Cu in soil using stable isotope dilution and isotope ratio analysis by ICP-MS. Analytical and Bioanalytical Chemistry 380, 789-797.

Ohfuji, H., Rickard, D., 2006. High resolution transmission electron microscopic study of synthetic nanocrystalline mackinawite. Earth and Planet. Science Letters 241, 227.

Ohmoto, H., Kakegawa, T., Lowe, D., 1993. 3.4-Billion-year-old biogenic pyrites from Barberton, South Africa: sulfur isotope evidence. Science 262, 555 -557.

Ohmoto, H., Goldhaber, M., 1997. Sulfur and carbon isotopes, in: Geochemistry of Hydrothermal Ore Deposits. Wiley, New York.

Ohmoto, H., 1996. Evidence in pre–2.2 Ga paleosols for the early evolution of atmospheric oxygen and terrestrial biota. Geology 24, 1135 -1138.

Ohmoto, H., Felder, R.P., 1987. Bacterial activity in the warmer, sulphate-bearing, Archaean oceans. Nature 328, 244-246.

Ohmoto, H., Watanabe, Y., Ikemi, H., Poulson, S.R., Taylor, B.E., 2006. Sulphur isotope evidence for an oxic Archaean atmosphere. Nature 442, 908-911.

O'Leary, M.H., 1981. Carbon isotope fractionation in plants. Phytochemistry 20, 553-567.

Oparin, A., 1938. The origin of Life. Dover, New York.

Ottonello, G., Zuccolini, M.V., 2009. Ab-initio structure, energy and stable Fe isotope equilibrium fractionation of some geochemically relevant H-O-Fe complexes. Geochimica et Cosmochimica Acta 73, 6447-6469.

Pace, N., 1997. A molecular view of microbial diversity and the biosphere. Science 276, 734-740.

Parker, V., Khodakovskii, I., 1995. Thermodynamic Properties of the aqueous Ions (2+ and 3+) of Iron and the Key Compounds of Iron. J. Phys. Ref. Data 24, 1699.

Parnell, J., Boyce, A.J., Mark, D., Bowden, S., Spinks, S., 2010. Early oxygenation of the terrestrial environment during the Mesoproterozoic. Nature 468, 290-293.

Patrick, W.A., Thompson, W.E., 1953. Standard Electrode Potential of the Iron—Ferrous Ion Couple at 25°. Journal of the American Chemical Society 75, 1184-1187.

Pavlov, A., Kasting, J., 2002. Mass-independent fractionation of sulfur isotopes in Archean sediments: Strong evidence for an anoxic Archean atmosphere. Astrobiology 2, 27-41.

Pearce, C., Cohen, A., Coe, A., Burton, K., 2008. Molybdenum isotope evidence for global ocean anoxia coupled with perturbations to the carbon cycle during the Early Jurassic. Geology 36, 231-234.

Pereira, M.M., Santana, M., Teixeira, M., 2001. A novel scenario for the evolution of haem-copper oxygen reductases. Biochimica et Biophysica Acta (BBA) - Bioenergetics 1505, 185-208.

Poitrasson, F., 2010. Iron Isotopes (Advances in Isotope Geochemistry). Springer.

Poitrasson, F., Freydier, R., 2005. Heavy iron isotope composition of granites determined by high resolution MC-ICP-MS. Chemical Geology 222, 132-147.

Poitrasson, F., Levasseur, S., Teutsch, N., 2005. Significance of iron isotope mineral fractionation in pallasites and iron meteorites for the core-mantle differentiation of terrestrial planets. Earth and Planetary Science Letters 234, 151-164.

Poitrasson, F., 2007. Does planetary differentiation really fractionate iron isotopes? Earth and Planetary Science Letters 256, 484-492.

Poitrasson, F., Halliday, A.N., Lee, D., Levasseur, S., Teutsch, N., 2004. Iron isotope differences between Earth, Moon, Mars and Vesta as possible records of contrasted accretion mechanisms. Earth and Planetary Science Letters 223, 253-266.

Pokrovsky, O., Viers, J., Freydier, R., 2005. Zinc stable isotope fractionation during its adsorption on oxides and hydroxides. Journal of Colloid and Interface Science 291, 192-200.

Polyakov, V., Clayton, R., Horita, J., Mineev, S., 2007. Equilibrium iron isotope fractionation factors of minerals: Reevaluation from the data of nuclear inelastic resonant X-ray scattering and Mössbauer spectroscopy. Geochimica et Cosmochimica Acta 71, 3833-3846.

Polyakov, V., Mineev, S., 2000. The use of Mossbauer spectroscopy in stable isotope geochemistry. Geochim Cosmochim Acta 64, 849-865.

Polyakov, V.B., 1997. Equilibrium fractionation of the iron isotopes: Estimation from Mossbauer spectroscopy data. Geochimica et Cosmochimica Acta 61, 4213-4217.

Poulson, R., Johnson, C., Beard, B., 2005. Iron isotope exchange kinetics at the nanoparticulate ferrihydrite surface. American Mineralogist 90, 758-763.

Poulson, R., Siebert, C., McManus, J., Berelson, W., 2006. Authigenic molybdenum isotope signatures in marine sediments. Geology 34, 617-620.

Poulton, S., Fralick, P., Canfield, D., 2004. The transition to a sulphidic ocean [sim] 1.84 billion years ago. Nature 431, 173-177.

Poulton, S., Fralick, P., Canfield, D., 2010. Spatial variability in oceanic redox structure 1.8[thinsp]billion years ago. Nature Geosci 3, 486-490.

Poulton, S.W., Canfield, D.E., 2005. Development of a sequential extraction procedure for iron: implications for iron partitioning in continentally derived particulates. Chemical Geology 214, 209-221.

Pyzik, A., Sommer, S., 1981. Sedimentary iron monosulfides: kinetics and mechanisms of formation. Geochim. Cosmochim. Acta 45.

Quitté, G., Meier, M., Latkoczy, C., Halliday, A., Günther, D., 2006. Nickel isotopes in iron meteorites-nucleosynthetic anomalies in sulphides with no effects in metals and no trace of 60Fe. Earth and Planetary Science Letters 242, 16-25.

Raiswell, R., Berner, R., 1985. Pyrite formation in euxinic and semi-euxinic sediments. Am. J. Sci. 285, 710-724.

Raiswell, R., Bottrell, S., Albiatty, H., Tan, M., 1993. The influence of bottom water oxygenation and reactive iron content on sulfur incorporation into bitumens from Jurassic marine shales. American Journal of Science 293, 569–596.

Raiswell, R., Canfield, D., 1998. Sources of iron for pyrite formation in marine sediments. Am J Sci 298, 219-245.

Raiswell, R., Newton, R., Wignall, P., 2001. An Indicator of Water-Column Anoxia: Resolution of Biofacies Variations in the Kimmeridge Clay (Upper Jurassic, U.K.). JOURNAL OF SEDIMENTARY RESEARCH 71, 286-294.

Randall, M., Frandsen, M., 1932. The standard electrode potential of iron and the activity coefficient of ferrous chloride. Journal of the American Chemical Society 54, 47-54.

Rasmussen, B., Buick, R., 1999. Redox state of the Archean atmosphere: Evidence from detrital heavy minerals in ca. 3250-2750 Ma sandstones from the Pilbara Craton, Australia. Geology 27, 115-118.

Reinhard, C., Raiswell, R., Scott, C., Anbar, A., Lyons, T., 2009. A Late Archean Sulfidic Sea Stimulated by Early Oxidative Weathering of the Continents.

Science 326, 713-716.

Revsbech, N., Jorgensen, B., Brix, O., 1981. Primary production of microalgae in sediments measured by oxygen microprofile, H14CO3- fixation, and oxygen exchange methods. Limnol. Oceanogr. 26, 717.

Revsbech, N., Madsen, B., Jorgensen, B., 1986. Oxygen production and consumption in sediments determined at high spatial resolution by computer simulation of oxygen microelectrode data. Limnol. Oceanogr. 31, 293-304.

Richter, F., Dauphas, N., Teng, F., 2009. Non-traditional fractionation of non-traditional isotopes: Evaporation, chemical diffusion and Soret diffusion. Chemical Geology 258, 92-103.

Richter, F.M., Davis, A.M., DePaolo, D.J., Watson, E.B., 2003. Isotope fractionation by chemical diffusion between molten basalt and rhyolite. Geochimica et Cosmochimica Acta 67, 3905-3923.

Rickard, D., 1969. The chemistry of iron sulfide formation at low temperatures. Stockh. Contrib. Geol. 20, 67–95.

Rickard, D., 1974. Kinetics and mechanisms of the sulfidation of goethite. Am. J. Sci. 274, 941-952.

Rickard, D., 1995. Kinetics of FeS precipitation: Part 1. Competing reaction mechanisms. Geochim. Cosmochim. Acta 59, 4367– 4379.

Rickard, D., 1997. Kinetics of pyrite formation by the H2S oxidation of iron (II) monosulfide in aqueous solutions between 25oC and 125oC: the rate equation. Geochim. Cosmochim. Acta 61, 115– 134.

Rickard, D., 2006. The solubility of FeS. Geochimica et Cosmochimica Acta 70, 5779-5789.

Rickard, D., Griffith, A., Oldroyd, A., Butler, I., Lopez-Capel, E., Manning, D., Apperley, D., 2006. The composition of nanoparticulate mackinawite, tetragonal iron (II) monosulfide. Chem. Geol. 235.

Rickard, D., Luther, G., 1997. Kinetics of pyrite formation by the H2S oxidation of iron (II) monosulfide in aqueous solutions between 25 8C and 125 8C: the mechanism. Geochim. Cosmochim. Acta 61, 135–147.

Rickard, D., Luther, G., 2006. Metal Sulfide Complexes and Clusters. Reviews in Mineralogy & Geochemistry 61, 421-504.

Rickard, D., Luther, G., 2007. Chemistry of Iron Sulfides. Chem. Rev. 107, 514-562.

Rickard, D., Morse, J., 2005. Acid Volatile Sulfide (AVS). Marine Chemistry 97,

141-197.

Rickard, D., 1975. Kinetics and mechanism of pyrite formation at low temperatures. Am J Sci 275, 636-652.

Rickard, D., Butler, I.B., Oldroyd, A., 2001. A novel iron sulphide mineral switch and its implications for Earth and planetary science. Earth and Planetary Science Letters 189, 85-91.

Roe, J., Anbar, A., Barling, J., 2003. Nonbiological fractionation of Fe isotopes: Evidence of an equilibrium isotope effect. Chem. Geol. 195.

Roscoe, S., 1957. Geology and uranium deposits, Quirke Lake-Elliot Lake, Blind River area, Ontario (preliminary report). Geological Survey of Canada 56.

Rosen, E., Tegman, R., 1971. A preparative and X-ray powder diffraction study of the polysulfides Na2S2, Na2S4, Na2S5. Acta. Chem. Scand. 25, 3329-3336.

Rosing, M.T., Rose, N.M., Bridgwater, D., Thomsen, H.S., 1996. Earliest part of Earth's stratigraphic record: A reappraisal of the >3.7 Ga Isua (Greenland) supracrustal sequence. Geology 24, 43-46.

Roskosz, M., Luais, B., Watson, H.C., Toplis, M.J., Alexander, C.M., Mysen, B.O., 2006. Experimental quantification of the fractionation of Fe isotopes during metal segregation from a silicate melt. Earth and Planetary Science Letters 248, 851-867.

Rotaru, M., Birck, J., Allegre, C., 1992. Clues to early Solar System history from chromium isotopes in carbonaceous chondrites. Nature 358, 465-470.

Rouxel, O., Dobbek, N., Ludden, J., Fouquet, Y., 2003. Iron isotope fractionation during oceanic crust alteration. Chem. Geol. 202, 155-182.

Rouxel, O., Fouquet, Y., Ludden, J., 2004. Subsurface processes at the lucky strike hydrothermal field, Mid-Atlantic ridge: evidence from sulfur, selenium, and iron isotopes. Geochimica et Cosmochimica Acta 68, 2295-2311.

Rouxel, O., Bekker, A., Edwards, K., 2005. Iron isotope constraints on the Archean and Paleoproterozoic ocean redox state. Science 307, 1088-1090.

Rouxel, O., Shanks III, W.C., Bach, W., Edwards, K.J., 2008a. Integrated Fe- and S-isotope study of seafloor hydrothermal vents at East Pacific Rise 9-10°N. Chemical Geology 252, 214-227.

Rouxel, O., Sholkovitz, E., Charette, M., Edwards, K.J., 2008b. Iron isotope fractionation in subterranean estuaries. Geochimica et Cosmochimica Acta 72,

3413-3430.

Rouxel, O.J., Auro, M., 2010. Iron Isotope Variations in Coastal Seawater Determined by Multicollector ICP-MS. Geostandards and Geoanalytical Research 34, 135-144.

Russell, M., Daniel, R., Hall, A., Sherringham, J., 1994. A hydrothermally precipitated catalytic iron sulphide membrane as a first step toward life. Journal of Molecular Evolution 39, 231-243.

Russell, M., Hall, A., 1997. The emergence of life from iron monosulphide bubbles at a submarine hydrothermal redox and pH front. Journal of the Geological Society 154, 377-402.

Russell, M., 2007. The Alkaline Solution to the Emergence of Life: Energy, Entropy and Early Evolution. Acta Biotheoretica 55, 133-179-179.

Rye, R., Holland, H., 1998. Paleosols and the evolution of atmospheric oxygen: a critical review. American Journal of Science 298, 621-672.

Schauble, E., 2004. Applying Stable Isotope Fractionation Theory to New Systems. Reviews in Mineralogy & Geochemistry 55, 65-111.

Schauble, E., Rossman, G., Taylor, H., 2001. Theoretical estimates of equilibrium Fe-isotope fractionations from vibrational spectroscopy. Geochimica et Cosmochimica Acta 65, 2487-2497.

Schidlowski, M., 1981. Uraniferous constituants of the Witwatersrand conglomerate: Ore microscope observations and implications for Witwatersrand metallogeny. US Geological Survay Professional Paper 1161.

Schidlowski, M., 1988. A 3,800-million-year isotopic record of life from carbon in sedimentary rocks. Nature 333, 313-318.

Schidlowski, M., 2001. Carbon isotopes as biogeochemical recorders of life over 3.8 Ga of Earth history: evolution of a concept. Precambrian Research 106, 117-134.

Schidlowski, M., Appel, P.W., Eichmann, R., Junge, C.E., 1979. Carbon isotope geochemistry of the 3.7 Ga 109-yr-old Isua sediments, West Greenland: implications for the Archaean carbon and oxygen cycles. Geochimica et Cosmochimica Acta 43, 189-199.

Schoenberg, R., von Blanckenburg, F., 2005. An assessment of the accuracy of stable Fe isotope ratio measurements on samples with organic and inorganic matrices by high-resolution multicollector ICP-MS. International Journal of Mass

Spectrometry 242, 257-272.

Schoenberg, R., von Blanckenburg, F.V., 2006. Modes of planetary-scale Fe isotope fractionation. Earth and Planetary Science Letters 252, 342-359.

Schoonen, M., Barnes, H., 1988. An approximation of the second dissociation constant for H2S. Geochim. Cosmochim. Acta 52, 649.

Schoonen, M., Barnes, H., 1991. Reactions forming pyrite and marcasite from solution: II via FeS precursors below 100oC. Geochim. Cosmochim. Acta 60, 115-134.

Schopf, J.W., 2006. Fossil evidence of Archaean life. Philosophical Transactions of the Royal Society B: Biological Sciences 361, 869 -885.

Schopf, J.W., Kudryavtsev, A.B., Czaja, A.D., Tripathi, A.B., 2007. Evidence of Archean life: Stromatolites and microfossils. Precambrian Research 158, 141-155.

Schopf, J., 1993. Microfossils of the Early Archean Apex chert: New evidence of the antiquity of life. Science 260, 640-646.

Schuessler, J.A., Schoenberg, R., Behrens, H., Blanckenburg, F.V., 2007. The experimental calibration of the iron isotope fractionation factor between pyrrhotite and peralkaline rhyolitic melt. Geochimica et Cosmochimica Acta 71, 417-433.

Severmann, S., Johnson, C., Beard, B., German, C., Edmonds, H., Chiba, H., Green, D., 2004. The effect of plume processes on the Fe-isotope composition of hydrothermally derived Fe in the deep ocean as inferred from the Rainbow vent site, Mid-Atlantic Ridge, 36o14'N. Earth and Planet. Science Letters 225, 63-76.

Severmann, S., Johnson, C., Beard, B., McManus, J., 2006. The effect of early diagenesis on the Fe isotope compositions of porewaters and authigenic minerals in continental margin sediments. Geochim Cosmochim Acta 70, 2006–2022.

Severmann, S., McManus, J., Berelson, W.M., Hammond, D.E., 2010. The continental shelf benthic iron flux and its isotope composition. Geochimica et Cosmochimica Acta 74, 3984-4004.

Shahar, A., Young, E., Manning, C., 2008. Equilibrium high-temperature Fe isotope fractionation between fayalite and magnetite: An experimental calibration. Earth and Planet. Science Letters 268, 330–338.

Sharma, M., Polizzotto, M., Anbar, A., 2001. Iron isotopes in hot springs along the Juan de Fuca Ridge. Earth. Planet. Sci. Lett. 194.

Shen, Y., Buick, R., Canfield, D., 2001. Isotopic evidence for microbial sulphate reduction in the early Archaean era. Nature 410, 77-81.

Shen, Y., Buick, R., 2004. The antiquity of microbial sulfate reduction. Earth-Science Reviews 64, 243-272.

Shen, Y., Knoll, A.H., Walter, M.R., 2003. Evidence for low sulphate and anoxia in a mid-Proterozoic marine basin. Nature 423, 632-635.

Shimamura, T., Lugmair, G., 1983. Ni isotopic compositions in Allende and other meteorites. Earth and Planetary Science Letters 63, 177-188.

Siebert, C., Kramers, J., Meisel, T., Morel, P., Nägler, T., 2005. PGE, Re-Os, and Mo isotope systematics in Archean and early Proterozoic sedimentary systems as proxies for redox conditions of the early Earth. Geochimica et Cosmochimica Acta 69, 1787-1801.

Siebert, C., McManus, J., Bice, A., Poulson, R., Berelson, W., 2006. Molybdenum isotope signatures in continental margin marine sediments. Earth and Planetary Science Letters 241, 723-733.

Siebert, C., Nägler, T., von Blanckenburg, F., Kramers, J., 2003. Molybdenum isotope records as a potential new proxy for paleoceanography. Earth and Planetary Science Letters 211, 159-171.

Sirevåg, R., Buchanan, B.B., Berry, J.A., Troughton, J.H., 1977. Mechanisms of CO₂ fixation in bacterial photosynthesis studied by the carbon isotope fractionation technique. Archives of Microbiology 112, 35-38-38.

Skei, J., 1988. Framvaren - Environmental Setting. Marine Chemistry 23, 209-218.

Skulan, J., Beard, B., Johnson, C., 2002. Kinetic and equilibrium Fe isotope fractionation between aqueous Fe(III) and hematite. Geochim. Cosmochim. Acta 66, 2995-3015.

Smith, R., Martell, A., 1976. Critical stability constants. Plenum, New York.

Staton, S., 2006. Iron isotope fractionation during photo-oxidation of aqueous ferrous iron. In: Astrobiology Science Conference.

Staubwasser, M., von Blanckenburg, F., Schoenberg, R., 2006. Iron isotopes in the early marine diagenetic iron cycle. Geology 34, 629 -632.

Stetter, K.O., 1996. Hyperthermophilic procaryotes. FEMS Microbiology Reviews 18, 149-158.

Straub, K., Benz, M., Schink, B., 2001. Iron metabolism in anoxic environments at near neutral pH. FEMS Microbiology Ecology 34, 181-186.

Suleimenov, O., Seward, T., 1997. A spectrophotometric study of hydrogen sulphide ionisation in aqueous solutions to 350dC. Geochim. Cosmochim. Acta 61, 5187.

Summons, R.E., Bradley, A.S., Jahnke, L.L., Waldbauer, J.R., 2006. Steroids, triterpenoids and molecular oxygen. Philosophical Transactions of the Royal Society B: Biological Sciences 361, 951 -968.

Summons, R.E., Jahnke, L.L., Hope, J.M., Logan, G.A., 1999. 2-Methylhopanoids as biomarkers for cyanobacterial oxygenic photosynthesis. Nature 400, 554-557.

Summons, R.E., Jahnke, L.L., Roksandic, Z., 1994. Carbon isotopic fractionation in lipids from methanotrophic bacteria: Relevance for interpretation of the geochemical record of biomarkers. Geochimica et Cosmochimica Acta 58, 2853-2863.

Sweeney, R., Kaplan, I., 1973. Pyrite framboid formation: laboratory synthesis and marine sediments. Econ. Geol. 68, 618– 634.

Sweeton, F., Baes, C., 1970. The solubility of magnetite and hydrolysis of ferrous ion in aqueous solutions at elevated temperatures. J. Chem. Thermodyn. 2, 479.

Taylor, P., Maeck, R., De Bievre, P., 1992. Determination of the absolute isotopic composition and atomic weight of a reference sample of natural iron. Int. J. Mass Spectrom. Ion Proc. 121, 111-125.

Teutsch, N., von Gunten, U., Porcelli, D., Cirpka, O., Halliday, A., 2005. Adsorption as a cause for iron isotope fractionation in reduced groundwater. Geochim Cosmochim Acta 69, 4175-4185.

Thode, H.G., Macnamara, J., Fleming, W.H., 1953. Sulphur isotope fractionation in nature and geological and biological time scales. Geochimica et Cosmochimica Acta 3, 235-243.

Tremaine, P.R., LeBlanc, J.C., 1980. The solubility of magnetite and the hydrolysis and oxidation of Fe²⁺ in water to 300°C. Journal of Solution Chemistry 9, 415-442-442.

Turner, D., Whitfield, M., Dickson, A., 1981. The equilibrium speciation of dissolved components in freshwater and sea water at 25°C and 1 atm pressure. Geochim Cosmochim Acta 45, 855-881.

Urey, H., 1947. The thermodynamic properties of isotopic substances. J. Chem. Soc.

562-581.

Valley, G., Anderson, H., 1947. A comparison of the abundance ratios of the isotopes of terrestrial and of meteoritic iron. J. Am. Chem. Soc. 69, 1871-1875.

Vargas, M., Kashefi, K., Blunt-Harris, E., Lovley, D., 1998. Microbiological evidence for Fe(III) reduction on early Earth. Nature 395, 65.

Vernadzky, V., 1929. La biosphere, 2eme edition revue et argumentee, Librairie Félix Alcan. ed. Paris.

Vogl, J., Klingbeil, P., Pritzkow, W., Riebe, G., 2003. High accuracy measurements of Fe isotopes using hexapole collision cell MC-ICP-MS and isotope dilution for certification of reference materials. Journal of Analytical Atomic Spectrometry 18, 1125 - 1132.

Von Damm, K.L., 1990. Seafloor Hydrothermal Activity: Black Smoker Chemistry and Chimneys. Annual Review of Earth and Planetary Sciences 18, 173.

Wächtershäuser, G., 1988. Pyrite formation, the first energy source for life: a hypothesis. System. Appl. Microbiol. 10, 204-210.

Wächtershäuser, G., 2006. From volcanic origins of chemoautotrophic life to Bacteria, Archaea and Eukarya. Phil Trans Roy Soc Lond (Ser B) 361, 1787-1808.

Walczyk, T., 1997. Iron isotope ratio measurements by negative thermal ionisation mass spectrometry using FeF4-molecular ions. int. J. Mass Spectrom. Ion Proc. 161, 217-227.

Walczyk, T., von Blanckenburg, F., 2002. Natural Iron Isotope Variations in Human Blood. Science 295, 2065 - 2066.

Waldbauer, J.R., Sherman, L.S., Sumner, D.Y., Summons, R.E., 2009. Late Archean molecular fossils from the Transvaal Supergroup record the antiquity of microbial diversity and aerobiosis. Precambrian Research 169, 28-47.

Walder, A., Freedman, P., 1992. Isotope ratio measurements using a double focusing magnetic sector mass analyser with an inductively coupled plasma ion source. J. Anal. At. Spectrom 7, 571.

Walder, A., Platzner, A., Freedman, P., 1993. Isotope ratio measurements of lead, neodymium and neodymium–samarium, hafnium–lutetium mixtures with a double focusing multiple collector mass spectrometer. J. Anal. At. Spectrom 8.

Walter, M.R., Buick, R., Dunlop, J.S.R., 1980. Stromatolites 3,400-3,500 Myr old from the North Pole area, Western Australia. Nature 284, 443-445.

Walter, M., 1983. Archean stromatolites: evidence of Earth's earliest benthos, in: Earth's earliest biosphere. Princeton University Press, Princeton, pp. 187–213.

Wei, D., Osseo-Asare, K., 1996. Particulate pyrite formation by the Fe3+/HS- reaction in aqueous solutions: effects of solution composition. Colloids and surfaces A: Physicochemical and Engineering Aspects 118, 51-61.

Welch, S., Beard, B., Johnson, C., Baterman, P., 2003. Kinetic and equilibrium Fe isotope fractionation between aqueous Fe(II) and Fe(III). Geochim. Cosmochim. Acta 67, 4231-4250.

Wells, M., Price, N., Bruland, K., 1995. Iron chemistry in seawater and its relationship to phytoplankton: a workshop report. Mar. Chem. 48, 157-182.

Weyer, S., Anbar, A., Brey, G., Munker, C., Mezger, K., Woodland, A., 2005. Iron isotope fractionation during planetary differentiation. Earth and Planet. Science Letters 240, 251–264.

Weyer, S., Schwieters, J., 2003. High precision Fe isotope measurements with high mass resolution MC-ICP-MS. Int. J. Mass Spectrom. Ion Proc. 226, 355-368.

Weyer, S., 2008. Geochemistry: What Drives Iron Isotope Fractionation in Magma? Science 320, 1600-1601.

Whitehouse, M., Fedo, C., 2007. Microscale heterogeneity of Fe isotopes in >3.71 Ga banded iron formation from the Isua Greenstone Belt, southwest Greenland. Geology 35, 719-722.

Whittermore, D., Langmuir, D., 1972. Standard Electrode Potential of Fe3+ + e- = Fe2+ from 5-35oC. J. Chem. Eng. Data 17, 288.

Widdel, F., Schnell, S., Heising, S., Ehrenreich, A., Assmus, B., Schink, B., 1993. Ferrous iron oxidation by anoxygenic phototrophic bacteria. Nature 362, 834-836.

Wiederhold, J.G., Kraemer, S.M., Teutsch, N., Borer, P.M., Halliday, A.N., Kretzschmar, R., 2006. Iron Isotope Fractionation during Proton-Promoted, Ligand-Controlled, and Reductive Dissolution of Goethite. Environmental Science & Technology 40, 3787-3793.

Wiederhold, J.G., Teutsch, N., Kraemer, S.M., Halliday, A.N., Kretzschmar, R., 2007. Iron isotope fractionation in oxic soils by mineral weathering and podzolization. Geochimica et Cosmochimica Acta 71, 5821-5833.

Wiesli, R., Beard, B., C.M., J., 2004. Experimental determination of Fe isotope fractionation between aqueous Fe(II), siderite and "green rust" in abiotic

systems. Chem. Geol. 211, 343-362.

Wiesli, R.A., Beard, B.L., Taylor, L.A., Johnson, C.M., 2003. Space weathering processes on airless bodies: Fe isotope fractionation in the lunar regolith. Earth and Planetary Science Letters 216, 457-465.

Wilkin, R., Barnes, H., 1996. Pyrite formation by reactions of iron monosulfides with dissolved inorganic and organic sulfur species. Geochim. Cosmochim. Acta 60, 41267– 44179.

Wilkin, R., Barnes, H., 1997. Formation processes of framboidal pyrite. Geochimica et Cosmochimica Acta 61, 323-339.

Wille, M., Kramers, J., Naegler, T., Beukes, N., Schroeder, S., Meisel, T., Lacassie, J., Voegelin, A., 2007. Evidence for a gradual rise of oxygen between 2.6 and 2.5 Ga from Mo isotopes and Re-PGE signatures in shales. Geochimica et Cosmochimica Acta 71, 2417-2435.

Wincott, P., Vaughan, D., 2006. Spectroscopic Studies of Sulfides. Reviews in Mineralogy & Geochemistry 61, 181-229.

Woese, C.R., Kandler, O., Wheelis, M.L., 1990. Towards a natural system of organisms: proposal for the domains Archaea, Bacteria, and Eucarya. Proceedings of the National Academy of Sciences of the United States of America 87, 4576 -4579.

Woese, C., 1987. Bacterial evolution. Microbiological reviews 51, 221-271.

Wolthers, M., van der Gaast, S., Charlet, L., Rickard, D., 2005. A surface and structural model describing the environmental reactivity of disordered mackinawite. Am. Mineral. 88, 2007-2015.

Wolthers, M., van der Gaast, S., Rickard, D., 2003. The structure of distored mackinawite. Am. Mineral. 88, 2007.

Wu, J., Boyle, E., Sunda, W., Wen, L., 2001. Soluble and Colloidal Iron in the Oligotrophic North Atlantic and North Pacific. Science 293, 847 -849.

Yamaguchi, K., C.M., J., Beard, B., Ohmoto, H., 2004. Iron-sulfur-carbon contents and isotope systematics of 2.7 Ga shallow and deep facies black shales from the Hamersley Basin, Australia. Geochim Cosmochim Acta 68, A795.

Yamaguchi, K., Johnson, C., Beard, B., Ohmoto, H., 2005. Biogeochemical cycling of iron in the Archean-Paleoproterozoic Earth: Constraints from iron isotope variations in sedimentary rocks from the Kaapvaal and Pilbara Cratons. Chem. Geol. 218, 135-169.

Yamaguchi, S., Katsurai, T., 1960. Zur Bildung des Ferromagnetischen Fe3S4. Colloid & Polymer Science 170, 147-148.

Yang, W., Holland, H.D., 2003. The Hekpoort paleosol profile in Strata 1 at Gaborone, Botswana: Soil formation during the Great Oxidation Event. Am J Sci 303, 187-220.

van der Zee, C., Roberts, D., Rancourt, D., Slomp, C., 2003. Nanogoethite is the dominant reactive oxyhydroxide phase in lake and marine sediments. Geology 31, 993-996.

Zhang, H., Huang, F., Gilbert, B., Banfield, J., 2003. Molecular Dynamics Simulations, Thermodynamic Analysis, and Experimental Study of Phase Stability of Zinc Sulfide Nanoparticles. The Journal of Physical Chemistry B 107, 13051-13060.

Zhu, X., Guo, Y., O'Nions, K., 2001. Isotopic homogeneity of iron in the early solar nebula. Nature 412, 311-313.

Zhu, X., Guo, Y., Williams, R., O'Nions, R., Matthews, A., Belshaw, N., Canters, G., de Waal, E., Weser, U., Burgess, B., Salvato, B., 2002. Mass Fractionation processes of transition metal isotopes. Earth and Planet. Science Letters 200, 47-62.

Zhu, X., O'Nions, R., Guo, Y., Belshaw, N., Rickard, D., 2000. Determination of natural Cu-isotope variation by plasma-source mass spectrometry: implications for use as geochemical tracers. Chem. Geol. 163, 139-149.

Zhu, X., O'Nions, R., Guo, Y., Reynolds, B., 2000. Secular Variation of Iron Isotopes in North Atlantic Deep Water. Science 287, 2000-2002.

van Zuilen, M.A., Lepland, A., Arrhenius, G., 2002. Reassessing the evidence for the earliest traces of life. Nature 418, 627-630.

Chapter II

Experimental and analytical methods for assessing Fe isotope fractionations in the low temperature Fe-S system

2.1. Introduction

In the previous chapter it was emphasised that although the diagenetic Fe-S system has been quite deeply explored experimentally, the record of studies on the behaviour of Fe isotopes within this system is meagre, and most of the work focuses on the measurement of natural samples. Since Fe(II) is subject to oxidation, even at very small O_2 concentrations, it is crucial to keep mineral assemblages or solutions anoxic. Mackinawite and greigite are pyrophoric; $Fe(II)_{aq}$ and pyrite's surface are readily oxidised in oxic environments. In this chapter I describe the experimental protocols used to reproduce anoxic conditions, to handle these air sensitive materials and to prepare them for precise and accurate Fe isotope analysis.

In order to determine experimentally isotope fractionations between two mineral phases, it is important to keep the experimental system as simple as possible, which minimises the observed fractionation due to experimental artefacts. As previously discussed, the competing mechanisms forming Fe-S mineral phases are pH dependent, mainly because $S(-II)_{aq}$ speciation itself changes as a function of pH. Together with keeping the system anoxic, another experimental challenge is thus to set the pH in order to ensure that the observed isotope fractionation can be linked to the dominant mechanism. Fortunately, the use of concentrated material reduces the need for buffering reagents that might influence or control the isotope fractionation. In certain experimental procedures, the use of a pH buffer was required, but particular care was taken not to use Fe(II) chelating buffers.

2.2. Background on using equations for the Fe isotope system

General equations used for traditional stable isotope systems must be used with caution in the Fe isotope system. This is due to the fact that unlike ^{18}O with respect to ^{16}O, ^{57}Fe and ^{54}Fe are not trace isotopes with respect to ^{56}Fe. As a result, even for a mass balance equation, the error will be significantly increased using usual isotopic ratios instead of the (mass of isotope)/(mass of element) ratios (Criss, 1999; Eq. 1.14a-b-c). For most systems, this phenomenon is however hidden by the large experimental error, but when using highly enriched material (up to a few hundreds ‰), the true equations must be used.

For any system, the isotope ratio R of a mixture Mix is the sum of isotopes α of the element N brought by all the end-members j divided by the sum of isotopes β of the same element brought by the same end-members (Eq. 2.1):

$$R_{Mix} = \left(\frac{^{\alpha}N}{^{\beta}N} \right)_{Mix} = \frac{\sum_{j=1}^{n} {}^{\alpha}N_j}{\sum_{j=1}^{n} {}^{\beta}N_j} \qquad (2.1)$$

In the case of Fe isotope ratios in a system with two components *A* and *B*, the equation follows (Eq. 2.2):

$$\left(\frac{^{56}Fe}{^{54}Fe} \right)_{Mix} = \frac{^{56}Fe_A + {}^{56}Fe_B}{\sum_{j=1}^{n} {}^{54}Fe_j} \qquad (2.2)$$

where $^{56}Fe_A$ is the number of ^{56}Fe atoms brought by component *A* and $\sum_{j=1}^{n} {}^{54}Fe_j$ is the sum of the ^{54}Fe atoms brought by *A* and *B*. This equation is the true mixing equation for any binary system and can be written as Eq. 2.3:

$$\left(\frac{^{56}Fe}{^{54}Fe} \right)_{Mix} = \frac{^{54}Fe_A}{\sum_{j=1}^{n} {}^{54}Fe_j} \left(\frac{^{56}Fe}{^{54}Fe} \right)_A + \frac{^{54}Fe_B}{\sum_{j=1}^{n} {}^{54}Fe_j} \left(\frac{^{56}Fe}{^{54}Fe} \right)_B \qquad (2.3)$$

Note that $^{54}Fe_A = \left(\frac{^{54}Fe}{Fe} \right)_A \frac{m(Fe)_A}{M(Fe)_A}$, where $m(Fe)_A$ is the mass of Fe in A and $M(Fe)_A$ is the molar mass of Fe in A, which is not necessarily the same as $M(Fe)_B$ in the case of enriched materials.

Eq. 2.3 can be further simplified into Eq. 2.4:

$$\left(\frac{^{56}Fe}{^{54}Fe} \right)_{Mix} = \varphi_A^{54Fe} \left(\frac{^{56}Fe}{^{54}Fe} \right)_A + \varphi_B^{54Fe} \left(\frac{^{56}Fe}{^{54}Fe} \right)_B \qquad (2.4)$$

where φ^{54Fe} is $\frac{^{54}Fe_j}{\sum_{j=1}^{n} {}^{54}Fe_j}$ and $\varphi_A^{54Fe} + \varphi_B^{54Fe} = 1$.

The mixing equation Eq. 2.4 can be rewritten in Eq. 2.5:

$$\left(\frac{^{56}Fe}{^{54}Fe} \right)_{Mix} = \left(\frac{^{56}Fe}{^{54}Fe} \right)_A + \varphi_B^{54Fe} \left[\left(\frac{^{56}Fe}{^{54}Fe} \right)_B - \left(\frac{^{56}Fe}{^{54}Fe} \right)_A \right] \qquad (2.6)$$

Eq. 2.6 permits to introduce the masses and isotopic composition of A and B in the mixture as Eq. 2.7 or, as the practical equation for preparing enriched material Eq. 2.8:

$$\left(\frac{^{56}Fe}{^{54}Fe}\right)_{Mix} = \frac{\left(\frac{^{56}Fe}{^{54}Fe}\right)_B + \left(\frac{^{56}Fe}{^{54}Fe}\right)_A \frac{\left(\frac{^{54}Fe}{Fe}\right)_A \frac{m(Fe)_A}{M(Fe)_A}}{\left(\frac{^{54}Fe}{Fe}\right)_B \frac{m(Fe)_B}{M(Fe)_B}}}{1 + \frac{\left(\frac{^{54}Fe}{Fe}\right)_A \frac{m(Fe)_A}{M(Fe)_A}}{\left(\frac{^{54}Fe}{Fe}\right)_B \frac{m(Fe)_B}{M(Fe)_B}}} \qquad (2.7)$$

$$\frac{m(Fe)_A}{m(Fe)_B} = \left[\frac{\left(\frac{^{56}Fe}{^{54}Fe}\right)_B - \left(\frac{^{56}Fe}{^{54}Fe}\right)_A}{\left(\frac{^{56}Fe}{^{54}Fe}\right)_{Mix} - \left(\frac{^{56}Fe}{^{54}Fe}\right)_A} - 1\right] \frac{\left(\frac{^{54}Fe}{Fe}\right)_B}{\left(\frac{^{54}Fe}{Fe}\right)_A} \frac{M(Fe)_A}{M(Fe)_B} \qquad (2.8)$$

An alternative to Eq. 2.8 has been given by Criss (1999), where the mixing equation is described by Eq. 2.9:

$$\frac{M_A}{M_B} = -\frac{C_B}{C_A}\left[\frac{R^*_{Mix} - R^*_B}{R^*_{Mix} - R^*_A}\right] \qquad (2.9)$$

where M_A and M_B are the masses of the compounds A and B, C_A and C_B are the mass concentrations of the bulk element in the compounds A and B, and R^* is the ratio ($m^{56}Fe/m_{total\ Fe}$) in A, B and the mixture.

2.3. Experimental methods

2.3.1. Reactants and equipment

All reagents and acids were of analytical grade and solutions were prepared using 17-18 MΩ cm deionised water, sparged with O_2-free grade N_2 for 30 min (Butler *et al.*, 1994). Iron solutions were made by dissolution of Mohr's salt $Fe(NH_4)_2(SO_4).6H_2O$ (Sigma Aldrich™) in N_2 sparged water. Mohr's salt was used for its ability to resist oxidation. Sulphide solutions were made by dissolution of $Na_2S.9H_2O$ (Sigma Aldrich™) in N_2 sparged water. $H_2S_{(g)}$ was produced by dissolution of $Na_2S.9H_2O$ with 50% v/v N_2 sparged H_2SO_4.

Buffers were prepared by dissolution of their sodium salt and HCl or NaOH titration to the required pH. Phosphate (pKa_2 = 7.21) has been used as a buffer in previous experimental studies for pyrite formation (*e.g.* Rickard, 1997; Butler *et al.*, 2004) but because it is strongly metal complexing we used the non-complexing

MOPS (3-N-morpholinopropanesulfonic acid, p*K*a = 7.31, Fisher™) "good buffer" (Kandegedara and Rorabacher, 1999) when Fe isotope experiments were carried out at the near neutral region.

Hydroxylamine hydrochloride and potassium permanganate were used to reduce quantitatively $Fe(III)_{aq}$ or oxidise $Fe(II)_{aq}$. When strongly reducing conditions were required, Ti(III) citrate was used to poise solutions to low Eh. Ti(III) citrate was prepared by adding 5 mL 15% $TiCl_3$ to 50 mL 0.2 M Na citrate dihydrate and buffered with Na_2CO_3 to pH 7 (Zehnder and Wuhrmann, 1976; Rickard, 1997). Eh level was measured using a platinum electrode and a Ag/AgCl reference electrode by comparison with a standard Zobell's solution (made of 1.4080 g potassium ferrocyanide, 1.0975 g potassium ferricyanide 7.4557 g potassium chloride, up to 1 L). The precision on the measured potential was calculated from the difference between measured Eh and theoretical Eh and was ± 16.5 mV.

Experiments and syntheses performed at the University of Edinburgh were carried out under oxygen-free N_2 conditions in a N_2-filled re-circulating Saffron alpha® anoxic chamber or under flowing N_2. Trace amounts of oxygen in the anoxic chamber were trapped in re-circulating catalysts by oxidation of CuCl granules. Catalysts were regenerated every 4 months by cool (ambient temperature) purging (30 min, 100 % N_2, then 30 min, 20% H_2 + 80% N_2), followed by hot (125°C) purging (5 hours, 20% H_2 + 80% N_2). During the process, H_2 reduces Cu oxides to form H_2O. Oxygen levels in the anoxic chamber were maintained anaerobic and were monitored qualitatively with a microbiology anaero-test (Merck™). Experiments and syntheses performed at Cardiff University were carried out under oxygen-free N_2 conditions (<1 ppmv O_2) in an MBraun Labmaster 130® re-circulating anoxic chamber which are equipped with hot metallic Cu catalysts.

Solid products were freeze-dried pending storage or solid phase analysis. Freeze-drying was carried out using a N_2-purged Mini-Lyotrap (LTE®) freeze-dryer. Products were attached to the freeze-dryer for three days and stored in the anoxic chamber for later application.

Reactions involving pressure or vacuum control and reaction with $H_2S_{(g)}$ were carried out on a gas transfer manifold. Vacuum was provided by a BNF Laboport® pump. The manifold pipes were evacuated and purged with N_2 three times before attaching the reaction vessel. Once the reaction vessel attached, the whole system was evacuated, N_2 purged and maintained under vacuum. Pressure was adjusted with N_2.

Continuous flow reactions were performed in a N_2-circulating chemostat. Trace amounts of oxygen in the oxygen-free grade N_2 supply were removed through a Supelco® gas carrier purifier. Reactants (*i.e.* $Fe(II)_{aq}$ and $S(-II)_{aq}$) were continuously introduced into a sealed 2 L glass reaction vessel *via* Masterflex® peristaltic pump. The pH was measured, monitored and controlled with a Eutech Instruments pH 190® pH/ORP controller adjusting the reaction pH with deoxygenated 0.005 M HCl and NaOH. The volume was maintained at a constant level with a float control and excess solution was pumped out to a Pb(II) acetate containing waste. Pb(II) acetate ensured quantitative H_2S precipitation as PbS.

2.3.2. Experimental procedures

2.3.2.1. Precipitation of FeS_m

FeS_m was synthesised by mixing equimolar $Fe(II)_{aq}$ and $S(-II)_{aq}$ solutions in the anoxic chamber. For experiments involving *in situ* precipitation of FeS_m, 10 mL 0.05 M S(-II) solution were injected into 100 mL 0.05 M Fe(II) solution in order to precipitate 10 % of Fe as mackinawite (Butler *et al.*, 2005). 90% of Fe remains dissolved in solution as calculated from the solubility data for mackinawite (Rickard, 2006) in PHREEQC Interactive 2.15.0®. FeS_m precipitate was filtered and rinsed on a Millipore™ filter (0.45 µm Whatman™ paper). With this filter size, filtrates are clear and the filter does not clog, although FeS_m is nanoparticulate. This is because FeS_m nanoparticles quickly aggregate in aqueous solutions and the aggregates are therefore prevented to pass through the 0.45 µm filter (*e.g.* Wolthers *et al.*, 2003; Guilbaud, Butler, *et al.*, 2010).

For experiments involving FeS_m as a reactant (*e.g.* for pyrite formation), larger amounts of FeS_m were precipitated by mixing 100 mL 0.6 M S(-II) and Fe(II) solutions in the anoxic chamber (Rickard, 1997). The precipitate was first filtered on a Buchner filter (Fisherbrand™ paper) and the filtrate was filtered on a Millipore™ filter (0.45 µm Whatman™ membrane). Precipitated FeS_m was collected from the filters, re-suspended in water and re-filtered three times for the recovery of clean FeS_m after filtration (Rickard *et al.*, 2006). Clean FeS_m was collected into a round-bottom flask, freeze-dried for three days and stored in the anoxic chamber for pending application.

2.3.2.2. Preparation of ^{56}Fe enriched FeS_m

$^{56}FeS_m$ was prepared at Cardiff University by mixing a source of ^{56}Fe enriched iron with $Fe(NH_4)_2(SO_4)_2.6H_2O$. The ^{56}Fe metal, for which the enrichment is given by $m(^{56}Fe)/m(Fe) = 0.997$, was supplied by CortecNet™. Relative amounts of both Fe sources were calculated using Eq. 2.8.

An accurately weighed aliquot of ^{56}Fe metal was dissolved in 40 mL hot 3 M HCl, evaporated to incipient dryness to remove the excess acid and the solution was made up to 100 mL. The pH of the solution was determined by an Orion Research EA920® pH meter and was 3 ± 0.1. After N_2 sparging, the solution was introduced into an MBraun Labmaster 130® re-circulating anoxic chamber. In the glove-box, ^{56}Fe solution was mixed with 20 mL 1.4 M hydroxylamine hydrochloride to reduce quantitatively Fe^{3+} to Fe^{2+}. Quantitative reduction to Fe^{2+} is crucial to prevent formation of S(0) with addition of dissolved HS^-. The $^{56}Fe(II)$ solution was mixed with 250 mL 0.16 M Fe(II) solution made from the dissolution of $Fe(NH_4)_2(SO_4)_2.6H_2O$ (Sigma Aldrich®) in N_2 sparged water. Reduction efficiency was checked by quantifying the residual $[Fe^{3+}]$ in the solution using the thiocyanate method described in section 2.2.3.2. An aliquot of the solution was acidified with 2 mL 2M HCl, reacted with 5 mL 4M thiocyanate and made up to 50 mL. The aliquot was analysed with a Perkin Elmer Lambda2® dual beam UV-Vis. Typical response was less than 0.2 ppm for $[Fe^{3+}]$ which represents ~ 0.005‰ of total [Fe].

$^{56}FeS_m$ was precipitated by mixing the bulk Fe solution with equimolar $Na_2S.9H_2O$ following the procedure described above and stored in the glove-box. The $^{56}FeS_m$ reservoirs produced in this way had isotopic compositions of ~308 ‰ and ~ 2.6 ‰. Assuming that the instrumental error on the isotope ratios for both the spike and the natural material used for precipitation of $^{56}FeS_m$ was $2se_{56/54} = 0.0015$ %, Eq. 2.6 indicates that the instrumental error increases when the proportion of the spike increases (Fig. 2.1).

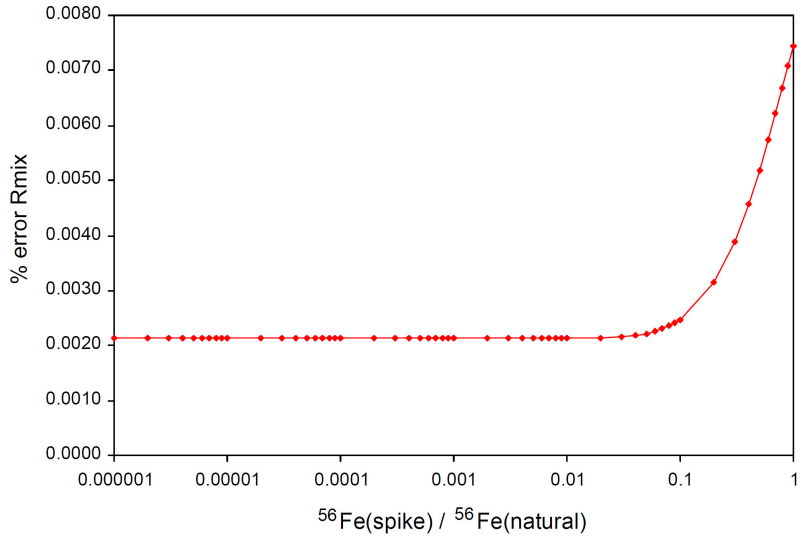

Figure 2.1: Increase of the theoretical error (2se) on the ratio $^{56/54}$Fe of the mixture when the spike contribution increases. It was assumed that the error of the ratios of the spike component and the natural component is 0.0015 ‰. The theoretical error was propagated from Eq. 2.6.

2.3.2.3. Pyrite formation using FeS_m and H_2S reactants

The following protocol was conducted to produce pyrite *via* the H_2S pathway (Eq. 1.8, chapter I). In order to do so, $S(-II)_{aq}$ speciation must be dominated by H_2S, and the pH must be maintained above 5 to avoid marcasite formation. In the glove box, 0.005 mol of freeze-dried FeS_m was introduced into a reaction-vessel and 10 mL of a 0.05 M MOPS or phosphate buffer (pH 6) were added. The reaction-vessel was either a heat sealed glass ampoule (Rickard, 1997; Butler and Rickard, 2000; Butler *et al.*, 2004 in the case of the "Py" experiments) or a rubber sealed serum bottle (Drobner *et al.*, 1990; Butler and Rickard, 2000 in the case of the "SB" experiments). Sealed reaction-vessels were closed and attached to a gas-transfer manifold (Rickard, 1997). The manifold was flushed with O_2-free grade N_2 and pumped down to ~ -14 PSI (~ -97 kPa, full vacuum) three times. A serum bottle containing a weighed amount of $Na_2S.9H_2O$ was attached to the manifold with a hypodermic needle and 50% v/v N_2 sparged H_2SO_4 was injected into the serum bottle *via* a syringe to generate H_2S (Fig. 2.2). After H_2S transfer into the reaction-vessel, the pressure was adjusted to slight under-pressure (~ -2.5 PSI or – 17 kPa) to ensure the sealing of the vessel. Excess H_2S was pumped out to waste. The sealed reaction-vessel was kept at constant temperature in a 100°C furnace or in a 40°C water bath. Vessels were allowed different durations of reaction, and stopped for pending mineral extraction.

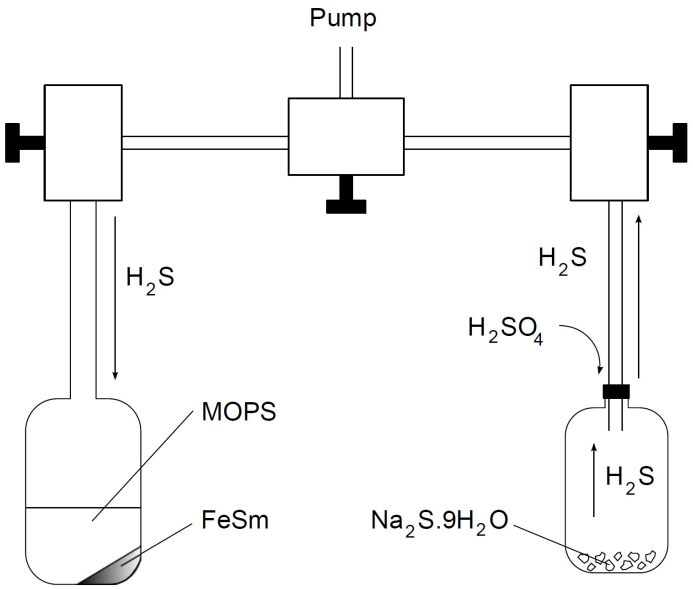

Figure 2.2: Scheme of the gas transfer manifold. H_2SO_4 is injected into the serum bottle containing the S(-II) salt, producing H_2S. H_2S is transferred into the reaction vessel and dissolves into the buffered solution.

At pH 6 and for the Σ[S(-II)] used, the equilibrium solubility of FeS_m is dominated by FeS^0_{aq}, at concentrations about two orders of magnitude higher than Fe^{2+}_{aq} (Rickard, 2006). Subsequent pyrite forming reaction is thus described by Eq. 1.8 (Chapter I).

2.3.2.4. Pyrite crystal growth from continuous flow chemostatic reaction

The following protocol was conducted to form pyrite *via* the same mechanism as described in section 2.2.2.3 (H_2S pathway, Eq. 1.8 in chapter I) with the difference that the FeS_m reactant is continually introduced into the system. Two pyrite seeds were encapsulated in an epoxy resin, allowing one pyrite surface to be in contact with the media. The pyrite surface was cleaned with 0.01 M HCl, rinsed with deionised water and freeze-dried to prevent from oxidation. Pyrite seeds were introduced into the N_2 sparging 0.2 M NaCl media and the chemostat reaction vessel was sealed (Fig. 2.3). All reagent solutions (*i.e.* 2 L 0.5 x 10^{-3} M $Fe(II)_{aq}$ and 2 L 10^{-3} M $S(-II)_{aq}$), and the pH adjusting solutions (*i.e.* 0.005 M HCl and 0.005 M NaOH) were prepared in 0.2 M NaCl. The liquid capacity of the chemostatic reaction vessel was set from the float high at 1.4 L.

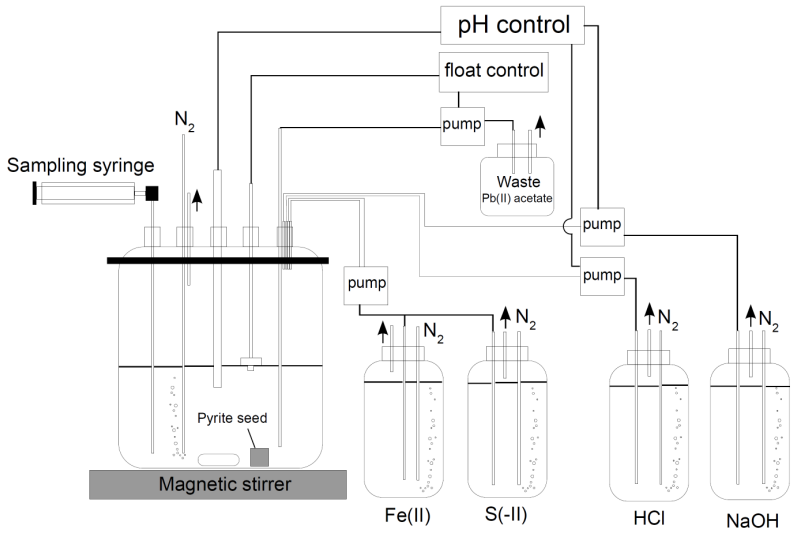

Figure 2.3: Scheme of the continuous flow chemostat. All reagents and the reaction vessel are sparged with oxygen free N_2. The rate of Fe(II) and S(-II) flows is 0.4 mL min^{-1}. The reaction pH is kept constant by controlled adjustment with H^+ or OH^-.

The pH of the $Fe(II)_{aq}$ solution was ~ 4, and at this pH the dominant Fe bearing species is the hexaqua $Fe[H_2O]_6^{2+}$ (normally referred as Fe^{2+}). Up to ~ 12% of the total dissolved Fe(II) was constituted by the weak outer-sphere SO_4^{2-} ligand complex, $Fe[H_2O]_6SO_4^0{}_{aq}$ (calculated in Visual MINTEQ 3.0®). In the alkaline sulphide solution, S(-II) speciation is dominated by HS^- (Fig. 1.5 in chapter I). Reagent solutions were pumped into the reaction vessel at a rate of 0.4 mL min^{-1}. The pH of the reaction was set at pH 7.00 ± 0.05. Fig. 2.4 shows that the reaction pH was constant through time.

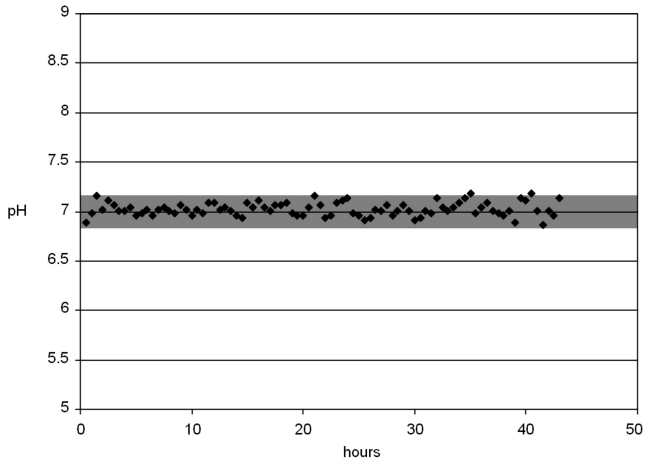

Figure 2.4: Monitoring of the pH in the reaction vessel for a 42 hours period. The pH controller was set at pH 7.00 ± 0.05. The HCl solution (0.01 M) was pumped into the reaction vessel when the pH > 7.05. Similarly, the NaOH solution (0.01 M) was pumped into the reaction vessel when the pH < 6.95.

At pH 7, the first Fe-S phase to form is FeS^0_{aq} at very low Fe^{2+} and HS^- concentrations. As $pK_1(H_2S)$ is 6.98 (Suleimenov and Seward, 1997), $\log K_{2,sp}(FeS_m)$ for reaction 10 is ~ -3.5. Under neutral to alkaline conditions, the equilibrium solubility of FeS_m is dominated by FeS^0_{aq}, with $\log K_0(FeS_m)$ = -5.7 (Rickard, 2006). This means that at pH 7, when mixing Fe^{2+}_{aq} and HS^- at low concentrations, FeS^0_{aq} forms when $\log\{Fe^{2+}\} + \log\{HS^-\} + pH \geq 2.2$. When $\log\{FeS^0_{aq}\} \geq -5.7$, mackinawite starts precipitating from solution. At pH 7 and for $\Sigma[S(-II)] = 10^{-3}$ M, equilibrium solubility of FeS_m is dominated by FeS^0_{aq} (Rickard, 2006). Experimental duration was seven days. The solution was sampled with a 50 mL syringe, filtered under flushing O_2-free grade N_2, freeze-dried and stored in the glove-box for pending analysis. Pyrite seeds were rinsed with deionised water, freeze-dried and stored in the glove-box for pending analysis.

2.3.2.5. Fe-S species separation by stepwise dissolution

Two techniques were experimented for the separation of the solid and liquid products: i) vacuum filtration under flushing N_2, which separates the solids (pyrite + FeS_m aggregates) from species in the filtrate (Fe^{2+} + FeS^0_{aq}); and ii) freeze-drying, which removes H_2O from the system.

2.3.2.5.1. Filtration-based separation of solid and liquid products

Solid phases were separated from aqueous phases by filtration on a 0.45 µm membrane Millipore™ filter and washed under flushing N_2. For the experiments performed with a phosphate buffer, the filtration process was fast and the filtrate was clear. However phosphate being metal complexing, the use of MOPS was preferred for Fe isotope studies. Interestingly, the filtration of experiments performed with MOPS lasted several hours and filtrate solutions were black-coloured, indicating that the 0.45 µm filter did not sufficiently prevent FeS_m nanoparticles to pass through. The use of 0.2 µm and 0.02 µm membranes did not improve the filtration process. As explained above, because FeS_m nanoparticles tend to aggregate quickly in aqueous solution, the use of 0.45 µm filters is usually sufficient to filter FeS_m after precipitation. We suspect that the use of the phosphate buffer further accentuates the formation of FeS_m aggregates. By contrast, it is possible that the non-complexing MOPS buffer prevents FeS_m aggregation, causing substantial amounts of FeS_m to pass

through the filter before the filter clogs off. The pH of the filtrates varied from 5.5 to 6.5. Nanoparticulate FeS_m present in the filtrate was dissolved with concentrated HCl on a hot plate, and evaporated to dryness for later removal of the organic buffer. Filtered solid products were freeze-dried for further XRD and SEM analysis and acid sequential separation of pyrite and FeS_m. Isotope analysis of the experiments processed through this procedure revealed that isotopic mass-balance was not reached. We suppose that the separation process itself, subjected to long durations and potential oxidation, is the source of non-matching isotopic mass-balance. We therefore developed another separation protocol to avoid potential oxidation.

2.3.2.5.2. Freeze-drying-based separation of solid and liquid products

The long duration of the filtration and the production of black filtrates when MOPS was used was not ideal because i) it was more difficult to collect Fe quantitatively from the filtrate and ii) the iron sulphides were exposed to larger risk of oxidation. The alternative to filtration was H_2O removal by freeze-drying.

The reaction vessel was first frozen to stop the reaction. Once frozen, the reaction vessel was opened under a fume cupboard and excess H_2S was flushed to waste using N_2. The reaction vessel was then attached to the freeze-dryer manifold. A portion of the solids (*i.e.* pyrite + FeS_m + various salts brought from MOPS) was kept for further XRD and SEM analysis and another portion was taken for acid sequential separation of pyrite and mackinawite.

2.3.2.5.3. Sequential separation of pyrite and mackinawite

Separation between pyrite, mackinawite and MOPS salts was completed using modified preferential dissolution from existing protocols (*e.g.* Huerta-Diaz and Morse, 1990; Severmann *et al.*, 2006). In the glove-box, 0.1 g of the solids was introduced into a serum bottle along with 2 mL H_2O and a few drops of Ti(III) citrate, and the serum bottle was rubber sealed. Ti(III) citrate ensures the complete dissolution of MOPS salts and FeS_m in HCl, avoiding the formation of insoluble S(0) by poising Eh to low negative values (Rickard *et al.*, 2006). Rickard *et al.* (2006) performed FeS_m digestion in hot 1.2 M or 6 M HCl and 5 mL Ti(III) citrate. Our aim was to maximise quantitative FeS_m dissolution with minimum Fe input from Ti(III) citrate and from FeS_2 partial dissolution. Best results were obtained by adding a few drops of Ti(III) citrate to FeS_m in 1.2 M HCl. This volume decreases the input of Fe

from Ti(III) citrate to < 0.7 % of Fe brought by FeS_m when FeS_m constitutes 5 % of total Fe. In other words, even for the lowest FeS_m concentrations, $Fe_{Ti(III)citrate}$ is still negligible compared to Fe_{FeSm}, and will have no impact on the measured isotopic compositions. Under a fume cupboard, 20 mL 1.2 M purged HCl were injected into the serum bottle *via* a hypodermic syringe in order to dissolve FeS_m and the MOPS-salts only. Remaining solids, essentially pyrite, were separated from solution on a 0.45 µm membrane Millipore™ filter and dissolved with a few drops of concentrated HNO_3. The risk of Fe_{pyrite} contamination during FeS_m dissolution with HCl was examined. This risk is enhanced when the ratio FeS_m/FeS_2 decreases. We used cold 1.2 M HCl rather than 6 M HCl in order to reduce FeS_2 dissolution and measured a maximum of 0.2 % dissolution from the initial FeS_2 phase in the blank. This means that when the FeS_m/FeS_2 ratio is the lowest, potential pollution of Fe_{pyrite} into Fe_{FeSm} represents at maximum 0.027 % of Fe_{FeSm}. Fig. 2.5 shows the theoretical Fe isotope composition of pyrite necessary to decrease by 0.1 ‰ the composition of observed FeS_m. The figure suggests that contamination bias may become a problem when > 95 % pyritisation has occurred (*i.e.* when < 5 % FeS_m remains in the system, shaded area). As none of our data correspond to this high %Py region, we conclude that our results are free from any significant cross-contamination.

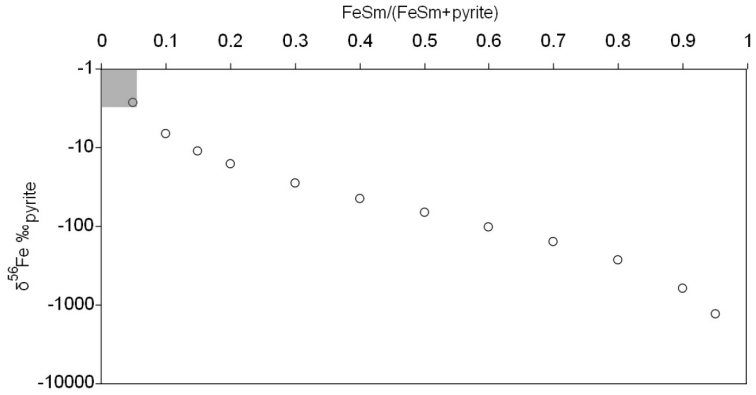

Figure 2.5: Theoretical $\delta^{56}Fe_{pyrite}$ values necessary to shift by – 0.1 ‰ the composition of the Fe(II) reservoir during the dissolution of 0.2 % pyrite. The shaded area represents the region where $\delta^{56}Fe_{pyrite}$ contamination is no longer negligible in respect with the observed $\delta^{56}Fe_{Fe(II)RES.}$

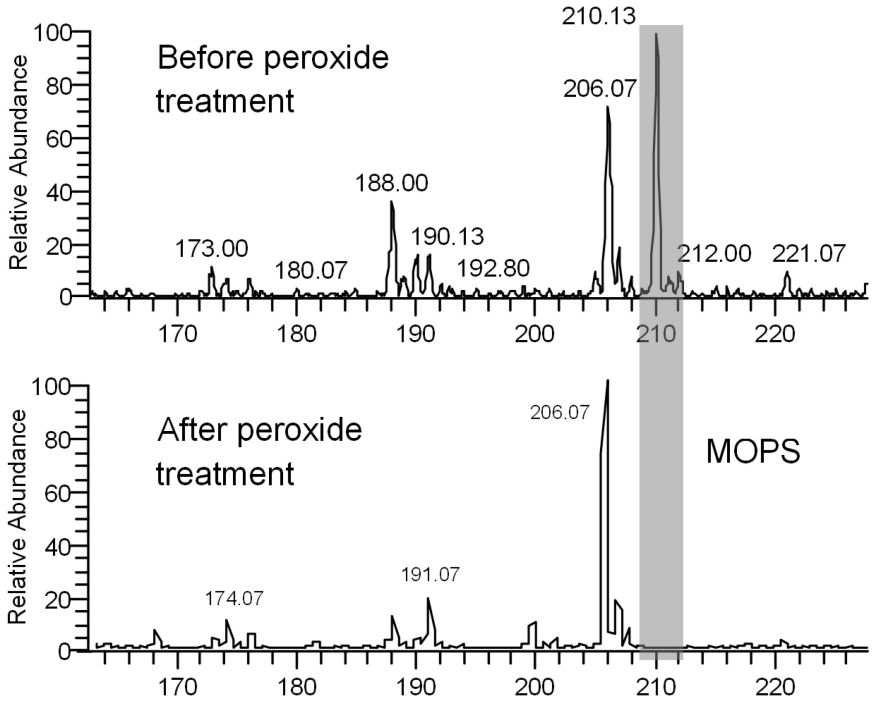

Figure 2.6: Comparison of an ESI-MS m/z scan for a MOPS solution before and after H_2O_2 treatment. The MOPS peak has disappeared after H_2O_2 removal of organic C. Other peaks are from the blank solution.

Both Fe_{pyrite} and Fe_{FeS} solutions were taken to dryness. Quantitative removal of organic carbon left by MOPS is essential to prevent the introduction of carbon into the mass spectrometer. The process was performed by C oxidation, and tested with both *aqua regia* and hydrogen peroxide (VWR™) as C oxidising reactants. 5 to 10 mL of the reactant were added to the solid residue and warmed up to 85°C and dried. The procedure was repeated several times. The final residue was dissolved in concentrated HCl and taken up to volume. 5 µL of the solutions were diluted four times in methanol for Electron Spray Ionisation Mass Spectrometry (ESI-MS). Results show that MOPS is still present in the solution oxidised with *aqua regia* whereas MOPS is not detectable in the solution oxidised with hydrogen peroxide (Fig. 2.6). NMR analysis showed the persistence of organic molecules in both solutions, but peaks were broad and difficult to analyse, perhaps indicating sulphur and nitrogen containing molecules. Total Organic Carbon (TOC) analyses showed that 99 % of carbon had been removed from the solution oxidised with hydrogen peroxide. Thus, we used the procedure involving hydrogen peroxide to eliminate most of the organic

carbon introduced with MOPS. Final solutions were $Fe(III)_{FeS}$ and $Fe(III)_{pyrite}$ in 5 % HNO_3.

Fig. 2.7 summarises the experimental protocols for the separation and extraction of FeS_m-Fe and FeS_2-Fe.

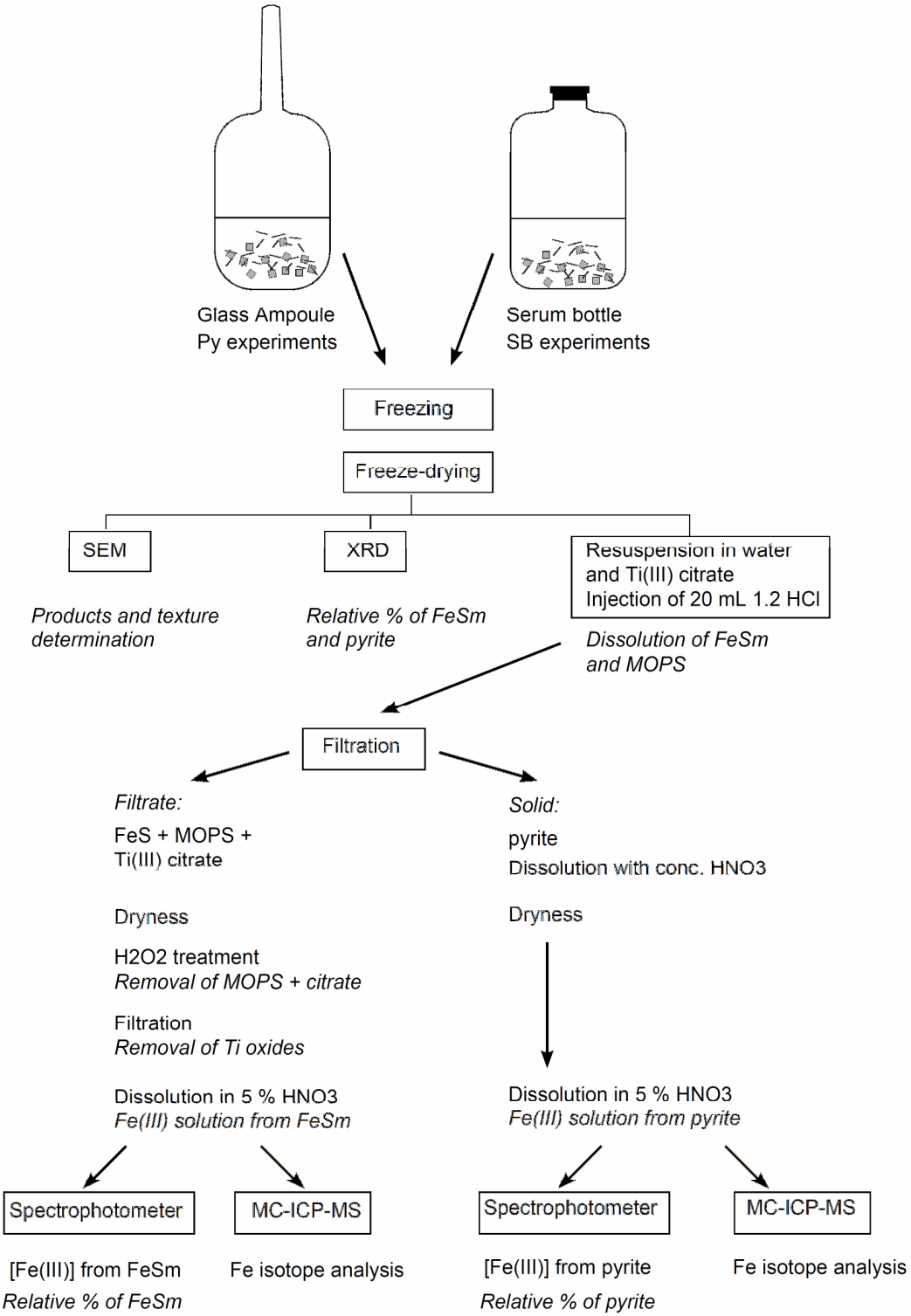

Figure 2.7: Procedure for chemical separation of pyrite from its Fe(II) reservoir (initially FeS_m).

2.4. Analytical methods

2.4.1. Analysis of solid products

2.4.1.1. X-ray diffraction analysis (XRD)

XRD analysis was performed to characterise solid materials synthesised as reactants or during a reaction. Essentially, it was used to i) detect the presence of any Fe(III) phase such as goethite or elemental sulphur that would indicate a certain extent of oxidation in our experiments; ii) track changes in crystallinity and the average size of mackinawite nanoparticles; and iii) determine the extent of pyrite (%Py) formed during a reaction, *i.e.* the degree of pyritisation.

The major challenge with XRD analysis was to keep the samples under N_2 in order to minimise or eliminate possible oxidation of the oxygen-sensitive Fe-S minerals. Powder samples were loaded onto a cavity in a metal (Al) holder and encapsulated in N_2 atmosphere to remain anoxic. Three designs of covers for anoxic XRD analysis were built and tested (Fig. 2.8).

The first design uses a flat acetate sheet as an oxygen-protective membrane. Acetate has been used successfully in other laboratories and seems to have a low diffusion rate. However, our design did not minimise the acetate thickness to be passed by the X-rays and did not favour transmission of low angle rays (Fig. 2.8.A). The second design uses an arch-shaped acetate membrane in order to get better signal at low angle. This design permitted us to obtain an adequate spectrum but did not correct for particle orientation since no rotation could be apply during the analysis (Fig. 2.8.B). The third design uses a dome-shaped polystyrene sheet. Polystyrene increased the signal intensity in respect with acetate, and the dome shape allowed us to perform rotating analysis (Fig. 2.8.C).

The presence of oxidising phases was checked analysing mackinawite powder over a 48 h period. Freeze-dried mackinawite was prepared as described above. About 0.1 g of the sample was loaded onto the metal support in the glove-box. The environmental holder containing the sample was loaded on a Bruker D8 Advance Diffractometer. XRD analysis was performed using Cu*K*α primary radiation generated at an accelerating voltage of 40KV in the range of 2-65° 2θ with a 1s/0.02° 2θ counting time. The diffracted X-rays were recorded by a Sol-x™ energy dispersive detector. Data were filtered to remove Cu*K*αII peaks. Results did not show any evidence of oxidation (*e.g.* S(0), goethite, greigite), indicating that we could analyse material immediately after experiments with confidence.

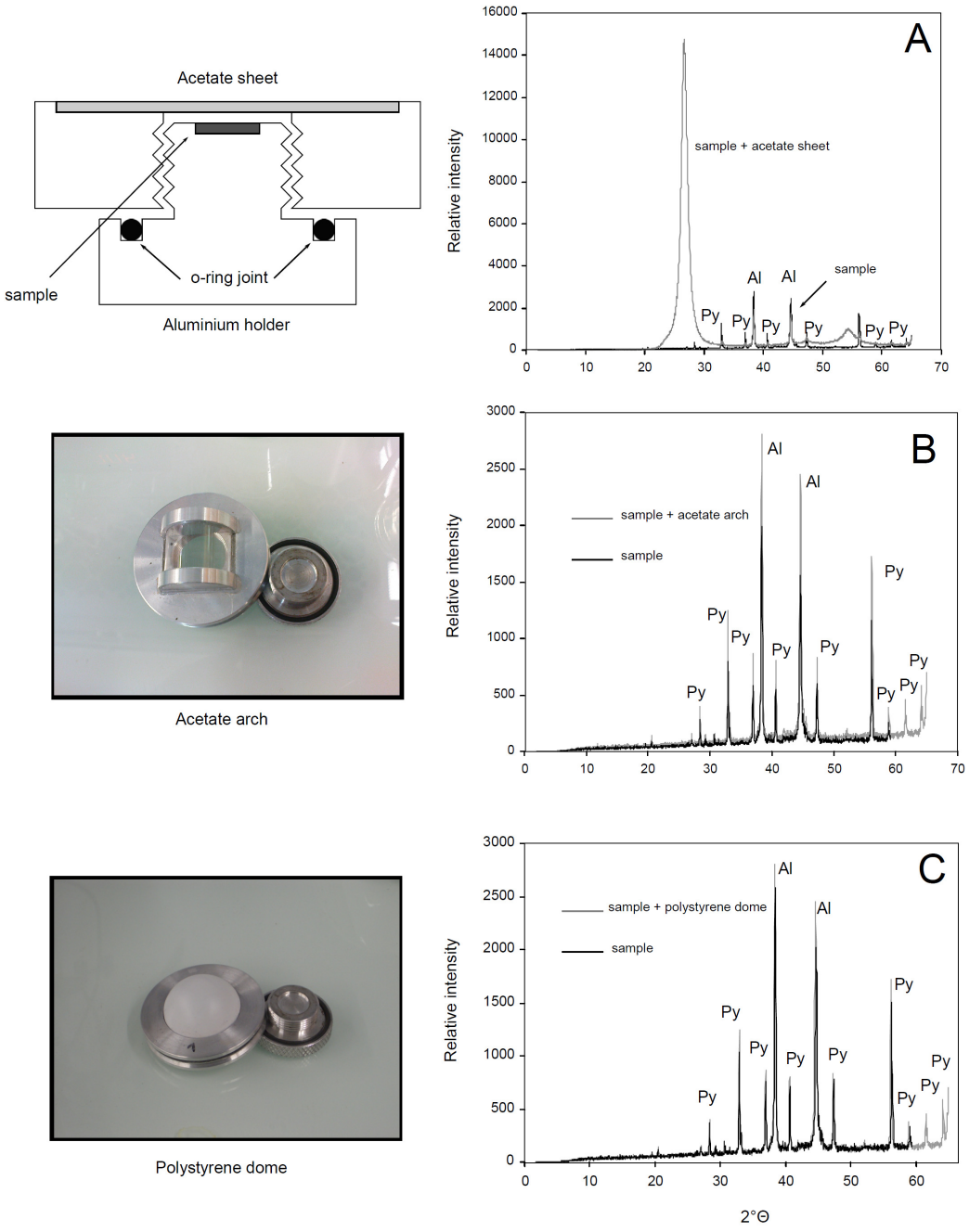

Figure 2.8: Three designs for the environmental sample holder. B and C show very similar results with little attenuation, contrary to A. The rotating design C was adopted routinely to eliminate the uncertainty due to sample surface's irregularity.

We used the Scherrer equation (Eq. 2.9) on the 16° 2θ peak to determine the average diameter of the crystalline size:

$$L = K\lambda(\beta\cos\theta)^{-1} \qquad (2.9)$$

where L is the size of the domain, K is 0.91 (Brindley, 1980), λ is the wavelength of the X-ray (0.154 nm for Cu$K\alpha$), β is the full with of the peak at half maximum

(FWHM, in radian) and θ is the angle of the peak. The Scherrer equation has been previously used to determine average domain size on FeS_m (Wolthers *et al.*, 2003; Jeong *et al.*, 2008) and on ZnS nanoparticles (Huang *et al.*, 2003). In these previous studies, crystal sizes given by the Scherrer equation were checked and confirmed by high-resolution transmission electron microscopy (for review and discussion, see Rickard and Luther, 2007, p 534). Precision on *L* was determined by measuring ten times the same sample, and was ± 0.7 nm (2σ). Fig. 2.9 shows the increase in mackinawite peak height with when ageing in aqueous solution, enabling the calculation of particle growth with the Scherrer equation.

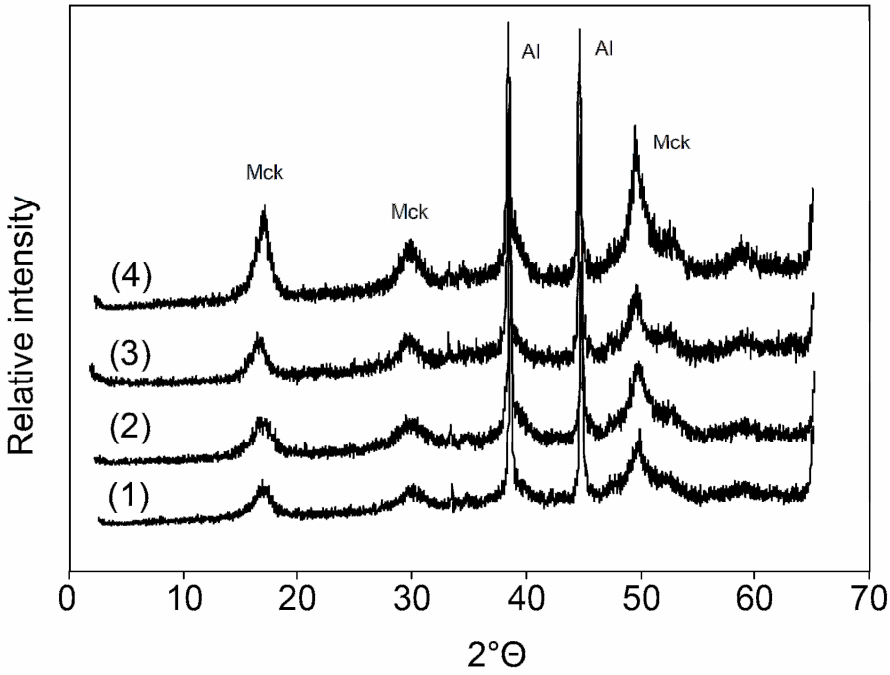

Figure 2.9: XRD scans of mackinawite after ageing times in aqueous solution of 30 min (1), 300 min (2), 3000 min (3) and 30000 min (4). During particle growth, mackinawite peaks get higher and higher and less and less broad.

We tested the potential determination of the pyrite percentage (%Py) from the high peak area (around 16° 2θ for mackinawite, and around 32° 2θ for pyrite) with standard mackinawite-pyrite mixtures. Freeze-dried mackinawite was prepared as described above. Natural pyrite was ground with a McCrone® mill for 12 min down to a mean diameter of 4 µm (analysed on a Beckman Coulter LS® particle size analyser), which is similar to the size of synthetic pyrite cubes documented by previous studies (*e.g.* Rickard, 1997; Butler and Rickard, 2000). Typical mixtures were 0, 20, 30, 50,

60, 70, 80, 85 and 100 wt%Py. About 0.1 g of the sample was loaded onto a metal support sample holder. The environmental holder containing the sample was loaded on a Bruker D8 Advance® Diffractometer. XRD analysis was performed using Cu*K*α primary radiation generated at an accelerating voltage of 40KV in the range of 2-65° 2θ with a 1s/0.02° 2θ counting time. The diffracted X-rays were recorded by a Sol-x™ energy dispersive detector. Data were filtered to remove Cu*K*αII peaks. Peak areas for mackinawite and pyrite correspond linearly to the weighted %Py from the standard mixtures (Fig. 2.10). Precision on %Py calculated from the peak areas is given by the calibration mixture replicates and is ± 7 % (2σ level). Measuring the peak areas for mackinawite and pyrite in our samples thus allowed us to determine a degree of pyritisation. The amorphous carbon-salts introduced by MOPS did not show any peak on the XRD spectra and did not perturb the standard response.

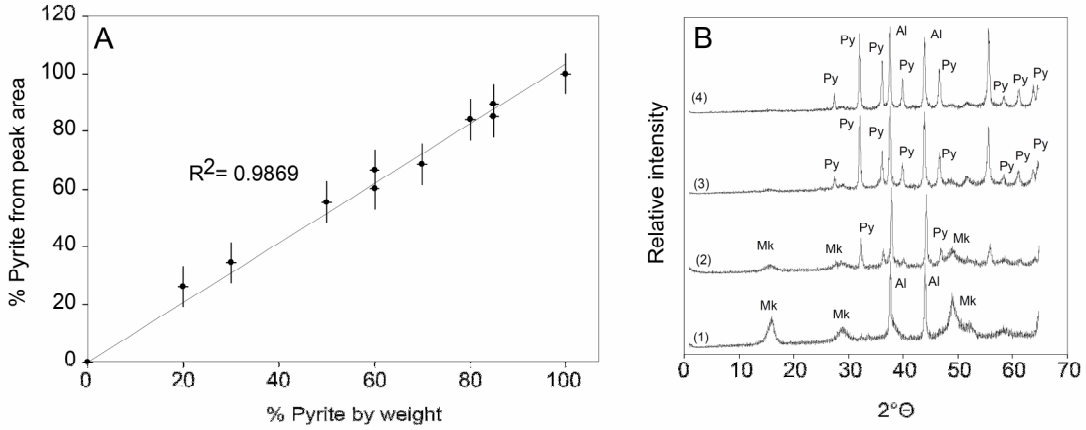

Figure 2.10: A: Calibration curve for %Py determination from XRD peaks. B: XRD scans for various pyrite formation reaction: initial mackinawite (1); 5 hours reaction (2); 2 days reaction (3) and 7 days reaction (4).

2.4.1.2. Scanning electron microscopy (SEM)

Sample imaging, mineral products determination and texture description were performed *via* backscatter detector on a Philips XL30CP® Scanning Electron Microscope (SEM) at 20 kV. Qualitative chemical analysis on the material surface was carried out with PGT® Spirit X-ray analysis as a mineral check.

Fig. 2.11 shows typical SEM images of pyrite micro-cubes forming in a FeS_m matrix after 7 days reaction.

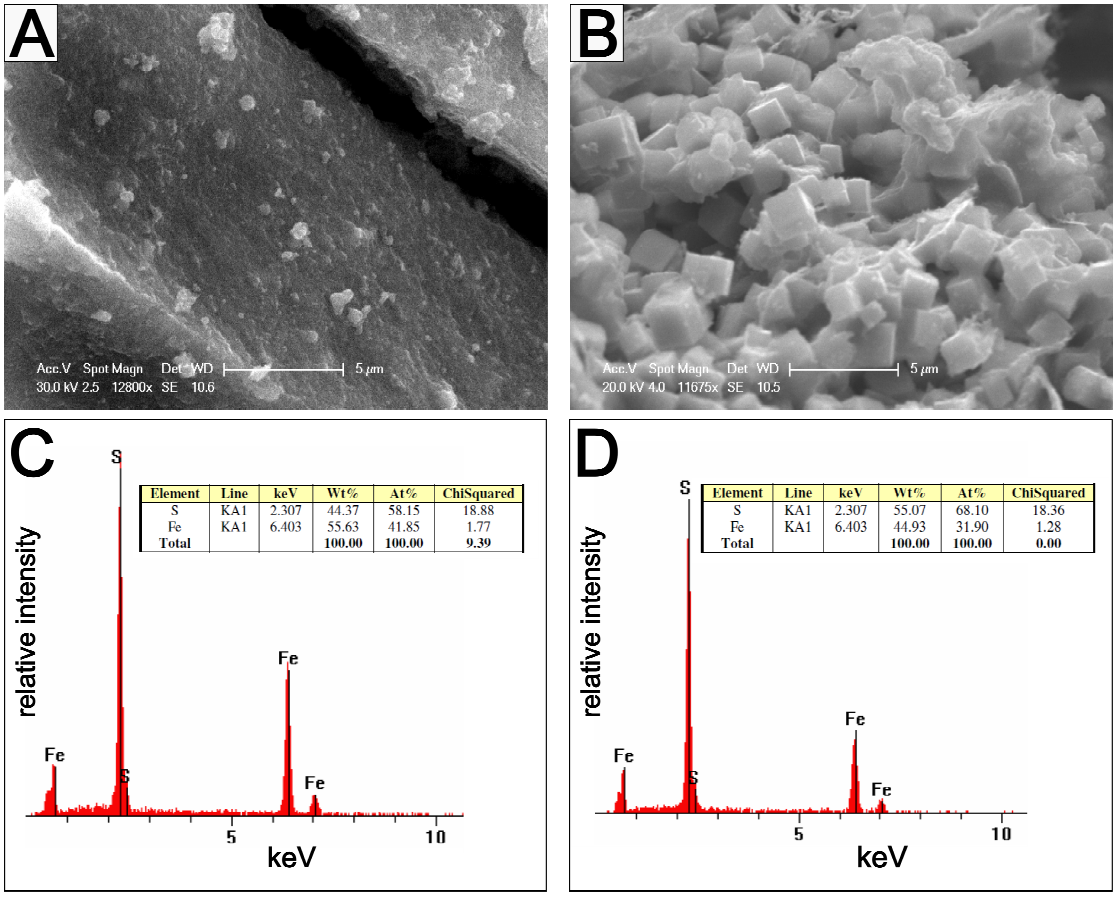

Figure 2.11: SEM imaging of the sample after 1 day reaction (A) and 1 week reaction (B). A shows typical partially reacted agglomerated FeS_m. B shows neoformed pyrite microcubes in a FeS_m matrix. Qualitative chemical spot analysis at the surface of mackinawite (C) and pyrite (D).

2.4.2. Analysis of liquid samples

2.4.2.1. Spectrophotometric determinations of [Fe(III)] and [Fe(II)]

Total Fe concentrations were determined using a M501 single beam UV-vis spectrophotometer (Spectronic Analytical Instruments®). The thiocyanate method (Vogel, 1951) was used for the determination of Fe(III) and the phenanthroline method for the determination of Fe(II) (Vogel, 1951). Both methods permit determination of Fe concentration by comparison with a calibration curve.

The thiocyanate method was used when solutions were acidified with HNO_3 conditions. Potassium thiocyanate (colourless) reacts with Fe^{3+} (colourless at low concentrations) to form a deep red $[Fe(CNS)]^{2+}$ complex. Fe solutions were acidified with 2 mL 1:5 HNO_3, quantitatively oxidised with a few drops of 0.2 M potassium permanganate, reacted with 5 mL 4 M potassium thiocyanate and made up to 50 mL. [Fe(III)] analysis was performed at 480 µm. The Beer-Lambert's law is followed for a 0 to 5 ppm [Fe] range with a precision $2\sigma \pm 0.1$ ppm. The presence of large amounts

of HCl makes the method inappropriate since HCl gets oxidised by potassium permanganate.

The phenanthroline method was used when HCl was present in too large quantities or when reducing agents such as Ti(III) citrate prevented oxidation by potassium permanganate. The method involves the pH dependent reduction of Fe(III) into Fe(II) by hydroxylamine hydrochloride and thus requires the use of buffer. Phenanthroline (colourless) reacts with Fe^{2+} (colourless) to form an orange $[Fe(Phen)_3]^{2+}$ complex. Fe solutions were buffered at pH 4.5 with 4 mL 2 M acetate and quantitatively reduced with 1 mL 1.4 M hydroxylamine-hydrochloride. 4 mL of 0.25% 1,10-phenanthroline were added and the solutions were made up to 50 mL. [Fe(II)] analysis was performed after 10 min ageing at 510 μm. The Beer-Lambert's law is followed for a 0 to 8 ppm [Fe] range with a precision $2\sigma = \pm 0.06$ ppm. Fig. 2.12 shows the calibration curves for both the thiocyanate and the phenanthroline methods, and an example of the colourations using the thiocyanate method.

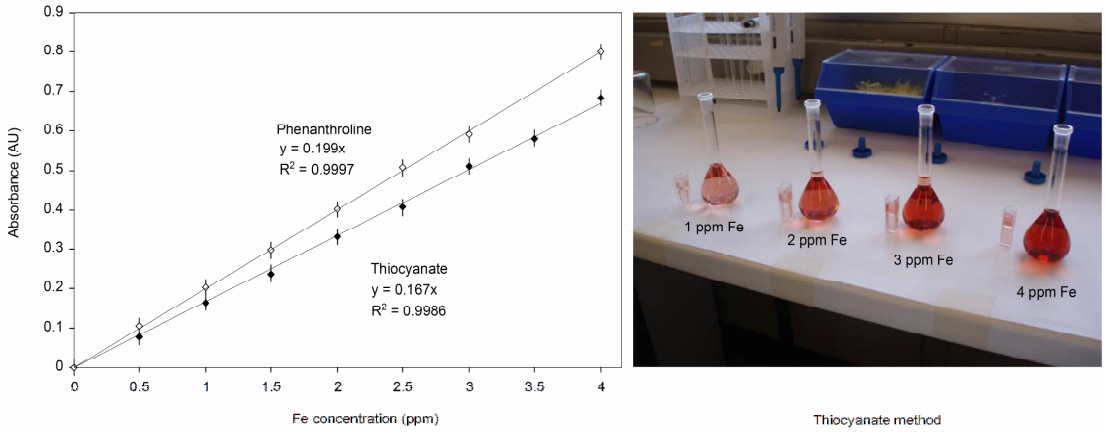

Figure 2.12: Comparison of the calibration curves obtained using the thiocyanate method and the phenanthroline method. The picture illustrates the increase in colour intensity of the $[Fe(CNS)]^{2+}$ complex when Fe(III) concentration increases.

2.4.2.2. The analysis of Fe isotope ratios

Fe isotope analysis was carried out on the GV Instruments® IsoProbe-P MC-ICP-MS at the Scottish Universities Environment Research Centre (SUERC). The detailed description of the developed protocols for the analysis of Fe isotope ratios is the subject of the next chapter. We here give an overview on the IsoProbe MC-ICP-MS and we focus upon the parameters that influence the intensity of the ion beam, the stability of the instrumental mass bias, and the associated errors for the final ratio.

2.4.2.2.1. Overview on the IsoProbe MC-ICP-MS

MC-ICP-MS has become the instrument of choice for Fe isotopes and more generally for most stable metal isotopes because of the high ionisation efficiency of the Ar plasma and the rapid sample throughput. Fig. 2.13 is a schematic representation of the IsoProbe MC-ICP-MS. Most commonly, metal samples are introduced by aspiration of a liquid (we use an uptake rate of ~ 50 µL min^{-1}) into an inlet system which permits the formation of a fine particle aerosol (Fig. 2.13 (1)). The ApexQ (Elemental Scientific™) inlet system used is comprised of a desolvating PFA (perfluoroalkoxy) microflow nebuliser (gas flow~ 0.1 mL min^{-1}) that accommodates very low uptake flows and produces the aerosol by pneumatic action of the gas flow that breaks down the liquid into droplets. Desolvating nebulisers can be operated with Ar and N_2 gases. The use of N_2 gas is usually avoided for Fe isotope analysis in order to minimise the formation of ArN^+ in the plasma chamber (*e.g.* Dauphas *et al.*, 2004). The second part of the ApexQ system is a cyclonic spray chamber that is particle size selective and ensures that largest aerosol particles (> 10 µm in diameter) coalesce as droplets and are pumped away. The size of the aerosol particles is crucial as particles that are too large are poorly ionised in the plasma chamber.

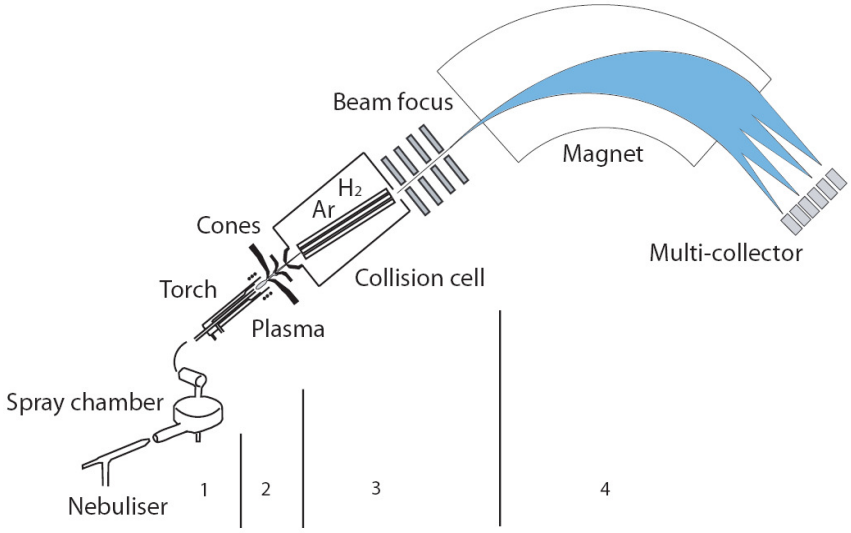

Figure 2.13: Simplified scheme of the IsoProbe MC-ICP-MS with the ApexQ inlet system comprised of a PFA nebuliser and a cyclonic spray chamber (1); the torch and the interface region (2); the hexapole collision cell and the ion optics (3) and the mass analyser and the faraday collectors (4).

The aerosol is then introduced into the plasma *via* a quartz Fessel type torch (Fig. 2.13 (2); detailed instrumentations are shown in *e.g.* Turner and Montaser, 1998), at a

~ 0.8 L min^{-1}. The sample carrier flow is surrounded by two other Ar gas flows: the intermediate flow (~ 1.3 L min^{-1}) and the cooling flow (~ 13 L min^{-1}). A radio frequency (RF) connected copper coil surrounds the end of the torch, creating an electromagnetic field. When the Ar gas flows, a high voltage spark causes the liberation of electrons from their Ar atoms. These electrons are accelerated in the induced magnetic field and collide with other Ar atoms to liberate other electrons, forming a chain collision induced ionisation of the Ar gas, and therefore, creating an Ar plasma. The temperature is variable from ~ 6000°K to ~ 10000°K within the different plasma regions. When the sample is introduced into the plasma, sample droplets are first desolved into solids, which are themselves vaporised into a gas. The gas is atomised and then ionised by the plasma ionisation potential (Fig. 2.14). Ar has an ionisation energy of 15.76 eV, and thus the Ar plasma is able to ionise elements with a lower ionisation energy at a temperature of ~8000°K. Interestingly, 15.76 eV corresponds to an energy comprised between the first and the second ionisation energies of most elements. As an example, Fe has a first ionisation energy of 7.93 eV and a second ionisation energy of 16.24 eV. As a result, sample ions are efficiently ionised as single charged ions, and all elements with a first ionisation energy < 8 eV are quantitatively ionised (>90 %, Jarvis *et al.*, 1992). As mentioned in the previous chapter, the plasma is also the source of isobaric interferences forming from the reaction between Ar and atmospheric elements such as O, N, C, H and matrix delivered elements.

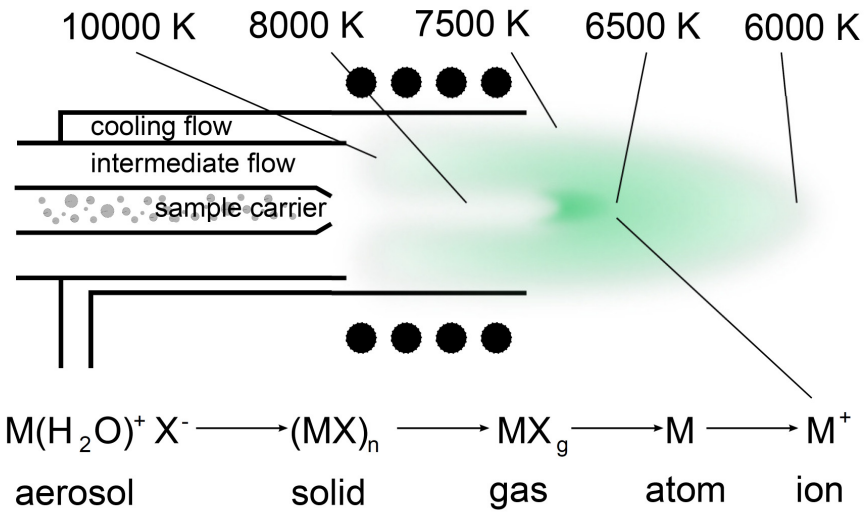

Figure 2.14: Variable temperature regions in the Ar plasma and the conversion of the aerosol sample droplets into singly charged metal ions.

The ion beam is introduced into the mass spectrometer *via* the interface region (Fig. 2.13 (3)), which consists in two Ni disks, the sampler cone and the skimmer cone. The interface region permits the transition from atmospheric pressure in the plasma (~ 760 Torr) to a high vacuum (~ 10^{-6} Torr) necessary for efficient focussing of the ion beam in the mass spectrometer. Argon neutrals being the dominant species in the plasma, the ions travel at the same velocity and their kinetic energy is controlled by their m/z ratio. A result of the differences in kinetic energies, the beam axis tends to concentrate heavier elements and isotopes whereas the outer beam assembles lighter ones. When the ion beam passes through the sampler cone, the pressure drops from atmospheric values to ~ 1-2 Torr, allowing the ion beam to expand, and the beam is sampled without change in composition (Douglas and Tanner, 1998; see also Albarede and Beard, 2004). By contrast, when the beam passes through the skimmer cone, the pressure drops to 10^{-6} Torr, electrons, neutrons and photons are diffused away from the ion beam and elements or isotopes with lower kinetic energy are more strongly repulsed than heavier isotopes. It is this so-called space charge effect which is thought to have a preponderant role in the instrumental mass bias (*e.g.* Douglas and Tanner, 1998; Marechal *et al.*, 1999; Fraser and Beauchemin, 2000; Becker, 2002). It results in a better transmission of the heavier isotopes with respect to lighter ones which is consistent with the general trend of ICP-MS to discriminate isotopes such as the ratio $R_{Light/Heavy(measured)} < R_{Light/Heavy(true)}$. By contrast, the mass fractionation observed using thermal ionisation mass spectrometers (TIMS) depends on the amount of sample consumed, and TIMS usually starts favouring the transmission of lighter isotopes with respect to heavy isotopes. Both negative and positive voltages can be applied to the cones in order to accelerate the ion beam. The relative effects of these two modes, called hard and soft extraction modes, are explored in the next chapter.

The plasma ion energy spread is ~ 30 eV, which is too large to be efficiently focussed by a single magnetic sector. Some mass spectrometers, such as the Neptune (Thermo Scientific®) MC-ICP-MS use a double focusing geometry to enable such high energy spread to be analysed. The IsoProbe MC-ICP-MS incorporates a collision/reaction cell hexapole between the skimmer cone and the ion optics, which reduces the ion energy spread to ~ 1 eV. There is another advantage in using the hexapole collision cell technology, particularly in the case of Fe isotope analysis. In

the previous chapter we documented the different approaches used with various facilities to reduce, eliminate, or resolve the isobaric polyatomic interferences produced in the Ar plasma. The IsoProbe has a mass resolution of ~ 500 Δm/m and therefore cannot resolve Fe isotope peaks from those induced by these interferences. The introduction of collision gases into the hexapole induces a series of ion-molecule reactions leading to the decrease of argides, oxides and hydrides in the ion beam (*e.g.* Beard *et al.*, 2003; Rouxel *et al.*, 2003; Vogl *et al.*, 2003; Dauphas *et al.*, 2004; Arnold *et al.*, 2008). The introduction of inert gases such as Ar into the hexapole reduces the energy spread of the incoming beam to ~ 1 eV. The introduction of H_2 permits the neutralisation of the interference by charge transfer from ArO^+ or $ArOH^+$ to H_2 forming Ar and H_2O^+ or H_3O^+, as described by Eq. 2.10:

$$ArOH^+ + H_2 \rightarrow Ar + H_3O^+ \qquad (2.10)$$

Unlike the interference, the analyte (single charged Fe ions) does not react with H_2 and is transmitted to the mass analyser. Arnold *et al.* (2008) explored the stability of argide interferences with varying Ar and H_2 rates and documented the collision reactions between H_2 and polyatomic interferences in the hexapole. We detail our own protocols in the next chapter. The ion optics are comprised of a stack of lenses that further direct the ion beam maximising the transmission of analyte ions to the mass separation device and minimising the transmission of matrix ions. The ion beam is accelerated through a potential and the lens geometry permits the transmission of positively charged ion whereas electrons, neutrons and photons are prevented to enter the mass separating device.

The magnet (Fig. 2.13 (4)) resolves the ion beam into different masses and a series of collectors aligned with the beam (Faraday cups) are impacted by incoming ions. The current caused by this impact is amplified through a large resistance (10^{11} Ω) and measured for each cup simultaneously.

2.4.2.2.2. Instrumental mass discrimination and its implications on the internal precision

The instrumental mass discrimination, or mass bias, varies in MC-ICP-MS roughly as a function of 1/mass, and can thus be up to a few percent per a.m.u for light elements (*e.g.* Becker, 2002). It is larger than the mass bias observed with TIMS. However, the mass bias fluctuations over time (Fig. 2.15.A) are smooth,

enabling temporal extrapolation for the standard-bracketing mass bias correction (*e.g.* Dauphas and Rouxel, 2006; Fig. 2.15.B). As explained above, the δ^{56}Fe nomenclature is a practical way to avoid corrections for accuracy, and the precision alone is crucial for analysing Fe isotope ratios.

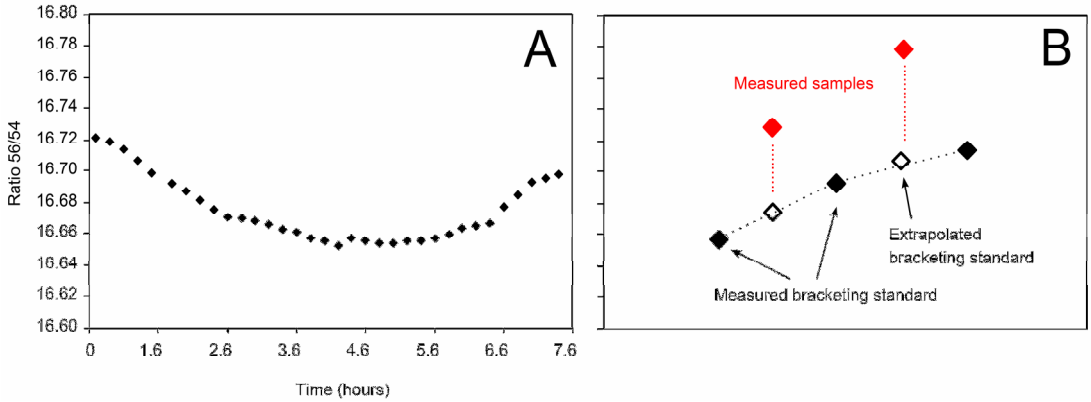

Figure 2.15: The smooth time fluctuations of the mass bias illustrated by the measurement of the ^{56}Fe/^{54}Fe ratio the IRMM-14 standard (A). The use of the $\delta^{56}Fe = \left(\frac{(^{56}Fe/^{54}Fe)sample}{(^{56}Fe/^{54}Fe)IRMM} - 1 \right) \times 10^3$ equation requires the time extrapolation of a ^{56}Fe/^{54}Fe value for IRMM-14 (B).

In this study, data collection consists in 20 blocks of 5 x 1 s integration followed by 4 min rinse in a 5 % HNO_3 + 2 % HF solution. Blank correction is performed by on-peak-zero (OPZ) measurement of a 5 % HNO_3 solution prior to each Fe solution. For masses < 60 a.m.u, tail intensities are less than 3 ppm and OPZ correction alone is sufficient (Thirlwall, 2001). The measured ratio R of one sample is given by the mean of the R_i for N integrations, with an internal precision given by Eqs. 2.11 and 2.12:

$$2se = \frac{2sd}{\sqrt{N}} \qquad (2.11), \text{ with}$$

$$sd = \sqrt{\frac{1}{N-1}\sum_{i=1}^{N}\left(R_i - \overline{R}\right)^2} \qquad (2.12)$$

As explored in Guilbaud, Ellam, *et al.* (2010) and the next chapter, we observed that the mass bias is enhanced when using the soft extraction mode with respect to the hard extraction mode. Fig. 2.16 compares the internal errors for a single measured ratio obtained using both soft and hard extractions.

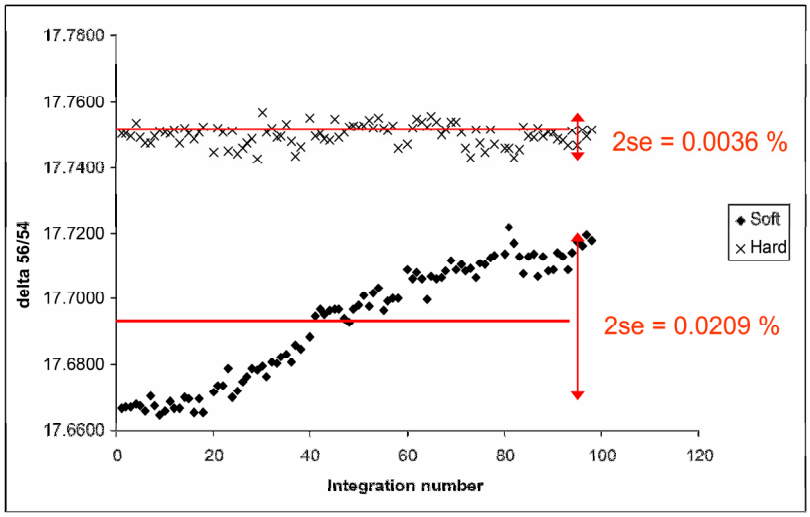

Figure 2.16: Comparison of the variations in $^{56}Fe/^{54}Fe$ during the 10 min of the sample's measurement. Mass bias effects seam less important using the hard extraction mode than using the soft extraction mode.

The internal error is a combination between the error on the measurement or ions (Shot noise), the noise produced by the Faraday amplifiers (Johnson noise) and the noise produced by the cosmic rays (Dark noise). The Dark noise being insignificant, Ludwig (1986) showed that the internal error depends on the Shot noise and the Johnson noise. Fig. 2.17 shows that the Johnson noise dominates the contributions to the internal error for intensities larger than 0.1 V. The figure also illustrates that the higher the signal, the lower the internal error.

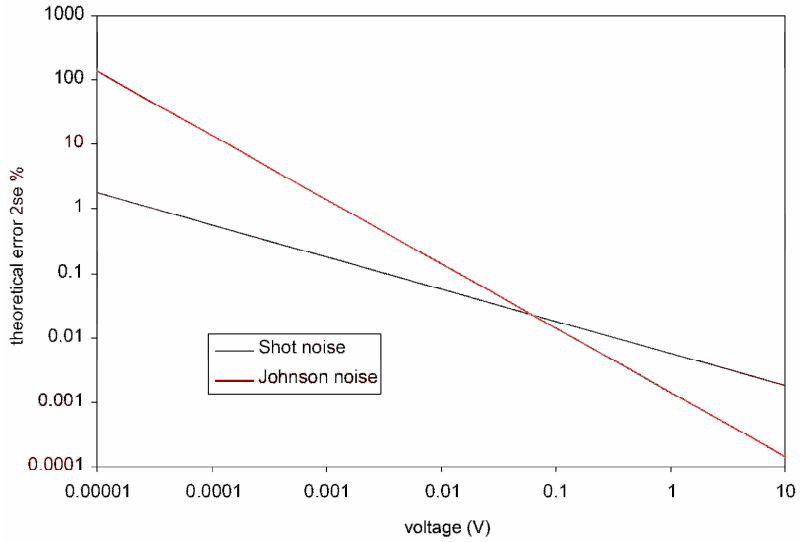

Figure 2.17: The theoretical relationship between the measurement intensity (voltage) and the internal error 2se, calculated from the Shot noise and Johnson noise equations (Ludwig, 1986; see also Eq. 3.3 in the next chapter).

2.4.2.2.3. External reproducibility and overall precision

Because the internal error does not account for the long term fluctuations such as the ionisation efficiency, matrix effects, and mass bias instability, the precision of a set of measurements is usually given by the reproducibility of an external standard measured at least twelve times in an analytical set. Fig. 2.18 represents the measurement of the Baker™ Fe standard measured over three years, with its reproducibility. For such long term measurement, the precision (± 0.08 ‰) is reduced by an increasing number of measures. However, although this precision reflects the expected precision for a set of samples, it does not necessarily represent the actual precision of the run. In the following chapters, we thus preferred to use the precision obtained for each set of experiments, rather than giving systematically our "best results".

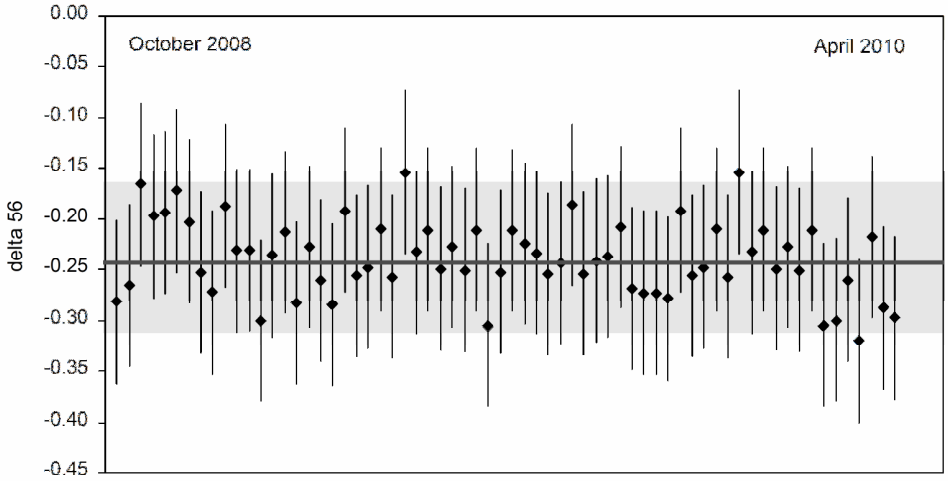

Figure 2.18: Analysis of the Baker™ Fe standard from October 2008 to April 2010. The mean value for $\delta^{56}Fe_{standard}$ is -0.24 ‰ ± 0.08 ‰ (2σ). This precision is, however, not necessarily representative of each set of analysis and in the next chapters, the precisions we give are representative of the set of analysis only.

2.5. References

Albarede, F., Beard, B., 2004. Analytical Methods for Non-Traditional Isotopes. Reviews in Mineralogy & Geochemistry 55, 113-152.

Arnold, T., Harvey, J., Weiss, D., 2008. An experimental and theoretical investigation into the use of H2 for the simultaneous removal of ArO+ and ArOH+ isobaric interferences during Fe isotope ratio analysis with collision cell based Multi-

Collector Inductively Coupled Plasma Mass Spectrometry. Spectrochimica Acta Part B: Atomic Spectroscopy 63, 666-672.

Beard, B., Johnson, C., Skulan, J., Nealson, K., Cox, L., Sun, H., 2003. Application of Fe isotopes to tracing the geochemical and biological cycling of Fe. Chem. Geol. 195, 87-117.

Becker, J., 2002. State-of-the-art and progress in precise and accurate isotope ratio measurements by ICP-MS and LA-ICP-MS. J. Anal. At. Spectrom. 17, 1172–1185.

Brindley, G., 1980. Order-disorder in clay mineral structures. In : Crystal structures of clay minerals and their X-ray identification. In : Crystal structures of clay minerals and their X-ray identification (G.W. Brindley and G. Brown, eds). Mineralogical Society London 125-195.

Butler, I., Archer, C., Vance, D., Oldroyd, A., Rickard, D., 2005. Fe isotope fractionation on FeS formation in ambient aqueous solution. Earth and Planet. Science Letters 236.

Butler, I., Bottcher, M., Rickard, D., Oldroyd, A., 2004. Sulfur isotope partitioning during experimental formation of pyrite *via* the polysulfide and hydrogen sulfide pathways: implications for the interpretation of sedimentary and hydrothermal pyrite isotope records. Earth and Planet. Science Letters 228, 495-509.

Butler, I., Rickard, D., 2000. Framboidal pyrite formation *via* the oxidation of iron (II) monosulfide by hydrogen sulphide. Geochim Cosmochim Acta 64, 2665–2672.

Butler, I., Schoonen, M., Rickard, D., 1994. Removal of dissolved oxygen from water: A comparison of four common techniques. Talanta 41, 211-215.

Criss, R., 1999. Principles of stable isotope distribution. Oxford University Press, New York 244pp.

Dauphas, N., Janney, P., Mendybaev, R., Wadhwa, M., Richter, F., Davis, A., van Zuilen, M., Hines, R., Foley, C., 2004. Chromatographic separation and multicollection-ICPMS analysis of iron. Investigating mass dependent and -independent isotope effects. Anal. Chem. 76, 5855-5863.

Dauphas, N., Rouxel, O., 2006. Mass Spectrometry and natural variations of iron isotopes. Mass Spectrometry Reviews 25, 515-550.

Douglas, D., Tanner, S., 1998. Fundamental Considerations in ICP-MS, in:

Inductively Coupled Plasma Mass Spectrometry. VCH Publishers, pp. 615-679.

Drobner, E., Huber, H., Wächtershäuser, G., Rose, D., Stetter, K., 1990. Pyrite formation linked with hydrogen evolution under anaerobic conditions. Nature 346, 742-744.

Fraser, M.M., Beauchemin, D., 2000. Effect of concomitant elements on the distribution of ions in inductively coupled plasma-mass spectroscopy. Part 1. Elemental ions. Spectrochimica Acta Part B: Atomic Spectroscopy 55, 1705-1731.

Guilbaud, R., Ellam, R., Butler, I., Gallagher, V., Keefe, K., 2010. A procedural development for the analysis of 56/54Fe and 57/54Fe isotope ratios with new generation IsoProbe MC-ICP-MS. J. Anal. At. Spectrom 25, 1598-1604.

Guilbaud, R., Butler, I.B., Ellam, R.M., Rickard, D., 2010. Fe isotope exchange between Fe(II)aq and nanoparticulate mackinawite (FeSm) during nanoparticle growth. Earth and Planetary Science Letters 300, 174-183.

Huang, F., Zhang, H., Banfield, J., 2003. Two-Stage Crystal-Growth Kinetics Observed during Hydrothermal Coarsening of Nanocrystalline ZnS. Nano Letters 3, 373-378.

Huerta-Diaz, M.A., Morse, J.W., 1990. A quantitative method for determination of trace metal concentrations in sedimentary pyrite. Marine Chemistry 29, 119-144.

Jarvis, K., Gray, A., Houk, R., 1992. Handbook of Inductively Coupled Plasma Mass Spectrometry. Chapman and Hall, New York.

Jeong, H., Lee, J., Hayes, K., 2008. Characterization of synthetic nanocrystalline mackinawite: Crystal structure, particle size, and specific surface area. Geochimica et Cosmochimica Acta 72, 493-505.

Kandegedara, A., Rorabacher, D.B., 1999. Noncomplexing Tertiary Amines as "Better" Buffers Covering the Range of pH 3−11. Temperature Dependence of Their Acid Dissociation Constants. Analytical Chemistry 71, 3140-3144.

Ludwig, K., 1986. Constraints in time efficient data-taking strategies for single-collector isotope-ratio mass spectrometers. U.S.G.S. Bull. 1622, 219-221.

Marechal, C., Telouk, P., Albarede, F., 1999. Precise analysis of copper and zinc isotopic compositions by plasmasource mass spectrometry. Chem. Geol. 156, 251-273.

Rickard, D., 1997. Kinetics of pyrite formation by the H2S oxidation of iron (II) monosulfide in aqueous solutions between 25oC and 125oC: the rate equation. Geochim. Cosmochim. Acta 61, 115– 134.

Rickard, D., 2006. The solubility of FeS. Geochimica et Cosmochimica Acta 70, 5779-5789.

Rickard, D., Griffith, A., Oldroyd, A., Butler, I., Lopez-Capel, E., Manning, D., Apperley, D., 2006. The composition of nanoparticulate mackinawite, tetragonal iron (II) monosulfide. Chem. Geol. 235.

Rickard, D., Luther, G., 2007. Chemistry of Iron Sulfides. Chem. Rev. 107, 514-562.

Rouxel, O., Dobbek, N., Ludden, J., Fouquet, Y., 2003. Iron isotope fractionation during oceanic crust alteration. Chem. Geol. 202, 155-182.

Severmann, S., Johnson, C., Beard, B., McManus, J., 2006. The effect of early diagenesis on the Fe isotope compositions of porewaters and authigenic minerals in continental margin sediments. Geochim Cosmochim Acta 70, 2006–2022.

Suleimenov, O., Seward, T., 1997. A spectrophotometric study of hydrogen sulphide ionisation in aqueous solutions to 350dC. Geochim. Cosmochim. Acta 61, 5187.

Thirlwall, M., 2001. Inappropriate tail corrections can cause large inaccuracy in isotope ratio determination by MC-ICP-MS. J. Anal. At. Spectrom. 16, 1121-1125.

Turner, I., Montaser, A., 1998. Plasma generation in ICPMS. In: Inductively Coupled Plasma Spectrometry Wikey-VCH, New York, 265-334.

Vogel, A., 1951. A text-book of Quantitative Inorganic Analysis, Therory and practice, second edition. Longmans, Green and Co.

Vogl, J., Klingbeil, P., Pritzkow, W., Riebe, G., 2003. High accuracy measurements of Fe isotopes using hexapole collision cell MC-ICP-MS and isotope dilution for certification of reference materials. Journal of Analytical Atomic Spectrometry 18, 1125 - 1132.

Wolthers, M., van der Gaast, S., Rickard, D., 2003. The structure of distored mackinawite. Am. Mineral. 88, 2007.

Zehnder, A., Wuhrmann, K., 1976. Titanium (III) citrate as a nontoxic oxidation-reduction buffering system for the culture of obligate anaerobes. Science 194, 1165-1166.

Chapter III

A procedural development for the analysis of $^{56/54}$Fe and $^{57/54}$Fe isotope ratios with new generation IsoProbe MC-ICP-MS

Article published as Guilbaud, R., Ellam, R., Butler, I., Gallagher, V., Keefe, K., 2010. A procedural development for the analysis of 56/54Fe and 57/54Fe isotope ratios with new generation IsoProbe MC-ICP-MS. J. Anal. At. Spectrom 25, 1598-1604.

Abstract

We have developed a procedure for iron isotope analysis using a hexapole collision cell MC-ICP-MS which is capable of Fe isotope ratio analysis using two different extraction modes. Matrix effects were minimised and the signal-to-background ratio was maximised using high-concentration samples (~ 5µg Fe) and introducing 1.8 mL/min Ar and 2 mL/min H_2 into the collision cell to decrease polyatomic interferences. The use of large intensity on the faraday cups considerably decreases the internal error of the ratios and ultimately, improves the external precision of a run. Standard bracketing correction for mass bias was possible when using hard extraction. Mass bias in soft extraction mode seems to show temporal instability that makes the standard bracketing inappropriate. The hexapole rf amplitude was decreased to 50 % to further decrease polyatomic interferences and promote the transmission of iron range masses. We routinely measure Fe isotopes with a precision of ± 0.05 ‰ and ± 0.12 ‰ (2σ) for δ^{56}Fe and δ^{57}Fe respectively.

Keywords: Fe isotopes, IsoProbe, MC-ICP-MS, hard extraction, soft extraction.

3.1. Introduction

The field of transition metal geochemistry has seen increasing development throughout the last twenty years and particularly since the introduction of multi-collector inductively coupled mass spectrometry MC-ICP-MS (Walder and Freedman, 1992; Walder *et al.*, 1993; Halliday *et al.*, 1998). Iron is the ninth most abundant element in the universe (Anders and Grevesse, 1989) with four stable isotopes: ^{54}Fe (5.845 %), ^{56}Fe (91.754 %), ^{57}Fe (2.1191 %) and ^{58}Fe (0.2819 %) (Taylor *et al.*, 1992). The first attempts to measure Fe isotopic ratios began 60 years ago (Valley and Anderson, 1947). Thermal ionisation mass spectrometry, TIMS, has been applied to iron since the 1980s (Gotz and Heumann, 1988; Walczyk, 1997; Bullen and McMahon, 1998) with a precision down to ± 0.6 ‰ (2σ) (Beard and Johnson, 1999; Johnson and Beard, 1999). However, TIMS was challenging because of the large spectrometer mass discrimination (mass fractionation) and the low ionisation efficiency for Fe analysis (the first ionisation potential is 7.870 eV). MC-ICP-MS, characterised by a higher ionisation efficiency and a very stable mass bias (although larger than TIMS, from 3 to 6%/amu), has become the technique of choice since its development in the 1990s.

Fe isotope analysis has seen growing attention in the Earth and environmental sciences for its potential use for tracing biogeochemical cycles. Because of their relative small mass difference, it was generally agreed that Fe isotopes could fractionate in nature solely *via* biological assimilation and preferential uptake by organisms. Recent studies have now indicated that Fe isotope fractionation can also occur abiotically in low temperature aqueous systems (*e.g.* Johnson *et al.*, 2002; Butler *et al.*, 2005; Severmann *et al.*, 2006) and at high temperature (*e.g.* Roskosz *et al.*, 2006; Dauphas, 2007; Shahar *et al.*, 2008; Richter *et al.*, 2009).

The principal difficulty in measuring precisely and accurately Fe isotope ratios is the removal of polyatomic and atomic mass interferences induced by the Ar plasma. Additional interferences can be due to sample matrix. Among these interferences are $^{40}Ar^{14}N^+$ and $^{54}Cr^+$ on $^{54}Fe^+$, $^{40}Ar^{16}O^+$ on $^{56}Fe^+$, $^{40}Ar^{16}OH^+$ on $^{57}Fe^+$, and $^{40}Ar^{18}O^+$ and $^{58}Ni^+$ on $^{58}Fe^+$. Various strategies have been developed to reduce interferences created by the Ar plasma: i) sample desolvation and the use of high-concentration samples (*e.g.* Anbar *et al.*, 2000; Belshaw *et al.*, 2000; Sharma *et al.*, 2001; Roe *et al.*, 2003; Arnold *et al.*, 2004; Schoenberg and von Blanckenburg, 2005), ii) cold plasma (Walczyk and von Blanckenburg, 2002; Kehm *et al.*, 2003), iii) collision cells (Beard

et al., 2003; Mullane *et al.*, 2003; Rouxel *et al.*, 2003; Dauphas *et al.*, 2004) and iv) high resolution multi-collection (*e.g.* Weyer and Schwieters, 2003; Poitrasson and Freydier, 2005; Dauphas *et al.*, 2009).

In this contribution, we detail a procedure developed for the analysis of Fe isotope ratios on a new generation GV Instruments (formerly Micromass) IsoProbe-P MC-ICP-MS at the Scottish Universities Environmental Research Centre (East Kilbride, UK). This instrument enables us to conduct the ion extraction in two modes: the hard and the soft extraction modes. Although Fe isotope ratios have been published using both extraction modes (Dauphas *et al.*, 2004, 2009), no study compares the effect of each mode on the external precision and the overall stability of the measurement of Fe isotope ratios. Therefore, we have inspected the effects of extraction voltage, sample uptake rate, the hexapole potential difference and the collision gases on the overall stability of Fe isotope analysis.

3.2. Analytical materials and methods

3.2.1. Samples and standards preparation

All samples used in this study are part of an experimental investigation of iron sulphide geochemistry; therefore all samples are synthetic iron sulphide species (FeS and FeS_2) and $Fe(II)_{aq}$. Solutions were prepared using 18.2 MΩcm deionised water. Fe and S source reagents were analytical grade $Fe(NH_4)_2(SO_4)_2.6H_2O$ and $Na_2S.9H_2O$ (Sigma Aldrich™) respectively. HNO_3 and HCl were twice distilled, HF was once distilled. Once experimentally synthesised, solid samples were separated and dissolved in 6 M HCl or concentrated HNO_3 depending on the mineral, taken to dryness and re-dissolved in 5 % v/v HNO_3. The solution was then effectively Fe(III) in nitric acid (S being removed as H_2S gas), and thus no column separation chemistry was performed on our samples.

IRMM-014 (IRMM™) was used as a bracketing reference standard for the δ calculation, *i.e.* before and after each sample. The isotopic concentrations of IRMM-14 are in percent, 5.845 ± 0.023 (2σ) for ^{54}Fe, 91.754 ± 0.024 for ^{56}Fe, 2.1192 ± 0.0065 for ^{57}Fe, and 0.2818 ± 0.0027 for ^{58}Fe (Taylor *et al.*, 1992). These concentrations are close to the natural Fe isotope distribution. IRMM-014 Fe wire was dissolved on a hot plate in 5 % v/v HNO_3. Our external standard for determination of precision was prepared from a 1 g/L Fe solution (J.T Baker™).

3.2.2. Mass Spectrometry

Analyses were performed using the GV Instruments (formerly Micromass) IsoProbe MC-ICP-MS. Table 3.1 summarises the routine instrumental settings for Fe isotope analysis. Mass 54, 56, 57 and 58 were measured simultaneously on the multi-collection faraday cups in a static mode (Fig. 3.1). Cr interferences were monitored on mass 52 for further correction on mass 54. However, since our samples were experimentally synthesised, Cr contributions were never detected. Ni interferences on mass 58 should be monitored on mass 60, but on our instrument, it was physically not possible to align mass 60 on any cup, the range of masses being so large. In the case of this study, that is not a problem since only $^{56/54}$Fe and $^{57/54}$Fe were required. Faraday cups were calibrated and displayed linear response over a 1 ppm to 8 ppm range. Typical response was 0.6 to 2 V/ppm and our sample solutions were 3 to 10 ppm Fe in 5% v/v HNO_3 (samples and/or standards) to obtain ~ 0.35 V on mass 54, ~ 6 V on mass 56, ~ 0.14 V on mass 57 and 0.024 V on mass 58.

ApexQ		**Argon flow rates*:**		**Torch position***	
Cooling	2 °C	Cooling	13.50 L/min	Vertical	-0.6
Heating chamber	100°C	Intermediate	1.35 L/min	Horizontal	-0.6
Neb 2	none	Nebuliser	0.85 L/min	Axial	4
Uptake rate	~ 50 µL/min				
Interface		**Hexapole gases**		**Extraction**	
Skimmer Cone	Ni	Ar	1.8 mL/min	rf power	1350 W
Sample Cone	Ni	H_2	2 mL/min	Extraction voltage*	-250 V (Hard)
				High Tension*	- 6000 V
Analysis				Hexapole rf amplitude*	50%
Sample concentration*	3- 10 ppm				
Mode	static				
Cup position					

	Elementar interferences	*Molecular interferences*	*Isotopes of interest*
L2	^{52}Cr		
Ax	^{54}Cr	ArN	^{54}Fe
H1		ArO	^{56}Fe
H4		ArOH	^{57}Fe
H7	^{58}Ni	ArO	^{58}Fe

Table 3.1: IsoProbe settings. Tuning parameters are followed by an asterisk.

Solutions were introduced into an ApexQ (Elemental Scientific™) inlet system which comprises a PFA nebuliser and a cyclonic desolvating spray chamber. The ApexQ was operated with Ar sweep gas and without the addition of N_2 to avoid further formation of $^{40}Ar^{14}N^+$ on mass 54. The condenser cooling temperature was set at 2°C and the temperature of the spray chamber at 100°C. Both 50 µL/min and 100 µL/min uptake rates were investigated.

The instrument high tension was set at -6000 V. Ion extraction from the source into the mass analyser can be run in two modes, called hard and soft extraction. We routinely run our samples using the hard extraction mode at -250V but both approaches were investigated and the results will be described later.

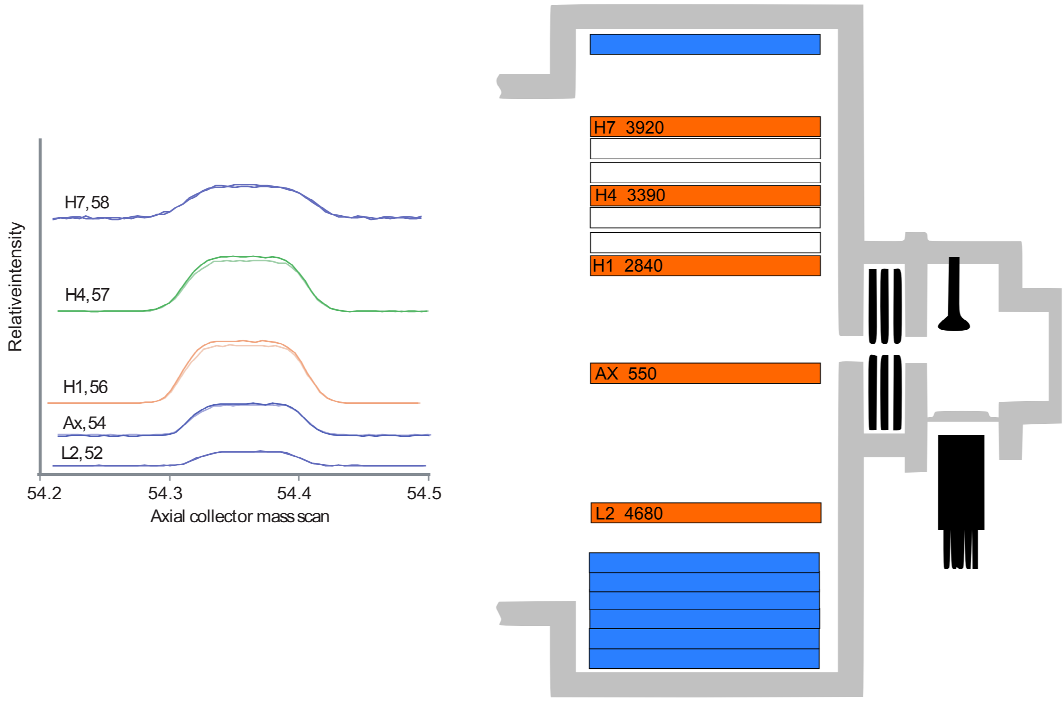

Figure 3.1: Alignment of the cups for simultaneous measurements of masses 52, 54, 56, 57 and 58.

The IsoProbe incorporates a hexapole to the standard MC-ICP-MS instrumentation - between the cones and the optics region - in order to reduce the ions' energy spread from ~ 30eV to ~ 1eV, allowing a single focusing magnetic sector analyser. Ions are transmitted with a mass resolution ~ 500 Δm/m which is not sufficient to separate Fe peaks from polyatomic interferences. Fe peaks can be separated from molecular interference peaks with a resolving power of ~3000 (Vogl *et al.*, 2003) and flat peaks can be preserved with resolving power of ~9000 (High resolution, Weyer and Schwieters, 2003). To reduce or remove polyatomic interferences, the hexapole can be used as a reaction cell. The introduction of collision gases (Ar and H_2) into the hexapole induces a series of ion-molecule reactions leading to the decrease of argides, oxides and hydrides in the ion beam. 1.8 mL/min Ar and 2 mL/min H_2 were introduced into the hexapole collision cell to completely remove $^{40}Ar^{14}N^+$ and $^{40}Ar^{16}OH^+$ on mass 54 and mass 57 respectively, and to decrease $^{40}Ar^{16}O^+$ on mass 56 to 0.006 V which represents 0.1 % of the Fe peak. After

subtraction, interference contributions were smaller than the analytical precision. There was no peak on mass 55 suggesting that FeH^+ did not form even at high Fe concentrations.

On-peak-zero correction was measured on a 5% v/v HNO_3 solution prior to each Fe solution (samples or standards). Data collection consisted of 5 blocks of 20 5 x 1s integrations, followed by a 4 min rinse in 5% v/v HNO_3 + 2% v/v HF. Mass bias was corrected using IRMM-014 as a bracketing standard (Eqs. 3.1 and 3.2). The external standard was measured five times before the run of samples. During the run, one external standard was measured after every four samples.

Data are reported in conventional fashion using per mil δ notation, $\delta^{56}Fe$ and $\delta^{57}Fe$, defined as (3.1) and (3.2):

$$\delta^{56}Fe = \left(\frac{(^{56}Fe/^{54}Fe)sample}{(^{56}Fe/^{54}Fe)std} - 1 \right) \times 10^3 \qquad (3.1)$$

$$\delta^{57}Fe = \left(\frac{(^{57}Fe/^{54}Fe)sample}{(^{57}Fe/^{54}Fe)std} - 1 \right) \times 10^3 \qquad (3.2)$$

where *std* is the reference material *IRMM-014* (IRMM™).

3.3. Procedural development

3.3.1. Theoretical and observed errors

The external precision on $\delta^{56}Fe$ and $\delta^{57}Fe$ is given by the 95% reproducibility (2σ standard deviation) of the δ external standard repeated at least twelve times. The external precision should approximate the internal error of each individual ratio (2se) which is the 95% confidence limits on the mean ratio. Ludwig (1986) showed that the internal error is the result of a combination of shot noise (error on the measurement of ions) and Johnson noise (from the Faraday amplifier). The overall theoretical error on a measured Fe isotope ratio is given by Eq. 3.3 (after Ludwig, 1986):

$$\%2se = 2 \times \frac{\frac{^{56}Fe}{^{54}Fe}\sqrt{\underbrace{\left(\frac{1}{V_{^{56}Fe}} + \frac{1}{V_{^{54}Fe}}\right) \times \left(\frac{1.6\times10^{-8}}{t}\right)}_{Shot-noise} + \underbrace{2 \times 0.000014^2 \times \left(\frac{1}{V^2_{^{56}Fe}} + \frac{1}{V^2_{^{54}Fe}}\right)}_{Faraday-noise}}}{\sqrt{N}} \qquad (3.3)$$

where V is the voltage on the peak and t is the time of the measurement (10 min).

It is intuitive to think that the larger the internal errors of the mean are, the larger the external error on the overall run should be. However, it is not possible to demonstrate this mathematically because in the 2sd calculation we do not take in account the internal error of each individual δ value. In Fig. 3.2.A, we plot the mean 2se of the ratios during several run times against the external precision of the run. We demonstrated graphically that for the external precision to be ≤ ± 0.1 ‰ and ≤ ± 0.15 ‰ (2σ) for δ^{56}Fe and δ^{57}Fe, the internal error over a run time should not exceed ~0.0018% and ~0.0025% for $^{56/54}$Fe and $^{57/54}$Fe respectively. Rearranging Eq. 3.3 demonstrates that the voltage on ^{56}Fe must be > 4V to produce such small errors, justifying the use of high-concentration samples. Collecting ~ 6V on mass 56 enables us to decrease the internal error down to 0.0013% (Fig. 3.2.B). We could measure accurately Fe isotope ratios with an internal error (%2se) systematically < 0.0020 % and < 0.0030 % for $^{56/54}$Fe and $^{57/54}$Fe respectively. The precision of our measurements was ± 0.05 ‰ and ± 0.12 ‰ (2σ) for δ^{56}Fe and δ^{57}Fe respectively.

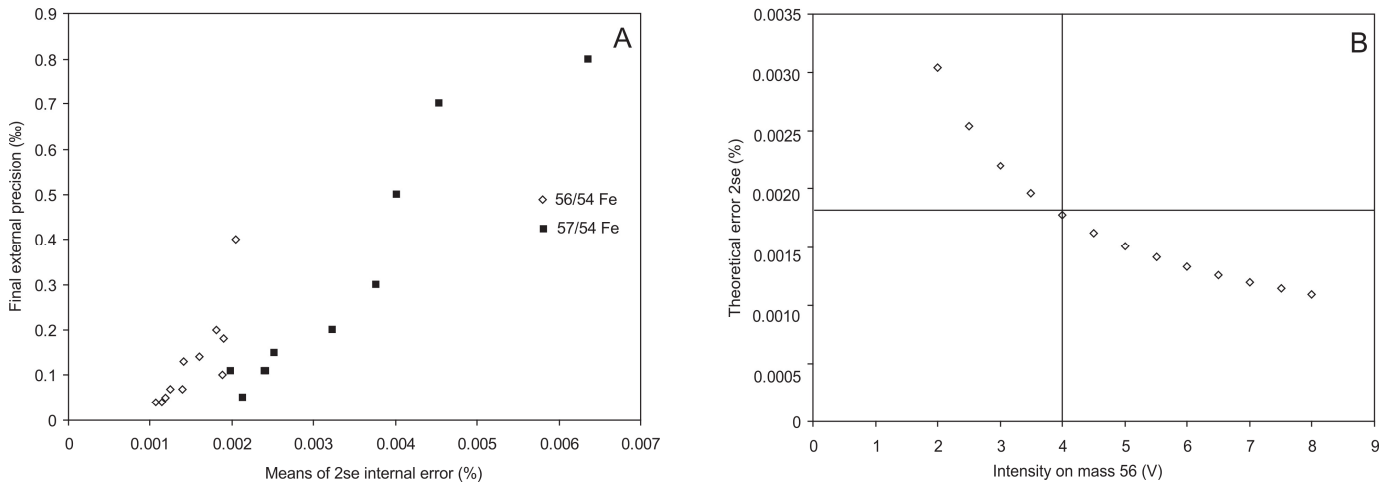

Figure 3.2: A: Empirical relationship between the mean of 2se during one set of measurement and the overall external precision of the run. B: Influence of the peak intensity (mass 56) on the theoretical error of the ratio $^{56/54}$Fe.

3.3.2. Matrix effects and sample uptake

The reduction of interferences and their effects is crucial for precise and accurate measurements. This was achieved by the use of collision gases (see below) and maximising the source-to-background ratio by introduction of high-concentration samples (up to 10 ppm). Sample matrix is a potential source of interferences, with

direct effects on the overall reproducibility. We compared bracketing our external standard (Fe solution from J.T.Baker™) with bracketing IRMM-014 itself. The Baker solution, which is essentially an iron sulphate solution led to a reproducibility of ± 0.05 ‰ and ± 0.12 ‰ (2σ) for δ^{56}Fe and δ^{57}Fe respectively. IRMM-014 solution, which is dissolved Fe in HNO_3, bracketed with itself, led to a precision as good as ± 0.05 ‰ and ± 0.05 ‰ (2σ) for δ^{56}Fe and δ^{57}Fe respectively.

The uptake rate is determined by the diameter of the auto-sampler capillary. Both 50 μL/min and 100 μL/min uptake rates were used. Twice as much material was consumed using the 100 μL/min rate, doubling the sensitivity. However, the stability of a measurement was systematically decreased as well, leading to internal errors > 0.0050% and > 0.0100% for $^{56/54}$Fe and $^{57/54}$Fe respectively. As a result, the measured Fe isotope ratios which are the mean of the 100 integrations were not reproducible within an acceptable precision. We suspect that this uptake rate introduced too much material for the ApexQ inlet system to quantitatively desolve the sample, leading to inconsistent variations in the signal.

We examined the effect of the Fe concentration matching between the samples and the reference standard IRMM-014 on the measured isotopic ratios. True ratios are obtained when both the sample and the standard have the same concentration (Fig. 3.3). The effect is more dramatic for $[Fe]_{sample}<[Fe]_{Std}$, as suggested by other authors (Belshaw *et al.*, 2000; Archer and Vance, 2004). We suspect that in this region, Fe concentration is small relative to the interferences and therefore the peaks are committed to variations in interference production from the plasma. The deviation from linear response is thus due to plasma behaviour and not detector non-linearity over that range.

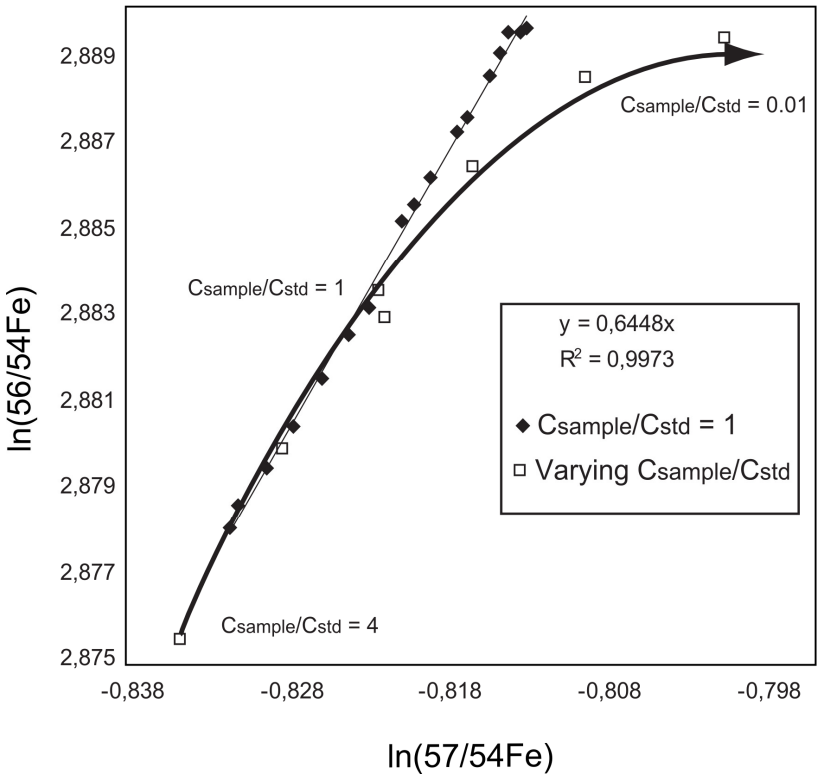

Figure 3.3: Concentration matching between samples and bracketing standards. Data plot on a mass fractionation line when both standards and samples have the same concentration.

3.3.3. Extraction mode: hard versus soft extraction

Both hard and soft extraction modes have been used in laboratories for the analysis of Fe isotopes (Mullane *et al.*, 2003; Dauphas *et al.*, 2004; Archer and Vance, 2006; Thompson *et al.*, 2007). The hard extraction mode applies a strong negative voltage to the cones (generally ~ -600V), while the soft extraction mode applies a small positive voltage to the cones (0 to 20V). The soft extraction mode has been available only on new generations of the IsoProbe, and has seen increasing interest since it considerably reduces molecular interferences and memory effects (Dauphas *et al.*, 2004). We investigated the stability of the measurement during 100 integrations of the analysis in both hard and soft extraction (Fig. 3.4). In hard extraction, internal errors (2se) produced on the ratios during 100 integrations (~ 10 min) are systematically less than 0.0020% and 0.0040% for $^{56/54}$Fe and $^{57/54}$Fe, while in soft extraction, internal errors are 0.0060% and 0.0100% for $^{56/54}$Fe and $^{57/54}$Fe respectively.

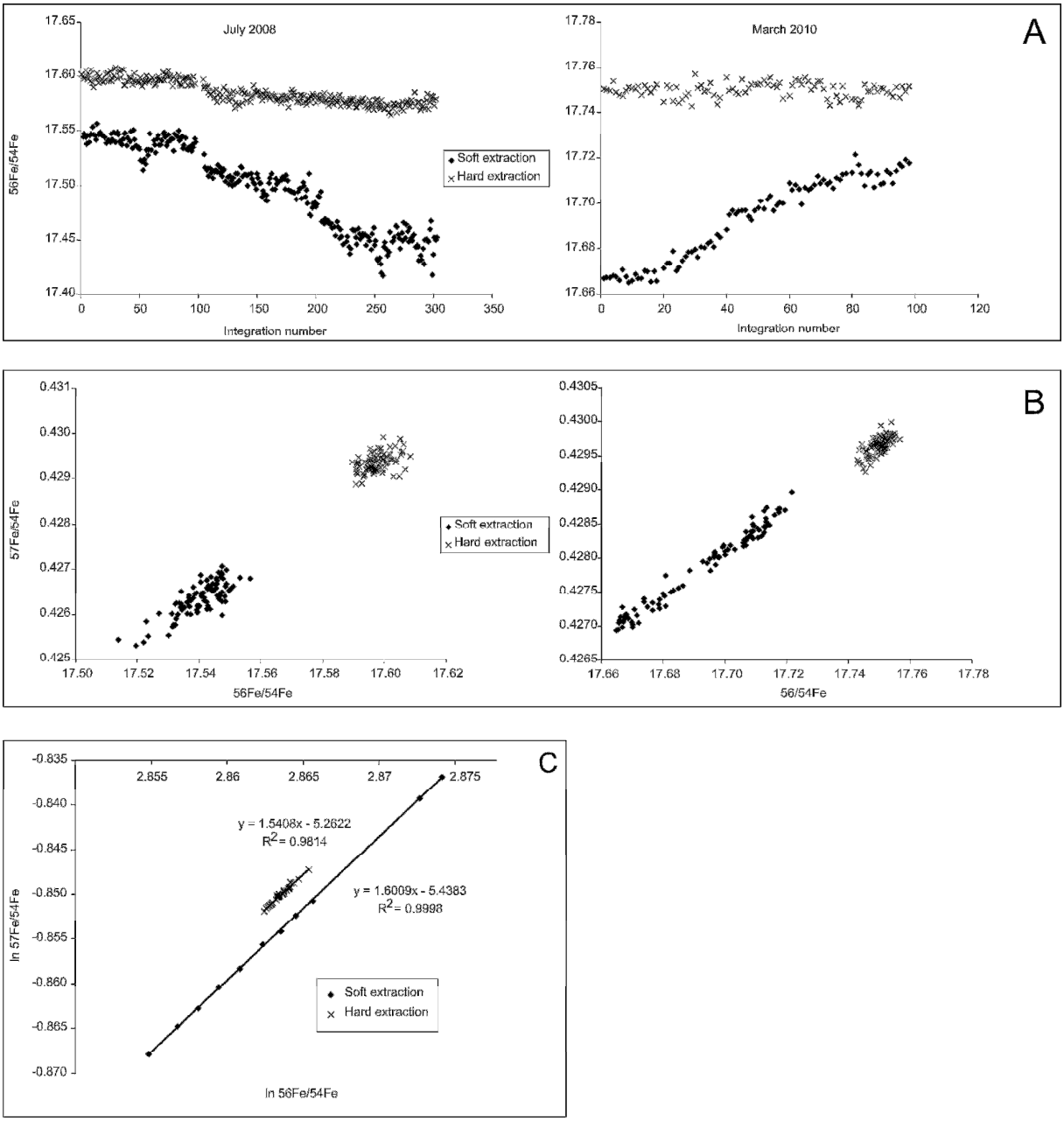

Figure 3.4: Comparison of soft and hard extraction modes. A: variations of the measured ratio with time (100 integrations ~ 10 min). B: Mass bias associated with time (same data as A). C: Resulting fractionation lines on a long sample run.

In all the applications we have utilised soft extraction, we observe increased mass bias but this is not necessarily detrimental if mass bias is internally corrected. However, for stable isotope measurements of iron we need to make an external mass bias correction by reference to bracketing standards. In soft extraction mode there is an increased time-dependent mass bias instability, even over timescales of a few minutes, compared to the hard extraction mode. As a result, a simple standard bracketing correction was not sufficient and the overall precision on long term runs

was always > ± 0.2 ‰ and > ± 0.6 ‰ (2σ) for $\delta^{56}Fe$ and $\delta^{57}Fe$ respectively. We suspect that small voltage fluctuations in soft extraction mode have a more dramatic effect on mass bias than in hard extraction considering their voltage range (0 to 20V versus 0 to -1500V for soft and hard extraction respectively). Thirlwall and Anczkiewicz (2004) did a comparative study for Hf, Nd and Pb isotopes using MC-ICP-MS and TIMS. They showed that for Nd isotope ratios, hard extraction produced a larger mass bias than soft extraction. This suggests that plasma chemistry and extraction voltage are not entirely comprehended yet.

Although hard extraction is usually operated at a cone voltage of ~ -600V or higher to maximise sensitivity, reducing the extraction potential to ~ -250 V was a key for successful Fe isotope measurements. At this voltage, molecular interferences on mass 52 are entirely removed, and transmission of masses 54, 56 and 57 is optimised. The instrumental mass bias is very stable and thus the standard bracketing technique is suitable.

3.3.4. Hexapole tuning

Hexapole tuning, i.e the rf amplitude (referred by some authors as Digital to Analogue Convertor settings, or D.A.C settings) and the introduction of collision gases plays a dominant role in optimising the transmission of ions. The IsoProbe collision cell can be used with two hexapole rf generator devices (6MΩ or 9MΩ), the 9 MΩ one being designed for measuring low mass elements. Reducing the rf amplitude to ~ 50 % enhances the transmission of low masses. In the literature, reported rf amplitudes vary from 40 % to 60 % (Mullane *et al.*, 2003; Dauphas *et al.*, 2004). The removal or reduction of $^{40}Ar^{14}N^+$ and $^{40}Ar^{16}O^+$, $^{40}Ar^{16}OH^+$, $^{40}Ar^{18}O^+$ and FeH^+ interferences was achieved by the introduction of collision gases (Ar and H_2) into the hexapole collision cell (Beard *et al.*, 2003; Rouxel *et al.*, 2003; Vogl *et al.*, 2003; Dauphas *et al.*, 2004; Arnold *et al.*, 2008). Arnold *et al.* (2008) studied the mechanisms of polyatomic interferences removal and the behaviour of $^{40}Ar^{16}O^+$, $^{40}Ar^{16}OH^+$ when varying Ar:H_2 ratios, flow rates, and the rf amplitude of the hexapole. In our routine, the rf amplitude was set at 50 % which decreases $^{40}Ar^{16}OH^+$, as Arnold *et al.* (2008) reported. Introducing 1.8 mL/min Ar into the hexapole removed completely ArN^+ interference on mass 54. We thus investigated the effect of different H_2 flow rates on the polyatomic interferences in a blank solution (Fig. 3.5).

Introduction of H_2 has larger effects on $ArOH^+$ (mass 57) than on ArO^+ (mass 56). $ArOH^+$ interferences were completely removed with a H_2 flow rate of 2 mL/min.

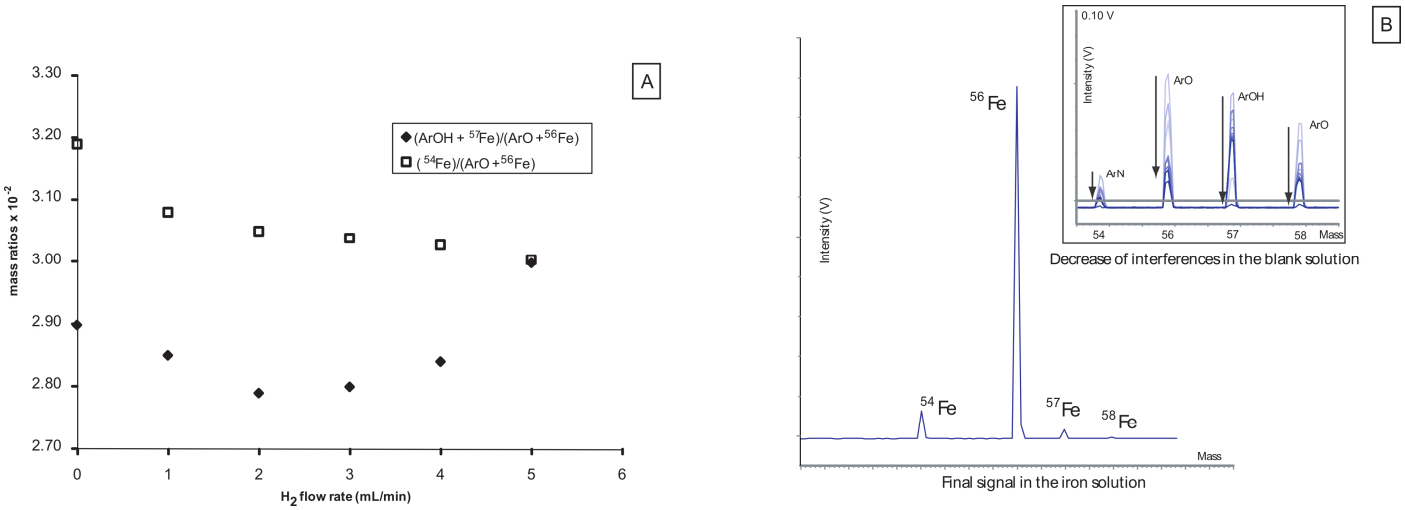

Figure 3.5: A: Influence of the H_2 flow rate on polyatomic interferences. Ar flow rate is set at 1.8 mL/min. B: Resulting Fe isotope spectrum after the decrease of the interferences.

3.3.5. Fe isotope analysis of synthesised iron-sulfide minerals

The procedure described above was applied to the analysis of synthetic iron sulphide species and $Fe(II)_{aq}$. Samples were standard bracketed with IRMM-014 and the precision was given by the external standard J.T.Baker Fe solution ($\delta^{56}Fe$ = -0.23 ± 0.05 ‰ and $\delta^{57}Fe$ -0.35 ± 0.12 ‰, Fig. 3.6). Marechal *et al.* (1999) demonstrated that Zn mass bias on their VG Plasma 54 instrument was best fitted with an exponential law. In the case of Fe, the expected mass bias slopes obtained with the power and the exponential laws are given respectively by Eqs. 3.4 and 3.5 (Albarede and Beard, 2004):

$$slope_{56/54}^{57/54} = \frac{M_{57Fe} - M_{54Fe}}{M_{56Fe} - M_{54Fe}} = 1.501 \qquad (3.4)$$

$$slope_{56/54}^{57/54} = \frac{\ln(M_{57Fe} / M_{54Fe})}{\ln(M_{56Fe} / M_{54Fe})} = 1.488 \qquad (3.5)$$

where M is the atomic mass of the nuclide.

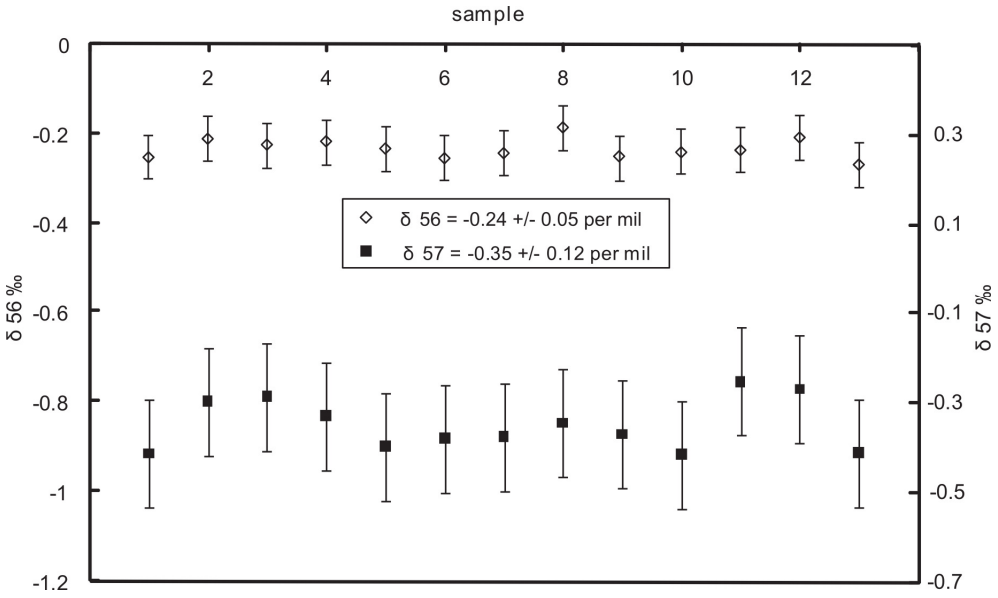

Figure 3.6: External precision given by the reproducibility of the measurement of a standard.

Our raw measurements all plot on the same mass fractionation line in a $\ln(^{57}Fe/^{54}Fe)$ versus $\ln(^{56}Fe/^{54}Fe)$ graph (Fig. 3.7), with a slope of 1.549 ± 0.003 which is consistent with Fe isotope mass difference. When standard-bracketing corrected, our data ($\delta^{56}Fe$ and $\delta^{57}Fe$) plot on the terrestrial mass fractionation line with a slope of 1.52 ± 0.02 (Fig. 3.8). Our experimental work on synthesised FeS and FeS_2 from $Fe(II)_{aq}$ shows large Fe isotope fractionations. These results are preliminary and further experimental data are needed.

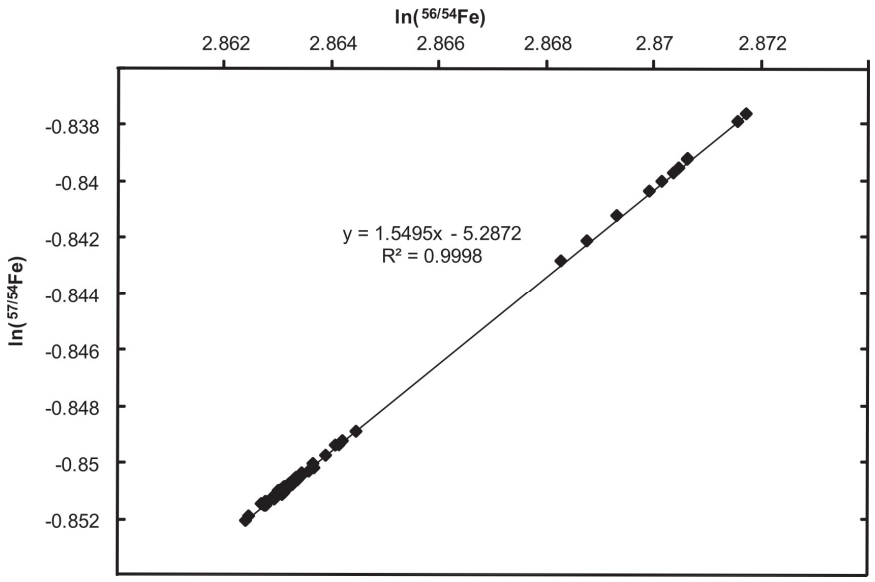

Figure 3.7: log-log plot of the row data. Error bars are included in the data point.

3.4. Conclusion

We have developed a procedure for the analysis of $^{56}Fe/^{54}Fe$ and $^{57}Fe/^{54}Fe$ ratios on a hexapole collision cell MC-ICP-MS with a precision of ± 0.05 ‰ and ± 0.12 ‰ (2σ) for $\delta^{56}Fe$ and $\delta^{57}Fe$ respectively. This precision was achieved maximising the signal-to-background ratio by using high-concentration samples (3 to 10 ppm) and introducing Ar and H_2 gases into the hexapole collision cell. On our instrument, precise measurements are more readily achieved using hard extraction, although in this mode the ArO^+ interference at mass 56 was not entirely removed. However, in hard extraction mode the instrument showed relatively stable mass bias characteristics that allow the phenomenon to be corrected by sample-standard bracketing. In soft extraction mode we observed temporal instability in mass bias to the extent that sample-standard bracketing does not provide a reliable mass bias correction.

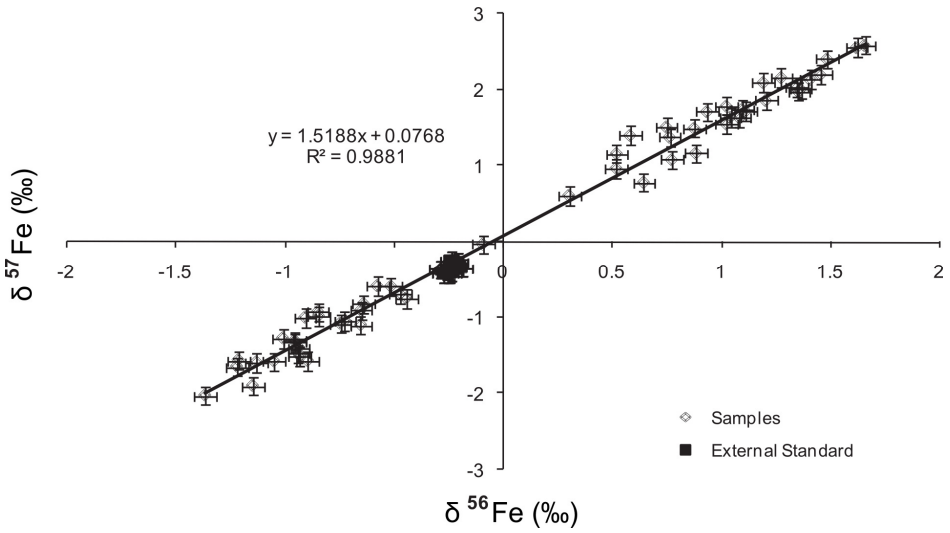

Figure 3.8: plot of $\delta^{57}Fe$ versus $\delta^{56}Fe$ for iron sulphide species. Error bars are given by the reproducibility 2 SD of the external standard.

3.5. Acknowledgements

We thank Marek Pękala, Valérie Olive, Corey Archer and Matthew Thirlwall for constructive discussions. This work was supported by an ECOSSE PhD studentship to RG and NERC research grant NE/E003958/1 to IBB.

3.6. References

Albarede, F., Beard, B., 2004. Analytical Methods for Non-Traditional Isotopes. Reviews in Mineralogy & Geochemistry 55, 113-152.

Anbar, A., Roe, J., Barling, J., Nealson, K., 2000. Nonbiological fractionation of iron isotopes. Science 288, 126-128.

Anders, E., Grevesse, N., 1989. Abundances of the elements: Meteoritic and solar. Geochim. Cosmochim. Acta 53, 197-214.

Archer, C., Vance, D., 2004. Mass discrimination correction in multiple-collector plasma source mass spectrometry: an example using Cu and Zn isotopes. J. Anal. At. Spectrom 19, 656-665.

Archer, C., Vance, D., 2006. Coupled Fe and S isotope evidence for Archean microbial Fe(III) and sulfate reduction. Geology 34, 153-156.

Arnold, G., Weyer, S., Anbar, A., 2004. Fe Isotope Variations in Natural Materials Measured Using High Mass Resolution Multiple Collector ICPMS. Analytical Chemistry 76, 322-327.

Arnold, T., Harvey, J., Weiss, D., 2008. An experimental and theoretical investigation into the use of H2 for the simultaneous removal of ArO+ and ArOH+ isobaric interferences during Fe isotope ratio analysis with collision cell based Multi-Collector Inductively Coupled Plasma Mass Spectrometry. Spectrochimica Acta Part B: Atomic Spectroscopy 63, 666-672.

Beard, B., Johnson, C., 1999. High precision iron isotope measurements of terrestrial and lunar materials. Geochim. Cosmochim. Acta 63, 1653-1660.

Beard, B., Johnson, C., Skulan, J., Nealson, K., Cox, L., Sun, H., 2003. Application of Fe isotopes to tracing the geochemical and biological cycling of Fe. Chem. Geol. 195, 87-117.

Belshaw, N., Zhu, X., Guo, Y., O'Nions, R., 2000. High precision measurement of iron isotopes by plasma source mass spectrometry. Int. J. Mass Spectrom 197, 191-195.

Bullen, T., McMahon, P., 1998. Using stable Fe isotopes to assess microbially-mediated Fe3+ reduction in a jet-fuel contaminated aquifer. Mineral. Mag. 62A, 255-256.

Butler, I., Archer, C., Vance, D., Oldroyd, A., Rickard, D., 2005. Fe isotope fractionation on FeS formation in ambient aqueous solution. Earth and Planet. Science Letters 236.

Dauphas, N., 2007. Diffusion-driven kinetic isotope effect of Fe and Ni during formation of the Widmanstaetten pattern. Meteoritics Planet. Sci. 42, 1597-1614.

Dauphas, N., Janney, P., Mendybaev, R., Wadhwa, M., Richter, F., Davis, A., van Zuilen, M., Hines, R., Foley, C., 2004. Chromatographic separation and multicollection-ICPMS analysis of iron. Investigating mass dependent and -independent isotope effects. Anal. Chem. 76, 5855-5863.

Dauphas, N., Pourmand, A., Teng, F., 2009. Routine isotopic analysis of iron by HR-MC-ICPMS: How precise and how accurate? Chemical Geology 267, 175-184.

Gotz, A., Heumann, K., 1988. Iron isotope ratio measurements with the thermal ionization technique using a compact quadrupole mass-spectrometer. int. J. Mass Spectrom. Ion Proc. 83, 319-330.

Halliday, A., Lee, D., Christensen, J., Rehkamper, M., Li, W., Luo, X., Hall, C., Ballentine, C., Pettlee, T., Stirling, C., 1998. Applications of multiple collector ICPMS to cosmochemistry, geochemistry and paleoceanography. Geochim. Cosmochim. Acta 62, 919-940.

Johnson, C., Beard, B., 1999. Correction of instrumentally produced mass fractionation during isotopic analysis of Fe by thermal ionization mass spectrometry. int. J. Mass Spectrom. Ion Proc. 193, 87-99.

Johnson, C., Skulan, J., Beard, B., Sun, H., Nealson, K., Braterman, P., 2002. Isotopic fractionation between Fe(III) and Fe(II) in aqueous solutions. Earth and Planetary Science Letters 195, 141-153.

Kehm, K., Hauri, E., Alexander, C., Carlson, R., 2003. High precision iron isotope measurements of meteoritic material by cold plasma ICPMS. Geochim Cosmochim Acta 67.

Ludwig, K., 1986. Constraints in time efficient data-taking strategies for single-collector isotope-ratio mass spectrometers. U.S.G.S. Bull. 1622, 219-221.

Marechal, C., Telouk, P., Albarede, F., 1999. Precise analysis of copper and zinc isotopic compositions by plasmasource mass spectrometry. Chem. Geol. 156, 251-273.

Mullane, E., Russell, S., Gounelle, M., Mason, T., Din, V., Weiss, D., Coles, B., 2003. Precise and accurate determination of iron isotopes by multi-collector inductively coupled plasma mass spectrometry. In plasma source mass spectrometry: Applications and emerging technologies. London: The Royal Society of Chemistry. 351-361.

Poitrasson, F., Freydier, R., 2005. Heavy iron isotope composition of granites

determined by high resolution MC-ICP-MS. Chemical Geology 222, 132-147.

Richter, F., Dauphas, N., Teng, F., 2009. Non-traditional fractionation of non-traditional isotopes: Evaporation, chemical diffusion and Soret diffusion. Chemical Geology 258, 92-103.

Roe, J., Anbar, A., Barling, J., 2003. Nonbiological fractionation of Fe isotopes: Evidence of an equilibrium isotope effect. Chem. Geol. 195.

Roskosz, M., Luais, B., Watson, H.C., Toplis, M.J., Alexander, C.M., Mysen, B.O., 2006. Experimental quantification of the fractionation of Fe isotopes during metal segregation from a silicate melt. Earth and Planetary Science Letters 248, 851-867.

Rouxel, O., Dobbek, N., Ludden, J., Fouquet, Y., 2003. Iron isotope fractionation during oceanic crust alteration. Chem. Geol. 202, 155-182.

Schoenberg, R., von Blanckenburg, F., 2005. An assessment of the accuracy of stable Fe isotope ratio measurements on samples with organic and inorganic matrices by high-resolution multicollector ICP-MS. International Journal of Mass Spectrometry 242, 257-272.

Severmann, S., Johnson, C., Beard, B., McManus, J., 2006. The effect of early diagenesis on the Fe isotope compositions of porewaters and authigenic minerals in continental margin sediments. Geochim Cosmochim Acta 70, 2006–2022.

Shahar, A., Young, E., Manning, C., 2008. Equilibrium high-temperature Fe isotope fractionation between fayalite and magnetite: An experimental calibration. Earth and Planet. Science Letters 268, 330–338.

Sharma, M., Polizzotto, M., Anbar, A., 2001. Iron isotopes in hot springs along the Juan de Fuca Ridge. Earth. Planet. Sci. Lett. 194.

Taylor, P., Maeck, R., De Bievre, P., 1992. Determination of the absolute isotopic composition and atomic weight of a reference sample of natural iron. Int. J. Mass Spectrom. Ion Proc. 121, 111-125.

Thirlwall, M., Anczkiewicz, R., 2004. Multidynamic isotope ratio analysis using MC-ICP-MS and the causes of secular drift in Hf, Nd and Pb isotope ratios. International Journal of Mass Spectrometry 235, 59-81.

Thompson, A., Ruiz, J., Chadwick, O., Titus, M., Chorover, J., 2007. Rayleigh fractionation of iron isotopes during pedogenesis along a climate sequence of Hawaiian basalt. Chemical Geology 238, 72-83.

Valley, G., Anderson, H., 1947. A comparison of the abundance ratios of the isotopes of terrestrial and of meteoritic iron. J. Am. Chem. Soc. 69, 1871-1875.

Vogl, J., Klingbeil, P., Pritzkow, W., Riebe, G., 2003. High accuracy measurements of Fe isotopes using hexapole collision cell MC-ICP-MS and isotope dilution for certification of reference materials. Journal of Analytical Atomic Spectrometry 18, 1125 - 1132.

Walczyk, T., 1997. Iron isotope ratio measurements by negative thermal ionisation mass spectrometry using FeF4-molecular ions. int. J. Mass Spectrom. Ion Proc. 161, 217-227.

Walczyk, T., von Blanckenburg, F., 2002. Natural Iron Isotope Variations in Human Blood. Science 295, 2065 - 2066.

Walder, A., Freedman, P., 1992. Isotope ratio measurements using a double focusing magnetic sector mass analyser with an inductively coupled plasma ion source. J. Anal. At. Spectrom 7, 571.

Walder, A., Platzner, A., Freedman, P., 1993. Isotope ratio measurements of lead, neodymium and neodymium–samarium, hafnium–lutetium mixtures with a double focusing multiple collector mass spectrometer. J. Anal. At. Spectrom 8.

Weyer, S., Schwieters, J., 2003. High precision Fe isotope measurements with high mass resolution MC-ICP-MS. Int. J. Mass Spectrom. Ion Proc. 226, 355-368.

Chapter IV

Fe isotope exchange between $Fe(II)_{aq}$ and nanoparticulate mackinawite (FeS_m) during nanoparticle growth

Article published as Guilbaud, R., Butler, I.B., Ellam, R.M., Rickard, D., 2010. Fe isotope exchange between Fe(II)aq and nanoparticulate mackinawite (FeSm) during nanoparticle growth. Earth and Planetary Science Letters 300, 174-183.

Abstract

We detail the results of an experimental study on the kinetics of Fe isotope exchange between aqueous $Fe(II)_{aq}$ and nanoparticulate mackinawite (FeS_m) at 25°C and 2°C over a one month period. The rate of isotopic exchange decreases synchronously with the growth of FeS_m nanoparticles. 100% isotopic exchange between bulk FeS_m and the solution is never reached and the extent of isotope exchange asymptotes to a maximum of ~ 75 %. We demonstrate that particle growth driven by Ostwald ripening would produce much faster isotopic exchange than observed and would be limited by the extent of dissolution-recrystallisation. We show that Fe isotope exchange kinetics are consistent with i) FeS_m nanoparticles that have a core-shell structure, in which Fe isotope mobility is restricted to exchange between the surface shell and the solution and ii) a nanoparticle growth *via* an aggregation-growth mechanism. We argue that because of the structure of FeS_m nanoparticles, the approach to isotopic equilibrium is kinetically restricted at low temperatures. FeS_m is a reactive component in diagenetic pyrite forming systems since FeS_m dissolves and reacts to form pyrite. Isotopic mobility and potential equilibration between FeS_m and $Fe(II)_{aq}$ thus have direct implications for the ultimate Fe isotope signature recorded in sedimentary pyrite.

Keywords: Fe isotopes, FeS, mackinawite, pyrite, nanoparticle growth.

4.1. Introduction

The omnipresence and utility of nanoparticles in bio- and geological systems make them the focus of various applications. For example, their role is important in industry (for their magnetic and electronic properties *e.g.* Alivisatos, 1996), in surface reactivity and environmental remediation (*e.g.* Charlet and Manceau, 1992, Luther and Rickard, 2005), for biochemistry (as components, along with clusters, of molecules, *e.g.* Harrison and Dutriazac, 1998) and perhaps in pre-biotic chemistry and the emergence of early life (*e.g.* Russell *et al.*, 1998; Martin and Russell, 2003). The study of the structure and the properties of natural nanoparticulate materials is difficult to access with conventional methods because of the size of the domain (< 100 nm). Nanoparticles differ from bulk materials because of their extreme surface-to-volume ratio. Nanoparticle surface characteristics are therefore critical to understanding the physicochemical behaviour of nanoparticulate material. The surface properties of metal sulphide nanoparticles have been characterised, and in particular those of FeS (*e.g.* Wolthers *et al.*, 2004), ZnS (*e.g.* Zhang *et al.*, 2003) and NiS (*e.g.* Huang *et al.*, 2009). In each case a surface zone with different physical and chemical properties to the core has been defined. Huang et al (2009) described this as a core-shell model by analogy with synthesised quantum dots (*e.g.* Chen and Rosenzweig, 2002) which have different materials in the core and the shell. The shell is crystallographically disordered whereas the core is crystalline with properties similar to the bulk material. In the case of the sulphide nanoparticles formed in aqueous media, such differences between the core and the shell can be due to the presence of water in a hydrated shell (as for NiS), or to interactions with the media for anhydrous materials as ZnS. By analogy, a similar effect to ZnS can be supposed for FeS since it is also anhydrous (Rickard *et al.*, 2006).

A consequence of this core-shell structure is that crystal growth of nanoparticles may proceed by a different process to that normally associated with the bulk material. In bulk crystals, crystal growth commonly occurs through the diffusion of nutrient monomers to the surface in a molecule-by-molecule process. This mechanism leads to Ostwald ripening where the driving force for crystal growth is the decrease in surface free energy (*e.g.* Steefel and Van Cappellen, 1990). In the case of nanoparticles however, crystal growth may occur by crystallographically controlled aggregation of the particles which is enabled by the surface chemistry but driven similarly by a decrease in surface free energy (*e.g.* Waychunas *et al.*, 2005). This process differs

from conventional particle aggregation where particles come together independently of crystallographic orientation and usually remain as discrete entities. Aggregation-growth has been demonstrated for a number of geologically relevant materials by Banfield and co-workers (*e.g.* Banfield et al 2000; Penn and Banfield 1998; Penn and Banfield, 1999; Penn *et al.*, 2001; Banfield and Zhang, 2001; Zhang and Banfield, 2004). The process has been expanded for transition metal sulphides by Luther and Rickard and their co-workers (Luther *et al.*, 1999, 2002; Rickard and Luther, 2006) to include the involvement of aqueous clusters of metal sulphides in the nucleation process.

The aggregation-growth mechanism for the growth of nanoparticles has wide consequences for the chemical behaviour of nanoparticles in solution. Chemically, aggregation-growth involves exchanges with the shell or surface phase whilst the crystalline core remains less affected. In the case of Ostwald ripening, smaller crystalline particles dissolve and larger particles grow, which means that there is a greater degree of exchange between the condensed phase and the solution. In this paper, we report the results of an investigation into the kinetics of Fe isotope exchange between nanoparticulate mackinawite (referred as FeS_m in the text) and aqueous Fe(II) solutions at 25°C and 2°C under ambient pressure. We followed similar experimental procedures to those from Butler *et al.* (2005). They showed that FeS_m precipitates lighter isotopes from $Fe(II)_{aq}$ with $\Delta^{56}Fe_{Fe(II)\text{-}FeS}$ varying from 0.85 ± 0.30 ‰ to 0.34 ‰. Here, we examine the kinetics of this exchange and, in a novel approach, we probe the growth of FeS_m nanoparticles using Fe isotope exchange to distinguish between alternate growth mechanisms.

4.2. Experimental methods

A portion of a Fe(II) solution was precipitated as FeS_m nanoparticles and grown *in situ* at different temperatures and for different periods. Solids and liquid were then separated for Fe isotope analysis and the determination of the fractionation $\Delta^{56}Fe_{Fe(II)\text{-}FeS}$.

4.2.1. Reagents

All reagents and acids were of analytical grade and solutions were prepared in a glove-box using 18.2 MΩcm deionised water, purged with O_2 free grade N_2 for 30 min (Butler *et al.*, 1994). Iron(II) solutions were made by dissolution of Mohr's salt

$Fe(NH_4)_2(SO_4)_2.6H_2O$ (Sigma Aldrich™) in purged water. Mohr's salt was used for its ability to resist oxidation in solution. Sulphide solutions were made by dissolution of $Na_2S.9H_2O$ (Sigma Aldrich™) in purged water. Long term 25°C experiments were performed at the University of Edinburgh under oxygen free conditions in a N_2-filled re-circulating Saffron alpha® anoxic chamber. Short term 25°C and 2°C experiments were performed at Cardiff University under oxygen free conditions (<1 ppmv O_2) in an MBraun Labmaster 130® re-circulating anoxic chamber.

4.2.2. Procedure

4.2.2.1. Isotopic exchange at 25°C and 2°C

In serum bottles, 10 mL 0.05 M S(-II) solution was injected into 100 mL 0.05 M Fe(II) solution to precipitate 10 % of Fe as FeS_m. 90 % of Fe remains dissolved in solution as calculated from the solubility data for mackinawite (Rickard, 2006) in PHREEQC Interactive 2.15.0®. After ageing, flocculation of FeS_m permits the solid phase to be separated from liquids by vacuum filtration with a 0.45 µm membrane Millipore™ filter. With this filter size, filtrates were clear and filters did not clog. Any isotopic contamination from small particles in the filtrate would be undetectable within analytical error because of the large Fe(II) concentration in solution. Once taken out of the glove-box, solid products were dissolved in concentrated HCl and filtrate solutions were acidified with a few drops of concentrated HCl pending Fe isotope analysis.

For 2°C experiments, Fe(II) solutions and S(-II) solutions were prepared and sealed in serum bottles in the glove-box. Serum bottles were placed at 2°C in Haake F6/C25 and Haake DC10/K10 refrigerated circulators. Once the temperature was down to 2°C, 10 mL 0.05 M S(-II) solution was injected with a hypodermic syringe into 100 mL 0.05 M Fe(II) solution to precipitate 10 % of Fe as FeS_m. After ageing, serum bottles were re-introduced into the glove-box for rapid filtration as for the 25°C experiment. Once taken out of the glove-box, solid products were dissolved in concentrated HCl and filtrates were acidified with a few drops of concentrated HCl pending Fe isotope analysis.

4.2.2.2. Mackinawite growth

FeS_m was precipitated and collected as described for the 25°C isotopic exchange experiment. After filtration, the solid phases were freeze-dried using a Mini-Lyotrap

(LTE®) freeze-dryer. In the glove-box, 0.1 g of freeze-dried FeS_m was loaded onto a metal support (Al). The sample was sealed within an environmental sample holder under N_2 and taken out of the glove-box for immediate XRD characterisation. A further series of experiments on FeS_m growth kinetics were carried out at higher nutrient concentrations (Wolthers *et al.*, 2003; Ohfuji and Rickard, 2006). FeS_m was precipitated by adding 10 mL 0.6 M S(-II) solution in 100 mL 0.6 Fe(II) solution. After ageing, FeS_m was filtered, washed and freeze-dried before XRPD analysis. Both series of experiments gave similar results within experimental error.

4.3. Analytical methods

4.3.1. Isotope ratios analysis

Samples (Fe(III) in HCl) were taken to dryness and re-dissolved in 5% HNO_3. No column chemistry was performed since our samples were experimentally synthesised from analytical grade reagents. $^{56/54}$Fe and $^{57/54}$Fe isotope ratios were measured on a GV IsoProbe (formerly Micromass) multi-collection inductively coupled mass spectrometer (MC-ICP-MS). The detailed analytical protocol has been described elsewhere (Guilbaud et al, 2010). The major challenge for accurate and precise measurement of Fe isotopes is the removal of atomic and polyatomic interferences induced by the Ar plasma. This was achieved by increasing the signal-to-background ratio (using high concentration samples and introducing collision gases into the hexapole to decrease and/or remove the interferences) and by stabilising the instrumental mass bias minimising the hexapole potential and decreasing the extraction voltage.

3-10 ppm Fe solutions were introduced into an ApexQ inlet system at 50 µL min^{-1} to maximise the signal to ~0.3 V on mass 54, ~6 V on mass 56 and ~0.02 V on mass 57. Hexapole rf amplitude was set at 50% which enhances transmission of Fe masses. The analysis was run in hard extraction mode (-250 V). 1.8 mL min^{-1} Ar and 2 mL min^{-1} H_2 were introduced into the hexapole collision cell to completely remove ArN^+ on mass 54 and $ArOH^+$ on mass 57 and to decrease ArO^+ on mass 56 to 0.006 V which represents 0.1% of the Fe peak. Cr^+ interferences on mass 54 were monitored on mass 52 but never detected. Instrumental mass bias was corrected by bracketing each sample with a standard and Fe isotope results are presented conventionally using the δ^{56}Fe and δ^{57}Fe notations in ‰ IRMM-014 (Eqs. 4.1 and 4.2):

$$\delta^{56}Fe = \left(\frac{(^{56}Fe/^{54}Fe)sample}{(^{56}Fe/^{54}Fe)IRMM} - 1 \right) \times 10^3 \qquad (4.1)$$

$$\delta^{57}Fe = \left(\frac{(^{57}Fe/^{54}Fe)sample}{(^{57}Fe/^{54}Fe)IRMM} - 1 \right) \times 10^3 \qquad (4.2)$$

The precision of our measurements was obtained from the standard deviation (at the 2σ level) of the repeated measurement (n = 10) of an external standard Fe solution. The precision was ± 0.1 ‰ and ± 0.15 ‰ (2σ) for δ^{56}Fe and δ^{57}Fe respectively. Experimental error was monitored with independent replicate experiments.

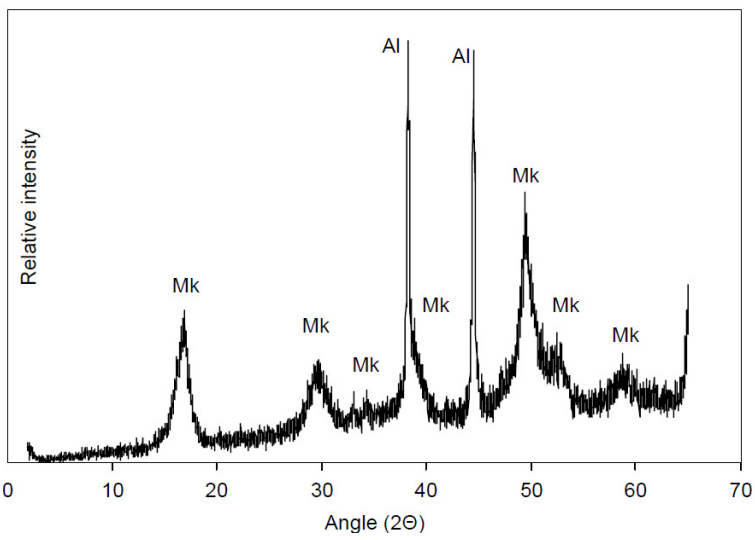

Aluminium anoxic sample holder

Figure 4.1: XRD scan for 7 days aged mackinawite (Mk). Al peaks are the background response from the aluminium sample holder.

4.3.2. XRD analysis

The environmental holder containing the sample was loaded on a Bruker D8 Advance Diffractometer (for the experiments starting with 0.05 M solutions) and on a Phillips PW1840 Diffractometer (for the experiments starting with 0.6 M solutions). XRD analysis was performed using Cu*K*α primary radiation generated at an accelerating voltage of 40KV in the range of 2-65° 2θ with a 1s/0.02° 2θ counting time. The diffracted X-rays were recorded by a Sol-x™ energy dispersive detector. Data were filtered to remove Cu*K*αII peaks. We used the Scherrer equation (Eq. 4.3) on the 16° 2θ peak to determine the average diameter of the crystalline size:

$$L = K\lambda(\beta \cos\theta)^{-1} \qquad (4.3)$$

where L is the size of the domain, K is 0.91 (Brindley 1980), λ is the wavelength of the X-ray (0.154 nm for Cu$K\alpha$), β is the full width of the peak at half maximum (FWHM, in radian) and θ is the angle of the peak. The Scherrer equation has been previously used to determine average domain size on FeS_m (Wolthers *et al.*, 2003, Jeong *et al.*, 2008) and on ZnS (Huang *et al.*, 2003) nanoparticles. In these previous studies, crystal sizes given by the Scherrer equation were checked and confirmed by high-resolution transmission electron microscopy (for review and discussion, see Rickard and Luther, 2007, p 534). Fig. 4.1 shows a typical spectrum for mackinawite, with the aluminium background peaks from the capsule. Precision on L was determined by measuring the same sample ten times, and was ± 0.7 nm (2σ).

4.4. Results

4.4.1. Fractionation factors

All experimental settings and isotope results are listed in Table 4.1.

Experimental quality control is established by monitoring the mass conservation law. At any time, the product of the fraction f and the isotopic signature (the mass) of each phase should equal the isotopic signature of the starting material. The Mohr's salt used for the Fe(II) solution has a $\delta^{56}Fe = 0.25‰$ (Eq. 4.4 and Fig. 4.2):

$$\left(f \times \delta^{56} Fe_{Fe(II)}\right) + \left((1-f) \times \delta^{56} Fe_{FeS}\right) = 0.25 \qquad (4.4)$$

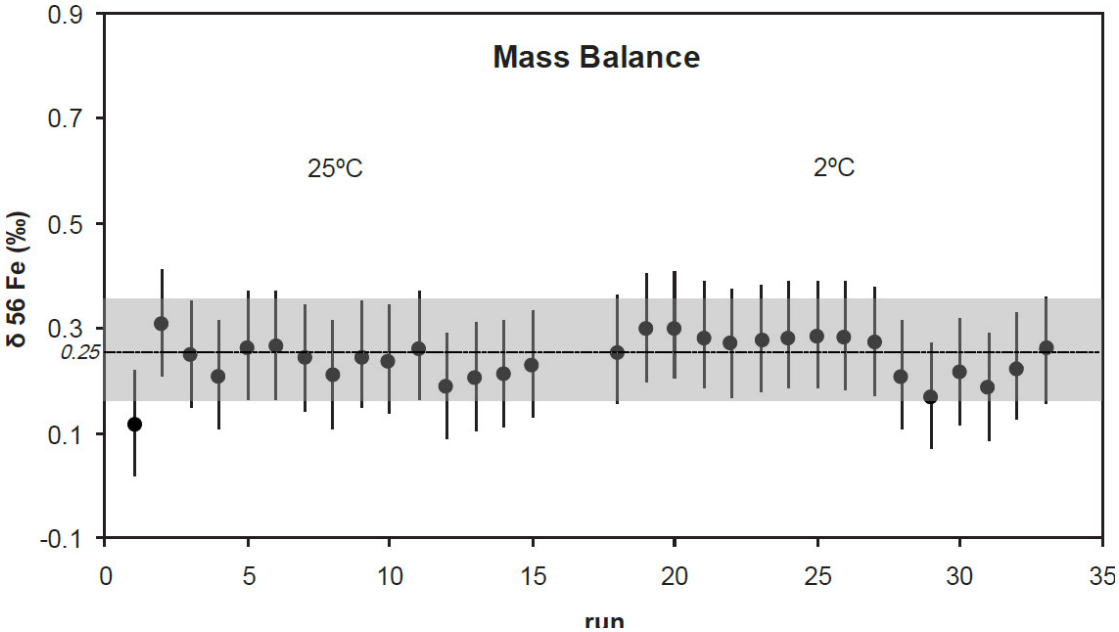

Figure 4.2: Experimental mass balance calculated from Eq. 4.4. The grey area represents the analytical uncertainty on an ideal experimental mass balance. The error bars represent the 2σ analytical precision.

	Sample	Experiental duration	δ^{56} Fe Fe(II) ‰	δ^{57} Fe Fe(II) ‰	δ^{56} Fe FeSm ‰	δ^{57} Fe FeSm ‰	Δ^{56} Fe(II)-FeSm ‰	mass balance	ξ
25°C experiment	K25-1-A	5 min	0.54	0.76	-0.63	-0.93	1.17	0.12	0.00
	K25-1-B	5min	0.40	0.43	-0.47	-0.56	0.86	0.31	0.18
	K25-2-A	15 min	0.33	0.34	-0.43	-0.60	0.76	0.25	0.22
	K25-2-B	15 min	0.28	0.29	-0.43	-0.41	0.71	0.21	0.22
	K25-3-A	60 min	0.34	0.24	-0.37	-0.55	0.70	0.27	0.30
	K25-3-B	60 min	0.34	0.27	-0.37	-0.41	0.70	0.27	0.30
	K25-4-A	120 min	0.30	0.23	-0.30	-0.41	0.60	0.24	0.37
	K25-4-B	120 min	0.27	0.19	-0.32	-0.40	0.59	0.21	0.35
	K25-5-A	240 min	0.29	0.20	-0.11	-0.16	0.40	0.25	0.59
	K25-6-A	480 min	0.28	0.30	-0.11	-0.15	0.39	0.24	0.59
	K25-6-B	480 min	0.31	0.34	-0.11	-0.12	0.41	0.27	0.60
	K25-7-A	1440 min	0.22	0.23	-0.07	-0.10	0.29	0.19	0.63
	K25-8-A	2880 min	0.24	0.21	-0.05	-0.01	0.29	0.21	0.66
	K25-9-A	8640 min	0.23	0.17	0.03	0.03	0.21	0.21	0.75
	K25-10-A	38820 min	0.25	0.19	0.03	0.03	0.23	0.23	0.75
2°C experiment	K2-1-A	7 min	0.35	0.48	-0.58	-0.74	0.93	0.26	0.06
	K2-2-A	10 min	0.38	0.45	-0.44	-0.53	0.82	0.30	0.21
	K2-2-B	10 min	0.40	0.49	-0.56	-0.71	0.96	0.31	0.07
	K2-3-A	30 min	0.37	0.47	-0.46	-0.40	0.83	0.29	0.19
	K2-3-B	30 min	0.35	0.47	-0.47	-0.42	0.82	0.27	0.18
	K2-4-A	60 min	0.36	0.46	-0.47	-0.43	0.83	0.28	0.18
	K2-5-A	120 min	0.36	0.48	-0.41	-0.65	0.77	0.29	0.25
	K2-6-A	240 min	0.35	0.46	-0.29	-0.54	0.64	0.29	0.39
	K2-7-A	480 min	0.34	0.42	-0.20	-0.38	0.54	0.29	0.48
	K2-8-A	1450 min	0.33	0.45	-0.21	-0.41	0.54	0.27	0.47
	K2-9-A	8640 min	0.25	0.48	-0.19	-0.33	0.44	0.21	0.50
	K2-9-B	8640 min	0.22	0.38	-0.23	-0.39	0.45	0.17	0.45
	K2-10-A	25920 min	0.25	0.46	-0.06	-0.06	0.31	0.22	0.64
	K2-10-B	25920 min	0.22	0.36	-0.12	-0.23	0.35	0.19	0.58
	K2-11-A	43200 min	0.25	0.36	-0.01	-0.01	0.26	0.23	0.71
	K2-11-B	43200 min	0.29	0.36	-0.05	-0.10	0.34	0.26	0.66
							Mean	0.25	
							2σ	± 0.09	

External standard (Baker) ‰

δ^{56} Fe	δ^{57} Fe
-0.35	-0.52
-0.28	-0.37
-0.27	-0.36
-0.17	-0.28
-0.20	-0.23
-0.19	-0.31
-0.17	-0.34
-0.20	-0.27
-0.25	-0.28
-0.27	-0.29
Mean -0.24	-0.33
2σ ± 0.1	± 0.15

Mackinawite growth (XRD analysis)

time	FWHL (Å)	mean particle diameter (nm)
5 min	2.322	3.5
15 min	2.017	4.1
30 min	2.151	3.8
100 min	1.850	4.5
100 min	2.022	4.0
300 min	1.621	5.0
500 min	1.766	4.7
1440 min	1.678	4.8
2880 min	1.621	5.0
3000 min	1.615	5.0
10080 min	1.590	5.1
30000 min	1.538	5.3
	1σ	± 0.3

Table 4.1: Experimental conditions and isotope analysis. Analytical precision is the 2 standard deviation (2σ) of the external standard (Baker™). The isotopic mass balance is calculated by Eq. 4.4. ξ is the extent of isotope exchange towards the bulk composition (Eq. 4.5).

All precipitated FeS_m products are ^{56}Fe depleted and solutions are ^{56}Fe enriched (Fig. 4.3). Zero-aged (effectively 5min) fractionation between Fe(II) and FeS_m is 1.17 ± 0.16‰ at 25°C and 0.98 ± 0.16‰ at 2°C. Fractionations decrease with ageing time to 0.23 ± 0.11‰ and 0.34 ± 0.11‰ at 25°C and 2°C respectively. After ageing between 10 and 30 days the fractionation is stable at 0.27 ± 0.11‰ for both experimental sets. Within error, there is no fractionation difference between 25°C and 2°C, and the results are consistent with the fractionations measured by Butler *et al.* (2005).

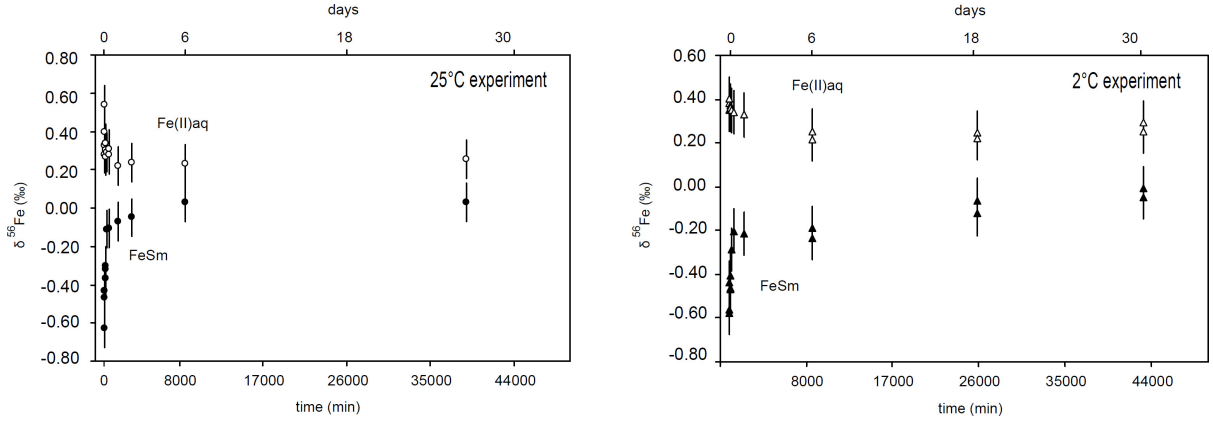

Figure 4.3: Evolution of the isotopic compositions of FeS_m (filled symbols) and $Fe(II)_{aq}$ (open symbols) at 25°C (circles) and 2°C (triangles) up to 1 month.

4.4.2. Rates and extent of isotopic exchange

We inspected the rates and extent of isotopic exchange in order to monitor the mobility of Fe atoms and the kinetics of exchange during particle growth. The fractional approach towards complete isotope homogenisation of the system was calculated using Eq. 4.5:

$$\xi = \frac{\delta^{56}Fe - \delta^{56}Fe_i}{\delta^{56}Fe_{bulk} - \delta^{56}Fe_i} \qquad (4.5)$$

where ξ is the extent of exchange towards the bulk composition (*i.e.* when the final composition of the phases equals the composition of the starting material), $\delta^{56}Fe$ is the composition of the phase at each time and the subscript *i* refers to the initial composition. This is different from the conventionally used *fractional approach*

towards equilibrium in the sense that isotopic equilibrium does not necessarily mean that 100 % of isotopes have exchanged. The use of Eq. 4.5 is discussed later.

In theory, ξ may be calculated using the δ value of either phase. In order to ensure the best constraints on ξ, we preferred to use the $\delta^{56}Fe_{FeS}$ data since if small FeS_m particles pass through the 0.45 µm filter during phase separation, $\delta^{56}Fe_{FeS}$ might bias $\delta^{56}Fe_{Fe(II)}$ leading to an apparent decrease of the Fe(II) isotope signature. However, our mass balanced results indicate that if any FeS_m particles had passed through the filter, it must have been in so small amounts that no $\delta^{56}Fe_{FeS}$ bias could be recorded above analytical precision in the $\delta^{56}Fe_{Fe(II)}$ signal. For the kinetics of isotope exchange towards the bulk composition, a general rate equation can be written (Eq. 4.6):

$$\frac{-d(1-\xi)}{dt} = k_n(1-\xi)^n \qquad (4.6)$$

where k is the rate constant and n the order of reaction. For a first-order rate reaction, Eq. 4.6 can be integrated into Eq. 4.7:

$$\ln(1-\xi) = -k_1 t \qquad (4.7)$$

Similarly for a second-order rate reaction, Eq. 4.6 can be integrated into Eq. 4.8:

$$\frac{\xi}{(1-\xi)} = k_2 t \qquad (4.8)$$

After integration into both a first-order or a second-order rate law, no single rate constant could fully describe the rate equation since ln(1- ξ) and ξ/(1- ξ) plots are not linear over time. Nonetheless, several changing rate constants can be calculated for different time periods (see below). For both the 25°C and 2°C experiments, the use of the second-order rate law was preferred since it systematically provided a better fit for a least square regression.

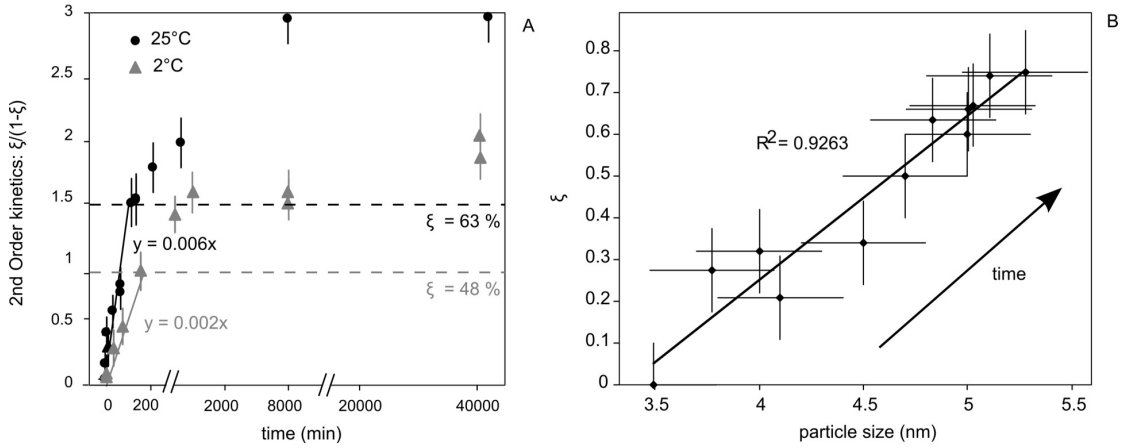

Figure 4.4: A. Rate of kinetic exchange for a second-order rate law (ξ /(1- ξ)) where ξ is the extent of isotope exchange (Eq. 4.6) at 25°C (black circles) and 2°C (grey triangles). The rate of exchange is approximately constant up to 240 min (25°C) and 480 min (2°C). B. Correlation between the evolution of particle size with time and the extent of isotopic exchange ξ (%) at 25°C. Errors on the particle size are 1σ.

At 25°C, (Fig. 4.4.A), the extent of isotopic exchange varies from 0 to 75± 12 %. During the first 240 min (where R^2 = 0.93 for a second-order rate law and R^2 = 0.78 for a first-order rate law), the second-order rate constant is 6 ± 1 x 10^{-3} min^{-1}. During this period, ξ varies from 0 to 63 ± 10 %. Between 240 and 8640 min (six days), the second-order rate constant decreases to 2 x 10^{-4} min^{-1} and finally approaches 0 after 8640 min, where 75 ± 12 % of Fe isotopes have exchanged between $Fe(II)_{aq}$ and FeS_m.

At 2°C, (Fig. 4.4.A), the extent of isotopic exchange varies from 0 to 71 ± 10 %. During the first 480 min (where R^2 = 0.90 for a second-order rate law and R^2 = 0.75 for a first-order rate law), the second-order rate constant is 2 ± 1 x 10^{-3} min^{-1}. During this period, ξ varies from 0 to 48 ± 8 %. After 480 min, the second-order rate constant decreases to 3 x 10^{-5} min^{-1}. At the end of the experiment (after 1 month), 71 ± 10 % of Fe isotopes have exchanged between Fe(II) and FeS_m.

4.4.3. Mackinawite growth

XRD results and mean particle size are presented in Table 4.2. The primary FeS_m particles precipitate with an average diameter of the crystalline domain *L* of 4.1 ± 0.7 nm. Techniques for FeS_m size determination were reviewed by Ohfuji and Rickard (2006) and Jeong *et al.* (2008). Wolthers *et al.* (2003) used the Scherrer equation for determining FeS_m particle sizes and Ohfuji and Rickard (2006) confirmed their

findings using transmission electron microscopy. They noted that the reason the Scherrer method appears to work at this domain size is unclear, but it may be related to the platy habit of the material. Within errors, our data compare well with the previously reported domain size for the first FeS_m precipitate (Wolthers *et al.*, 2003; Ohfuji and Rickard, 2006; Jeong *et al.*, 2008).

During the first 300 min, *L* rapidly increases from 4.1 to 4.7 ± 0.7 nm (Table 4.2). After 500 min, the average diameter of the FeS_m nanoparticles asymptotes at 5.3 ± 0.7 nm which represents a doubling of the volume based on a cubic particle. Fig. 4.4,B shows a direct correlation between the extent of isotope exchange and the particle size ($R^2 = 0.9263$), suggesting that changes in the rate of isotopic exchange and in the rate of particle growth are synchronous.

Mackinawite growth (XRD analysis)		
time	FWHL (Å)	mean particle diameter (nm)
5 min	2.322	3.5
15 min	2.017	4.1
30 min	2.151	3.8
100 min	1.850	4.5
100 min	2.022	4.0
300 min	1.621	5.0
500 min	1.766	4.7
1440 min	1.678	4.8
2880 min	1.621	5.0
3000 min	1.615	5.0
10080 min	1.590	5.1
30000 min	1.538	5.3
	1σ	± 0.3

Table 4.2: XRD results and mean particle size calculations. FWHL is the full width of the FeS_m (001) peak at half height in Å. L is calculated from Eq. 4.3.

4.5. Discussion: Fe isotope fractionation, crystal growth and isotopic exchange models

The Fe isotope fractionation between mackinawite and $Fe(II)_{aq}$ at time = 0 is 1.17 ± 0.16 ‰ at 25°C and 0.98 ± 0.16 ‰ at 2°C which, within error, is consistent with the fractionation determined by Butler *et al.* (2005) of 0.85 ± 0.30 ‰. After ageing between 10 and 30 days the fractionation is stable at 0.27 ± 0.11‰ for both experimental sets. Within experimental error, there is thus no observable temperature effect upon the fractionation. Butler *et al.* (2005) noted that kinetic fractionations are

often less temperature sensitive than equilibrium fractionations. However, the temperature has an effect on the rates of isotope exchange as shown in Fig. 4.3.

4.5.1. Mechanisms and kinetics of isotope exchange towards the bulk composition

The kinetics of isotope exchange are usually determined with enriched materials and conventionally integrated from the fractional approach to equilibrium *F* (Graham, 1981; Criss, 1999; Johnson *et al.*, 2002) described by Eq. 4.9:

$$F = \frac{\delta^{56}Fe - \delta^{56}Fe_i}{\delta^{56}Fe_{eq} - \delta^{56}Fe_i} \qquad (4.9)$$

where the subscripts *i* and *eq* stand for *initial* and *equilibrium*, respectively. When using isotopically enriched starting material, the value of the equilibrium $\delta^{56}Fe_{eq}$ (a few per mil) is negligible compared to the starting fractionation (a few hundred per mil) and replaceable by $\delta^{56}Fe_{final}$. In our case, the value of $\delta^{56}Fe_{eq}$ is unknown and perhaps not negligible with respect to the starting fractionation. For this reason, we described the fractional approach towards *100 % of atom exchange*, ξ using Eq. 4.5.

Our kinetic results show that several different second-order rate constants can be calculated for different portions of the reaction duration. The reason why second-order rate laws give the best fit to the data remains unclear. Rickard (1995) showed that the precipitation of FeS_m from aqueous Fe(II) involves two pH-dependant competing mechanisms. They reported an observed first-order rate constant for the reaction of Fe^{2+}_{aq} with H_2S_{aq} and an observed second-order rate constant for reaction of Fe^{2+}_{aq} and HS^-_{aq}. Pankow and Morgan (1980) reported that the rate of FeS_m dissolution is first-order under acidic conditions and depends on $\{H^+\}$. For the experimental acidic pH, the dominant dissolution-precipitation processes are characterised by first-order kinetics. The observed best fit by a second-order rate law may indicate dependence not only upon dissolution-precipitation, but also on a second factor, potentially the particle size and surface area. The significance of the rate law itself is secondary to the observation that the isotope exchange kinetics for our experiment cannot be described using a simple rate with a unique rate constant.

Varying rate constants can indicate a change in the experimental materials or conditions, and consequently a change in the mechanism of transformation. Kinetics and mechanisms for both FeS_m precipitation and dissolution are well established (Rickard, 1995; Pankow and Morgan, 1980). Any changes in mechanism are pH

dependent. During our experiments, there is no shift in pH, temperature, or total reactant concentrations. This means that for the rate constant to vary, physical changes (*i.e.* in the surface area) are most likely to be responsible for those shifts. FeS_m particle dimensions, specific surface area (SSA) and changes in crystal size with time have been documented (*e.g.* Ohfuji & Rickard, 2006; Jeong *et al.*, 2008 and Wolthers *et al.*, 2003). The main size of the domain we found with XRD analysis compare well with these authors' results. Microscale FeS_m aggregates (*e.g.* Butler & Rickard, 2000) consist of platy-structured nanoscale particles with large surface area as suggested by TEM and BET (Ohfuji & Rickard, 2006; Jeong *et al.*, 2008). The correlation between the nanoparticle average size and the isotopic exchange between the liquid and FeS_m (Fig. 4.4.B) suggests that the continuously altering kinetics of isotopic exchange are a function of nanoparticle growth during the experiment.

4.5.2. Ostwald ripening versus aggregation models

For the Ostwald ripening mechanism, the average grain size is given by (Eq. 4.10, Joesten, 1991):

$$D - D_0 = k(t - t_0)^{1/n} \qquad (4.10)$$

where D is the diameter, t the time (the subscript 0 meaning initial), k is a constant, and n an integer describing the physical mechanism, normally between $2 < n < 5$. When $n = 2$, the crystal growth is controlled by precipitation-dissolution along the particle/matrix interface; when $n = 3$, the growth is controlled by volume diffusion of ions in the matrix; when $n = 4$, crystal growth is controlled by diffusion on the grain/matrix interface; when $n = 5$, crystal growth is controlled by dislocation-pipe-diffusion, which is the atomic migration along or close to dislocations rather than through regular matrix. The parameters k and n can be extracted by taking the logarithm of Eq. 4.11:

$$\ln(D - D_0) = \ln k + \frac{1}{n}\ln(t - t_0) \qquad (4.11)$$

which describes a Y = b + aX type equation with a = 1/n and b = ln k. With our data, we found $k = 0.189 \pm 0.026$ min^{-1} and $n \approx 5.4$. The decimal value for n has no mechanistic meaning, we thus used $n = 5$ for our model. Interestingly, in the nanoparticulate FeS system one would expect the growth mechanism to be controlled by precipitation-dissolution, and thus n to be = 2. The parameter $n = 5$ would imply

the rather improbable scenario of FeS_m nanoparticle growth *via* the migration of atoms along dislocations.

Huang *et al.* (2003) developed a crystal growth model during the aggregation of near spherical nanoparticulate ZnS (Eq. 4.12):

$$D = \frac{D_0\left(\sqrt[3]{2}kt + 1\right)}{kt + 1} \qquad (4.12)$$

In this model nanoparticles grow via oriented aggregation, *i.e.* the attachment of the nanoparticle interface occurs according to the crystallographic structure of each particle (Fig. 4.5).

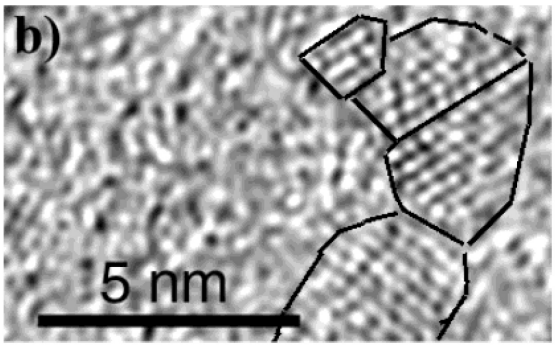

Figure 4.5: TEM image of oriented aggregation of multiple ZnS nanoparticle interfaces. The figure is from Huang et al. (2003).

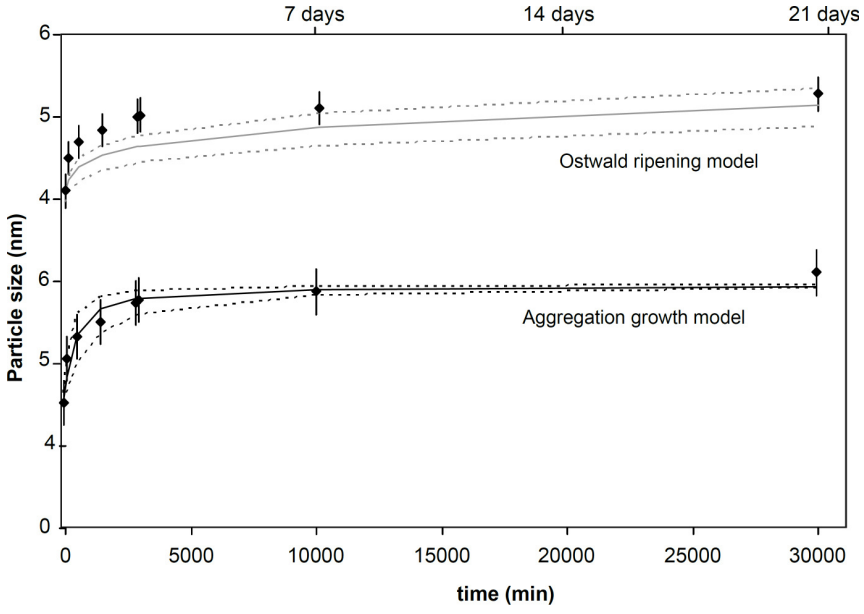

Figure 4.6: Comparison between our XRD results up to 21 days for the Ostwald ripening model (grey line) and the aggregation-growth model (black line). Dashed lines represent the uncertainties on the models. The Ostwald ripening model is calculated by Eq. 4.11 and the aggregation-growth model by Eq. 4.12. Error bars on the data are 1σ.

Fig. 4.6 compares the two models with our XRD average size data up to 21 days. Although the aggregation-growth model fits the data more closely, neither of the models can be strictly rejected, in particular in the region > 5000 min. Note that Eq. 4.12 describes the aggregation of spherical particles, and although the platy shape of FeS_m is likely to have major impacts on surface energy (Banfield and Zhang, 2001), effects on Eq. 4.12 are unknown. However, we tested each model by comparing the deviations from the data. We obtained the correlation coefficients of $R^2 = 0.91$ and $R^2 = 0.89$ for the aggregation model and the Ostwald ripening model, respectively. The root-mean-squared-error (RMSE) was applied for the upper and lower limits of the model and RMSE = 0.16 and 0.31 for the aggregation model and the Ostwald ripening model, respectively. These simple tests and the fact that we obtain an *n* value suggesting an unlikely mechanism ($n = 5$), make the aggregation-growth model our preferred model. No further discrimination between the models can be made based solely on our XRD dataset. Huang *et al.* (2003) demonstrated that the growth of nanoparticulate ZnS involved first an aggregation mechanism and then Ostwald ripening. The driving force for Ostwald ripening is the differences in solubility of particles, which is a function of the grain size since smaller grains have a higher surface energy (Steefel and van Capellen, 1990). In monodisperse systems, there is limited driving force of Ostwald ripening. However, the aggregation of monodisperse systems could create a driving force for Ostwald ripening, which would explain the occurrence of stages with different growth mechanisms.

4.5.3. Isotopic exchange during Ostwald ripening

Isotope exchange models between liquids and crystals exist for oxygen and hydrogen systematics for high temperature silicate-water and carbonate-water systems (Northrop & Clayton, 1966; Graham, 1981; Cole *et al.*, 1983; Matthews *et al.*, 1983a,b; Graham *et al.*, 1984; Graham and Elphick, 1991; Stoffregen, 1996; Criss, 1999). Dubinina and Lakshtanov (1997) developed three models for isotopic exchange during dissolution-precipitation processes including crystal synthesis and Ostwald ripening. During Ostwald ripening, smaller particles dissolve in favour of larger particles and thus the number of particles decreases. The dissolution depends on the solubility of the small particles, and thus on their critical radius and the degree of supersaturation of the solution. In their Ostwald ripening model, Dubinina and

Lakshtanov (1997) use the evolution of the crystal size distribution with time to calculate the amount of mass dissolved.

Ohfuji & Rickard (2006) determined the particle size distribution of freshly precipitated mackinawite with HRTEM. They showed that the average thickness and length of FeS_m is 3.6 x 5.6 nm. With the Scherrer equation we only calculated the average size of the domain, and not the particle size distribution in our experiments. This makes direct use of the Dubinina and Lakshtanov approach difficult. We thus estimated the number of Fe atoms *X* released at time t from the number of particles *P* present in solution at time t and the amount N_{FeS} of Fe atoms in FeS_m (Eqs. 4.13 and 4.14):

$$P_{t+1} = \frac{\rho \times V_{particle_{t+1}}}{M_{totalFeS}} \qquad (4.13)$$

and

$$X_{t+1} = (P_t - P_{t+1}) \times \frac{N_{FeS}}{P_0} \qquad (4.14)$$

where ρ is the density of mackinawite (4.1 g cm^{-3}) and *V* is the volume calculated from the average size data and $M_{totalFeS}$ is the total mass of FeS_m precipitated in the experiment (0.044 g), N_{FeS} is the constant total number of Fe atoms in FeS_m and P_0 is the number of FeS_m particles at t=0.

When a fraction of FeS_m dissolves into the solution and releases *X* atoms of Fe, the isotopic composition of $Fe(II)_{aq}$ is then given by Eq. 4.15:

$$\delta^{56}Fe_{Fe(II)_{t+1}} = \frac{\left(N_{sol} \times \delta^{56}Fe_{Fe(II)_t}\right) + \left(X_{t+1} \times \delta^{56}Fe_{FeS_t}\right)}{N_{sol} + X_{t+1}} \qquad (4.15)$$

where N_{sol} is the constant total number of Fe atoms in $Fe(II)_{aq}$. The subsequent re-crystallisation of the *X* into larger FeS_m particles gives a bulk FeS_m composition of (Eq. 4.16):

$$\delta^{56}Fe_{FeS_{t+1}} = \frac{\left(N_{FeS} \times \delta^{56}Fe_{FeS_t}\right) - \left(X \times \delta^{56}Fe_{FeS_t}\right) + \left(X \times \delta^{56}Fe_{Fe(II)_{t+1}}\right)}{N_{FeS}} \qquad (4.16)$$

Fig. 4.7 shows that the Oswald ripening isotopic exchange model overestimates the rate of isotopic exchange, *i.e.* Fe isotopes stop exchanging at a very early stage, and the model is limited by the extent of dissolution-recrystallisation. The particle size evolution indicates that the amount of particles *P* decreases by ~ 2 during the experiment (Fig. 4.4.B, Eq. 4.13), meaning that about at least half of total FeS_m

should dissolve, mixing Fe atoms with the solution, and recrystallise into larger particles. Such scenario does not represent the observed variations in $\delta^{56}Fe$ of FeS_m, as it supports an extent of exchange towards bulk composition of $\xi \sim 42$ %. However, the experimental data show that $\xi \sim 75$ % at the end of the experiment.

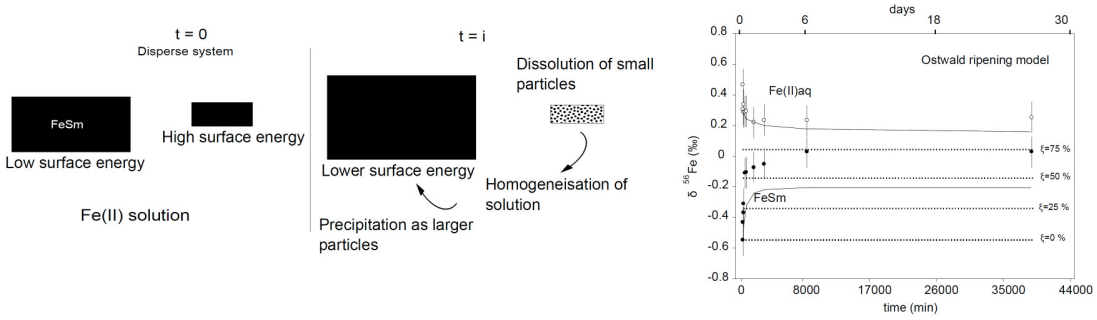

Figure 4.7: Isotopic exchange between FeS_m and $Fe(II)_{aq}$ during Ostwald ripening. The cartoon illustrates the release of Fe atoms into the solution during the dissolution of smaller particles. The graph compares our 25°C isotope data for $Fe(II)_{aq}$ (open circles) and FeS_m (filled circles) with a model for isotopic exchange *via* Ostwald ripening (solid lines). Dashed lines represent the theoretical evolution of $\delta^{56}Fe_{FeS}$ with increasing ξ.

4.5.4. Isotopic exchange during aggregation

We based this model on nanoparticle structure and growth observations by Banfield and Zhang (2001), Zhang *et al.* (2003) and Huang *et al.* (2009). They described nanoparticulate TiO_2, ZnS and NiS to be composed of a structured core and a distorted surface layer. In our model, we consider the measured composition of FeS_m as a mixture between a non-exchanging FeS_m core and an exchanging surface layer. We assume that the total exchange between the surface and the solution is limited to 100 % of isotope exchange. The thickness h of the surface layer is a function of the media (Banfield and Zhang, 2001), *i.e.* the strength of H_2O molecules on the surface of FeS_m nanoparticles, and is constant with nanoparticle growth (Banfield and Zhang, 2001). Particles grow by aggregation-growth, meaning that the non-exchanging core grows as the bulk particle grows, and as the number of atoms in the surface decreases. The thickness h of the surface layer is set as a constant and different values for h were applied to the model. For each given h we can calculate the variation of number of Fe atoms N with time in the core, the surface layer and the solution.

At any time the composition of FeS_m is (Eq. 4.17):

$$\delta^{56}Fe_{FeS_{t+1}} = \left(\delta^{56}Fe_{core_{t+1}} \times \frac{N_{core_{t+1}}}{N_{FeS}}\right) + \left(\delta^{56}Fe_{surface_{t+1}} \times \frac{N_{surface_{t+1}}}{N_{FeS}}\right) \qquad (4.17)$$

If q represents the amount of Fe atoms transported from the surface to the solution, and from the solution to the surface, we can calculate the composition of the surface and the solution from the mass balance (Eqs. 4.18 and 4.19):

$$\delta^{56}Fe_{surface_{t+1}} = \frac{\left(\delta^{56}Fe_{surface_t} \times N_{surface_t}\right) - q_t \times \delta^{56}Fe_{surface_t} + q_t \times \delta^{56}Fe_{Fe(II)_t}}{N_{surface_{t+1}}} \qquad (4.18)$$

$$\delta^{56}Fe_{Fe(II)_{t+1}} = \frac{\left(\delta^{56}Fe_{Fe(II)_t} \times N_{sol}\right) - q_t \times \delta^{56}Fe_{Fe(II)_t} + q_t \times \delta^{56}Fe_{FeS_t}}{N_{sol}} \qquad (4.19)$$

with q given by the differences in composition of the solution and the surface layer (Eq. 4.20):

$$q_{t+1} = \frac{\left(\delta^{56}Fe_{Fe(II)_{t+1}} \times N_{sol}\right) - \left(\delta^{56}Fe_{Fe(II)_t} \times N_{sol}\right)}{\left(\delta^{56}Fe_{surface_t} - \delta^{56}Fe_{Fe(II)_t}\right)} \qquad (4.20)$$

At t+1, the growing core incorporates a fraction of the surface and its composition is given by Eq. 4.21:

$$\delta^{56}Fe_{core_{t+1}} = \frac{\left(\delta^{56}Fe_{core_t} \times N_{core_t}\right) + \left(\left(N_{surface_t} - N_{surface_{t+1}}\right) \times \delta^{56}Fe_{surface_t}\right)}{N_{core_{t+1}}} \qquad (4.21)$$

For our model, we assume that at t=0, $\delta^{56}Fe_{surface_0} = \delta^{56}Fe_{core_0} = \delta^{56}Fe_{FeS_0}$. Fig. 4.8 shows the isotopic evolution of the surface layer (dashed lines), the solution (black lines) and bulk FeS_m (grey lines) for varying h. Our model curves' shapes are consistent with observed isotope exchange. Our model best fits the isotopic data for h ~ 0.8 nm, based on a maximum isotope exchange of 100 %.

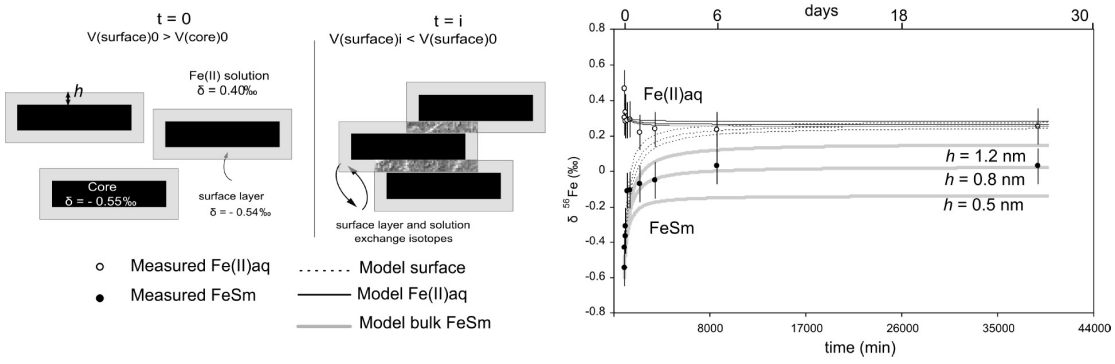

Figure 4.8: Isotopic exchange between the mackinawite surface layer and the solution, assuming a constant surface layer thickness h and a non-exchanging core. The cartoon uses FeS_m nanoparticle shape data from Ohfuji and Rickard (2006) and assumes aggregation-growth on <001> as suggested by

that work. At t=0, the volume of the nanoparticle surface or shell layer (grey) is greater than that of the core (black). After aggregation-growth (t=i) on (001) the surface volume has decreased. The shadowed areas represent the volume of the surface incorporated into the core. The graph compares our 25°C isotope data for $Fe(II)_{aq}$ (open circles) and FeS_m (filled circles) and a model for isotopic exchange *via* aggregation-growth. Dashed lines represent the compositions of the surface layer. Grey lines represent the composition of bulk FeS_m. Black lines represent the composition of the solution. The values chosen for the thickness of the surface layer, *h*, are consistent with the amount of exchange observed and the measured size particle. Note that this model is only true assuming a maximum exchange of 100 %.

In their work, Wolthers et al (2003) could not discriminate a surface layer for FeS_m nanoparticles from their X-ray diffraction analysis. Wolthers *et al.* (2005b) developed a surface structural model of mackinawite nanoparticles based on titration methods. They showed that the FeS_m surface is characterised by a doubly protonated weak surface site which they represented as $\equiv Fe_3SH_2^+$ and suggested that this possibly reflected that one of the Fe-S bonds $\equiv Fe_3SH_2^+$ is broken. This would facilitate rapid cation exchange between the surface and the solution. In contrast to the HRTEM observations on ZnS and TiO_2 nanoparticles (Banfield and Zhang, 2001), FeS_m nanoparticles are not suitable for direct observations of aggregation-growth. Reference to the HRTEM images of Ohfuji and Rickard (2006, Fig. 4.9) shows that the FeS_m nanoparticles consist of tabular crystals only 2-6 nm thick but with 3-11nm edge lengths. Although it is possible that some interfaces in these HRTEM images reflect aggregation-growth, it is not possible to distinguish with certainty between aggregation-growth interfaces between these plates and random overlap of two or more plates. It is even more difficult as FeS_m nanoparticles tend to flocculate readily. However, the edges of the FeS_m nanoparticles are diffuse, which is consistent with a disordered surface phase. Interestingly, FeS_m is anhydrous (Rickard *et al.*, 2006), in contrast to NiS nanoparticles (Huang *et al.*, 2009) and thus the surface layer is disordered rather than hydrated. This means that the density of the FeS_m surface layer is relatively close to that of bulk FeS_m as we here assume in our model. It seems probable that aggregation-growth in FeS_m nanoparticles occurs between the large <001> surfaces and this is intuitively consistent with development of the layered structure of bulk mackinawite.

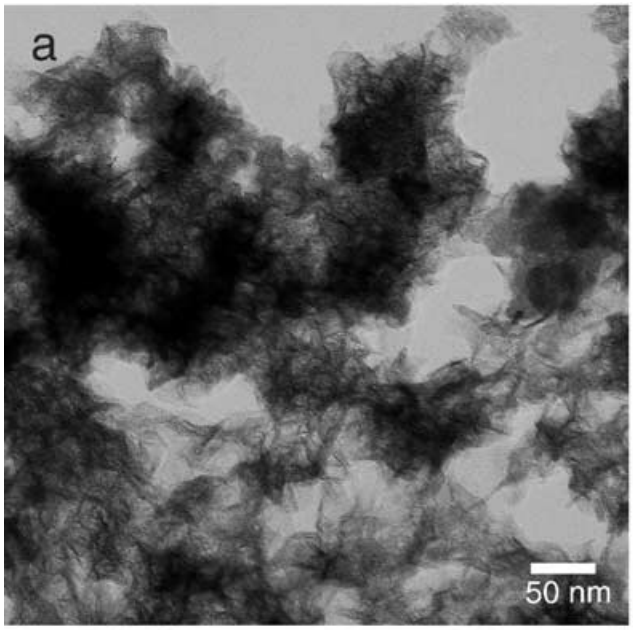

Figure 4.9: TEM images of aggregates of FeS_m nanoparticles. The figure is from Ohfuji and Rickard (2006).

4.5.5. Implications for natural systems

In our experiments, we precipitated 10% of available dissolved Fe, thus the measured fractionation can be recorded in sedimentary environments where only a small portion of Fe precipitates from the $Fe(II)_{aq}$ reservoir as FeS_m (Butler *et al.*, 2005). Rickard (1995) showed that in acidic environments, the precipitation of FeS_m is rapid (<1s) when the IAP for Fe^{2+} and H_2S exceeds the solubility condition determined by Rickard (2006), *i.e.* where $\log\{Fe^{2+}\} + \log\{H_2S\} - 2\log\{H^+\} \geq 3.5$. In neutral to alkaline environments, FeS_m precipitation is pH independent and the equilibrium solubility condition is given by $\log K_{sp} = \log\{FeS^0_{aq}\} = -5.7$. This means that our experimental set up is representative of natural systems in which {Fe(II)} >> {S(-II)} or where {Fe(II)} and {S(-II)} are low, *i.e.* where the I.A.P. only just exceeds the K_{sp}. In sediments, [Fe(II)] increases with the reduction of Fe(III) (oxy-hydr)oxides by microbial dissimilatory iron(III) reduction (DIR) or H_2S reduction. Fe isotope fractionation on mackinawite might thus be recorded at the oxic-anoxic interface where sulphide starts forming from sulphate reduction or within the anoxic zone in which H_2S reduces Fe(III) species to Fe^{2+}. In environments in which Fe reduction is extensive, the process may be localised to the boundary between the suboxic and the anoxic zones.

Severmann *et al.* (2006) documented $\delta^{56}Fe$ values for pore waters, pyrite, and HCl extractable solid phases (*i.e.* FeS_m and $Fe(OH)_3$) in modern anoxic margin basins. In these sediments, where DIR can be extensive, pore water $Fe(II)_{aq}$ is ^{56}Fe depleted (down to ~ -3 ‰). Fe isotope data from benthic fluxes (Severmann *et al.*, 2010), estuarine pore waters (Rouxel *et al.*, 2008) and Fe(II) adsorption experiments (Teutsch *et al.*, 2005) suggest that the production of such highly ^{56}Fe depleted pore water $Fe(II)_{aq}$ is not only due to DIR but also to Fe partial removal as ^{56}Fe enriched (hydr)oxides and Fe adsorption onto Fe (hydr)oxides. If we consider that $\delta^{56}Fe_{FeS}$ are reflected by the HCl extractable solid fraction for which $Fe(II)_{HCl}/Fe(III)_{HCl} > 80$ % as suggested by Johnson *et al.* (2008), the data imply that most natural $Fe(II)_{aq}$ and FeS_m isotope signatures give $\Delta^{56}Fe_{Fe(II)\text{-}FeS}$ far from those found in our experiments. This is because of the highly ^{56}Fe depleted values measured in $Fe(II)_{aq}$. However, fractionation factors can not be directly calculated from the measured Fe isotopic compositions of the natural phases since $Fe(II)_{aq}$ can remain dissolved for large temporal scales and there is no reason why within the same sediment, FeS_m should have been precipitated directly from surrounding pore waters (Rickard and Luther, 2007). Mackinawite is a key mineral for pyrite formation since systems that contain FeS_m are close to the pyrite supersaturation limit (Rickard and Luther, 2007). Pyrite formation involving mackinawite as a reactant may thus have been an important pathway in $Fe(II)_{aq}$ rich, Proterozoic and Archean oceans. FeS_m dissolves into FeS clusters which react with $S(-II)_{aq}$ to from pyrite. As pyrite solubility is very low, the sequestration of Fe_{FeS} into the ultimate pyrite product is a unidirectional process and the kinetic Fe isotope fractionation on mackinawite may be transferred to pyrite. Where pyrite formation is fast, Fe isotope fractionation on mackinawite formation may thus contribute to the recorded Fe isotope signature. Further experiments on Fe isotope fractionation during the formation of pyrite are required to address the discrepancies between measured compositions (Rouxel *et al.*, 2005) and calculated fractionation factors (Polyakov & Mineev, 2000, Polyakov *et al.*, 2007), beyond those due to variations in the reservoir composition.

A model in which nanoparticles are composed by a structured core and a distorted surface layer and grow *via* aggregation-growth is consistent with the observations that the rate constant of Fe isotope exchange between FeS_m and $Fe(II)_{aq}$ changes over time. Fe isotopes are mobile within the surface-solution system, but the signature of bulk FeS_m cannot provide a constant rate of exchange since only a varying part of the

particle is exchanging, the core of the particle being prevented from exchange. Because a part of Fe isotopes are sequestered into the core, it is unlikely that the final isotopic composition of FeS_m, although in an apparent steady-state, could represent isotopic equilibrium. This supports Butler *et al.* (2005) who suggested that the final system was in isotopic metastable disequilibrium rather than in true equilibrium. Where ageing time between FeS_m and $Fe(II)_{aq}$ is sufficient, the core-shell structure we propose for FeS_m should favour progressive FeS_m depletion in ^{56}Fe as Fe atoms contained in the shell exchange with surrounding ^{56}Fe depleted $Fe(II)_{aq}$.

Poulson *et al.* (2005) found similar behaviour for the exchange of Fe isotopes between dissolved Fe and the surface of nanoparticulate ferrihydrite. Waychunas *et al.* (2005) showed that goethite nanoparticle growth results from an aggregation process. Such a growth process has implications for the retention of toxic metals within the aggregate structure. Once adsorbed at the surface of nanoparticles, toxic metals may be trapped during the aggregation growth process, with no possibility to exchange and be released into solution (Waychunas *et al.*, 2005). Our nanoparticle growth model for FeS_m has similar implications for the role of FeS_m in removing contaminant metal cations from solution (*e.g.* Morse and Arakaki, 1993; Arakaki and Morse, 1993; Watson *et al.*, 1995; Wolthers *et al.*, 2005a; Waychunas *et al.*, 2005).

4.6. Conclusions

The Fe isotope fractionation between mackinawite and $Fe(II)_{aq}$ at time = 0 is 1.17 ± 0.16 ‰ at 25°C and 0.98 ± 0.16 ‰ at 2°C which, within error, is consistent with the fractionation determined by Butler *et al.* (2005) of 0.85 ± 0.30 ‰.

The rate of Fe isotope exchange between FeS_m and $Fe(II)_{aq}$ changes over time, and approaches 0 when ~ 75 % of Fe isotopes have exchanged. The extent of isotopic exchange is dependent on the growth of FeS_m nanoparticles, which supports an aggregation-growth model rather than Ostwald ripening. In the aggregation-growth model, FeS_m nanoparticles are composed by a structured core and a distorted surface layer, and Fe isotopes are only mobile between the surface layer and the media. With time, particles growth and the relative proportion of the surface layer decreases with respect to the core. The rate constant of Fe isotope exchange is second-order during the early stages of nanoparticle growth, *i.e.* when the proportion of non-exchangeable core in the bulk FeS_m is still negligible. The rate constant of Fe isotope exchange is

approaching zero when the non-exchangeable core is a major component of the bulk FeS_m.

Our experimentation does not permit the determination of equilibrium $\Delta^{56}Fe_{Fe(II)\text{-}FeS}$, which would require the use of an enriched tracer. However, the core-shell structure of FeS_m nanoparticles forbids isotopes contained in the core to exchange with the media and the final isotopic composition of FeS_m is thus unlikely to reflect isotopic equilibrium.

4.7. Acknowledgements

We thank Nick Odling, Anthony Oldroyd, Vinnie Gallagher and Kathleen Keefe for technical support. We also thank Marek Pękala and Alan Matthews for constructive discussions, and three anonymous reviewers for their comments on the original manuscript. This work was funded by an ECOSSE PhD studentship to RG and NERC research grant NE/E003958/1 to IBB.

4.8. References

Alivisatos, A.P., 1996. Perspectives on the Physical Chemistry of Semiconductor Nanocrystals. The Journal of Physical Chemistry, 100(31): 13226-13239.

Arakaki, T., Morse, J.W., 1993. Coprecipitation and adsorption of Mn(II) with mackinawite (FeS) under conditions similar to those found in anoxic sediments. Geochimica et Cosmochimica Acta, 57(1): 9-14.

Banfield, J.F., Welch, S.A., Zhang, H., Ebert, T.T., Penn, R.L., 2000. Aggregation-Based Crystal Growth and Microstructure Development in Natural Iron Oxyhydroxide Biomineralization Products. Science, 289(5480): 751-754.

Banfield, J.F., Zhang, H., 2001. Nanoparticles in the environment. Reviews in Mineralogy & Geochemistry, 44: 1-58.

Brindley, G.W., 1980. Order-disorder in clay mineral structures. In : Crystal structures of clay minerals and their X-ray identification. In : Crystal structures of clay minerals and their X-ray identification (G.W. Brindley and G. Brown, eds). Mineralogical Society London: 125-195.

Butler, I.B., Archer, C., Vance, D., Oldroyd, A., Rickard, D., 2005. Fe isotope fractionation on FeS formation in ambient aqueous solution. Earth and Planet. Science Letters, 236(430-442).

Butler, I.B., Rickard, D., 2000. Framboidal pyrite formation via the oxidation of iron (II) monosulfide by hydrogen sulphide. Geochim Cosmochim Acta, 64: 2665–2672.

Butler, I.B., Schoonen, M.A.A., Rickard, D.T., 1994. Removal of dissolved oxygen from water: A comparison of four common techniques. Talanta, 41(2): 211-215.

Charlet, L., Manceau, A.A., 1992. X-ray absorption spectroscopic study of the sorption of Cr(III) at the oxide-water interface : II. Adsorption, coprecipitation, and surface precipitation on hydrous ferric oxide. Journal of Colloid and Interface Science, 148(2): 443-458.

Chen, Y., Rosenzweig, Z., 2002. Luminescent CdS Quantum Dots as Selective Ion Probes. Analytical Chemistry, 74(19): 5132-5138.

Cole, D.R., Ohmoto, H., Lasaga, A.C., 1983. Isotopic exchange in mineral-fluid systems. I. Theoretical evaluation of oxygen isotopic exchange accompanying surface reactions and diffusion. Geochimica et Cosmochimica Acta, 47(10): 1681-1693.

Criss, R.E., 1999. Principles of stable isotope distribution. Oxford University Press, New York: 244pp.

Dubinina, E.O., Lakshtanov, L.Z., 1997. A kinetic model of isotopic exchange in dissolution-precipitation processes. Geochimica et Cosmochimica Acta, 61(11): 2265-2273.

Graham, C.M., 1981. Experimental hydrogen isotope studies III: Diffusion of hydrogen in hydrous minerals, and stable isotope exchange in metamorphic rocks. Contributions to Mineralogy and Petrology, 76(2): 216-228.

Graham, C.M. and Elphick, S.C., 1991. Some experimental constraints on the role of hydrogen in oxygen and hydrogen diffusion and Al-Si interdiffusion in silicates. In: Diffusion, Atomic Ordering, and MassTransport. Adv. Phys. Chem. (Ganguly, J. ed), 8: 248-285.

Graham, C.M., Harmon, R.S., Sheppard, S.M.F., 1984. Experimental hydrogen isotope studies: Hydrogen isotope exchange between amphibole and water. Am. Mineral., 69: 128-138.

Guilbaud, R., Ellam, R.M., Butler, I.B., Gallagher, V., Keefe, K., 2010. A procedural development for the analysis of $^{56/54}$Fe and $^{57/54}$Fe isotope ratios with new generation IsoProbe MC-ICP-MS. J. Anal. At. Spectrom., 25:1598-1604.

Harrison, P.M., Dutriazac, J.E., 1998. Ferric oxyhydroxide core of ferritin. Nature, 216: 1188-1190.

Huang, F., Zhang, H., Banfield, J.F., 2003. Two-Stage Crystal-Growth Kinetics Observed during Hydrothermal Coarsening of Nanocrystalline ZnS. Nano Letters, 3(3): 373-378.

Huang, S., Harris, K.D.M., Lopez-Capel, E., Manning, D.A.C., Rickard, D., 2009. "Amorphous Nickel Sulfide" Is Hydrated Nanocrystalline NiS with a Core-Shell Structure. Inorganic Chemistry, 48(24): 11486-11488.

Jeong, H.Y., Lee, J.H., Hayes, K.F., 2008. Characterization of synthetic nanocrystalline mackinawite: Crystal structure, particle size, and specific surface area. Geochimica et Cosmochimica Acta, 72(2): 493-505.

Joesten, R., 1991. Grain-boundary diffusion kinetics in silicates and oxide minerals. In: Diffusion, Atomic Ordering, and MassTransport. Adv. Phys. Chem. (Ganguly, J. ed), 8: 345-395.

Johnson, C.M., Skulan, J.L., Beard, B.L., Sun, H., Nealson, K.H., Braterman, P.S., 2002. Isotopic fractionation between Fe(III) and Fe(II) in aqueous solutions. Earth and Planetary Science Letters, 195(1-2): 141-153.

Johnson, Clark M., Brian L. Beard, and Eric E. Roden., 2008. The Iron Isotope Fingerprints of Redox and Biogeochemical Cycling in Modern and Ancient Earth. Annual Review of Earth and Planetary Sciences, 36: 457-493.

Luther, G. W., Rickard, D., 2005. Metal Sulfide Cluster Complexes and their Biogeochemical Importance in the Environment. Journal of Nanoparticle Research, 7(4): 389-407.

Luther, G.W., Theberge, S.M., Rickard, D.T., 1999. Evidence for aqueous clusters as intermediates during zinc sulfide formation. Geochimica et Cosmochimica Acta, 63(19-20): 3159-3169.

Luther, G.W., Theberge, S.M., Rozan, T.F., Rickard, D., Rowlands, C.C., Oldroyds, A., 2002. Aqueous Copper Sulfide Clusters as Intermediates during Copper Sulfide Formation. Environmental Science & Technology, 36(3): 394-402.

Martin, W., Russell, M.J., 2003. On the origins of cells: a hypothesis for the evolutionary transitions from abiotic geochemistry to chemoautotrophic prokaryotes, and from prokaryotes to nucleated cells. Philosophical Transactions of the Royal Society of London. Series B: Biological Sciences, 358(1429): 59-85.

Matthews, A., Goldsmith, J.R., Clayton, R.N., 1983a. On the mechanisms and kinetics of oxygen isotope exchange in quartz and feldspars at elevated temperatures and pressures. Geol. Soc. Am. Bul., 94: 396-412.

Matthews, A., Goldsmith, J.R., Clayton, R.N., 1983b. Oxygen isotope fractionation involving pyroxenex: the calibration of mineral-pair geothermometers. Geochim. Cosmochim. Acta, 47: 631-644.

Morse, J.W., Arakaki, T., 1993. Adsorption and coprecipitation of divalent metals with mackinawite (FeS). Geochimica et Cosmochimica Acta, 57(15): 3635-3640.

Northrop, D.A., Clayton, R.N., 1966. Oxygen isotope fractionations in systems containing dolomite. J. Geol., 74(174-196).

Ohfuji, H., Rickard, D., 2006. High resolution transmission electron microscopic study of synthetic nanocrystalline mackinawite Earth and Planet. Sci. Letters, 241: 227.

Pankow, J., Morgan, J., 1980. Dissolution of Tetragonal Ferrous Sulfide (Mackinawite) in Anoxic Aqueous Systems. 2. Implications for the Cycling of Iron, Sulfur, and Trace Metals. Environmental Engineering Science 14, 183.

Penn, R.L., Banfield, J.F., 1998. Imperfect Oriented Attachment: Dislocation Generation in Defect-Free Nanocrystals. Science, 281(5379): 969-971.

Penn, R.L., Banfield, J.F., 1999. Morphology development and crystal growth in nanocrystalline aggregates under hydrothermal conditions: insights from titania. Geochimica et Cosmochimica Acta, 63(10): 1549-1557.

Penn, R.L. Oskam, G., Strathmann, T.J., Searson, P.C., Stone, A.T., Veblen, D.R., 2001. Epitaxial Assembly in Aged Colloids. The Journal of Physical Chemistry B, 105(11): 2177-2182.

Polyakov, V.B., Clayton, R.N., Horita, J., Mineev, S.D., 2007. Equilibrium iron isotope fractionation factors of minerals: Reevaluation from the data of nuclear inelastic resonant X-ray scattering and Mössbauer spectroscopy. Geochimica et Cosmochimica Acta, 71(15): 3833-3846.

Polyakov, V.B., Mineev, S.D., 2000. The use of Mossbauer spectroscopy in stable isotope geochemistry. Geochim Cosmochim Acta, 64: 849-865.

Poulson, R.L., Johnson, C.M., Beard, B.L., 2005. Iron isotope exchange kinetics at the nanoparticulate ferrihydrite surface. American Mineralogist, 90(4): 758-763.

Rickard, D., 1995. Kinetics of FeS precipitation: Part 1. Competing reaction mechanisms. Geochim. Cosmochim. Acta 59, 4367– 4379.

Rickard, D., 2006. The solubility of FeS. Geochimica et Cosmochimica Acta, 70(23): 5779-5789.

Rickard, D., Griffith, A., Oldroyd, A., Butler, I.B., Lopez-Capel, E., Manning, D.A., Apperley, D.C., 2006. The composition of nanoparticulate mackinawite, tetragonal iron (II) monosulfide. Chem. Geol., 235(286).

Rickard, D., Luther, G.W., III, 2007. Chemistry of Iron Sulfides. Chem. Rev., 107: 514-562.

Rickard, D., Luther III, G.W., 2006. Metal sulfide Complexes and Clusters. Reviews in Mineralogy & Geochemistry, 61: 421-504.

Rouxel, O.J., Bekker, A., Edwards, K.J., 2005. Iron isotope constraints on the Archean and Paleoproterozoic ocean redox state. Science, 307: 1088-1090.

Rouxel, Olivier, Edward Sholkovitz, Matthew Charette, and Katrina J. Edwards., 2008. Iron isotope fractionation in subterranean estuaries. Geochimica et Cosmochimica Acta, 72: 3413-3430.

Russell, M.J., Daia, D., Hall, A.J., 1998. The emergence of life from FeS bubbles at alkaline hot springs in an acid ocean. in: J. Weigel, M.W. Adams (Eds.), Thermophiles: The Keys to Molecular Evolution and the Origin of Life? Taylor and Francis, London: 77-126.

Severmann, S., C.M. Johnson, B.L. Beard, and J. McManus., 2006. The effect of early diagenesis on the Fe isotope compositions of porewaters and authigenic minerals in continental margin sediments. Geochim Cosmochim Acta, 70: 2006–2022.

Severmann, Silke, James McManus, William M. Berelson, and Douglas E. Hammond. 2010. The continental shelf benthic iron flux and its isotope composition. Geochimica et Cosmochimica Acta 74: 3984-4004.

Steefel, C.I., Van Cappellen, P., 1990. A new kinetic approach to modeling water-rock interaction: The role of nucleation, precursors, and Ostwald ripening. Geochimica et Cosmochimica Acta, 54(10): 2657-2677.

Stoffregen, R., 1996. Numerical simulation of mineral-water isotope exchange via Ostwald ripening. Am J Sci, 296: 908-931.

Teutsch N., von Gunten U., Porcelli D., Cirpka O. A., and Halliday A. N., 2005. Adsorption as a cause for iron isotope fractionation in reduced groundwater. Geochim Cosmochim Acta, 69: 4175-4185.

Watson, J.H.P., Ellwood, D.C., Deng, Q., Mikhalovsky, S., Hayter, C.E., Evans, J., 1995. Heavy metal adsorption on bacterially produced FeS. Minerals Engineering, 8(10): 1097-1108.

Waychunas, G.A., Kim, C.S., Banfield, J.F., 2005. Nanoparticulate Iron Oxide Minerals in Soils and Sediments: Unique Properties and Contaminant Scavenging Mechanisms. Journal of Nanoparticle Research, 7(4): 409-433.

Wolthers, M., van der Gaast, S.J., Charlet, L., Rickard, D., 2004. A surface and structural model describing the environmental reactivity of disordered mackinawite. Am. Mineral., 88: 2007-2015.

Wolthers, M., Charlet, L., van Der Weijden, C.H., van der Linde, P.R., Rickard, D., 2005a. Arsenic mobility in the ambient sulfidic environment: Sorption of arsenic(V) and arsenic(III) onto disordered mackinawite. Geochimica et Cosmochimica Acta, 69(14): 3483-3492.

Wolthers, M., van der Gaast, S.J., Charlet, L., Rickard, D., 2005b. A surface and structural model describing the environmental reactivity of disordered mackinawite. Am. Mineral., 88: 2007-2015.

Wolthers, M., van der Gaast, S.J., Rickard, D., 2003. The structure of distored mackinawite. Am. Mineral., 88: 2007.

Zhang, H., Banfield, J.F., 2004. Aggregation, Coarsening, and Phase Transformation in ZnS Nanoparticles Studied by Molecular Dynamics Simulations. Nano Letters, 4(4): 713-718.

Zhang, H., Huang, F., Gilbert, B., Banfield, J.F., 2003. Molecular Dynamics Simulations, Thermodynamic Analysis, and Experimental Study of Phase Stability of Zinc Sulfide Nanoparticles. The Journal of Physical Chemistry B, 107(47): 13051-13060.

Chapter V

Experimental determination of the equilibrium Fe isotope fractionation between Fe^{2+}_{aq} and FeS_m (mackinawite) at 25°C and 2°C

The published version of this chapter is attached to this thesis: Guilbaud, R., Butler, I.B., Ellam, R.M., Rickard, D. and Oldroyd, A. Experimental determination of the equilibrium Fe isotope fractionation between Fe^{2+}_{aq} and FeS_m (mackinawite) at 25°C and 2°C. Geoch.. Cosmochim. Acta

Abstract

We report the first experimentally-determined metal isotope equilibrium fractionation factors for a metal sulfide at ambient temperatures and pressures. Mackinawite, FeS_m, can be a reactive component in diagenetic pyrite formation and the extent of equilibration between FeS_m and dissolved Fe(II) has direct implications the $\delta^{56}Fe$ signatures recorded in ultimate diagenetic pyrite. The measured equilibrium Fe isotope fractionation between $Fe(II)_{aq}$ and FeS_m is $\Delta^{56}Fe_{Fe(II)\text{-}FeS}$ = -0.52 ± 0.16 ‰ at 2°C and $\Delta^{56}Fe_{Fe(II)\text{-}FeS}$ = -0.33 ± 0.12 ‰ at 25°C. At the experimental pH of 4, the equilibrium fractionation factor between all dissolved Fe(II) species and FeSm ($\Delta^{56}Fe_{Fe(II)\text{-}FeS}$) equates to the fractionation factor between Fe^{2+}_{aq} and FeS_m ($\Delta^{56}Fe_{Fe2+\text{-}FeS}$). The measured fractionations are of the same order as other non–redox fractionations measured in low-temperature Fe-C-O systems. We show that at low temperature, the $Fe(II)_{aq}$ – FeS_m system is slowly asymptotic to isotopic equilibrium and consequently, FeS_m is likely to partially conserve kinetically derived isotopic signatures generated on precipitation. Combined with the range of published kinetic fractionations measured on FeS_m precipitation, our data suggest that, subject to the degree of isotope exchange during equilibration, FeS_m can display $\delta^{56}Fe$ compositions encompassing in a ~ 1.4 ‰ range.

Keywords: Fe isotopes, equilibrium, FeS, mackinawite, pyrite

5.1. Introduction

In the past decade, transition metal isotope analyses have become widespread as a means of probing present-day and ancient environmental processes and the evolution of (bio)geochemical cycles. Many of these studies have utilised metal-sulfide isotope systems, and interpreting their results has often been restricted to the lack of provision of experimental data that quantify the direction and extent of isotope fractionations. Iron isotope systematics applied on Fe sulfides and especially pyrite, the major environmentally significant transition metal sulfide, are an eloquent example. Most terrestrial rocks have very homogeneous δ^{56}Fe signatures clustered around ~ 0 ‰ (*e.g.* Beard and Johnson, 2004; Dauphas and Rouxel, 2006, for review). Fe isotope excursions (where δ^{56}Fe varies from ~ +1 ‰ to ~ -3.5 ‰) recorded in Precambrian, anoxic, sulphidic sediments (*e.g.* Rouxel *et al.*, 2005) in which pyrite is the dominant Fe-S species, raised divergent interpretations (*e.g.* Archer and Vance, 2006; Rouxel *et al.*, 2005). Various theories have been proposed to explain those variation (*e.g.* Yamaguchi *et al.*, 2005; Anbar and Rouxel, 2007; Johnson *et al.*, 2008). Major questions are whether or not i) pyrite is a passive recorder of the Fe(II) reservoir; ii) its formation is accompanied by significant Fe isotope fractionation; and iii) microbial activity is responsible for those Fe isotope signatures. To date, none of the proposed mechanisms responsible for the observed variations has been confirmed experimentally.

Experimental data on aqueous Fe species, Fe-oxides and Fe-carbonates have been documented and demonstrate that the largest Fe isotope fractionations are produced during redox reactions in both biologically mediated (Brantley *et al.*, 2001,2004; Anbar, 2004; Johnson *et al.*, 2004; Beard *et al.*, 1999,2003; Icopini *et al.*, 2004; Croal *et al.*, 2004; Teutsch *et al.*, 2005) and abiotic systems (Anbar *et al.*, 2000; Bullen *et al.*, 2001; Skulan *et al.*, 2002 Brantley *et al.*, 2004; Welch *et al.*, 2003; Matthews *et al.*, 2004; Jang *et al.*, 2008, Handler *et al.*, 2009; Hill *et al.*, 2008; McAnena, 2009, Beard *et al.*, 2010). Smaller, but significant fractionations have been seen in abiotic non-redox reactions (Wiesli *et al.*, 2004), including the ligand-exchange process involved in mackinawite (FeS_m) formation (Butler *et al.*, 2005).

FeS_m is a metastable nanoparticulate tetragonal Fe(II) monosulfide (Rickard and Luther, 2007, and references therein) and is a potential reactive iron source in pyrite forming systems since FeS_m dissolves and reacts to form pyrite (Rickard and Luther, 1997). Isotopic mobility and potential equilibration between FeS_m and coexisting

dissolved Fe(II) species ($Fe(II)_{aq}$) have direct implications for the ultimate Fe isotope signature of pyrite preserved in geological record. Rickard (2006) showed that in acidic environments, the pH dependent solubility of Fes_m is described by log K_{sp1} = $\log\{Fe^{2+}\}+\log\{H_2S\}-2\log\{H^+\}\geq 3.5$. In neutral to alkaline environments, FeS_m precipitation is pH independent. Total dissolved Fe(II) is dominated by FeS clusters, FeS^0_{aq}, and log K_{sp2} = log $\{FeS^0_{aq}\}$ = -5.7. For all natural environments where its solubility product is exceeded, FeS_m is the first Fe-S phase to precipitate.

The kinetics and mechanisms of FeS_m formation from aqueous solutions have been reported (Rickard, 1995) and the fast precipitation process is a ligand-exchange reaction which follows Eigen-Wilkins kinetics. FeS_m is readily formed in aqueous solutions as a nanoparticulate precipitate (Wolthers *et al.*, 2003; Michel *et al.*, 2005; Ohfuji and Rickard, 2006; Rickard *et al.*, 2006; Jeong *et al.*, 2008). FeS_m nucleation involves the initial formation of FeS^0_{aq} (Theberge and Luther, 1997; Luther and Rickard, 2005).

Since FeS_m formation is fast and readily reversible (*cf.* Rickard, 2006), the FeS_m-$Fe(II)_{aq}$ system is particularly suitable for equilibrium fractionation studies. However, experimental measurements are limited to kinetic fractionation factors (Butler *et al.*, 2005). Butler and co-workers (Butler *et al.*, 2005; Guilbaud *et al.*, 2009) observed that the precipitation of FeS_m nanoparticles from Fe(II) solution at low temperature is accompanied by a kinetic fractionation ranging from $\Delta^{56}Fe_{Fe(II)\text{-}FeS}$ ~ + 0.9 to ~ 0.3 ‰. The observation that FeS_m systematically incorporates the lighter isotopes (Butler *et al.*, 2005) has often been generalised to pyrite, assuming that a fractionation of a similar magnitude would be recorded during pyrite formation (Severmann *et al.*, 2006; Matthews *et al.*, 2004; Rouxel *et al.*, 2005; Archer and Vance, 2006; Yamagushi *et al.*, 2005). This resulted in various interpretations for the highly ^{56}Fe depleted Archean pyrite signatures. In particular, the calculated reduced partition factor ($\beta^{56/54}$) for the Fe^{2+}-pyrite couple, described by Eq. 5.1, predict ^{56}Fe enrichment in pyrite (*e.g.* Polyakov *et al.*, 2000; Polyakov and Mineev, 2007; Blanchard *et al.*, 2009):

$$10^3 \ln \alpha^{56/54}_{Fe^{2+}-pyrite} = 10^3 \ln \beta^{56/54}_{Fe^{2+}} - 10^3 \ln \beta^{56/54}_{pyrite} \qquad (5.1)$$

where α stands for the fractionation factor and β for the reduced partition factor.

Butler *et al.* (2005) noted that even at steady state, the observed $\Delta^{56}Fe_{Fe(II)\text{-}FeS}$ did not necessarily represent isotopic equilibrium. Their arguments were based on the fact

that i) FeS_m is a sparingly soluble mineral (Rickard, 2006) and isotopic exchange is likely to happen *via* dissolution-precipitation between the mineral surface and the solution rather than the bulk mineral and the solution; and ii) the temperature independence of fractionation within the range 2-40°C which supports kinetic effects rather than equilibrium. Formation and dissolution of FeS_m is kinetically anisotropic, and the dissolution kinetics are inhibited by transport of reaction components through the diffusion boundary layer (*cf.* Rickard and Sjoberg, 1983). Extrapolations of kinetic isotope fractionations to equilibrium values gave unreasonably large apparent equilibrium factors (Matsuhisa *et al.*, 1978). Matsuhisa *et al.* (1978) developed the three-isotope method to overcome this problem and determine experimentally equilibrium isotope fractionations.

In this contribution, we use the three isotope method to determine experimentally the equilibrium Fe isotope fractionation between Fe^{2+}_{aq} and FeS_m. We assess whether or not isotopic equilibrium can be rapidly reached at low temperatures in the aqueous Fe-S system and we discuss our results in terms of computationally derived data and implications of sedimentary pyrite formation. So far, only one other experimental study has been published on Fe isotope fractionations occurring within the Fe-S system (Butler *et al.*, 2005). Our results are the first reported experimental equilibrium metal isotope fractionation in any metal sulfide system.

5.2. Methods

5.2.1. The three isotope method

The three isotope method (Matsuhisa *et al.*, 1978) is a robust experimental method that allows the determination of equilibrium fractionation factors for elements with three or more stable isotopes. Its principle is to track the evolution of a two end-member system initially far from isotopic equilibrium. It involves the spike-enrichment of one phase in order to shift its isotopic composition away from the terrestrial mass fractionation line (TFL, Fig. 5.1). The system is then allowed to exchange and equilibrate towards a secondary fractionation line (SFL, or equilibrium fractionation line). Since the SFL is mass dependant, it is parallel to the TFL and lies between the composition of the spiked starting material and the TFL. Any deviation from the bulk composition along the SFL is the measured equilibrium isotopic fractionation between the two phases. In low temperature systems, in which the kinetics are slow, experiments might fail to reach equilibrium, *i.e.* to reach the

secondary fractionation line in adequate time for experimental purposes. In such cases, the equilibrium fractionation can be determined from the best fits of the evolution of the phases.

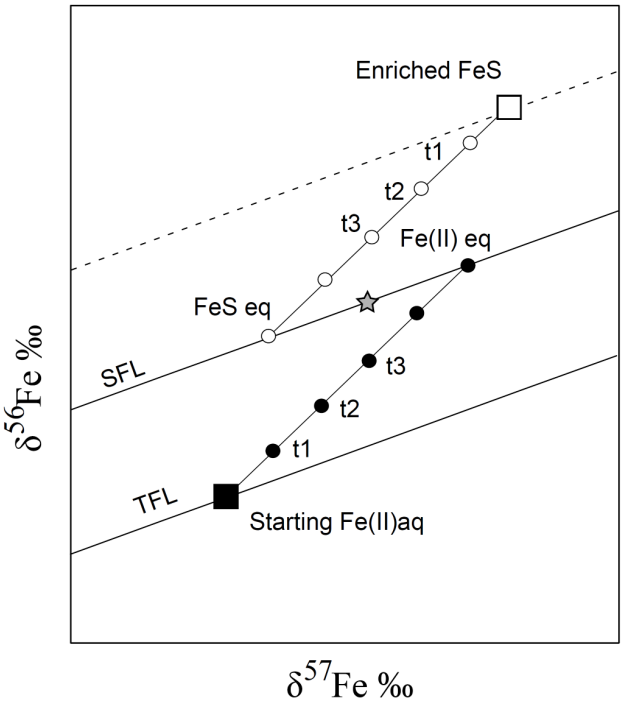

Figure 5.1: Principle of the three isotope method. Starting materials are represented by squares. Starting $Fe(II)_{aq}$ lies on the terrestrial fractionation line (TFL), enriched ^{56}FeS has a composition shifted from the TFL. Circles represent the evolution of isotopic compositions of both phases with time. When the system reaches isotopic equilibrium, the final compositions will lie on the secondary fractionation line (SFL). If $\Delta_{equilibirum} = 0‰$, final compositions will meet at the bulk composition represented by a star. If $\Delta_{equilibirum} \neq 0‰$, it equals the difference between $\delta_{Fe(II),\ equilibrium}$ and $\delta_{FeS,\ equilibrium}$.

The three isotope method was first used for studies on O (*e.g.* Matsuhisa, 1979; Matthews *et al.*, 1983a,b). More recently, three studies applied this method to the Fe isotope systematics: between oxide and silicate phases at high temperature (Shahar *et al.*, 2008), between chloro-complexes in aqueous solutions (Hill and Schauble, 2008), and between $Fe(II)_{aq}$ and goethite (Beard *et al.*, 2010). In our experiments, we aged ^{56}Fe enriched mackinawite ($^{56}FeS_m$) with an $Fe(II)_{aq}$ solution of "normal" isotopic abundance.

The equilibrium isotope fractionation between $Fe(II)_{aq}$ and FeS_m, $\Delta^{57}Fe_{Fe(II)\text{-}FeS}$, is the difference between the intersections of the regression lines, $\delta^{57}Fe_{Inters.i}$, with the SFL. Their values are given by Eq. 5.2:

$$\delta^{57}Fe_{Inters_i} = \frac{b - d_i}{c_i - a} \qquad (5.2)$$

where *a* and *c* are the slopes of the regression lines and the SFL, respectively, *b* and *d* are the intercepts of the regression lines and the SFL, respectively, and *i* stands for the phase of interest. The uncertainties on $\delta^{57}Fe_{Inters.Fe(II)}$ and $\delta^{57}Fe_{Inters.FeS}$, the upper and lower intercepts between the 95% envelopes on the regression lines, were calculated with the R 2.4.1.® statistical package. The coordinates of the lower and upper 95 % confidence envelopes are given conventionally by Eq. 5.3 (*e.g.* Ludwig, 1980; Borradaile, 2003):

$$Y = y \pm t_{\alpha/2} s_R \left[\frac{1}{n} + \frac{\left(x - \bar{x}\right)^2}{\sum \left(x_i - \bar{x}\right)^2} \right]^{\frac{1}{2}} \qquad (5.3)$$

where Y is the coordinate of the 95% envelope for each corresponding x on the regression line (y = ax + c), n is the number of data points, $t_{\alpha/2}$ is the value of the t-statistic for a two-tailed test (with n - 2), the coordinate of the regression line, x_i is the coordinate of data points and $\bar{x}$ is the mean of the x coordinates. Uncertainties on $\Delta^{57}Fe_{FeS\text{-}Fe(II)}$ are propagated from the uncertainties on $\delta^{57}Fe$ with Eq. 5.4:

$$\sigma_{\Delta^{57}Fe} = \left[\left(\sigma_{\delta^{57}Fe_{lower}} \right)^2 + \left(\sigma_{\delta^{57}Fe_{upper}} \right)^2 \right]^{\frac{1}{2}} \qquad (5.4)$$

$\Delta^{57}Fe_{FeS\text{-}Fe(II)}$ and its uncertainties were converted into $\Delta^{56}Fe_{FeS\text{-}Fe(II)}$ notation.

5.2.2. Preparation of ^{56}Fe enriched FeS_m

Although some workers have used enriched $Fe(II)_{aq}$ solutions, we preferred the solid phase (*i.e.* mackinawite) to be the enriched phase for practical reasons. The preparation of clean, contamination-free ^{56}Fe enriched FeS_m is easier experimentally than preparing ^{56}Fe enriched $Fe(II)_{aq}$ from $^{56}Fe(0)$ metal, which would involve the use of metal-complexing species to keep the solution reduced, and which consequently may influence the experimental results. Two $^{56}FeS_m$ reservoirs of different composition were produced. All reagents and acids were analytical grade and solutions were prepared under oxygen free conditions using 18.2 MΩ cm deionised water, sparged with O_2 free grade N_2 for 20-40 min (Butler *et al.*, 1994). Rigorous exclusion of oxygen is essential because FeS_m is pyrophoric and $Fe(II)_{aq}$ itself is prone to oxidation. $^{56}FeS_m$ was prepared by mixing a source of ^{56}Fe enriched iron with $Fe(NH_4)_2(SO_4)_2.6H_2O$ (Sigma Aldrich™). The ^{56}Fe metal, for which the enrichment is

given by m(^{56}Fe)/m(Fe) = 0.997, was supplied by CortecNet™. For any system, the isotope ratio of a mixture is Eq. 5.5:

$$\left(\frac{{}^{\alpha}N}{{}^{\beta}N}\right)_{Mix} = \frac{\sum_{j=1}^{n} {}^{\alpha}N_j}{\sum_{j=1}^{n} {}^{\beta}N_j} \qquad (5.5)$$

where α and β are isotopes of element N, and j is the sum of all the end-members containing N. In the case of Fe isotope ratios in a system with two components A and B, the equation follows Eq. 5.6:

$$\left(\frac{{}^{56}Fe}{{}^{54}Fe}\right)_{Mix} = \frac{{}^{56}Fe_A + {}^{56}Fe_B}{\sum_{j=1}^{n} {}^{54}Fe_j} \qquad (5.6)$$

where $^{56}Fe_A$ is the number of ^{56}Fe atoms brought by component A and $\sum_{j=1}^{n} {}^{54}Fe_j$ is the sum of the ^{54}Fe atoms brought by A and the ^{54}Fe atoms brought by B. This equation is the true mixing equation for any binary system and can be written as Eq. 5.7:

$$\left(\frac{{}^{56}Fe}{{}^{54}Fe}\right)_{Mix} = \frac{{}^{54}Fe_A}{\sum_{j=1}^{n} {}^{54}Fe_j}\left(\frac{{}^{56}Fe}{{}^{54}Fe}\right)_A + \frac{{}^{54}Fe_B}{\sum_{j=1}^{n} {}^{54}Fe_j}\left(\frac{{}^{56}Fe}{{}^{54}Fe}\right)_B \qquad (5.7)$$

with $$ {}^{54}Fe_A = \left(\frac{{}^{54}Fe}{Fe}\right)_A \frac{m(Fe)_A}{M(Fe)_A}$$

where $m(Fe)_A$ is the mass of Fe in A and $M(Fe)_A$ is the molar mass of Fe in A, which is not necessarily the same as $M(Fe)_B$ in the case of enriched materials since enriched materials have a mass different from bulk. The mass of Fe required for both solutions is calculated using the mixing equation Eq. 5.8:

$$\frac{m(Fe)_A}{m(Fe)_B} = \left[\frac{\left(\frac{{}^{56}Fe}{{}^{54}Fe}\right)_B - \left(\frac{{}^{56}Fe}{{}^{54}Fe}\right)_A}{\left(\frac{{}^{56}Fe}{{}^{54}Fe}\right)_{Mix} - \left(\frac{{}^{56}Fe}{{}^{54}Fe}\right)_A} - 1\right]\frac{\left(\frac{{}^{54}Fe}{Fe}\right)_B}{\left(\frac{{}^{54}Fe}{Fe}\right)_A}\frac{M(Fe)_A}{M(Fe)_B} \qquad (5.8)$$

An accurately weighed aliquot of ^{56}Fe metal was dissolved in 40 mL hot 3 M HCl, evaporated to incipient dryness to remove the excess acid and the solution was made up to 100 mL. The pH of the solution was determined by an Orion Research EA920®

pH meter and was 3 ± 0.1. After N_2 purging, the solution was introduced into an MBraun Labmaster 130® re-circulating anoxic chamber. In the glove-box, ^{56}Fe solution was mixed with 20 mL 1.4 M hydroxylamine hydrochloride to reduce quantitatively Fe^{3+} to Fe^{2+}. Quantitative reduction to Fe^{2+} is crucial to prevent formation of S(0) with addition of dissolved HS^-. The $^{56}Fe(II)$ solution was mixed with 250 mL 0.16 M Fe(II) solution made from the dissolution of $Fe(NH_4)_2(SO_4)_2.6H_2O$ (Sigma Aldrich®) in N_2 sparged water. Reduction efficiency was checked by quantifying the residual $[Fe^{3+}]$ in the solution with thiocyanate. An aliquot of the solution was acidified with 2 mL 2M HCl, reacted with 5 mL 4M thiocyanate and made up to 50 mL. The aliquot was analysed with a Perkin Elmer Lambda2® dual beam UV-Vis. Typical response was less than 0.2 ppm for $[Fe^{3+}]$ which represents ~ 0.005‰ of total [Fe].

^{56}FeS was precipitated by mixing the bulk Fe solution with equimolar $Na_2S.9H_2O$ (Sigma Aldrich®). The precipitate was filtered with a Buchner filter (Whatman® No. 1 paper) and the filtrate was filtered with a 0.45 µm membrane Millipore™ filter. Freshly precipitated $^{56}FeS_m$ was re-suspended in water and re-filtered three times, freeze-dried for three days (Rickard *et al.*, 2006) and stored in the glove-box. The ^{56}FeS reservoirs produced in this way had isotopic compositions of ~308 ‰ and ~ 2.6 ‰.

5.2.3. Procedure

In the glove-box, 0.001 mol of freeze-dried $^{56}FeS_m$ was weighed into a serum bottle, 20 mL 0.05 M Fe(II) solution (pH 4) were added and the serum bottle was sealed with a butyl stopper and an aluminium crimp seal. The serum bottles were placed for ageing on a shaking platform for 25°C experiments and in Haake F6/C25® and Haake DC10/K10® refrigerated circulators for 2°C experiments. After ageing (ageing time up to four months for the 25°C experiment and one month for the 2°C experiments), the solid phase was separated from the aqueous phase by vacuum filtration on a 0.45 µm membrane Millipore® filter. The filtrate solution was acidified with concentrated HCl and $^{56}FeS_m$ was dissolved by the addition of a few drops of concentrated HCl. H_2S was allowed to degas from sample in a fume hood.

5.2.4. Analysis

Samples (Fe(III) in HCl) were taken to dryness and re-dissolved in 5% HNO_3. No column chemistry was performed since our samples were experimentally synthesised from analytical grade reagents. $^{56/54}$Fe and $^{57/54}$Fe isotope ratios were measured on a GV IsoProbe (formerly Micromass) multi-collection inductively coupled mass spectrometer (MC-ICP-MS). The detailed analytical protocol has been described elsewhere (Guilbaud *et al.*, 2010). The major challenge for accurate and precise measurement of Fe isotopes is the removal of atomic and polyatomic interferences induced by the Ar plasma. This was achieved by increasing the signal-to-background ratio (using high concentration samples and introducing collision gases into the hexapole to decrease and/or remove the interferences) and by stabilising the instrumental mass bias minimising the hexapole potential and decreasing the extraction voltage.

3-10 ppm Fe solutions were introduced into an ApexQ inlet system at 50 µL min^{-1} to maximise the signal to ~0.3 V on mass 54, ~6 V on mass 56 and ~0.02 V on mass 57. Hexapole rf amplitude was set at 50% which enhances transmission of Fe masses. The analysis was run in hard extraction mode (-250 V). 1.8 mL min^{-1} Ar and 2 mL min^{-1} H_2 were introduced into the hexapole collision cell to remove completely ArN^+ on mass 54 and $ArOH^+$ on mass 57 and to decrease ArO^+ on mass 56 to 0.006 V which represents 0.1% of the Fe peak. Cr^+ interferences on mass 54 were monitored on mass 52 but never detected. Instrumental mass bias was corrected by bracketing each sample with a standard and Fe isotope results are presented conventionally using the δ^{56}Fe and δ^{57}Fe notations in ‰ IRMM-014 (Eqs. 5.9 and 5.10):

$$\delta^{56}Fe = \left(\frac{(^{56}Fe/^{54}Fe)sample}{(^{56}Fe/^{54}Fe)IRMM} - 1 \right) \times 10^3 \qquad (5.9)$$

$$\delta^{57}Fe = \left(\frac{(^{57}Fe/^{54}Fe)sample}{(^{57}Fe/^{54}Fe)IRMM} - 1 \right) \times 10^3 \qquad (5.10)$$

The precision of our measurements was the reproducibility 2sd obtained by measuring an external standard and was ± 0.08 ‰ and ± 0.17 ‰ (2σ) for δ^{56}Fe and δ^{57}Fe respectively.

5.2.5. Experimental errors and data handling using spiked material in the Fe isotope system

General equations used for traditional stable isotope systems must be used with precaution in the Fe isotope system. This is due to the fact that unlike ^{18}O in the O system, ^{57}Fe and ^{54}Fe are not trace isotopes with respect to ^{56}Fe. As a result, when mass balancing equations, the error will be significantly increased using usual isotopic ratios (Eq 1.14a-b-c in Criss, 1999) instead of the (mass of isotope)/(mass of element) ratios. For most systems, this phenomenon is hidden by the large experimental error, but when using highly enriched material (as we did for ^{56}FeS ~ 308 ‰), it becomes crucial to use the true equation.

Thus for mass balance calculations on enriched material, we considered the reproducibility between two duplicates to be the true external precision.

5.3. Results

Experimental conditions, analytical results and fractionations are presented in Table 5.1. Experimental quality control was performed by monitoring the mass conservation law. At any time during the experiment, the weighted sum of the constituents must equal the isotopic signature of the bulk (Eq. 5.11, Fig. 5.2):

$$\left(f \times \frac{^{56}Fe}{Fe}_{Fe(II)}\right) + \left((1-f) \times \frac{^{56}Fe}{Fe}_{FeS}\right) = \frac{^{56}Fe}{Fe}_{bulk} \qquad (5.11)$$

where f is the mass fraction of Fe in the solution. For the experiment starting with $\delta^{56}Fe_{FeS}$ ~ 308 ‰, the bulk composition of the system was 102 ± 3 ‰. For the experiment starting with $\delta^{56}Fe_{FeS}$ ~ 2.6 ‰, the bulk composition of the system was 0.83 ± 0.25 ‰. There is a systematic ^{56}Fe enrichment for early experiments, resulting in a shift from mass balance towards higher $\delta^{56}Fe$ values. The likely explanation is that this phenomenon is due to $^{56}FeS_m$ nanoparticles passing through the 0.45 µm filter in the early stages of the experiment, *i.e.* before FeS_m nanoparticles have agglomerated. Small amounts of highly ^{56}Fe enriched FeS_m would then contaminate the $Fe(II)_{aq}$ isotope signature by shifting it towards higher $\delta^{56}Fe$ values. During filtration of samples which have aged more extensively the 0.45 µm filter becomes clogged by FeS_m nanoparticle flocks forming an efficient filter bed and no FeS_m contribution is seen in the liquid phase. Because imperfectly mass-balanced

experiments only concern the very first experiments, it has no observable effect on our extrapolation and predicted fractionations.

		2°C experiment				25°C experiment							
Sample	Experiment duration(min)	δ^{56} Fe Fe(II) ‰	δ^{57} Fe Fe(II) ‰	δ^{56} Fe FeSm ‰	δ^{57} Fe FeSm ‰	δ^{56} Fe Fe(II) ‰	δ^{57} Fe Fe(II) ‰	δ^{56} Fe FeSm ‰	δ^{57} Fe FeSm ‰	mass balance 2°C	mass balance 25°C	*F* 2°C	*F* 25°C
Eq-0	0	0.20	0.20	308.30	5.80	0.20	0.20	308.30	5.80	112.79	112.79	0.00	0.00
Eq-1-A	24	25.00	0.67	243.34	4.97	55.05	1.62	171.68	4.00	108.37	101.87	0.31	0.54
Eq-1-B	24	24.56	0.67	234.51	4.85	56.29	1.67	169.06	4.11	105.05	101.64	0.36	0.55
Eq-2-A	48	33.65	0.89	229.16	4.62	66.08	1.88	143.38	3.69	109.16	97.71	0.38	0.65
Eq-2-B	48	29.57	0.89	217.66	4.56	68.29	1.88	146.56	3.83	102.45	100.30	0.44	0.67
Eq-3-A	96	44.38	1.12	201.43	4.21	71.83	1.92	136.66	3.50	106.19	98.52	0.52	0.70
Eq-3-B	96	43.99	1.12	192.04	4.19	78.24	1.89	141.60	3.74	102.50	104.35	0.56	0.77
Eq-4-A	144	51.03	1.25	180.50	4.05	77.97	2.02	129.75	3.23	102.68	99.43	0.62	0.76
Eq-4-B	144	50.62	1.25	178.82	4.05	77.43	1.98	130.86	3.25	101.79	99.55	0.63	0.76
Eq-5-A	432	60.66	1.28	158.15	3.68	81.73	2.12	120.41	3.33	100.16	97.86	0.73	0.80
Eq-5-B	432	58.63	1.30	163.87	3.94	79.98	2.07	118.79	3.22	101.11	96.16	0.70	0.78
Eq-6-A	768	65.77	1.56	150.23	3.62	82.69	2.13	118.19	3.20	100.21	97.52	0.77	0.81
Eq-6-B	768	66.26	1.51	151.92	3.61	83.21	2.15	119.52	3.21	101.18	98.37	0.76	0.82
Eq-7-A	2880	-	-	-	-	86.79	2.20	109.73	3.24	-	96.43	-	0.85
	Predicted equilibirum		2.20		2.96		2.57		3.05				
	upper limit		2.32		3.06		2.66		3.15				
	lower limit		2.08		2.85		2.49		2.95				
	Δ^{57} Fe(II)-FeSm ‰		***0.76*** ±0.24				***0.48*** ±0.17						
	Δ^{56}Fe(II)-FeSm ‰		***0.51*** ±0.16				***0.32*** ±0.12						

Table 5.1: Experimental conditions and isotopic analysis. Analytical precision of the isotopic data is the 2standard deviation (2σ) of the external standard (Baker™ Fe solution) and was ± 0.08 ‰ and ± 0.17 ‰ for $\delta^{56}Fe$ and $\delta^{57}Fe$ respectively. $\Delta^{56}Fe_{Fe(II)\text{-}FeS}$ was calculated from $\Delta^{57}Fe_{Fe(II)\text{-}FeS}$. Errors on $\Delta^{56}Fe_{FeS\text{-}Fe(II)}$ are propagated from those determined by the intercepts between the 95% confidence envelopes and the secondary fractionation line from Eqs. 5.2 and 5.3. The mass balance and the extent of reaction *F* were calculated from Eqs. 5.11 and 5.12, respectively.

5.3.1. Experiment starting with $\delta^{56}Fe_{FeS}$ ~ 308 ‰ at 25°C and 2°C

Working with metastable nanoparticulate phases that are oxygen sensitive and responsive to small pH variations generally makes experimental errors large compared to analytical errors. For technical reasons, both analytical and experimental errors increase significantly when using enriched material. Experimentally, this is because, when even small amounts of the enriched material contaminate the natural component, it may considerably affect the bulk isotope signature. Analytically, the signal of the non-enriched isotope peaks decreases considerably, making the isotope ratio analysis irreproducible. Starting with initial $\Delta^{56}Fe_{Fe(II)\text{-}FeS}$ as large as -308 ‰, one would expect to produce large error bars on the predicted equilibrium $\Delta^{56}Fe_{Fe(II)\text{-}FeS}$ using the three isotope method. However in our case, the enrichment was so large that experimental and analytical errors are diluted on the projection on the SFL. The extent of isotopic exchange *F* is given by (Graham *et al.*, 1981; Criss, 1999; Johnson *et al.*, 2002) Eq. 5.12:

$$F = \frac{\delta^{56}Fe - \delta^{56}Fe_0}{\delta^{56}Fe_{eq} - \delta^{56}Fe_0} \qquad (5.12)$$

where the subscripts *0* and *eq* stand for *initial* and *equilibrium*, respectively. The advantage when using enriched starting material, is that the value of the equilibrium $\delta^{56}Fe_{eq}$ (a few per mil) is negligible compared to the starting fractionation (a few hundred per mil) and so *F* can be determined precisely.

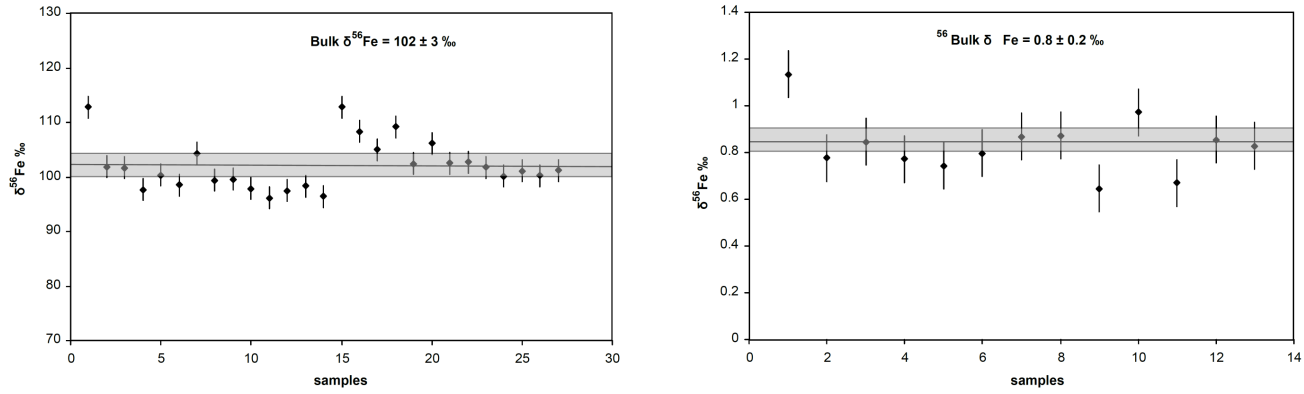

Figure 5.2: Experimental mass balance for the $\delta^{56}Fe_{FeS}$ ~ 308 ‰ and $\delta^{56}Fe_{FeS}$ ~ 2.6 ‰ starting experiments, calculated from Eq. 5.11. Grey areas represent the experimental external precision based on the reproducibility of the replicates.

Fig. 5.3 describes the evolution of the isotope composition of $Fe(II)_{as}$ and FeS_m as a function of time. Isotopes exchange rapidly within the first 96 hours of ageing. After 96 hours, the exchange slows down and the extent of isotopic exchange is asymptotic to the equilibrium composition. At the end of the experiment, 75 % of isotopes had exchanged at 2°C and 85 % of isotopes had exchanged at 25°C after 4 months ageing. At equilibrium, the three isotope methods predicts ^{56}Fe enriched FeS_m with respect to $Fe(II)_{aq}$ for both 25°C and 2°C (Fig. 5.4). Fe isotope fractionation is larger at 2°C where $\Delta^{56}Fe_{Fe(II)\text{-}FeS}$ = -0.52 ± 0.16 ‰ than at 25°C where $\Delta^{56}Fe_{Fe(II)\text{-}FeS}$ = -0.33 ± 0.12 ‰, although within error, these are strictly the same.

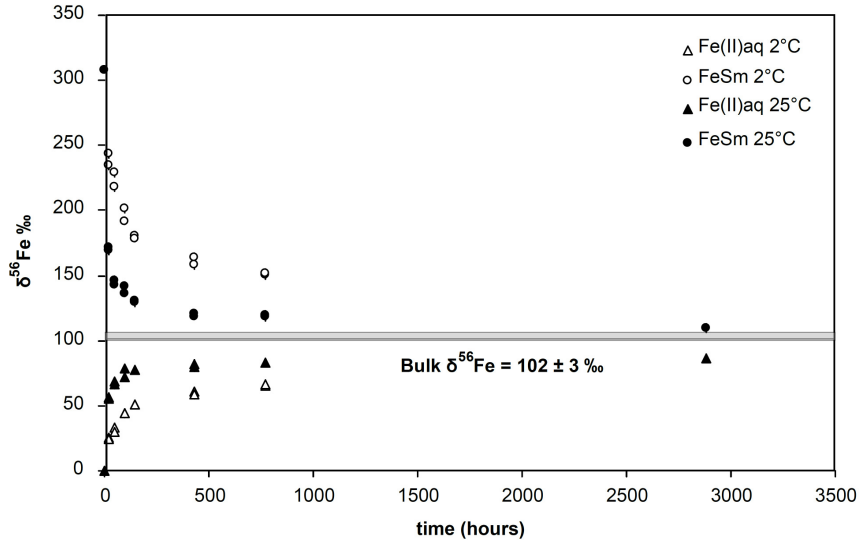

Figure 5.3: Time evolution of Fe isotope compositions of FeS_m (circles) and $Fe(II)_{aq}$ (triangles) at 25°C (filled signs) and 2°C (open signs). 2°C experiments were stopped after one month. 25°C experiments were stopped after four months. The grey area is the bulk composition of the system including errors.

5.3.2. Experiment starting with $\delta^{56}Fe_{FeS}$ ~ 2.6 ‰ at 25°C

For the reasons explained above, it was assumed that decreasing the initial fractionation between the phases from ~ 308 ‰ to ~ 2.6 ‰ would produce smaller error bars on the predicted $\Delta^{56}Fe_{Fe(II)\text{-}FeS}$. However in actuality, because the compositions of the starting materials are so near to the equilibrium value, the experimental error is too large to determine $\Delta^{56}Fe_{Fe(II)\text{-}FeS}$ with precision. Although trends were visible on a three isotope plot, the 95 % confidence envelopes were larger than the predicted fractionation.

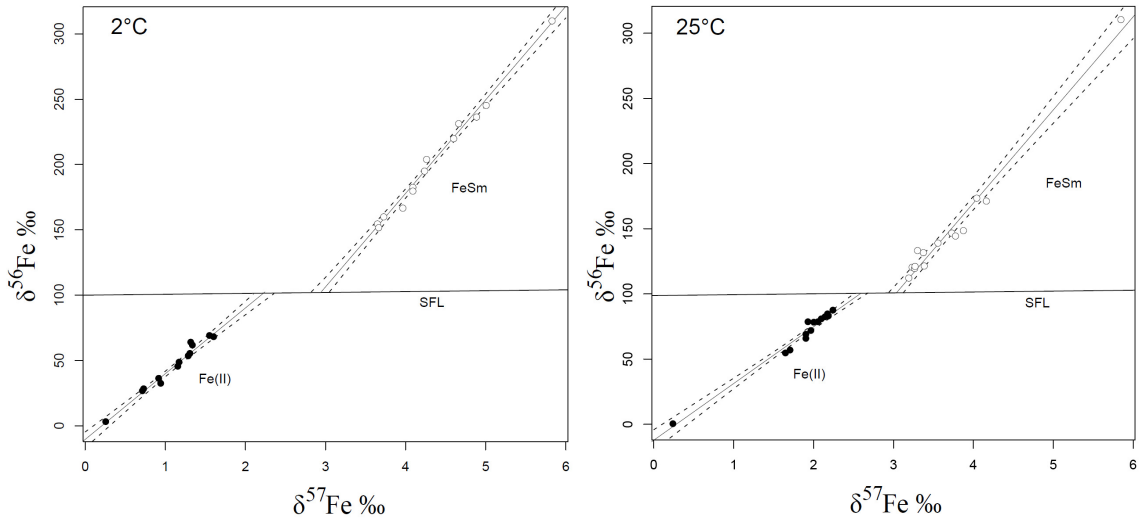

Figure 5.4: Three isotope plots starting with $\delta^{56}Fe_{FeS}$ ~ 308 ‰ and predicted equilibrium Fe isotope fractionations on the SFL between FeS_m (open circles) and $Fe(II)_{aq}$ (filled circles). $\Delta^{56}Fe_{Fe(II)\text{-}FeS}$ is the difference between the intersections of the regression lines with the SFL. 95 % confidence envelopes are calculated from Eq. 5.2.

5.4. Discussion

5.4.1. Equilibrium fractionation and mechanisms for isotope exchange

The Fe isotope equilibrium fractionation factor for the exchange reaction between $Fe(II)_{aq}$ and FeS_m (Eq. 5.13), $\alpha^{56/54}_{Fe(II)_{aq}-FeS_m}$, is 0.99948 ± 0.00002 at 2°C and 0.99967 ± 0.00002 at 25°C, and is given by Eq. 5.14:

$$^{56}FeS_m + {}^{54}Fe(II)_{aq} = {}^{54}FeS_m + {}^{56}Fe(II)_{aq} \qquad (5.13)$$

$$\alpha^{56/54}_{Fe(II)_{aq}-FeS_m} = \frac{\delta^{56}Fe_{Fe(II)_{aq}} + 1000}{\delta^{56}Fe_{FeS_m} + 1000} \qquad (5.14)$$

Our experimentation demonstrates that at equilibrium, mackinawite is enriched in ^{56}Fe in respect with $Fe(II)_{aq}$. This confirms that the Fe isotope fractionation between

FeS_m and $Fe(II)_{aq}$ after 168 hours ageing, first observed by Butler *et al.* (2005) does not represent equilibrium, but a dynamic steady state. Similarly, Böttcher *et al.* (1998) came to the same conclusion from their S isotope study on FeS_m precipitation. We suggest that the reasons for the slow isotope exchange in the aqueous Fe-S system involve the asymmetric kinetics of dissolution and precipitation of FeS_m and the growth of FeS_m nanoparticles. As noted in the introduction, the rates of precipitation (including nucleation and crystal growth) and dissolution of FeS_m in the FeS_m-H_2O system are well known (*e.g.* Rickard, 1995; Pankow and Morgan, 1978; Rickard and Luther, 2007). The rate of FeS_m dissolution is limited by the transport of components through the particle diffusion boundary layer. This means that the driving force for the rate is essentially the chemical components potential (including Fe^{2+}, S(-II) and H^+) between the FeS_m surface and the solution. As the bulk system approaches equilibrium, the chemical potential becomes smaller and the rate decreases. Moreover, the exchange process might be complicated by crystal growth, which includes oriented aggregation growth and Ostwald ripening, where small particles dissolve in favour of bigger ones. Interestingly, studies on growth mechanisms for ZnS nanoparticles (*e.g.* Huang *et al.*, 2003) and other Fe oxides nanoparticulate systems (*e.g.* Waychunas *et al.*, 2005) indicate that in the nanoscale domain, particles are likely to grow *via* aggregation growth rather than *via* Ostwald-ripening. Rickard (2006) discussed the solubility of FeS_m and showed that FeS_m is sparingly soluble (pK_{sp} = 3.5 ± 0.25). This means that if the mechanism responsible for Fe isotope exchange is dissolution-precipitation, it might be restricted to the mineral-media interface, rather than between whole FeS_m particles and the solution, as one would expect with Ostwald-ripening. Since the particle surface area is inversely proportional to the rate of dissolution (*e.g.* Pankow and Morgan, 1978; Rickard and Sjoberg, 1983), this tends to further inhibit the rate of approach to equilibrium. Experimentally, after 30 days, Fe isotopic exchange reaches an apparent constant value of ~ 75% and ~ 85% of exchange for 2°C and 25°C, respectively. The temperature dependence of the isotopic exchange suggests that at higher temperatures, the system would reach equilibrium more rapidly.

The pH of the Fe(II) solution was ~ 4, and the dominant Fe bearing species in the aqueous solution is the hexaqua $Fe[H_2O]_6^{2+}$ (normally referred as Fe^{2+}). Up to ~ 45% of the total dissolved Fe(II) was constituted by the weak outer-sphere SO_4^{2-} ligand

complex, $Fe[H_2O]_6SO_4^0{}_{aq}$ (PHREEQC Interactive 2.15.0® gave 45% and Visual MINTEQ 2.61® 42%). In $Fe[H_2O]_6SO_4^0{}_{aq}$, there is no Fe-SO_4^{2-} bond as SO_4^{2-} is only bonded to the inner-sphere of Fe^{2+}. Its participation in $Fe(II)_{aq}$ speciation has thus a negligible effect on the recorded Fe isotope fractionation since the ligand-exchange mechanism occurring remains unaffected. Rickard (2006) showed that under acidic conditions, the equilibrium solubility of FeS_m is described by $\log K_{sp} = \log \{Fe^{2+}\} + \log \{H_2S\} - 2 \log \{H^+\}$. Under neutral to alkaline conditions, the equilibrium solubility of FeS_m is pH independent, and FeS_m dissolves into $FeS^0{}_{aq}$. In our experiment, the $Fe(II)_{aq}$ solution was ~ pH 4 and Σ[S(-II)] was 0.05 M. Fig. 5.5 shows the solubility curves for FeS_m at various Σ[S(-II)]. For Σ[S(-II)] = 0.05 M (this study) the dominant Fe(II) species at pH 4 is Fe^{2+}. For these reasons, the measured equilibrium fractionation between $Fe(II)_{aq}$ and FeS_m equates to the equilibrium isotope fractionation between the chemical species $Fe^{2+}{}_{aq}$ and FeS_m, $\Delta^{56}Fe_{Fe^{2+}\text{-}FeS}$.

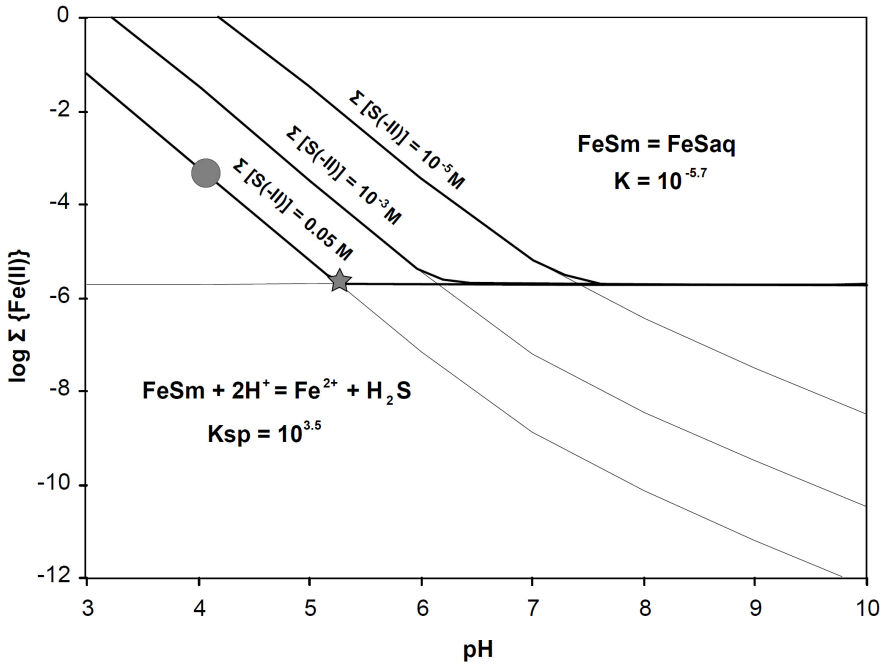

Figure 5.5: Modified from Rickard (2006). Total dissolved Fe(II) activity in equilibrium with FeS_m for various total [S(-II)] (bold lines). pH dependent and independent reactions are showed as fine lines. Our experiment corresponds to the region marked by a circle. The grey star represents the limit at which FeS_{aq} becomes the dominant $Fe(II)_{aq}$ species, as opposed to Fe^{2+} (pH ~ 5.2 for Σ[S(-II)] = 0.05 M).

For pH > 5.2, FeS_m solubility is pH independent and total dissolved Fe(II) species are dominated by $FeS^0{}_{aq}$. Rickard and Morse (2005) characterised $FeS^0{}_{aq}$ as

multinuclear Fe-S complexes whose stoichiometry ranges from Fe_2S_2 to $Fe_{150}S_{150}$ where the first condensed phase precipitates. Luther and Rickard (2005) showed that metal sulfide clusters in the Fe-S, Cu-S and Zn-S systems are structurally congruent with the first-formed solid phase. This leads to a limited energy barrier in the nucleation of these phases from solution. Rickard and Morse (2005) emphasised on the structural similarity between Fe_2S_2 and FeS_m. This means that the alkaline dissolution of FeS_m into FeS^0_{aq} may involve less Fe-S bond breaking than under acidic conditions, and the majority of Fe(II) is ligated by S both in solution or in the solid phase. For these reasons we propose that under neutral to alkaline conditions, the resulting Fe isotope fractionation between FeS_m and FeS^0_{aq} is small and insignificant. The equilibrium isotope distribution between Fe^{2+}_{aq} and FeS_m is independent of the two FeS_m forming pathways (Eqs. 5.15 and 5.16):

$$pH < 5.2 : Fe^{2+} + H_2S \rightarrow FeS_m \qquad (5.15)$$

$$pH > 5.2 : Fe^{2+} + H_2S \rightarrow FeS^0_{aq} \rightarrow FeS_m \qquad (5.16)$$

Consequently, we propose that $\Delta^{56}Fe_{Fe^{2+}-FeS_m} \approx \Delta^{56}Fe_{Fe^{2+}-FeS^0_{aq}}$, and that the fractionation factor determined in this study is applicable to equilibrium isotope distributions between Fe^{2+}_{aq} and FeS_m at alkaline pH. It is important to emphasise however that, unlike at acid pH, the analytically measured isotopic fractionation between $Fe(II)_{aq}$ (*i.e.* all dissolved Fe(II) species) and FeS_m at neutral to alkaline pH is controlled by the predominance of the FeS^0_{aq} reservoir over the Fe^{2+}_{aq} reservoir. Unfortunately, the low total dissolved Fe concentrations present at alkaline pH make this area difficult to access experimentally.

5.4.2. Comparison with calculated predictions

To our knowledge, no calculated data exist for the equilibrium fractionation between $Fe(II)_{aq}$ and FeS_m. However, β-factors for aqueous Fe(II), pyrite and the Fe(II) monosulfide troilite have been documented (*e.g.* Schauble *et al.*, 2001; Anbar *et al.*, 2005; Polyakov *et al.*, 2000; Polyakov and Mineev, 2007; Blanchard *et al.*, 2009). Schauble *et al.* (2001) used published vibrational data and empirical force field model (the Modified Urey-Bradley Force Field model, MUBFF) to estimate the β-factors of numerous Fe(II) and Fe(III) aqueous complexes including hexaqua Fe(II). Jarzecki *et al.* (2004) and Anbar *et al.* (2005) used Density Function Theory (DFT) to estimate the β-factors of hexaqua Fe(III) and hexaqua Fe(II). Polyakov and Mineev (2000) and

Polyakov *et al.* (2007) used Mössbauer and inelastic nuclear resonant X-ray scattering (INRXS) data to provide β-factors for pyrite and troilite among others. In order to interpret natural data measured in pyrite, they assumed that the β-factors for mackinawite would be similar to those for troilite, since both are Fe(II) monosulfides. Blanchard *et al.* (2009) used first principles calculations (Schauble *et al.*, 2001,2006) to discuss the pyrite β-factors given by the technique from Polyakov and co-workers. Fig. 5.6 shows the temperature dependence of equilibrium $\Delta^{56}Fe_{Fe(II)\text{-}sulfide}$ for pyrite, troilite and our experiment. β-factors for $Fe(II)_{aq}$ are from Schauble *et al.* (2001) and Anbar *et al.* (2005). β-factors for pyrite and troilite are from Blanchard *et al.* (2009), Polyakov and Mineev (2000) and Polyakov *et al.* (2007). Our results demonstrate that mackinawite and troilite, do not display similar fractionations with respect to $Fe(II)_{aq}$, which is expected since troilite is a hexagonal Fe(II) monosulfide, with no stability region at low temperature (Rickard and Luther, 2007). Equilibrium enrichment of heavier Fe isotopes in FeS_m is consistent with calculated fractionations for pyrite, which is predicted to incorporate heavy isotopes.

Beard *et al.* (2010) observed that in general, comparisons between predicted and observed equilibrium fractionations are more consistent for fluid-fluid or mineral-mineral fractionations, rather than for fluid-mineral fractionations. In our case, calculated values for FeS_m β-factors are needed to assess the consistency between theory and experiments.

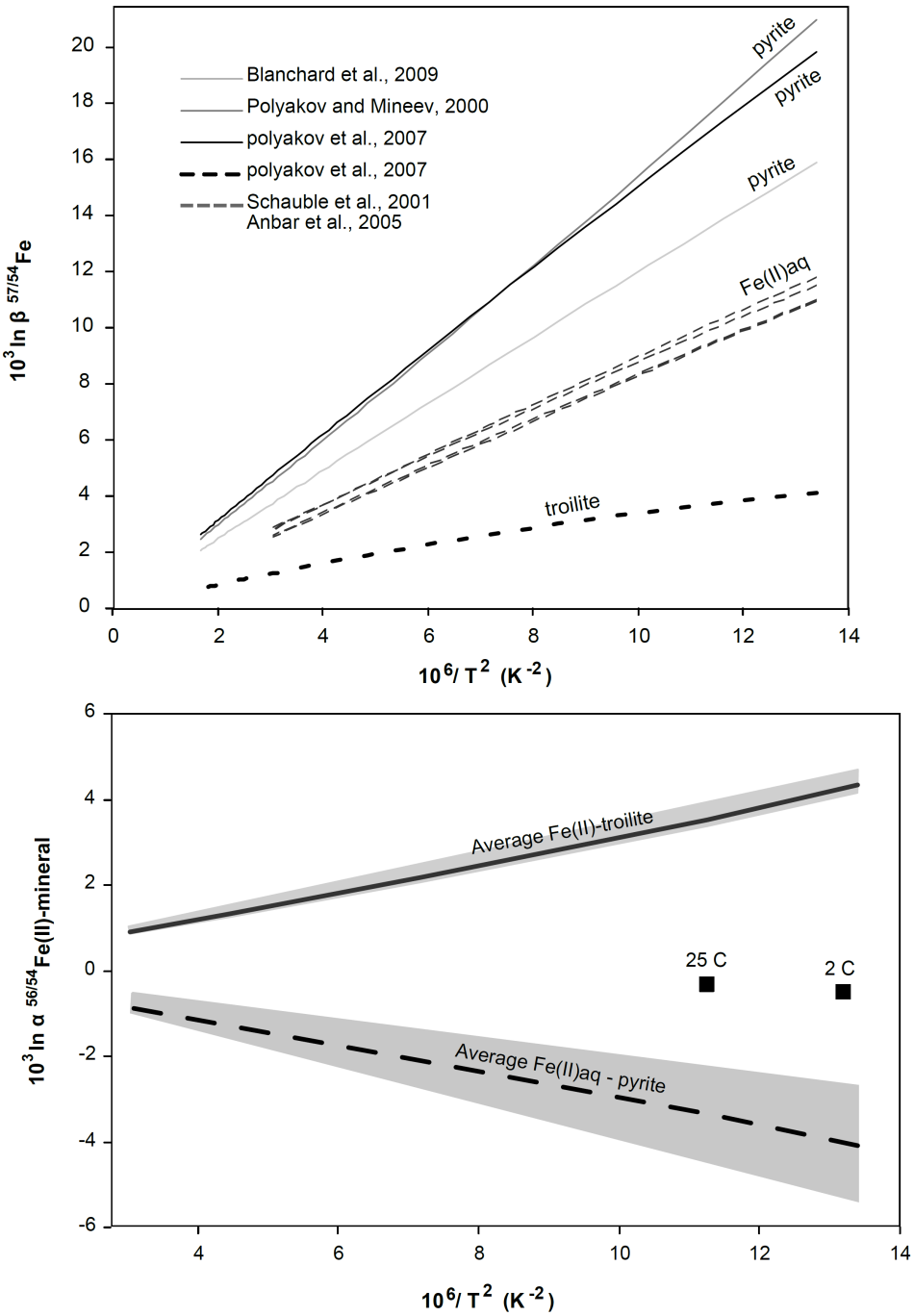

Figure 5.6: A: *β*-factors for troilite (bold-dot line, Polyakov *et al.*, 2007), $Fe(II)_{aq}$ (grey dot lines, Schauble *et al.*, 2001; Anbar *et al.*, 2005) and pyrite (plain lines, Blanchard *et al.*, 2009; Ployakov and Mineev, 2000; Polyakov *et al.*, 2007). B: Temperature dependence of $\Delta^{56}Fe_{Fe(II)\text{-mineral}}$ for average pyrite (bold line), average troilite (dot-line) and our experimental results (filled squares) calculated from the *β*-factors from A. Grey areas correspond to the uncertainties from calculations.

5.4.3. Comparison with other experimental studies

Experimental studies have shown that redox processes produce the largest equilibrium Fe isotope fractionations. At 20°C, equilibrium fractionation between

$Fe(III)_{aq}$ and $Fe(II)_{aq}$ is ~ +3 ‰ (Johnson *et al.*, 2002; Welch *et al.*, 2003), $\Delta^{56}Fe_{Fe(II)aq\text{-}hematite}$ is ~ - 3 ‰ (Johnson *et al.*, 2002; Skulan *et al.*, 2002; Welch *et al.*, 2003); $\Delta^{56}Fe_{Fe(II)aq\text{-}magnetite}$ is ~ -1.3 ‰ (Johnson *et al.*, 2005), and $\Delta^{56}Fe_{Fe(II)aq\text{-}Fe(III)oxide}$ is ~ -0.9 ‰ (Bullen *et al.*, 2001) and Beard *et al.* (2010) observed a $\Delta^{56}Fe_{Fe(II)aq\text{-}goethite}$ of ~ -1 ‰. In our experiment, [Fe] was equimolar in FeS_m and $Fe(II)_{aq}$ and no redox process was involved. By analogy, Wiesli *et al.* (2004) found that the equilibrium fractionation recorded between the non-redox $Fe(II)_{aq}$-siderite couple was ~ 0.48 ‰.

Amongst all transition metal-sulfides, only the behaviour of Cu and Zn isotopes during the precipitation of CuS and ZnS have been studied. CuS precipitates from $Cu(II)_{aq}$ with $\Delta^{65}Cu_{Cu(II)aq\text{-}CuS} = 3.06 \pm 0.14$ ‰ (Ehrlich *et al.*, 2004). Ehrlich *et al.* (2004) interpreted this result as a redox effect, since the precipitate is reduced to Cu(I)S from the aqueous Cu(II). Like FeS and CuS, Archer (2007) showed that ZnS precipitates from $Zn(II)_{aq}$ with depletion in heavy isotopes ($\Delta^{66}Zn_{Zn(II)aq\text{-}ZnS}$ ~ 0.4 ‰). However, both Ehrlich *et al.* (2004) and Archer (2007) argued that their values were likely to be kinetic fractionations, CuS and ZnS being significantly less soluble than FeS_m ($Ksp_{FeS} = 3.5$, (Rickard, 2006); $Ksp_{CuS} = 22.2$, (Smith *et al.*, 1976); $Ksp_{sphalerite} = 10.93$, (Dyrssen and Kremling, 1990); where *K*sp values given here are for free hexaqua species and the minerals).

5.4.4. Implications for modern natural systems

In marine sedimentary environments, the predominant Fe aqueous species include Fe(III)hydroxyl complexes and Fe^{2+} (Turner *et al.*, 1981). Rickard and Morse (2005) argued that in anoxic, sulfidic environments, Fe(III) species are not significant and concluded that Fe^{2+} is the dominant Fe non-sulfide species under those conditions. In anoxic sedimentary systems isolated from hydrothermal inputs, sources for Fe^{2+} include i) microbial Fe(III) reduction and ii) sulfidation of detrital and/or authigenic highly reactive Fe(III) oxides. Both mechanisms occur at the early stages of diagenesis (Canfield *et al.*, 1992; Poulton and Raiswell 2002). Raiswell and Canfield (1998) showed that modern anoxic/suboxic sediments (*e.g.* Black Sea, Cariaca Basin, Framvaren Fjord) are enriched in highly reactive Fe minerals. Mechanisms for Fe(III) (oxy)hydroxides reduction to Fe(II) are summarised by Wells *et al.* (1995). Sulfidation of Fe(III) oxyhydroxides, such as goethite, is a fast process (Rickard, 1974; Pyzik and Sommer, 1981; Wei and Osseo-Asare, 1996) that occurs *via* dissolution of the mineral surface, reduction of Fe(III) to Fe(II) and subsequent

precipitation of FeS_m. In such environments, the major source for S(-II) is bacterial sulfate reduction, BSR (Raiswell and Berner, 1985) which occurs at a lower rate than Fe reduction (*e.g.* Berner, 1981; Canfield *et al.*, 1992). Canfield *et al.* (1992) thus concluded that enrichment in dissolved S(-II) in those environments could only occur after partial sulfidation of Fe(III) oxides. Hence, FeS_m and dissolved Fe(II) should coexist in most environments in which $\Sigma\{S(-II)\}$ and $\Sigma\{Fe(II)\}$ are low (where I.A.P just exceeds Ksp_{FeS}) or where $\Sigma\{Fe(II)\}$ is significantly greater than $\Sigma\{S(-II)\}$, *i.e.* in some marginal environments (costal, deltaic and ridge areas), at the oxic-anoxic interface where sulfide starts forming from sulphate reduction or within the anoxic zone in which H_2S reduces Fe(III) species to Fe^{2+}. In environments in which Fe reduction is extensive, the process may be localised to the boundary between the suboxic and the anoxic zones. Rickard and Morse (2005) noted that FeS_m has been principally observed in Fe rich environments, and rarely observed under "normal" marine conditions. They showed that where FeS_m is present, Fe(II) remains in solution as FeS^0_{aq} or as $Fe(II)_{aq}$ at quite large concentrations. Our results and those from Butler *et al.* (2005) converge to the same conclusion: in the 2-40°C range, the Fe-S system is slow to attain isotopic equilibrium. This means that for surface environments, the equilibrium number cannot be simply applied, and naturally occurring FeS_m is likely to conserve its slow-exchange kinetic signature. Severmann *et al.* (2006) measured the Fe isotope compositions of highly reactive Fe in the anoxic margin basins. They documented $\delta^{56}Fe$ values for pore waters, pyrite, and HCl extractable solid phases (*i.e.* FeS_m and $Fe(OH)_3$). Fig. 5.7 compares the natural measurements with experimentally determined kinetic and equilibrium fractionations between $Fe(II)_{aq}$ and the solids. The data suggest that under diagenetic conditions, the solid products are not in equilibrium with the pore water. Rickard *et al.* (2007) showed in a cross-over plot that there is no direct link between FeS_m, AVS, and pyrite within the same sediment, since $Fe(II)_{aq}$ can remain dissolved for large temporal and spatial scales in anoxic environments. Therefore, the measured compositions of natural sediments do not necessarily provide fractionation factors between the phases but reflect complicated interaction between the solids and the surrounding liquid.

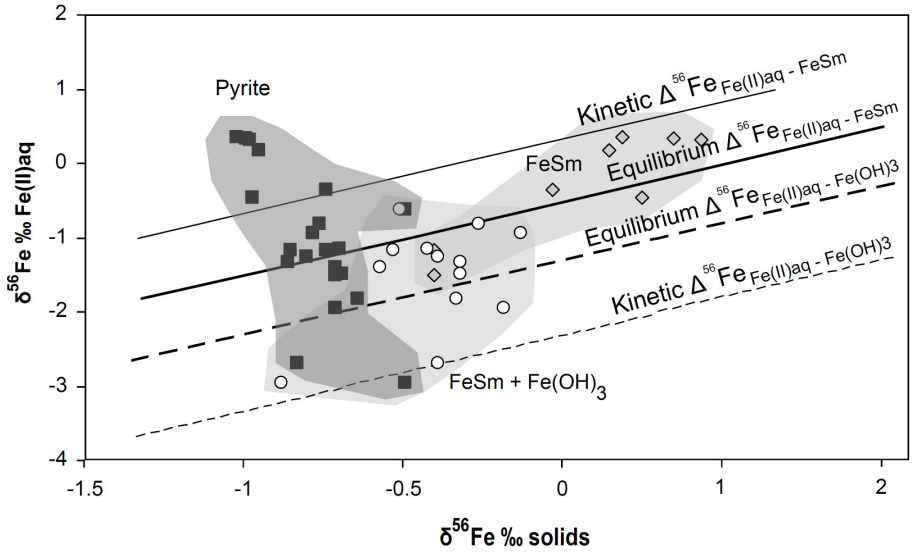

Figure 5.7: Plot of the isotopic compositions of pore water versus the solid highly reactive iron phases, modified after Johnson *et al.* (2008). Data for pyrite (filled squares) and HCl extracted phases (grey diamonds and open circles) are from Severmann *et al.* (2006). Compositions for FeS_m were derived from HCl extraction data where $Fe(II)_{HCl}$ > 80%, as suggested by Johnson *et al.* (2008). Kinetic $\Delta^{56}Fe_{Fe(II)aq\text{-}FeSm}$ are from Butler *et al.* (2005). We used our 2°C values for equilibrium $\Delta^{56}Fe_{Fe(II)aq\text{-}FeSm}$. Kinetic and equilibrium $\Delta^{56}Fe_{Fe(II)aq\text{-}Fe(OH)3}$ are from Johnson *et al.* (2004).

5.4.5. Implications for ancient sedimentary signatures

In the Fe-S system, Fe is eventually sequestered into pyrite. At least 28 different reactions have been reported for low temperature aqueous synthesis of pyrite (Rickard and Luther, 2007). The use of FeS_m as the Fe(II) reactant for one of these reactions is popular amongst the experimental community since FeS_m first precipitates, giving sufficient nutrient concentration to produce a useful mass of pyrite. In modern natural environments, as mentioned above, FeS_m as a reactant is limited to inshore and freshwater systems or as a surface product of Fe oxyhydroxide sulfidation. Thus the Fe isotope fractionation recorded during the formation of FeS_m need not influence the Fe isotope composition of pyrite from all geological environments. However, it is possible that FeS_m may have played a major role in diagenetic pyrite formation in sedimentary systems older than ~ 2.4 Ga, in which oceans were $Fe(II)_{aq}$ rich and anoxic (*e.g.* Holland, 1984). Interestingly, it is in those Proterozoic to Archean sediments that pyrite displays the largest Fe isotope excursions. There has been widespread interest in the possible use of $\delta^{56}Fe_{pyrite}$ as a paleo-proxy for seawater compositions (*e.g.* Anbar and Rouxel, 2007; Archer and Vance, 2006). But the fractionation involved during the pyrite formation stage is still unknown. Rouxel *et al.*

(2005) showed that Proterozoic pyrites display positive $\delta^{56}Fe$, which is in agreement with the equilibrium calculations for pyrite (Polyakov *et al.*, 2007; Polyakov and Mineev, 2000) and our experimental prediction for mackinawite. However the negative isotopic composition of Archean pyrites implies that further fractionating mechanisms are involved.

The results of this experimentation, along with those reported by Butler *et al.* (2005), suggest that FeS_m Fe isotope compositions are contained in a ~ 1.4 ‰ range depending on the degree of FeS_m precipitation and equilibration. Depending on the rate of pyrite formation, pyrite might record the lowest $\delta^{56}Fe$ where Fe_{FeS} is rapidly incorporated into pyrite. Mechanistically, FeS_m dissolves into FeS_{aq} which reacts with S(-II) to form pyrite. The final composition of pyrite will thus depend on the fractionation occurring during FeS_m dissolution, on the extent of mixing with free hexaqua Fe(II) and on the extent of pyritisation. For higher temperatures, *i.e.* during later stages of diagenesis, isotopic equilibration between FeS_m and $Fe(II)_{aq}$ might be reached.

5.5. Conclusions

We have determined the Fe isotope equilibrium fractionation between $Fe(II)_{aq}$ and mackinawite at 2°C and 25°C using the three-isotope method. Equilibrium fractionation $\Delta^{56}Fe_{Fe(II)\text{-}FeS}$ is -0.52 ± 0.16 ‰ at 2°C and -0.33 ± 0.12 ‰ at 25°C and is equivalent to the distribution between the species Fe^{2+}_{aq} and FeS_m ($\Delta^{56}Fe_{Fe2+\text{-}FeS}$). Fractionations produce ^{56}Fe enriched mackinawite and ^{56}Fe depleted dissolved Fe(II). Our results contrast with the kinetic fractionation of $\Delta^{56}Fe_{Fe(II)\text{-}FeS}$ = +0.85 to +0.30 ‰ determined by (Butler *et al.*, 2005) with which mackinawite remains depleted even after long term ageing. This means that depending on the degree of FeS_m precipitation from solution, and the degree of isotope exchange during equilibration, FeS_m displays $\delta^{56}Fe$ values in a ~ 1.4 ‰ range. At low temperatures, equilibrium is not reached in periods of less than years. This means that in natural systems, FeS_m is likely to be depleted with regard to its equilibrium value and record a kinetic signature. Further experiments are required to assess the mechanisms responsible for the Fe isotope exchange between aqueous and solid phases.

Our experimental predictions are significantly below the calculated fractionations for the hexagonal Fe(II) monosulfide troilite. There is no obvious evidence why troilite and mackinawite should produce similar β-factors.

Here, we provide the first experimentally determined equilibrium numbers for any metal sulfides. This work is fundamental to isolate and understand each step of Fe isotope fractionations during the formation of pyrite under diagenetic conditions. Further experiments are required to investigate the Fe isotope fractionations occurring in the neutral to alkaline region, where $Fe(II)_{aq}$ speciation is dominated by the clusters FeS^0_{aq}. However, we predict that the fractionation between FeS^0_{aq} and FeS_m will be small. Experimental isotopic studies in this system would be helpful in further elucidating the roles of the aqueous sulfide clusters in the nucleation of solid phases from solution.

5.6. Acknowledgements

We are thankful to Alan Matthews, Veniamin Polyakov, Mark Naylor and Marek Pękala for constructive discussions that helped improving the experimental set up and the manuscript. We also thank Kathleen Keefe and Vincent Gallagher for technical support. This work was funded by an ECOSSE PhD studentship to RG and NERC research grant NE/E003958/1 to IBB.

5.7. References

Anbar A. D. (2004) Iron stable isotopes: beyond biosignatures. *Earth and Planetary Science Letters* **217**, 223-236.

Anbar A. D., Jarzecki A. A., and Spiro T. G. (2005) Theoretical investigation of iron isotope fractionation between $Fe(H_2O)_6^{3+}$ and $Fe(H_2O)_6^{2+}$: Implication for iron stable isotope geochemistry. *Geochim. Cosmochim. Acta* **69**(4), 825-837.

Anbar A. D., Roe J. E., Barling J., and Nealson K. H. (2000) Nonbiological fractionation of iron isotopes. *Science* **288**, 126-128.

Anbar A. D. and Rouxel O. (2007) Metal Stable Isotopes in Paleoceanography. *Annu. Rev. Earth Planet. Sci.* **35**, 717–746.

Archer C. (2007) The application of transition metal isotope systems to biogeochemical studies of the early Earth. PhD thesis. Royal Holloway University London.

Archer C. and Vance D. (2006) Coupled Fe and S isotope evidence for Archean microbial Fe(III) and sulfate reduction. *Geology* **34**, 153-156.

Beard B. and Johnson C. (2004) Fe Isotope Variations in the Modern and Ancient Earth and Other Planetary Bodies. *Reviews in Mineralogy & Geochemistry* **55**, 319-357.

Beard B. L., Handler R. M., Scherer M. M., Wu L., Czaja A. D., Heimann A., and Johnson C. M. (2010) Iron isotope fractionation between aqueous ferrous iron and goethite. *Earth and Planetary Science Letters* **295**(1-2), 241-250.

Beard B. L., Johnson C. M., Cox L., Nealson K. H., and Aguilar C. (1999) Iron isotope biosignatures. *Science* **285**, 1889-1892.

Beard B. L., Johnson C. M., Skulan J. L., Nealson K. H., Cox L., and Sun H. (2003) Application of Fe isotopes to tracing the geochemical and biological cycling of Fe. *Chem. Geol.* **195**, 87-117.

Berner R. A. (1981) A New Geochemical Classification of Sedimentary Environments. *J. Sediment. Research* **51**.

Blanchard M., Poitrasson F., Méheut M., Lazzeri M., Mauri F., and Balan E. (2009) Iron isotope fractionation between pyrite (FeS2), hematite (Fe2O3) and siderite (FeCO3): A first-principles density functional theory study. *Geochimica et Cosmochimica Acta* **73**(21), 6565-6578.

Borradaile G. (2003) Statistics of Earth Science Data. Springer-Verlag.

Böttcher M. E., Smock A. M., and Cypionka H. (1998) Sulfur isotope fractionation during experimental precipitation of iron(II) and manganese(II) sulfide at room temperature. *Chemical Geology* **146**(3-4), 127-134.

Brantley S. L., Liermann L., and Bullen T. D. (2001) Fractionation of Fe isotopes by soil microbes and organic acids. *Geology* **29**(6), 535-538.

Brantley S. L., Liermann L. J., Guynn R. L., Anbar A., Icopini G. A., and Barling J. (2004) Fe isotopic fractionation during mineral dissolution with and without bacteria. *Geochimica. Cosmochim. Acta* **68**, 3189–3204.

Bullen T. D., White A. F., Childs C. W., Vivit D. V., and Schulz M. S. (2001) Demonstration of significant abiotic ion isotope fractionation. *Geology* **29**, 699-702.

Butler I. B., Archer C., Vance D., Oldroyd A., and Rickard D. (2005) Fe isotope fractionation on FeS formation in ambient aqueous solution. *Earth and Planet. Science Letters* **236**(430-442).

Butler I. B., Schoonen M. A. A., and Rickard D. T. (1994) Removal of dissolved oxygen from water: A comparison of four common techniques. *Talanta* **41**(2), 211-215.

Canfield D. E., Raiswell R., and Bottrell S. H. (1992) The reactivity of sedimentary iron minerals toward sulfide. *American Journal of Science* **292**, 659-683

Criss R. E. (1999) Principles of stable isotope distribution. *Oxford University Press, New York*, 244pp.

Croal L. R., Johnson C. M., Beard B. L., and Newman D. K. (2004) Iron isotope fractionation by Fe(II)-oxidizing photoautotrophic bacteria. . *Geochim Cosmochim Acta* **68**, 1127-1242.

Dauphas N. and Rouxel O. (2006) Mass Spectrometry and natural variations of iron isotopes. *Mass Spectrometry Reviews* **25**, 515-550.

Dyrssen D., Kremling, K. (1990) Increasing hydrogen sulfide concentration and race metal behaviour in the anoxic Baltic waters. *Marine Chemistry* **30**, 193-204.

Ehrlich S., Butler I., Halicz L., Rickard D., Oldroyd A., and Matthews A. (2004) Experimental study of the copper isotope fractionation between aqueous Cu(II) and covellite, CuS. *Chemical Geology* **209**(3-4), 259-269.

Graham C. M. (1981) Experimental hydrogen isotope studies III: Diffusion of hydrogen in hydrous minerals, and stable isotope exchange in metamorphic rocks. *Contributions to Mineralogy and Petrology* **76**(2), 216-228.

Guilbaud R., Ellam R. M., Butler I. B., and Rickard D. (2008) Fe isotope fractionation in the Fe-S system at low temperature. *American Geophysical Union, Fall Meeting* (abstract).

Guilbaud R., Ellam R. M., Butler I. B., Gallagher V., and Keefe K. (2010) A procedural development for the analysis of $^{56/54}$Fe and $^{57/54}$Fe isotope ratios with new generation IsoProbe MC-ICP-MS. *J. Anal. At. Spectrom*. DOI: 10.1039/c004876c.

Handler R. M., Beard B. L., Johnson C. M., and Scherer M. M. (2009) Atom Exchange between Aqueous Fe(II) and Goethite: An Fe Isotope Tracer Study. *Environmental Science & Technology* **43**(4), 1102-1107.

Hill P. S. and Schauble E. A. (2008) Modeling the effects of bond environment on equilibrium iron isotope fractionation in ferric aquo-chloro complexes. *Geochimica et Cosmochimica Acta* **72**(8), 1939-1958.

Holland H. D. (1984) The chemical evolution of the atmosphere and oceans. *New York: Princeton University Press.*

.

Huang F., Zhang H., and Banfield J. F. (2003) Two-Stage Crystal-Growth Kinetics Observed during Hydrothermal Coarsening of Nanocrystalline ZnS. *Nano Letters* **3**(3), 373-378.

Icopini G. A., Anbar A. D., Ruebush S. S., Tien M., and Brantley S. L. (2004) Iron isotope fractionation during microbial reduction of iron: The importance of adsorption. . *Geology* **32**, 205-208.

Jang J.-H., Mathur R., Liermann L. J., Ruebush S., and Brantley S. L. (2008) An iron isotope signature related to electron transfer between aqueous ferrous iron and goethite. *Chemical Geology* **250**(1-4), 40-48.

Jarzecki A. A., Anbar A. D., and Spiro T. G. (2004) DFT Analysis of $Fe(H_2O)_6^{3+}$ and $Fe(H_2O)_6^{2+}$ Structure and Vibrations; Implication for Isotope Fractionation. *J. Phys. Chem. A.* **108**, 2726-2732.

Jeong H. Y., Lee J. H., and Hayes K. F. (2008) Characterization of synthetic nanocrystalline mackinawite: Crystal structure, particle size, and specific surface area. *Geochimica et Cosmochimica Acta* **72**(2), 493-505.

Johnson C. M., Beard B. L. and Roden E. E. (2008) The iron isotope fingerprints of redox and biogeochemical cycles in modern and ancient Earth. *Annu. Rev. Earth Planet. Sci.* **36**, 457–93.

Johnson C. M., Beard B. L., Roden E. E., Newman D. K., and Nealson K. H. (2004) Isotopic Constraints on Biochemical Cycling of Fe. *Reviews in Mineralogy & Geochemistry* **55**, 359-408.

Johnson C. M., Beard B. L., Welch S., Croal L., Newman D., and Nealson K. (2005) Experimental constraints on Fe isotope fractionations during biogeochemical cycling of Fe. *Geochim. Cosmochim. Acta* **66**, A371.

Johnson C. M., Skulan J. L., Beard B. L., Sun H., Nealson K. H., and Braterman P. S. (2002) Isotopic fractionation between Fe(III) and Fe(II) in aqueous solutions. *Earth and Planetary Science Letters* **195**(1-2), 141-153.

Ludwig K. R. (1980) Calculation of uncertainties of U-Pb isotope data. *Earth. Planet. Sc. Lett.* **46**, 212-220.

Luther G. W. and Rickard D. T. (2005) Metal sulfide cluster complexes and their biogeochemical importance in the environment. *Journal of Nanoparticle Research* **7**, 212-220.

Matsuhisa Y., Goldsmith J. R., and Clayton R. N. (1978) Mechanisms of hydrothermal crystallization of quartz at 250°C and 15 kbar. *Geochimica et Cosmochimica Acta* **42**(2), 173-182.

Matsuhisa Y., Goldsmith J. R., and Clayton R. N. (1979) Oxygen isotopic fractionation in the system quartz-albite-anorthite-water. *Geochimica et Cosmochimica Acta* **43**(7), 1131-1140.

Matthews A., Goldsmith J. R., and Clayton R. N. (1983a) On the mechanisms and kinetics of oxygen isotope exchange in quartz and feldspars at elevated temperatures and pressures. *Geol. Soc. Am. Bul.* **94**, 396-412.

Matthews A., Goldsmith J. R., and Clayton R. N. (1983b) Oxygen isotope fractionation involving pyroxenex: the calibration of mineral-pair geothermometers. *Geochim. Cosmochim. Acta* **47**, 631-644.

Matthews A., Morgans-Bell H. S., Emmanuel S., Jenkyns H. C., Erel Y., and Halicz L. (2004) Controls on iron-isotope fractionation in organic-rich sediments (Kimmeridge Clay, Upper Jurassic, Southern England). *Geochimica et Cosmochimica Acta* **68**(14), 3107-3123.

McAnena A., Severmann S., and Poulton S. W. (2009) Abiotic Fe isotope fractionation during sulfide mediated reductive dissolution of Fe oxide minerals. *Goldschmidt Conference Abstracts*.

Michel F. M., Antao S. M., Chupas P. J., Lee P. L., Parise J. B. and Schoonen M. A. A. (2005) Short- to medium- range atomic order and crystallite size of the initial FeS precipitate from pair distribution function analysis. *Chem. Mater.* **17**, 6246-6255.

Ohfuji H. and Rickard D. (2006) High resolution transmission electron microscopic study of synthetic nanocrystalline mackinawite *Earth and Planet. Science Letters* **241**, 227.

Pankow J. F. and Morgan J. J. (1980) Dissolution of Tetragonal Ferrous Sulfide (Mackinawite) in Anoxic Aqueous Systems. 2. Implications for the Cycling of Iron, Sulfur, and Trace Metals. *Environmental Engineering Science* **14**, 183.

Polyakov V. B., Clayton R. N., Horita J., and Mineev S. D. (2007) Equilibrium iron isotope fractionation factors of minerals: Reevaluation from the data of

nuclear inelastic resonant X-ray scattering and Mössbauer spectroscopy. *Geochimica et Cosmochimica Acta* **71**(15), 3833-3846.

Polyakov V. B. and Mineev S. D. (2000) The use of Mossbauer spectroscopy in stable isotope geochemistry. *Geochim Cosmochim Acta* **64**, 849-865.

Poulton S. W. and Raiswell R. (2002) The low-temperature geochemical cycle of iron: From continental fluxes to marine sediment deposition. *Am J Sci* **302**(9), 774-805.

Pyzik A. J. and Sommer S. E. (1981) Sedimentary iron monosulfides: kinetics and mechanisms of formation. *Geochim. Cosmochim. Acta* **45**(687-698).

Raiswell R. and Berner R. A. (1985) Pyrite formation in euxinic and semi-euxinic sediments. *Am. J. Sci.* **285**, 710-724.

Raiswell R. and Canfield D. E. (1998) Sources of iron for pyrite formation in marine sediments. *Am J Sci* **298**(3), 219-245.

Rickard D. (1974) Kinetics and mechanisms of the sulfidation of goethite. *Am. J. Sci.* **274**, 941-952.

Rickard D. (1995) Kinetics of FeS precipitation: Part 1. Competing reaction mechanisms. *Geochim. Cosmochim. Acta* **59**, 4367– 4379.

Rickard D. (2006) The solubility of FeS. *Geochimica et Cosmochimica Acta* **70**(23), 5779-5789.

Rickard D., Griffith A., Oldroyd A., Butler I. B., Lopez-Capel E., Manning D. A., and Apperley D. C. (2006) The composition of nanoparticulate mackinawite, tetragonal iron (II) monosulfide. *Chem. Geol.* **235**(286).

Rickard D. and Luther G. W., III. (1997) Kinetics of pyrite formation by the H_2S oxidation of iron(II) monosulfide in aqueous solutions between 25°C and 125°C: The mechanism. *Geochimica Cosmochimica Acta* **61**, 135-147.

Rickard D. and Luther G. W., III. (2007) Chemistry of Iron Sulfides. *Chem. Rev.* **107**, 514-562.

Rickard D. and Morse J. W. (2005) Acid Volatile Sulfide (AVS). *Marine Chemistry* **97**, 141-197.

Rickard D. and Sjoberg E. L. (1983) Mixed kinetic control of calcite dissolution rates. *American Journal of Science* **283**, 815-830.

Rouxel O. J., Bekker A., and Edwards K. J. (2005) Iron isotope constraints on the Archean and Paleoproterozoic ocean redox state. *Science* **307**, 1088-1090.

Schauble E. A., Ghosh P., and Eiler J. M. (2006) Preferential formation of 13C-18O bonds in carbonate minerals, estimated using first-principles lattice dynamics. *Geochimica et Cosmochimica Acta* **70**(10), 2510-2529.

Schauble E. A., Rossman G. R., and Taylor H. P. (2001) Theoretical estimates of equilibrium Fe-isotope fractionations from vibrational spectroscopy. *Geochimica et Cosmochimica Acta* **65**(15), 2487-2497.

Severmann S., Johnson C. M., Beard B. L., and McManus J. (2006) The effect of early diagenesis on the Fe isotope compositions of porewaters and authigenic minerals in continental margin sediments. *Geochim Cosmochim Acta* **70**, 2006–2022.

Shahar A., Young E. D., and Manning C. E. (2008) Equilibrium high-temperature Fe isotope fractionation between fayalite and magnetite: An experimental calibration. *Earth and Planet. Science Letters* **268**, 330–338.

Skulan J. L., Beard B. L., and Johnson C. M. (2002) Kinetic and equilibrium Fe isotope fractionation between aqueous Fe(III) and hematite. *Geochim. Cosmochim. Acta* **66**, 2995-3015.

Smith R. M., Martell, A.E. (1976) Critical Stability Constants, v.4, Inorganic Complexes. *Plenum Press*.

Teutsch N., von Gunten U., Porcelli D., Cirpka O. A., and Halliday A. N. (2005) Adsorption as a cause for iron isotope fractionation in reduced groundwater. *Geochim Cosmochim Acta* **69**, 4175-4185.

Theberge S. M. and Luther G.W., III. (1997) Determination of the electrochemical properties of a soluble aqueous FeS cluster present in sulfidic systems. *Aquatic Geochemistry* **3**, 191-211.

Turner D. R., Whitfield M., and Dickson A. G. (1981) The equilibrium speciation of dissolved components in freshwater and sea water at 25°C and 1 atm pressure. *Geochim Cosmochim Acta* **45**, 855-881.

Waychunas G. A., Kim C. S., and Banfield J. F. (2005) Nanoparticulate Iron Oxide Minerals in Soils and Sediments: Unique Properties and Contaminant Scavenging Mechanisms. *Journal of Nanoparticle Research* **7**(4), 409-433.

Wei D. and Osseo-Asare K. (1996) Particulate pyrite formation by the $Fe3^{+}/HS^{-}$ reaction in aqueous solutions: effects of solution composition. *Colloids and surfaces A: Physicochemical and Engineering Aspects* **118**, 51-61.

Welch S. A., Beard B. L., Johnson C. M., and Baterman P. S. (2003) Kinetic and equilibrium Fe isotope fractionation between aqueous Fe(II) and Fe(III). *Geochim. Cosmochim. Acta* **67**, 4231-4250.

Wells M. L., Price N. M., and Bruland K. W. (1995) Iron chemistry in seawater and its relationship to phytoplankton: a workshop report. *Mar. Chem.* **48**, 157-182.

Wiesli R. A., Beard B. L., and C.M. J. (2004) Experimental determination of Fe isotope fractionation between aqueous Fe(II), siderite and "green rust" in abiotic systems. *Chem. Geol.* **211**, 343-362.

Wolthers M., van der Gaast S. J., and Rickard D. (2003) The structure of distored mackinawite. *Am. Mineral.* **88**, 2007.

Yamaguchi K. E., Johnson C. M., Beard B. L., and Ohmoto H. (2005) Biogeochemical cycling of iron in the Archean-Paleoproterozoic Earth: Constraints from iron isotope variations in sedimentary rocks from the Kaapvaal and Pilbara Cratons. *Chem. Geol.* **218**, 135-169.

Chapter VI

A large Fe isotope fractionation during abiological pyrite formation

Manuscript submitted as Guilbaud, R., Butler, I.B. and Ellam, R.M. A large Fe isotope fractionation during abiological pyrite formation. Science.

Abstract

We provide the first quantification of the extent and the direction of Fe isotope fractionation associated with low temperature pyrite formation. We demonstrate that abiotic pyrite formation is accompanied by a large Fe isotope fractionation without the intervention of any Fe(II) redox change. The measured kinetic isotope fractionation factor $\alpha'_{FeS\text{-}pyrite}$ = 1.0022 ± 0.0007. Combined fractionation factors between Fe^{2+}_{aq}, mackinawite (FeS_m) and pyrite permit the generation of pyrite with Fe isotope signatures that encapsulate the full range of sedimentary $\delta^{56}Fe_{pyrite}$ recorded in both Archean and modern sediments. Archean Fe isotope excursions reflect various degrees of pyritisation, extent of $Fe(II)_{aq}$ utilisation, and variations in source composition rather than microbial dissimilatory Fe(III) reduction only. Our results show that sedimentary pyrite is not a passive recorder of the Fe isotope composition of the reactive Fe(II) reservoir forming pyrite. It is the formation process itself that influences pyrite Fe isotope signatures with consequent implications for the interpretation of sedimentary pyrite Fe isotope compositions throughout geological time.

Keywords: Fe isotopes, pyrite, Archean.

6.1. Introduction

Going backwards in geological time, the analysis and interpretation of textural, compositional and isotopic signatures contained within pyrite become progressively more important as a means to inform debate concerning models for the evolution of the Earth, ocean and atmosphere system. Over the last decade growing interest in Fe isotopes as biogeochemical tracers has led to the collection of a spectrum of data which illustrates the variation of $\delta^{56}Fe$ for sedimentary pyrite throughout the Earth's history. In modern anoxic basins, diagenetic pyrite displays isotopic compositions of between -0.5 and -1 ‰ (Severmann *et al.*, 2006). A compilation of Phanerozoic to Mesoproterozoic pyrite (Matthews *et al.*, 2004; Anbar and Rouxel, 2007) and bulk black shales (Yamaguchi *et al.*, 2005; Rouxel *et al.*, 2005), in which pyrite is the dominant Fe bearing mineral, records larger variations ($\delta^{56}Fe$ ~ +0.2 to -1 ‰). The late Paleoproterozoic (2.3 Ga to 1.7 Ga) is characterised by more positive $\delta^{56}Fe_{pyrite}$ and a range comprised between ~ +1.2 to -0.5 ‰ (Yamaguchi *et al.*, 2005; Rouxel *et al.*, 2005). Early Paleoproterozoic and Archean sedimentary pyrites are characterised by the appearance of very negative $\delta^{56}Fe_{pyrite}$ with a range comprised between ~ +0.5 to -3.5 ‰ (Rouxel *et al.*, 2005; Archer and Vance, 2006; Czaja *et al.*, 2010).

Detailed interpretations of the fluctuating secular $\delta^{56}Fe_{pyrite}$ trends are still debated. It has been generalised that abiotic pyrite formation should record a fractionation of a similar magnitude to those occurring during FeS_m precipitation (Severmann *et al.*, 2006; Matthews *et al.*, 2004; Yamaguchi *et al.*, 2005; Rouxel *et al.*, 2005; Archer and Vance, 2006; Czaja *et al.*, 2010; Nishizawa *et al.*, 2010) where $\Delta^{56}Fe_{Fe(II)\text{-}FeS}$ varies from +0.9 ‰ to +0.3 ‰ (Butler *et al.*, 2005). This is because FeS_m, the first iron sulphide to form on mixing $Fe(II)_{aq}$ and $S(-II)_{aq}$, has been conventionally considered to play a central role in diagenetic pyrite formation. Polyakov *et al.* (2007) suggested that ^{56}Fe depletion observed in sedimentary pyrite is a product of a rapid non-fractionating conversion from FeS_m. Such assumptions required that some mechanism was necessary in order to produce ^{56}Fe isotope excursions more negative than - 1 ‰ as recorded in Archean sedimentary rocks. Some workers (Czaja *et al.*, 2010; Johnson *et al.*, 2008a,b) have sought to invoke microbial processes to explain the observed Fe isotope fractionations. Under anoxic conditions, the two major microbial respiration mechanisms involve the reduction of highly reactive Fe(III) (oxy)hydroxides (DIR), and sulphate reduction (BSR) (Berner, 1981) and both mechanisms produce large Fe and S isotope fractionations (Icopini *et al.*, 2004; Crosby *et al.*, 2007; Johnson *et al.*,

2005; Habicht and Canfield, 1997). Johnson *et al.* (2008b) emphasised that DIR can produce large amounts of ^{56}Fe depleted $Fe(II)_{aq}$ that could explain the large Fe isotope variations observed in sedimentary pyrite and BIFs. This was supported by co-variations in Fe and S isotope systematics observed in Archean pyrite that have been interpreted as evidence for coupled Fe(III) and sulphate microbial reductions (Archer and Vance, 2006). In contrast, other workers (Anbar and Rouxel, 2007; Rouxel *et al.*, 2005) proposed that Proterozoic and Archean pyrite Fe isotope variations were more likely to reflect global redox changes in the oceans as suggested by the synchroneity between Fe isotope variations and the long term redox scheme made from S and C isotope data (Canfield *et al.*, 2000; Bekker *et al.*, 2004). They put emphasis on the correlation between the evolution of $\delta^{56}Fe_{pyrite}$ and the progressive increase of atmospheric O_2 partial pressure, 10^{-5} times the present atmospheric level during the Archean and the Hadean (Bekker *et al.*, 2004; Canfield, 2005), with progressive atmospheric O_2 increase ~ 50 Ma before the so called "Great Oxidation Event" (GOE, 2.2-2.45 Ga) (Anbar *et al.*, 2007; Reinhard *et al.*, 2009). They proposed that Fe removal as Fe (oxy)hydroxides and BIFs precursor minerals would produce isotopically light seawater $Fe(II)_{aq}$ which would be then incorporated as Fe sulphides, and argued that if DIR and BSR alone were responsible for those Fe isotope signatures, such large variations should be as well identified in modern anoxic sediments, where these microbial processes are substantial (Raiswell and Canfield, 1998; Poulton and Raiswell, 2002).

Interestingly, both of these models are based on the hypothesis that pyrite is a passive recorder of the $Fe(II)_{aq}$ reservoir from which it forms. The assumption is that in order to produce isotopically light pyrite, the required condition is the prior formation of an isotopically light $Fe(II)_{aq}$ pool, and laboratories have focused on determining which processes could contribute to the formation of such a reservoir (Nishizawa *et al.*, 2010). In the absence of measured or calculated fractionation factors for sedimentary pyrite formation, these divergent interpretations remain difficult or impossible to test. Reduced partition $\beta^{56/54}$-factors have been calculated for various Fe(II) and Fe(III) dissolved species, including hexaqua Fe(II) and Fe(III) (Anbar *et al.*, 2005) and for pyrite (Polyakov *et al.*, 2007; Blanchard *et al.*, 2009). Theoretical fractionation factors between $Fe(II)_{aq}$ and $Fe(III)_{aq}$ are consistent with experimentally determined fractionation (Welch *et al.*, 2003) with $\Delta^{56}Fe_{Fe(II)-Fe(III)}$ ~ -3 ‰ at 20°C. Theoretical computations predict ^{56}Fe enriched pyrite up to ~ +1 ‰ with

$\Delta^{56}Fe_{Fe(II)\text{-}pyrite}$ varying from ~ -2.5 to -4.5 ‰ at 20°C (Polyakov *et al.*, 2007; Blanchard *et al.*, 2009). However, there has been no experimentally measured Fe isotope fractionation for pyrite formation to date. The collection of experimental data on Fe isotope fractionations within the Fe-S system is meagre, since only two experimental studies (Butler *et al.*, 2005; Guilbaud *et al.*, 2010) have been published and both focus on kinetic isotope fractionations between $Fe(II)_{aq}$ and FeS_m. Here, we report the first experimentally derived Fe isotope fractionation factor for abiotic pyrite formation at 40°C and 100°C at pH 6.

6.2. Kinetic Fe isotope fractionation

Pyrite was synthesised from FeS_m (initial $\delta^{56}Fe_{FeS}$ was +0.3 ‰) and H_2S reactants under anoxic conditions *via* the H_2S pathway (Rickard, 1997; Rickard and Luther, 1997; Butler *et al.*, 2004) (See end and supplementary data for detailed experimental and analytical methods and tabulated results). Our results (Fig. 6.1a) show that at 40°C and 100°C, the abiotic fractionation $\Delta^{56}Fe_{Fe(II)RES\text{-}pyrite}$ (where the subscript "RES" stands for "reservoir") varies from +1.7 to +3.0 ‰ ± 0.1 ‰ (~2.2 ‰ on average). Isotopic mass balance for each experiment (Supplementary Table S1) indicates that the experimental error is small and our results are reproducible. The kinetic fractionation factors, α', are $\alpha'_{Fe(II)RES\text{-}pyrite}$ = 1.0025 ± 0.0007 and 1.0021 ± 0.0004 at 40°C and 100°C, respectively. Within errors, these fractionation factors are indistinguishable and no temperature dependence is determinable. The overall kinetic fractionation factor is $\alpha'_{Fe(II)RES\text{-}pyrite}$ = 1.0022 ± 0.0007. This experimentally determined fractionation factor is large compared to the assumed fractionations described above. The kinetics and mechanism of the reaction of FeS_m and H_2S were explored by Rickard (1997) and Rickard and Luther (1997) using experimental protocols and reactants identical to those utilised in this study. We found maximum rates of pyrite formation (~2.8 x 10^{-6} mol pyrite l^{-1} s^{-1}) close to those described by Rickard (1997) (~ 3 x 10^{-6} mol pyrite l^{-1} s^{-1}). Since over the 25°C-125°C temperature range, the pyrite forming process is mechanistically uniform (Rickard, 1997; Rickard and Luther, 1997), the observed temperature independent effect indicates that our results may be extrapolated with reasonable confidence to ambient temperatures. Rickard (1997) and Rickard and Luther (Rickard and Luther, 1997) found that FeS_m dissolves into FeS clusters, FeS^0_{aq}, which react with H_2S to form pyrite (Eqs. 6.1 and 6.2):

$$FeS_m \rightarrow FeS^0_{aq} \qquad (6.1)$$

$$FeS^0_{aq} + H_2S = FeS_2 + H_2 \qquad (6.2)$$

In our experimental protocol we could only separate pyrite from the Fe(II) reservoir which is $Fe(II)_{RES} = FeS_m + FeS^0_{aq}$. Fe isotope fractionation during FeS_m dissolution into FeS^0_{aq} is unknown, but supposedly very small since FeS_m and FeS^0_{aq} are structurally congruent (Luther and Rickard, 2005). This means that essentially, measured $\Delta^{56}Fe_{Fe(II)RES\text{-}pyrite} = \Delta^{56}Fe_{FeSm\text{-}pyrite} \sim \Delta^{56}Fe_{FeS(0)aq\text{-}pyrite}$.

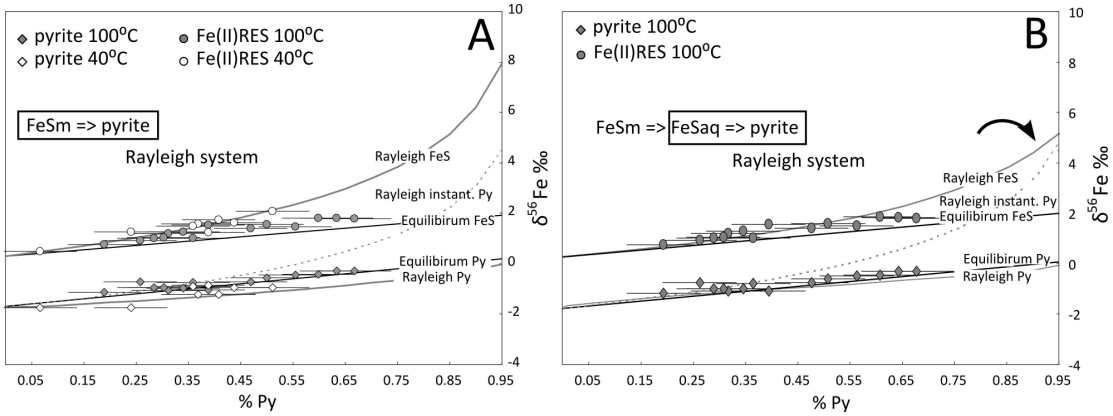

Figure 6.1: Experimental results. Rayleigh models (grey curves) for which FeS_m transfers into pyrite in a closed system (A) or for which FeS_m first dissolves into FeS^0_{aq} which homogenises with FeS_m before transfering into pyrite with a 2.2 ‰ fractionation (B). White and grey symbols represent the experiments at 40°C and 100°C, respectively.

$\delta^{56}Fe$ values for $Fe(II)_{RES}$ and pyrite fit with a simple Rayleigh model for the experiments carried out at 40°C (Fig. 6.1a, details of the models are given in the Supplementary Data Section III). In this model, $Fe(II)_{RES}$ is considered as one phase transferred into pyrite in a closed system. Applying a simple Rayleigh equation to the 100°C experiments does not describe the trend of the experimental data, and the system apparently evolves along an isotopically equilibrated pathway (Fig. 6.1a). However, mechanistically, only FeS^0_{aq} transfers into pyrite (Eq. 6.2). This means that when a portion of FeS^0_{aq} is sequestered into pyrite, $Fe(II)_{RES}$ is comprised of FeS_m and ^{56}Fe enriched FeS^0_{aq}. We suggest that the process of pyrite formation from FeS^0_{aq} itself is accompanied by $\Delta^{56}Fe_{FeS(0)aq\text{-}pyrite} \sim 2.2$ ‰. At 100°C, ^{56}Fe enriched FeS^0_{aq} remaining in the reservoir equilibrates with FeS_m. Fig. 6.1b shows a Rayleigh model that allows continuous FeS_m-FeS^0_{aq} equilibration within the reservoir during pyrite precipitation. Thus, although the closed system is described by a kinetic fractionation

until complete conversion of one phase into another, the isotopic evolution curves can be mistaken for equilibrium lines.

Our experimentally determined results differ considerably from the theoretical computations that predict ^{56}Fe enrichment in pyrite at equilibrium (Polyakov *et al.*, 2007; Blanchard *et al.*, 2009). Pyrite is very sparingly soluble in sedimentary environments (Rickard and Luther, 2007), and pyrite formation is effectively a unidirectional reaction. Therefore the subsequent fractionation cannot reflect isotopic equilibrium. The reason why such large fractionation is recorded during a reaction that does not involve any redox change for Fe(II) atoms is not certain. Significantly lower fractionations have been observed during non-redox FeS_m formation from $Fe(II)_{aq}$ (Butler *et al.*, 2005) ($\Delta^{56}Fe_{Fe(II)\text{-}FeS}$ varying from +0.9 to +0.3 ‰). Although there is no redox change occurring for Fe(II) during pyrite formation, there is a shift from Fe(II) in a tetrahedrally coordinated high spin d^6 configuration in FeS^0_{aq} to Fe(II) in an octahedrally coordinated low spin d^6 configuration in pyrite (Rickard and Luther, 2007). Preferential incorporation of ^{56}Fe depleted Fe(II) into pyrite may be related to selection during this change of coordination and spin state (Schauble, 2004) during pyrite formation.

6.3. Implications for modern and ancient sedimentary pyrite signatures

In most sedimentary environments, the H_2S pathway is the dominant pyrite forming mechanism since polysulphide is a minor $S(-II)_{aq}$ species relative to H_2S_{aq} under acidic to neutral pH (Luther *et al.*, 2003). It is unlikely that polysulphides accumulate in the ferruginous pool without quickly nucleating pyrite and further pyrite formation involves H_2S. Such a large fractionation between FeS^0_{aq} and pyrite *via* the H_2S pathway has major implications for ancient sedimentary rocks. The predominance of the H_2S pathway in pyrite formation may even have been increased in more acidic (Grotzinger and Kasting, 1993) Archean and Proterozoic oceans. Moreover, the role of FeS_m as a reactant for pyrite formation may have been particularly important in Proterozoic and Archean oceans, which were characterised by a high $Fe(II)_{aq}$-to-sulphate ratio due to extensive hydrothermal weathering of basalt seafloor, and low oxidative continental weathering (Isley, 1995; Canfield, 2004). In anoxic Archean oceans, the precipitation of iron sulphides was thus restricted to regions were BSR was actively producing S(-II). If we assume that at those times, hydrothermal activity continually provided the oceans with intense $Fe(II)_{aq}$ fluxes

with an isotopic composition ~ 0 ‰ (Yamaguchi *et al.*, 2005; Johnson *et al.*, 2008a), Fe(II) would be partly removed from solution as FeS_m in regions where BSR occurs with isotopic compositions varying from -0.9 to -0.3 ‰ (Butler *et al.*, 2005). As the fractionation between FeS_m and FeS^0_{aq} should be insignificant, FeS_m dissolution into FeS^0_{aq} and potential exchange between FeS^0_{aq} and Fe^{2+}_{aq} would produce a range of isotopic compositions varying from -0.9 to +0.5 ‰ for FeS^0_{aq} (Guilbaud *et al.*, 2010, 2009). Depending on the rate and the extent of pyrite formation, subsequent pyrite would record isotopic compositions varying from ~ -3.1 to + 0.5 ‰ (Fig. 6.2). This means that combining our result for $\Delta^{56}Fe_{FeS(0)aq\text{-}pyrite}$ with kinetic and equilibrium Fe isotope fractionation between Fe^{2+}_{aq} and FeS_m, the almost entire range of natural pyrite compositions falls within the range of possible compositions generated by the abiological pyrite formation process itself and that Archean excursions need not reflect particular redox or DIR contributions.

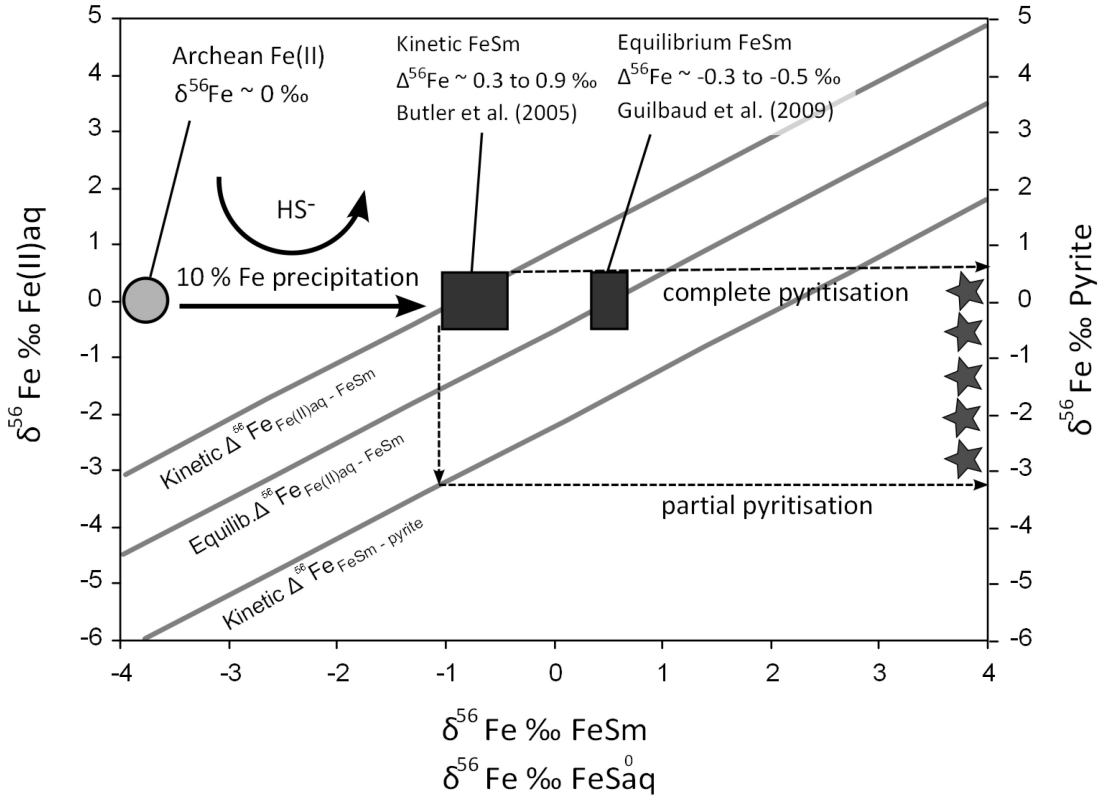

Figure 6.2: Schematic diagram representing the abiotic formation of ^{56}Fe depleted pyrite. The light grey circle represents the isotopic composition of Archean Fe^{2+}_{aq} seawater. The two dark grey rectangles represent the kinetic and equilibrium isotopic compositions of FeS_m when 10 % of Archean Fe^{2+}_{aq} precipitates as FeS_m. 100 % pyritisation from FeS_m would produce pyrite isotopic compositions (grey stars) close to those of FeS_m. Partial pyritisation would kinetically fractionate lighter isotopes such as $\Delta^{56}Fe_{FeSm\text{-}pyrite}$ = 2.2 ‰ and subsequent pyrite formation could record $\delta^{56}Fe$ values as low as – 3.2 ‰.

The idea that a large ^{56}Fe depleted $Fe(II)_{aq}$ pool in the Archean was required in order to produce depleted pyrite raised the following question: in what sediment is the mass-balancing ^{56}Fe enriched Fe reservoir recorded (Czaja *et al.*, 2010; Johnson *et al.*, 2008b)? Johnson *et al.* (2008a,b) pointed out that although BIFs also display some negative $\delta^{56}Fe$, their mean isotopic composition is ~ 0 ‰. Similarly, even though Archean pyrites display $\delta^{56}Fe_{pyrite}$ values down to -3.5 ‰, the isotopic distribution clusters between -1.2 and 2.2 ‰ (Fig. 6.3). If the pyrite forming mechanism itself is characterised by a 2.2 ‰ fractionation, most Archean sedimentary pyrite signatures indicate that the Fe isotope composition of the $Fe(II)_{aq}$ reservoir was ~ 0 ‰. Also, considering that the mineral-forming mechanism is the origin of the fractionation, there is no need for a large ^{56}Fe depleted $Fe(II)_{aq}$ to be produced prior to pyrite formation, and therefore no need for a large mass-balancing ^{56}Fe enriched reservoir $Fe(II)_{aq}$ to remain after pyrite formation. This is particularly true for an environment in which $Fe(II)_{aq}$ with $\delta^{56}Fe$ ~ 0 ‰ is continually injected into the system by hydrothermal vents as it is the case in the Archean, because the ^{56}Fe enriched Fe(II) produced during pyrite formation is then diluted in the large $Fe(II)_{aq}$ pool. Certainly, both DIR and the removal of $Fe(II)_{aq}$ as BIFs in ferruginous regions would promote the production of ^{56}Fe depleted fluids enabling the formation of light sedimentary pyrite. DIR produces ^{56}Fe depleted $Fe(II)_{aq}$ such as at equilibrium, $\Delta^{56}Fe_{Fe(II)aq\text{-}ferric\ oxide}$ ~ -1.3 ‰ (Crosby *et al.*, 2007; Johnson *et al.*, 2005). If one assumes that the initial $\delta^{56}Fe_{ferric\ oxide}$ varies from ~ 0 to +1.5 ‰ (Johnson *et al.*, 2008a), one could expect $\delta^{56}Fe_{pyrite}$ values as low as – 4.4 ‰ if DIR was the major Fe(II) source. However, such low values have not been observed in any sediment and the low ^{56}Fe compositions of Archean sedimentary pyrites are not a clear cut signature for DIR. We suggest that low $\delta^{56}Fe$ signatures in Archean sedimentary pyrite indicate that the portion of Fe removed as pyrite was relatively small in respect with the portion of Fe remaining in the Fe(II) pool (Canfield, 2005).

There is now an increasing body of evidence that implies a progressive increase of atmospheric P_{O2} 50 to 100 Ma before the GOE, stimulating H_2S production through the increase sulphate fluxes due to oxidative continental weathering (Scott *et al.*, 2008; Reinhard *et al.*, 2009; Kendall *et al.*, 2010). Persistence of euxinia throughout the Proterozoic would have enhanced $Fe(II)_{aq}$ utilisation as sulphides, narrowing down the range of $\delta^{56}Fe_{pyrite}$. In the Proterozoic oceans, strongly stratified with oxic

shallow waters, euxinic mid-depth proximal regions and deep, distal ferruginous waters (Poulton *et al.*, 2010), both pyritic black shales and BIFs or their Fe oxide precipitate precursors are quantitative $Fe(II)_{aq}$ sinks and BIFs deposition ends in the late Proterozoic. In these oceans in which $Fe(II)_{aq}$ is extensively utilised as pyrite or oxides, $\delta^{56}Fe$ would progressively reflect the values of the $Fe(II)_{aq}$ source. The 2.3 to ~1.8 Ga period, for which $\delta^{56}Fe_{pyrite}$ displays values up to ~ +1.2 ‰, also coincides with sporadic BIFs deposition. Isley and Abbott (Isley and Abbott, 1999) suggested that BIFs deposition may reflect episodic reducing Fe-rich pulses from hydrothermal activity rather than permanent ferruginous oceans. Assuming that $Fe(II)_{aq}$ inputs from hydrothermal vents decrease, ^{56}Fe enriched Fe(III) bearing (hydr)oxides would then become a potential contributor for $Fe(II)_{aq}$ sources. Dissolution of Fe(III) (hydr)oxides by H_2S produces ^{56}Fe enriched $Fe(II)_{aq}$ (McAnena *et al.*, 2009), and the isotopic composition of the source would be ^{56}Fe enriched. Dissolution of siderite would also contribute to the production of ^{56}Fe enriched $Fe(II)_{aq}$ (Johnson *et al.*, 2005).

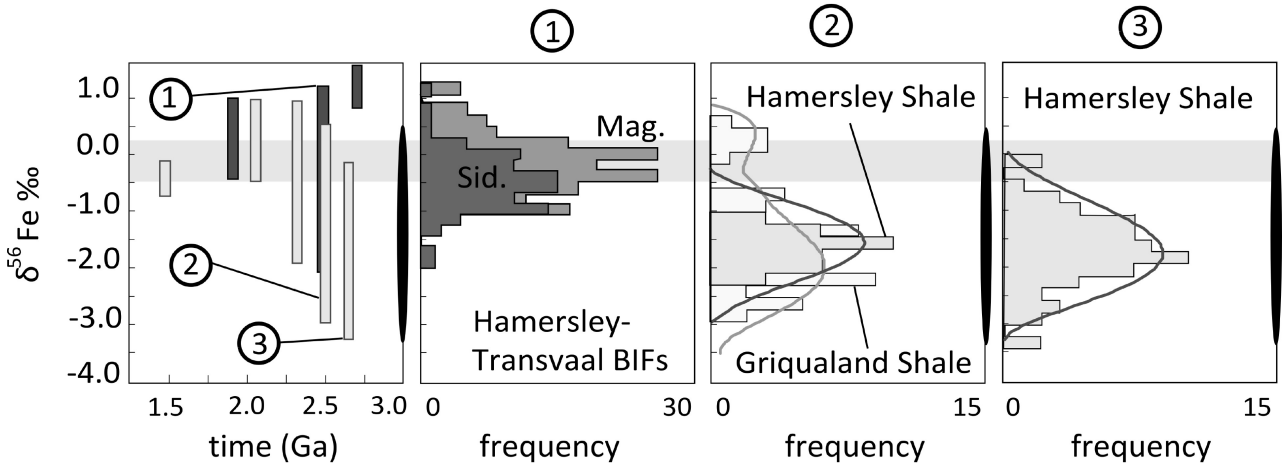

Figure 6.3: Modified after Johnson *et al.* (2008b). The Fe isotopic distribution of some Archean BIFs minerals (magnetite and siderite) in the Hamersley and Transvaal Basins (1) and of some Archean sulphidic shales (pyrite and pyrite nodules) in the Hamersley (2 and 3) and Griqualand Basins (2). BIFs data are from Johnson *et al.* (2008a, 2003). Pyrite data are from Rouxel *et al.* (2005). The mean weighed value is ~ 0 ‰ for BIFs and ~ -1.5 ‰ for Archean sedimentary pyrite. The black areas represent the possible spectrum of pyrite isotope signatures (this study) when pyrite forms from precipitated FeS_m that represents 10 % of the $Fe(II)_{aq}$ reservoir (Butler *et al.*, 2005; Guilbaud *et al.*, 2010b, 2009). The grey area represents the composition range between igneous rocks and hydrothermal fluids.

The end of the Proterozoic is characterised by the decrease of $Fe(II)_{aq}$ in oceans and the spatial limitation of anoxic and ferruginous basins. In this context, major DIR

and H_2S reduction become the major $Fe(II)_{aq}$ sources with respect to hydrothermal Fe^{2+}_{aq} inputs. Lower $Fe(II)_{aq}$:sulphate would promote higher degrees of sulphide precipitation. The implication is that where [S(-II)] is not a limiting factor for pyrite formation, pyrite should display $\delta^{56}Fe_{pyrite}$ values rapidly approaching $\delta^{56}Fe_{source}$. $\delta^{56}Fe_{pyrite}$ values varying from ~ -0.5 to ~ -1 ‰ in euxinic sediments where [$Fe(II)_{aq}$] can be very low and pyrite represents up to ~ 60 % of the highly reactive iron (Santa Barbara basin, Severmann *et al.*, 2006) support our data. In these modern sediments, where DIR can be extensive (Monterey Canyon, Severmann *et al.*, 2006), pore water $Fe(II)_{aq}$ is ^{56}Fe depleted. However, fractionation factors cannot be directly calculated from the measured Fe isotopic compositions of the natural phases since $Fe(II)_{aq}$ can remain dissolved for large temporal scales and there is no evidence why coexisting Fe^{2+}_{aq}, FeS_m and pyrite within a sediment should be cogenetic (Rickard and Morse, 2005). Rickard and Luther (2007) note that sedimentary sulphides cannot be treated in terms of static mass balance. Fe isotope data from benthic fluxes (Severmann *et al.*, 2010), estuarine pore waters (Rouxel *et al.*, 2008) and Fe(II) adsorption experiments (Teutsch *et al.*, 2005) suggest that the production of ^{56}Fe depleted pore water $Fe(II)_{aq}$ is not only due to DIR but also to Fe partial removal as ^{56}Fe enriched (hydr)oxides and Fe adsorption onto Fe (hydr)oxides.

The equilibrium Fe isotope fractionation between Fe^{2+}_{aq} and pyrite has not been experimentally determined. Under normal sedimentary conditions it is unlikely that isotope exchange and equilibration significantly modify primary pyrite compositions due to the extremely low solubility of pyrite. Theoretical computations predict ^{56}Fe enriched pyrite (Polyakov *et al.*, 2007; Blanchard *et al.*, 2009). Homogeneous, ^{56}Fe enriched secondary pyrites ($\delta^{56}Fe$ ~ +0.95 ‰) were documented in the amphibolite-facies metamorphosed (~550°C) Isua Greenstone Belt BIFs (~ 3.8 Ga) (Whitehouse and Fedo, 2007). Although it is difficult to assess whether or not these signatures could reflect isotopic equilibrium with secondary fluids, it is worth noting that these secondary, high temperature pyrite signatures differ consequently from those recorded in sedimentary pyrite, and that the direction of the fractionation is in agreement with equilibrium predictions.

6.4. Conclusions

Our work gives new perspectives for the use of Fe isotope fractionations as biogeochemical proxy. In particular, we show that highly ^{56}Fe depleted pyrite as

found in the Archean can be produced abiotically, without redox involvement for Fe(II), and is therefore not indicative of DIR nor redox processes. We propose that the pyrite forming process itself is responsible for the large Fe isotope fractionation and that the extent of Fe utilisation as sulphides determines the Fe isotope variations recorded in pyrite throughout the Earth's history. Where pyrite formation is extensive, the measured $\delta^{56}Fe_{pyrite}$ may reflect the composition of the Fe(II) reservoir. Our data are consistent with the recent understanding of the oceans redox and chemical evolutions. In Archean oceans, BSR active regions favoured sulphidic Fe sequestration and the removed Fe constituted a small portion of the total Fe budget in the widespread ferruginous oceans. When coupled with C and S isotope systematics, the use of Fe isotopes remains a very powerful tool for reconstructing paleo-biogeochemical processes across basin wide scales (Archer and Vance, 2006; Czaja *et al.*, 2010).

6.5. Methods

Full experimental and analytical methods are detailed in the Supplementary Data sections. Under anoxic conditions, 0.05 mol FeS_m was weighed into a reaction vessel and 10 mL MOPS (3-N-morpholinopropanesulfonic acid) pH 6 was added. The reaction vessel was attached to a gas transfer manifold, purged with O_2-free grade N_2 and evacuated. H_2S was produced by reacting 50 vol% H_2SO_4 with $NaSO_4.9H_2O$ and transferred into the reaction vessel through the manifold. Reactions were performed at 100°C or 40°C for durations up to five days. Products were freeze-dried and characterised by XRD and SEM analysis. Pyrite was separated from $Fe(II)_{RES}$ by preferential acid dissolution. Both $^{56/54}Fe_{pyrite}$ and $^{56/54}Fe_{Fe(II)RES}$ were analysed with an IsoProbe MC-ICP-MS following established protocol(Guilbaud *et al.*, 2010). Precision on $\delta^{56}Fe$ and $\delta^{57}Fe$ was ± 0.08 ‰ and ± 0.16 ‰, respectively. Extent of pyritisation (% Py) was determined by calibrated XRD analysis and by spectrophotometric [Fe] determination.

6.6. Acknowledgements

This work was funded by an ECOSSE PhD studentship to RG and NERC research grant NE/E003958/1 to IBB. We are thankful to Kathleen Keefe and Vincent Gallagher, Nick Odling, Ben Roach and Steve Mowbray for technical support. We

also thank Alan Matthews, Alison McAnena, Veniamin Polyakov, Dave Rickard, Marek Pękala and Claudia Fricke for constructive discussions.

6.7. Supplementary Data Section I: Experimental methods

All reagents were of analytical grade and solutions were prepared using 17-18 MΩcm deionised water, sparged with O_2-free grade N_2 for 30 min (Butler *et al.*, 1994). FeS_m synthesis and the preparation of solutions were performed under O_2 free conditions in a N_2-filled re-circulating Saffron alpha® anoxic chamber. Iron solutions were made by dissolution of Mohr's salt $Fe(NH_4)(SO_4).6H_2O$ (Sigma Aldrich™) in N_2 sparged water. Mohr's salt was used for its ability to resist oxidation. Sulphide solutions were made by dissolution of $Na_2S.9H_2O$ (Sigma Aldrich™) in N_2 sparged water. FeS_m was precipitated mixing 100 mL 0.6 M $Na_2S.9H_2O$ solution with 100 mL 0.6 M $(NH_4)_2Fe(SO_4)_2$ solution (Rickard, 1997). The precipitate was filtered with a Buchner filter (Whatman™ No. 1 paper) and the filtrate was filtered with a 0.45 μm membrane Millipore™ filter. Freshly precipitated FeS_m was re-suspended in water and re-filtered three times, freeze-dried for three days on a Mini-Lyotrap (LTE®) freeze-dryer and stored in the glove-box (Rickard *et al.*, 2006). The non-metal complexing buffer (Kandegedara and Rorabacher, 1999) MOPS (3-N-morpholinopropanesulfonic acid, p*K*a = 7.31, Fisher™) was made by dissolution of its sodium salt and buffered to pH 6 by NaOH titration. Ti(III) citrate was prepared adding 5 mL 15% $TiCl_3$ to 50 mL 0.2 M Na citrate and buffered to pH 7 with Na_2CO_3 (Zehnder and Wuhrman, 1976; Rickard, 1997).

In the glove box, 0.005 mol of freeze-dried FeS_m was introduced into a reaction-vessel and 10 mL of a 0.05 M MOPS (pH 6) buffer were added. The reaction-vessel was either a heat-sealed glass ampoule (Rickard, 1997; Butler and Rickard, 2000; Butler *et al.*, 2004 in the case of the "Py" experiments) or a rubber sealed serum bottle (Drobner *et al.*, 1990; Butler and Rickard, 2000 in the case of the "SB" experiments). Sealed reaction-vessels were closed and attached to a gas-transfer manifold (Rickard, 1997). The manifold was flushed with O_2-free grade N_2 and pumped down to ~ -14 PSI (~ -97 kPa, full vacuum) three times. A serum bottle containing a weighed amount of $Na_2S.9H_2O$ was attached to the manifold with a hypodermic needle and 50% v/v N_2 sparged H_2SO_4 was injected into the serum bottle *via* a syringe to generate H_2S. After H_2S transfer into the reaction-vessel, the pressure was adjusted to slight under-pressure (~ -2.5 PSI or ~ -17 kPa) to ensure the sealing of the vessel

using a glassblower's torch (for Py experiments). Excess H_2S was pumped out to waste. The sealed reaction-vessel was kept at constant temperature in a 100°C furnace or in a 40°C water bath. Vessels were allowed different durations of reaction, and frozen to stop the reaction for pending mineral extraction.

Once frozen, the reaction-vessel was opened, flushed with N_2 to remove the excess of H_2S from the head-space, and attached to a freeze-dryer for three days. In the glove-box, ~ 0.1 g of the solids, *i.e.* a mixture of mackinawite, pyrite and MOPS salts, was loaded and sealed onto the metal (Al) support of an environmental sample holder for immediate XRD characterisation (Guilbaud *et al.*, 2010a). A small portion of the solids were carbon coated for immediate SEM analysis. Separation between pyrite and mackinawite from the remaining solids was completed using modified preferential dissolution of existing protocols (*e.g.* Huerta-Diaz and Morse, 1990; Severmann *et al.*, 2006). Fig. 2.7 (chapter II) shows the technical protocol for the separation between pyrite and its Fe(II) reservoir (initially FeS_m). Solids (0.1 g) were introduced into a serum bottle along with 2 mL H_2O and a few drops of Ti(III) citrate. Ti(III) citrates ensures the complete dissolution of FeS_m in HCl, avoiding the formation of insoluble S(0) by poising Eh to low negative values (Rickard *et al.*, 2006). Ti(III) is not sufficiently reducing to encourage the dissolution of pyrite. Rickard *et al.* (2006) performed FeS_m digestion in hot 1.2 M or 6 M HCl and 5 mL Ti(III) citrate. Our aim was to maximise quantitative FeS_m dissolution with minimum Fe input from Ti(III) citrate and from FeS_2 partial dissolution. Best results were obtained by adding a few drops Ti(III) citrate to FeS_m in 1.2 M HCl. This volume decreases the input of Fe from Ti(III) citrate to < 0.7 % of Fe brought by FeS_m when FeS_m constitutes 5 % of total Fe. In other words, even for the lowest FeS_m concentrations, $Fe_{Ti(III)citrate}$ is still negligible compared to Fe_{FeSm}, and has no impact on the measured isotopic compositions. In a fume cupboard, 20 mL 1.2 M purged HCl was injected into the serum bottle *via* a hypodermic syringe in order to dissolve only FeS_m and the MOPS salts. Remaining solids, essentially pyrite, were separated from solution on a 0.45 µm membrane Millipore™ filter and dissolved with a few drops of concentrated HNO_3. No solids passed the filter. Potential partial dissolution of pyrite into the Fe_{FeS} solution and its consequences are discussed later. Both Fe_{pyrite} and Fe_{FeS} solutions were taken to dryness, treated with H_2O_2 for quantitative removal of the carbon-salts left by MOPS. During this process, Ti from Ti(III) citrate precipitated as insoluble Ti-oxides that were removed by filtration. Fe solutions were dissolved in

aqua regia, evaporated and re-dissolved in 5 % HNO_3 for pending [Fe] determination and Fe isotope ratios analysis.

6.8. Supplementary Data Section II: Analytical methods

We tested the determination of the pyrite percentage (%Py) from the high peak area (around 16° 2θ for mackinawite, and around 32° 2θ for pyrite) with standard mackinawite-pyrite mixtures. Freeze-dried mackinawite was prepared as described above. Natural pyrite was ground with a McCrone® mill for 12 min down to a mean diameter of 4 μm (analysed on a Beckman Coulter LS® particle size analyser). Typical mixtures were 0, 20, 30, 50, 60, 70, 80, 85 and 100 wt%Py. About 0.1 g of the sample was loaded onto a metal environmental sample holder. The environmental holder containing the sample was loaded on a Bruker D8 Advance® Diffractometer. XRD analysis was performed using Cu*K*α primary radiation generated at an accelerating voltage of 40KV in the range of 2-65° 2θ with a 1s/0.02° 2θ counting time. The diffracted X-rays were recorded by a Sol-x™ energy dispersive detector. Data were filtered to remove Cu*K*αII peaks. Peak areas for mackinawite and pyrite respond linearly to the weighted %Py from the standard mixtures (Fig. 2.10 in chapter II). Precision on %Py calculated from the peak areas is given by replicates measurements of the calibration mixture and is ± 7 % (2σ level). Measuring the peak areas for mackinawite and pyrite in our samples thus allowed us to determine a degree of pyritisation. The MOPS salts did not show any peak on the XRD spectra and did not perturb the standard response.

Total Fe concentrations in Fe_{FeS} and Fe_{pyrite} solutions were determined in order to confirm the extent of pyritisation given by the XRD scans. We used the thiocyanate method (Vogel, 1951) to determine [Fe(III)] in the solutions by comparison with a calibration curve. Fe solutions were acidified with 2 mL 1:5 HNO_3, oxidised with a few drops of 0.2 M potassium permanganate, reacted with 5 mL 4 M potassium thiocyanate and made up to 50 mL. [Fe(III)] analysis was performed on a M501 single beam spectrophotometer (Spectronic Analytical Instruments®) using a wavelength of 480 μm. The Beer-Lambert's law is followed for a 0 to 5 ppm [Fe(III)] range with a precision 2σ = ± 0.1 ppm. Table S1 compares the relative %Py obtained with [Fe(III)] analysis and with XRD analysis.

Sample imaging, mineral products determination and texture description were performed *via* backscatter detector on a Philips XL30CP® Scanning Electron Microscope (SEM) at 20 kV. Qualitative chemical analysis on the material surface was carried out with PGT® Spirit X-ray analysis as a mineralogical check.

Fe isotope analysis has been described in detail elsewhere (Guilbaud *et al.*, 2010b). Samples (Fe(III) in HCl) were taken to dryness and re-dissolved in 5% HNO_3. No column chemistry was performed since our samples were experimentally synthesised from analytical grade reagents. $^{56/54}$Fe and $^{57/54}$Fe isotope ratios were measured on a GV IsoProbe (formerly Micromass) multi-collection inductively coupled mass spectrometer (MC-ICP-MS). The major challenge for accurate and precise measurement of Fe isotopes is the removal of atomic and polyatomic interferences induced by the Ar plasma. This was achieved by increasing the signal-to-background ratio (using high concentration samples and introducing collision gases into the hexapole to decrease and/or remove the interferences) and by stabilising the instrumental mass bias minimising the hexapole potential and decreasing the extraction voltage. 3-10 ppm Fe solutions were introduced into an ApexQ inlet system at 50 µL.min^{-1} to maximise the signal to ~0.3 V on mass 54, ~6 V on mass 56 and ~0.02 V on mass 57. Hexapole rf amplitude was set at 50% which enhances transmission of Fe masses. The analysis was run in hard extraction mode (-250 V). 1.8 mL min^{-1} Ar and 2 mL min^{-1} H_2 were introduced into the hexapole collision cell to completely remove ArN^+ on mass 54 and $ArOH^+$ on mass 57 and to decrease ArO^+ on mass 56 to 0.006 V which represents 0.1% of the Fe peak. Cr^+ interferences on mass 54 were monitored on mass 52 but never detected. Instrumental mass bias was corrected by bracketing each sample with a standard and Fe isotope results are presented conventionally using the δ^{56}Fe and δ^{57}Fe notations in ‰ IRMM-014:

$$\delta^{56}Fe = \left(\frac{(^{56}Fe/^{54}Fe)sample}{(^{56}Fe/^{54}Fe)IRMM} - 1 \right) \times 10^3$$

$$\delta^{57}Fe = \left(\frac{(^{57}Fe/^{54}Fe)sample}{(^{57}Fe/^{54}Fe)IRMM} - 1 \right) \times 10^3$$

The precision of our measurements was the reproducibility 2sd for the sample set described in this manuscript, obtained by measuring an external standard and was ± 0.08 ‰ and ± 0.16 ‰ (2σ) for δ^{56}Fe and δ^{57}Fe respectively.

6.9. Supplementary Data Section III: Modelling approach

Models for the isotopic evolution of the FeS_m-FeS^0_{aq}-pyrite system at 40°C and 100°C have been calculated in Matlab 7.7.0 (MathWorks®). If we consider a system in which phase A (here $Fe(II)_{RES}$ = FeS_m + FeS^0_{aq}) incrementally transfers into phase B (pyrite) with the Fe isotope fractionation $\Delta^{56}Fe_{Fe(II)RES\text{-}pyrite}$ without any further exchange between A and B, the isotopic evolution of the system is described by the incremental Rayleigh equation (*e.g.* Criss, 1999):

$$\frac{1000+\delta^{56}_{Fe(II)RES_t}}{1000+\delta^{56}_{Fe(II)RES\ initial}} = f^{\alpha_{pyrite-Fe(II)RES}-1}$$

where f is the fraction of $Fe(II)_{RES}$ remaining in the system at each time t, and α stands for the fractionation factor between pyrite and $Fe(II)_{RES}$. This simple Rayleigh fractionation has been applied to the 40°C data (Fig. 6.1a), but is not a close fit to the 100°C data.

For the 100°C data, we considered the fact that only FeS^0_{aq} transfers into pyrite with the $\Delta^{56}Fe_{FeS(0)aq\text{-}pyrite}$ fractionation, and that at this temperature the remaining ^{56}Fe enriched FeS^0_{aq} can homogenise with FeS_m. The isotopic evolution of each phase is calculated for three steps: i) the dissolution of FeS_m into FeS^0_{aq}, ii) the ^{56}Fe depleted pyrite forming reaction from FeS^0_{aq} and iii) the isotopic homogenisation between FeS_m and ^{56}Fe enriched FeS^0_{aq}.

i) FeS_m dissolution step

In this step pyrite is not formed yet, and we assume that there is no Fe isotope fractionation involved during the dissolution of FeS_m into FeS^0_{aq}. If q is the amount of FeS_m dissolved into FeS^0_{aq}, the concentration at every time of both phases is given by:

$$C^{i+1}_{FeSm} = C^{i}_{FeSm} - q\,,$$

$$C^{i+1}_{FeS(0)aq} = C^{i}_{FeS(0)aq} + q\,,\ and$$

$$C^{i+1}_{Pyrite} = C^{i}_{Pyrite}\,.$$

The isotopic composition of each phase is given by:

$$\delta^{i+1}_{FeSm} = \frac{C^{i}_{FeSm}\delta^{i}_{FeSm} - q\delta^{i}_{FeSm}}{C^{i+1}_{FeSm}} = \delta^{i}_{FeSm},$$

$$\delta^{i+1}_{FeS(0)aq} = \frac{C^i_{FeS(0)aq}\delta^i_{FeS(0)aq} + q\delta^i_{FeSm}}{C^{i+1}_{FeS(0)aq}} = \frac{C^i_{FeS(0)aq}\delta^i_{FeS(0)aq} + q\delta^i_{FeSm}}{C^i_{FeS(0)aq} + q}, \text{ and}$$

$$\delta^{i+1}_{Pyrite} = \delta^i_{Pyrite}.$$

ii) Pyrite forming step

In this step, FeS_m is unchanged, whereas z amount of FeS^0_{aq} is transferred into pyrite with an isotope fractionation F. The concentration of each phase is given by:

$$C^{i+2}_{FeSm} = C^{i+1}_{FeSm} = C^i_{FeSm} - q,$$

$$C^{i+2}_{FeS(0)aq} = C^{i+1}_{FeS(0)aq} - z = C^i_{FeS(0)aq} + q - z, \text{ and}$$

$$C^{i+2}_{Pyrite} = C^{i+1}_{Pyrite} = C^i_{Pyrite} + z.$$

The isotopic composition of each phase is given by:

$$\delta^{i+2}_{FeSm} = \delta^{i+1}_{FeSm} = \delta^i_{FeSm},$$

$$\delta^{i+2}_{FeS(0)aq} = \frac{C^{i+1}_{FeS(0)aq}\delta^{i+1}_{FeS(0)aq} - z\left(\delta^{i+1}_{Fe(0)aq} - F\right)}{C^{i+2}_{FeS(0)aq}}$$

$$= \frac{\left(C^i_{FeS(0)aq} + q\right)\left(\frac{C^i_{FeS(0)aq}\delta^i_{FeS(0)aq} + q\delta^i_{FeSm}}{C^i_{FeS(0)aq} + q}\right) - z\left(\frac{C^i_{FeS(0)aq}\delta^i_{FeS(0)aq} + q\delta^i_{FeSm}}{C^i_{FeS(0)aq} + q} - F\right)}{C^i_{FeS(0)aq} + q - z}$$

$$= \frac{\left(C^i_{FeS(0)aq}\delta^i_{FeS(0)aq} + q\delta^i_{FeSm}\right) - z\left(\frac{C^i_{FeS(0)aq}\delta^i_{FeS(0)aq} + q\delta^i_{FeSm}}{C^i_{FeS(0)aq} + q} - F\right)}{C^i_{FeS(0)aq} + q - z}$$

$$\delta^{i+2}_{Pyrite} = \frac{C^i_{Pyrite}\delta^i_{Pyrite} + z\left(\delta^{i+1}_{Fe(0)m} - F\right)}{C^{i+2}_{Pyrite}}$$

$$= \frac{C^i_{Pyrite}\delta^i_{Pyrite} + z\left(\frac{C^i_{FeS(0)aq}\delta^i_{FeS(0)aq} + q\delta^i_{FeSm}}{C^i_{FeS(0)aq} + q} - F\right)}{C^i_{Pyrite} + z}$$

iii) Homogenisation of the Fe(II) reservoir

In this step, pyrite is unchanged, whereas FeS_m and FeS^0_{aq} exchange and homogenise (still assuming that there is no isotope fractionation between FeS_m and FeS^0_{aq}). The isotopic composition of the reservoir is given by:

$$\delta^{i+3}_{FeS(0)aq} = \delta^{i+3}_{FeSm} = \frac{C^{i+2}_{FeS(0)aq}\delta^{i+2}_{FeS(0)aq} + C^{i+2}_{FeSm}\delta^{i+2}_{FeSm}}{C^{i+3}_{FeS(0)aq} + C^{i+3}_{FeSm}}$$

$$\delta^{i+3}_{FeS(0)aq} = \delta^{i+3}_{FeSm} = \frac{\left(C^{i}_{FeS(0)aq} + q - z\right)\dfrac{\left(C^{i}_{FeS(0)aq}\delta^{i}_{FeS(0)aq} + q\delta^{i}_{FeSm}\right) - z\left(\dfrac{C^{i}_{FeS(0)aq}\delta^{i}_{FeS(0)aq} + q\delta^{i}_{FeSm}}{C^{i}_{FeS(0)aq} + q} - F\right)}{C^{i}_{FeS(0)aq} + q - z} + \left(C^{i}_{FeSm} - q\right)\delta^{i}_{FeSm}}{C^{i}_{FeS(0)aq} + C^{i}_{FeSm} - z}$$

$$\delta^{i+3}_{FeS(0)aq} = \delta^{i+3}_{FeSm} = \frac{\left(C^{i}_{FeS(0)aq}\delta^{i}_{FeS(0)aq} + q\delta^{i}_{FeSm}\right) - z\left(\dfrac{C^{i}_{FeS(0)aq}\delta^{i}_{FeS(0)aq} + q\delta^{i}_{FeSm}}{C^{i}_{FeS(0)aq} + q} - F\right) + \left(C^{i}_{FeSm} - q\right)\delta^{i}_{FeSm}}{C^{i}_{FeS(0)aq} + C^{i}_{FeSm} - z}$$

The three steps mentioned above were calculated until complete consumption of the Fe(II) reservoir. We used the FeS_m solubility data from Rickard (2006) to determine the concentration of FeS^0_{aq}. In order to keep the concentration of FeS^0_{aq} constant, we set equal values for *q* and *z*, *i.e.* we assume that dissolution of FeS_m to FeS^0_{aq} is equal or faster than consumption of FeS^0_{aq} to form FeS_2.

6.10. Supplementary Data Section IV: Results and discussion for the separation procedure

Experimental results are summarised in Table S1. For all experiments, final products were pyrite and mackinawite. No Fe(II) oxidation happened during reaction. The use of hermetically sealed glass ampoules or serum bottles gave identical Fe isotope results. The only effect we could identify using different reaction vessels was the rate of pyrite formation. Initial $\delta^{56}Fe_{FeSm}$ was 0.30 ± 0.08 ‰ Isotopic mass balance for each experiment (0.29 ± 0.09 ‰) indicates that the experimental error is small and our results are reproducible. A three-isotope plot (Fig. S1) supports the quality of our data points which are consistent with Fe isotope fractionation along the terrestrial mass fractionation line. Our data highlight the large fractionation occurring during pyrite formation with FeS_m and H_2S as reactants. Final precision on the extent of pyritisation (%Py) is ± 10 %. Typical SEM images of pyrite micro-cubes and mackinawite aggregates for different reaction durations with qualitative (standard free) chemical analysis at the mineral surface are shown by Fig. 2.11 (chapter II).

Figure S1: Analytical quality control for all experimental samples including the Baker Fe solution (external standard, in red) normalised with IRMM-14 in a three isotope plot. The slope of the line is consistent with the terrestrial mass fractionation line.

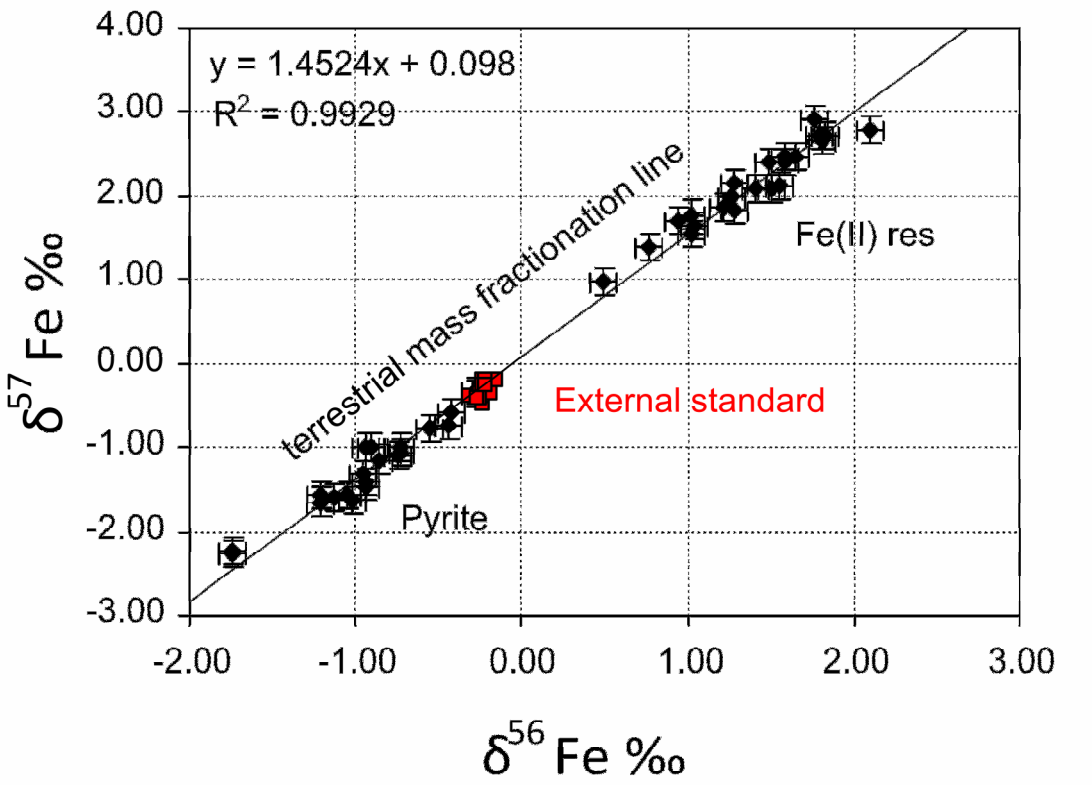

The risk of Fe_{pyrite} contamination during FeS_m dissolution with HCl was examined. This risk is enhanced when the ratio FeS_m/FeS_2 decreases. We used cold 1.2 M HCl rather than 6 M HCl in order to reduce FeS_2 dissolution and measured a maximum of 0.2 % dissolution from the initial FeS_2 phase. This means that when the FeS_m/FeS_2 ratio is the lowest, potential pollution of Fe_{FeSm} by Fe_{pyrite} represents at maximum 0.027 % of Fe_{FeSm}. The theoretical Fe isotope composition of pyrite necessary to decrease by 0.1 ‰ the composition of observed FeS_m is shown by Fig. 2.5 (chapter II). The figure suggests that contamination bias may become a problem when > 95 % pyritisation has occurred (*i.e.* when < 5 % FeS_m remains in the system, shaded area). None of our data correspond to this high %Py region, and we conclude that our results are free from cross-contamination.

Removal of organic matter left by MOPS after freeze-drying was crucial to prevent carbon to be introduced into the MC-ICP-MS. Both *aqua regia* and hydrogen peroxide (VWR™) were tested to oxidatively remove organic carbon. 5 to 10 mL of the oxidant was added to the residue and warmed up to 85°C and dried. The procedure was repeated three times. The final residue was dissolved in concentrated HCl and taken up to volume. 5 µL of the solutions were diluted four times in methanol for Electron Spray Ionisation Mass Spectrometry (ESI-MS). Results showed that MOPS is still present in the solution oxidised with *aqua regia* whereas MOPS is not

detectable in the solution oxidised with hydrogen peroxide. NMR analysis showed the persistence of organic molecules in both solutions, but peaks were broad and difficult to analyse, perhaps indicating sulphur and nitrogen containing molecules. Total Organic Carbon (TOC) analyses showed that 99 % of carbon had been removed from the solution oxidised with hydrogen peroxide.

Table S1: Experimental conditions and analytical results. Precision on %Py is ± 10 %. Products were identified by XRD and SEM analyses. Analytical precision on δ^{56}Fe was given by the reproducibility of an external standard (Baker®) at a 2σ level and was ± 0.08 ‰ and ± 0.16 ‰ for δ^{56}Fe and δ^{57}Fe respectively. The isotopic composition of starting FeS_m was 0.30 ± 0.08 ‰. The kinetic fractionation factors between FeS_m and pyrite, $\alpha'_{FeS\text{-}pyrite}$ was given by $\alpha'_{FeS-pyrite} = \frac{1000 + \delta^{56}Fe_{FeS}}{1000 + \delta^{56}Fe_{FeS}}$. Precision on $\alpha'_{FeS\text{-}pyrite}$ is ± 0.0007. The fractionation between FeS_m and pyrite was $\Delta^{56}Fe_{FeS-pyrite} = \delta^{56}Fe_{FeS} - \delta^{56}Fe_{pyrite}$ and was given with a precision of ± 0.11 ‰.

Samples	T °C	Duration (hours)	Products	% Py spectr.	% Py XRD	FeSm $\delta^{56}Fe$ (‰)	FeSm $\delta^{57}Fe$ (‰)	Pyrite $\delta^{56}Fe$ (‰)	Pyrite $\delta^{57}Fe$ (‰)	$\alpha'_{FeS\text{-}pyrite}$	$\Delta^{56}Fe_{FeS\text{-}pyrite}$	mass balance $\delta^{56}Fe$ = 0.3 ‰	Baker external standard $\delta^{56}Fe$ (‰)	Baker external standard $\delta^{57}Fe$ (‰)
SB-1HA	100	3	py, mk	0.33	0.34	0.94	1.71	-0.72	-1.05	1.0017	1.66	0.37	-0.25	-0.40
SB-1HB	100	3	py, mk	0.38	0.45	1.03	1.55	-0.74	-1.08	1.0018	1.77	0.23	-0.21	-0.36
SB-1DA	100	17.5	py, mk	0.34	0.26	0.77	1.38	-1.13	-1.59	1.0019	1.89	0.27	-0.26	-0.42
SB-1DB	100	19.5	py, mk	0.40	0.4	1.21	1.86	-1.05	-1.58	1.0023	2.25	0.31	-0.15	-0.19
SB-2DA	100	48	py, mk	0.32	0.39	1.04	1.64	-0.93	-1.47	1.0020	1.98	0.27	-0.23	-0.19
SB-2DB	100	48	py, mk	0.43	0.37	1.03	1.79	-0.95	-1.33	1.0020	1.98	0.30	-0.21	-0.27
SB-3DB	100	72	py, mk	0.41	0.43	1.28	2.16	-0.95	-1.31	1.0022	2.23	0.32	-0.25	-0.33
Py1DE	100	24	py, mk	0.75	0.64	1.49	2.41	-0.44	-0.75	1.0019	1.93	0.25	-0.23	-0.50
Py2DC	100	48	py, mk	0.80	0.74	1.80	2.74	-0.28	-0.36	1.0021	2.08	0.26	-0.25	-0.34
PyA1	100	122	py, mk	0.70	0.71	1.81	2.66	-0.28	-0.32	1.0021	2.10	0.33	-0.21	-0.19
PyA2	100	25	py, mk	0.58	0.59	1.58	2.46	-0.55	-0.76	1.0021	2.13	0.32	-0.30	-0.38
PyA3	100	5.5	py, mk	0.56	0.56	1.40	2.10	-0.72	-0.99	1.0021	2.13	0.21	-0.25	-0.42
PyA4	100	50	py, mk	0.69	0.68	1.83	2.73	-0.42	-0.60	1.0023	2.25	0.30	-0.21	-0.30
PyA5	100	1.5	py, mk	0.50	0.48	1.55	2.11	-1.03	-1.62	1.0026	2.57	0.31	-0.22	-0.29
													-0.23	-0.40
SB-5HA	40	5	py, mk	0.33	0.46	1.59	2.42	-1.22	-1.65	1.0028	2.80	0.30	-0.25	-0.38
SB-5HB	40	5	py, mk	0.55	0.5	1.76	2.90	-1.21	-1.56	1.0030	2.97	0.27	-0.24	-0.38
SB-1DC	40	24	py, mk	0.62	0.53	1.64	2.47	-0.93	-1.40	1.0026	2.58	0.28	-0.19	-0.35
SB-2DC	40	48	py, mk	0.46	0.45	1.50	2.10	-0.90	-1.00	1.0024	2.40	0.42	-0.25	-0.37
SB-2DD	40	48	py, mk	0.48	0.6	2.10	2.80	-0.94	-0.98	1.0030	3.04	0.28	-0.24	-0.42
PyA6	40	122	py, mk	0.31	0.48	1.26	1.98	-0.86	-1.14	1.0021	2.11	0.24	-0.24	-0.26
PyA7	40	25	py, mk	0.32	0.32	1.28	1.83	-1.75	-2.26	1.0030	3.02	0.31	-0.21	-0.27
PyA8	40	5.5	py, mk	0.15	0.1	0.49	0.97	-1.75	-2.25	1.0022	2.25	0.27	-0.27	-0.42

6.11. References

Anbar, A., Jarzecki, A., Spiro, T., 2005. Theoretical investigation of iron isotope fractionation between Fe(H2O)63+ and Fe(H2O)62+: Implication for iron stable isotope geochemistry. Geochim. Cosmochim. Acta 69, 825-837.

Anbar, A., Rouxel, O., 2007. Metal Stable Isotopes in Paleoceanography. Annu. Rev. Earth Planet. Sci. 35, 717–746.

Anbar, A.D., Duan, Y., Lyons, T.W., Arnold, G.L., Kendall, B., Creaser, R.A., Kaufman, A.J., Gordon, G.W., Scott, C., Garvin, J., Buick, R., 2007. A Whiff of Oxygen Before the Great Oxidation Event? Science 317, 1903-1906.

Archer, C., Vance, D., 2006. Coupled Fe and S isotope evidence for Archean microbial Fe(III) and sulfate reduction. Geology 34, 153-156.

Bekker, A., Holland, H., Wang, P., Rumble, D., Stein, H., Hannah, J., Coetzee, L., Beukes, N., 2004. Dating the rise of atmospheric oxygen. Nature 427, 117-120.

Berner, R., 1981. A New Geochemical Classification of Sedimentary Environments. J. Sediment. Research 51.

Blanchard, M., Poitrasson, F., Méheut, M., Lazzeri, M., Mauri, F., Balan, E., 2009. Iron isotope fractionation between pyrite (FeS2), hematite (Fe2O3) and siderite (FeCO3): A first-principles density functional theory study. Geochimica et Cosmochimica Acta 73, 6565-6578.

Butler, I., Archer, C., Vance, D., Oldroyd, A., Rickard, D., 2005. Fe isotope fractionation on FeS formation in ambient aqueous solution. Earth and Planet. Science Letters 236.

Butler, I., Bottcher, M., Rickard, D., Oldroyd, A., 2004. Sulfur isotope partitioning during experimental formation of pyrite via the polysulfide and hydrogen sulfide pathways: implications for the interpretation of sedimentary and hydrothermal pyrite isotope records. Earth and Planet. Science Letters 228, 495-509.

Butler, I., Rickard, D., 2000. Framboidal pyrite formation via the oxidation of iron (II) monosulfide by hydrogen sulphide. Geochim Cosmochim Acta 64, 2665–2672.

Butler, I., Schoonen, M., Rickard, D., 1994. Removal of dissolved oxygen from water: A comparison of four common techniques. Talanta 41, 211-215.

Canfield, D.E., 2004. The evolution of the Earth surface sulfur reservoir. Am J Sci

304, 839-861.

Canfield, D., 2005. The early history of atmospheric oxygen: Homage to Robert M. Garrels. Annual Review of Earth and Planetary Sciences 33, 1-36.

Canfield, D., Habicht, K., Thamdrup, B., 2000. The Archean Sulfur Cycle and the Early History of Atmospheric Oxygen. Science 288, 658-661.

Crosby, H.A., Roden, E.E., Johnson, C.M., Beard, B.L., 2007. The mechanisms of iron isotope fractionation produced during dissimilatory Fe(III) reduction by Shewanella putrefaciens and Geobacter sulfurreducens. Geobiology 5, 169-189.

Czaja, A., Johnson, C., Beard, B., Eigenbrode, J., Freeman, K., Yamaguchi, K., 2010. Iron and carbon isotope evidence for ecosystem and environmental diversity in the ~ 2.7 to 2.5 Ga Hamersley Province, Western Australia. Earth and Planetary Science Letters 292, 170-180.

Drobner, E., Huber, H., Wachtershauser, G., Rose, D., Stetter, K.O., 1990. Pyrite formation linked with hydrogen evolution under anaerobic conditions. Nature 346, 742-744.

Grotzinger, J., Kasting, J., 1993. Nem constaints on Precambrian ocean composition. J. Geol. 101, 235-243.

Guilbaud, R., Ellam, R., Butler, I., Gallagher, V., Keefe, K., 2010a. A procedural development for the analysis of 56/54Fe and 57/54Fe isotope ratios with new generation IsoProbe MC-ICP-MS. J. Anal. At. Spectrom 25, 1598-1604.

Guilbaud, R., Ellam, R., Butler, I., Rickard, D., 2009. Fe isotope fractionation in the Fe-S system at low temperature. American Geophysical Union, Fall Meeting 2009, abstract V11C-1975.

Guilbaud, R., Butler, I.B., Ellam, R.M., Rickard, D., 2010b. Fe isotope exchange between Fe(II)aq and nanoparticulate mackinawite (FeSm) during nanoparticle growth. Earth and Planetary Science Letters 300, 174-183.

Habicht, K.S., Canfield, D.E., 1997. Sulfur isotope fractionation during bacterial sulfate reduction in organic-rich sediments. Geochimica et Cosmochimica Acta 61, 5351-5361.

Huerta-Diaz, M.A., Morse, J.W., 1990. A quantitative method for determination of trace metal concentrations in sedimentary pyrite. Marine Chemistry 29, 119-144.

Icopini, G., Anbar, A., Ruebush, S., Tien, M., Brantley, S., 2004. Iron isotope

fractionation during microbial reduction of iron: The importance of adsorption. Geology 32, 205-208.

Isley, A., 1995. Hydrothermal Plumes and the Delivery of Iron to Banded Iron Formation. The Journal of Geology 103, 169-185.

Isley, A., Abbott, D., 1999. Plume-related mafic volcanism and the deposition of banded iron formation. J. Geophys. Res. 104, 15461-15477.

Johnson, C., Beard, B., Beukes, N., Klein, C., O'Leary, J., 2003. Ancient geochemical cycling in the Earth as inferred from Fe isotope studies of banded iron formations from the Transvaal Craton. Contributions to Mineralogy and Petrology 523-547.

Johnson, C., Beard, B., Klein, C., Beukes, N., Roden, E., 2008a. Iron isotopes constrain biologic and abiologic processes in banded iron formation genesis. Geochim Cosmochim Acta 72, 151-169.

Johnson, C., Beard, B., Welch, S., Croal, L., Newman, D., Nealson, K., 2005. Experimental constraints on Fe isotope fractionations during biogeochemical cycling of Fe. Geochim. Cosmochim. Acta 66, A371.

Johnson, C.M., Beard, B.L., Roden, E.E., 2008b. The Iron Isotope Fingerprints of Redox and Biogeochemical Cycling in Modern and Ancient Earth. Annual Review of Earth and Planetary Sciences 36, 457-493.

Johnson, C.M., Roden, E.E., Welch, S.A., Beard, B.L., 2005. Experimental constraints on Fe isotope fractionation during magnetite and Fe carbonate formation coupled to dissimilatory hydrous ferric oxide reduction. Geochimica et Cosmochimica Acta 69, 963-993.

Kandegedara, A., Rorabacher, D.B., 1999. Noncomplexing Tertiary Amines as “Better” Buffers Covering the Range of pH 3−11. Temperature Dependence of Their Acid Dissociation Constants. Analytical Chemistry 71, 3140-3144.

Kaufman, A., Johnston, D., Farquhar, J., Masterson, A., Lyons, T., Bates, S., Anbar, A., Arnold, G., Garvin, J., Buick, R., 2007. Late Archean Biospheric Oxygenation and Atmospheric Evolution. Science 317, 1900-1903.

Kendall, B., Reinhard, C.T., Lyons, T.W., Kaufman, A.J., Poulton, S.W., Anbar, A.D., print. Pervasive oxygenation along late Archaean ocean margins. Nature Geosci 3, 647-652.

Luther, G., Rickard, D., 2005. Metal Sulfide Cluster Complexes and their Biogeochemical Importance in the Environment. Journal of Nanoparticle

Research 7, 389-407.

Luther, G., Taillefert, M., Rozan, T., Rickard, D., 2003. Geochemical implications of the polysulfide vs. sulfide pyrite formation reactions based on real time measurements of soluble reactants. Abstr. Pap. - Am. Chem. Soc. GEOC9.

Matthews, A., Morgans-Bell, H., Emmanuel, S., Jenkyns, H., Erel, Y., Halicz, L., 2004. Controls on iron-isotope fractionation in organic-rich sediments (Kimmeridge Clay, Upper Jurassic, Southern England). Geochimica et Cosmochimica Acta 68, 3107-3123.

McAnena, A., Severmann, S., Poulton, S., 2009. Abiotic Fe isotope fractionation during sulfide mediated reductive dissolution of Fe oxide minerals. Goldschmidt Conference Abstracts.

Nishizawa, M., Yamamoto, H., Ueno, Y., Tsuruoka, S., Shibuya, T., Sawaki, Y., Yamamoto, S., Kon, Y., Kitajima, K., Komiya, T., Maruyama, S., Hirata, T., 2010. Grain-scale iron isotopic distribution of pyrite from Precambrian shallow marine carbonate revealed by a femtosecond laser ablation multicollector ICP-MS technique: Possible proxy for the redox state of ancient seawater. Geochimica et Cosmochimica Acta 74, 2760-2778.

Polyakov, V., Clayton, R., Horita, J., Mineev, S., 2007. Equilibrium iron isotope fractionation factors of minerals: Reevaluation from the data of nuclear inelastic resonant X-ray scattering and Mössbauer spectroscopy. Geochimica et Cosmochimica Acta 71, 3833-3846.

Poulton, S., Fralick, P., Canfield, D., 2010. Spatial variability in oceanic redox structure 1.8[thinsp]billion years ago. Nature Geosci 3, 486-490.

Poulton, S., Raiswell, R., 2002. The low-temperature geochemical cycle of iron: From continental fluxes to marine sediment deposition. Am J Sci 302, 774-805.

Raiswell, R., Canfield, D., 1998. Sources of iron for pyrite formation in marine sediments. Am J Sci 298, 219-245.

Reinhard, C., Raiswell, R., Scott, C., Anbar, A., Lyons, T., 2009. A Late Archean Sulfidic Sea Stimulated by Early Oxidative Weathering of the Continents. Science 326, 713-716.

Rickard, D., 1997. Kinetics of pyrite formation by the H2S oxidation of iron (II) monosulfide in aqueous solutions between 25oC and 125oC: the rate equation. Geochim. Cosmochim. Acta 61, 115– 134.

Rickard, D., Luther, G., 1997. Kinetics of pyrite formation by the H2S oxidation of

iron (II) monosulfide in aqueous solutions between 25 8C and 125 8C: the mechanism. Geochim. Cosmochim. Acta 61, 135–147.

Rickard, D., Luther, G., 2007. Chemistry of Iron Sulfides. Chem. Rev. 107, 514-562.

Rickard, D., 2006. The solubility of FeS. Geochim. Cosmochim. Acta 70, 5779-5789.

Rickard, D., Griffith, A., Oldroyd, A., Butler, I., Lopez-Capel, E., Manning, D., Apperley, D., 2006. The composition of nanoparticulate mackinawite, tetragonal iron (II) monosulfide. Chem. Geol. 235.

Rickard, D., Morse, J., 2005. Acid Volatile Sulfide (AVS). Marine Chemistry 97, 141-197.

Rouxel, O., Bekker, A., Edwards, K., 2005. Iron isotope constraints on the Archean and Paleoproterozoic ocean redox state. Science 307, 1088-1090.

Rouxel, O., Sholkovitz, E., Charette, M., Edwards, K.J., 2008. Iron isotope fractionation in subterranean estuaries. Geochimica et Cosmochimica Acta 72, 3413-3430.

Schauble, E., 2004. Applying Stable Isotope Fractionation Theory to New Systems. Reviews in Mineralogy & Geochemistry 55, 65-111.

Scott, C., Lyons, T.W., Bekker, A., Shen, Y., Poulton, S.W., Chu, X., Anbar, A.D., 2008. Tracing the stepwise oxygenation of the Proterozoic ocean. Nature 452, 456-459.

Severmann, S., Johnson, C., Beard, B., McManus, J., 2006. The effect of early diagenesis on the Fe isotope compositions of porewaters and authigenic minerals in continental margin sediments. Geochim Cosmochim Acta 70, 2006–2022.

Severmann, S., McManus, J., Berelson, W.M., Hammond, D.E., 2010. The continental shelf benthic iron flux and its isotope composition. Geochimica et Cosmochimica Acta 74, 3984-4004.

Teutsch, N., von Gunten, U., Porcelli, D., Cirpka, O., Halliday, A., 2005. Adsorption as a cause for iron isotope fractionation in reduced groundwater. Geochim Cosmochim Acta 69, 4175-4185.

Vogel, A., 1951. A text-book of Quantitative Inorganic Analysis, Therory and practice, second edition. Longmans, Green and Co.

Welch, S., Beard, B., Johnson, C., Baterman, P., 2003. Kinetic and equilibrium Fe isotope fractionation between aqueous Fe(II) and Fe(III). Geochim. Cosmochim. Acta 67, 4231-4250.

Whitehouse, M., Fedo, C., 2007. Microscale heterogeneity of Fe isotopes in >3.71 Ga banded iron formation from the Isua Greenstone Belt, southwest Greenland. Geology 35, 719-722.

Yamaguchi, K., Johnson, C., Beard, B., Ohmoto, H., 2005. Biogeochemical cycling of iron in the Archean-Paleoproterozoic Earth: Constraints from iron isotope variations in sedimentary rocks from the Kaapvaal and Pilbara Cratons. Chem. Geol. 218, 135-169.

Zehnder, A., Wuhrmann, K., 1976. Titanium (III) citrate as a nontoxic oxidation-reduction buffering system for the culture of obligate anaerobes. Science 194, 1165-1166.

Chapter VII

Experimental development for the determination of the Fe isotope fractionation associated with pyrite formation at natural reactant concentrations and FeS_m undersaturation: preliminary results

7.1. Introduction

7.1.1. Fe isotopes signatures of sedimentary pyrite

It has been proposed that the secular variations in the Fe isotope signatures of sedimentary pyrite should provide a powerful insight into Archean and Proterozoic biogeochemistry (*e.g.* Matthews *et al.*, 2004; Rouxel *et al.*, 2005; Yamaguchi *et al.*, 2005; Archer and Vance, 2006; Johnson, Beard, Klein, *et al.*, 2008; Johnson, Beard, and Roden, 2008). Early Paleoproterozoic and Archean sedimentary pyrites display a large range of Fe isotope compositions, with $\delta^{56}Fe_{pyrite}$ varying from ~ +0.5 to -3.5 ‰ (Rouxel *et al.*, 2005; Archer and Vance, 2006; Czaja *et al.*, 2010). The late Paleoproterozoic (2.3 Ga to 1.7 Ga), bracketed between the rise of atmospheric oxygen and the cessation of the deposition of Banded Iron Formations, is characterised by a range comprised between ~ +1.2 to -0.5 ‰ (Rouxel *et al.*, 2005; Yamaguchi *et al.*, 2005). Finally, Mesoproterozoic to modern pyrites display compositions ranging from ~ +0.2 to -1 ‰ (Matthews *et al.*, 2004; Severmann *et al.*, 2006; Anbar and Rouxel, 2007).

Interpretations for the negative Archean $\delta^{56}Fe_{pyrite}$ excursions have mostly focused on the formation of a ^{56}Fe depleted Fe(II) pool prior to Fe(II) sequestration into pyrite. Potential processes responsible for the formation of such a depleted pool involved intense bacterial dissimilatory iron reduction (DIR, *e.g.* Archer and Vance, 2006; Johnson, Beard, Klein, *et al.*, 2008; Johnson, Beard, and Roden, 2008; Czaja *et al.*, 2010), or prior Fe oxidation (*e.g.* Rouxel *et al.*, 2005; Anbar and Rouxel, 2007). This is because both DIR and Fe oxidation are known to produce ^{56}Fe depleted $Fe(II)_{aq}$ fluids (*e.g.* Johnson *et al.*, 2002, 2005; Skulan *et al.*, 2002; Welch *et al.*, 2003; Croal *et al.*, 2004; Icopini *et al.*, 2004; Balci *et al.*, 2006; Crosby *et al.*, 2007). However, it was shown in chapter VI that the mechanisms responsible for the formation of iron sulphides, and ultimately pyrite, are themselves accompanied by large Fe isotope fractionations, and therefore suffice to encapsulate the whole range of sedimentary pyrite Fe isotope signatures.

7.1.2. Pyrite formation pathways

Pyrite formation requires two distinct processes: nucleation and crystal growth. The relative rates of pyrite nucleation and crystal growth have been discussed in Rickard and Luther (2007), and once pyrite starts nucleating, the rate of pyrite formation is controlled by the rate of pyrite crystal growth, and it is crystal growth

that is responsible for bulk pyrite formation in sediments. The stoichiometry and rates of pyrite formation have been described for two mechanisms: the polysulphide pathway and the H_2S pathway (*e.g.* Luther, 1991; Rickard, 1997; Rickard and Luther, 1997). As $S(-II)_{aq}$ speciation strongly depends on pH (chapter I, section 1.2.1.1), both mechanisms depend themselves on the reaction pH. Voltammetric evidence (Luther, 1991; Rickard, 1997) support the involvement of the dissolved Fe(II) species FeS^0_{aq} in both reactions, and Rickard *et al.* (2001) observed that FeS^0_{aq} suppression inhibits subsequent pyrite formation.

Butler et al. (2004) compared the rates of both pathways for the experimental conditions described by Wilkin and Barnes (1996), who used 100 mg FeS_m and a H_2S partial pressure of 0.03 atm. Using surface areas of 30 $m^2\ g^{-1}$ for FeS_m and 1.4 x 10^3 $cm^2\ g^{-1}$, they showed that at pH 7, pyrite forms at a rate of ~ 8 x 10^{-11} M $L^{-1}\ s^{-1}$ *via* the polysulphide pathway when FeS_m is present:

$$FeS_m \rightarrow FeS^0_{aq} \qquad (7.1)$$

$$FeS^0_{aq} + S^{2-}_n = [(FeS)S_n]^{2-} \qquad (7.2)$$

$$[(FeS)S_n]^{2-} = FeS_2 + S^{2-}_{n-1} \qquad (7.3)$$

$$\overline{FeS^0_{aq} + S^{2-}_n = FeS_2 + S^{2-}_{n-1}} \qquad (7.4)$$

The reaction with H_2S forms pyrite for the conditions described above at a rate of ~ 2 x 10^{-8} M $L^{-1}\ s^{-1}$ at pH 7 when FeS_m is present:

$$FeS_m \rightarrow FeS^0_{aq} \qquad (7.5)$$

$$FeS^0_{aq} + H_2S = [FeS - SH_2] \qquad (7.6)$$

$$[FeS - SH_2] = FeS_2 + H_2 \qquad (7.7)$$

$$\overline{FeS^0_{aq} + H_2S = FeS_2 + H_2} \qquad (7.8)$$

Amongst all pyrite forming reactions reviewed by Rickard and Luther (2007), FeS_m tends to be a popular Fe(II) reagent in experimental protocols because systems saturated with respect to FeS_m are close to the supersaturation conditions required for rapid pyrite nucleation (Rickard *et al.*, 2007). As explained in chapter I, pyrite formation is a dissolution reaction, and the nature of the reactant (FeS_m amongst others) is therefore irrelevant. Interestingly, out of the numerous pyrite forming reactions using FeS_m as a reagent reviewed by Rickard and Luther (2007), only one successfully synthesised pyrite from undersaturation with respect to FeS_m and under

FeS^0_{aq} stability field (Harmandas *et al.*, 1998). Harmandas *et al.* (1998) used pyrite seeds as nucleation surface to favour pyrite growth in a continuous flow reactor. Because nucleation is favoured for substrates where the surface free energy difference between the substrate and the nucleating phase tends to zero, the presence of pyrite seeds facilitates pyrite nucleation. Even though, pyrite growth is an oxidation reaction (where S(-II) in H_2S needs to be oxidised into S(-I) in S_2^{2-}) and not simply an accretion of Fe and S atoms. In Harmandas *et al.* (1998) experiments, pyrite grew *via* the H_2S pathway (Eq. 7.8). The rates of pyrite forming pathways indicate that the polysulphide pathway might be the controlling mechanism for pyrite nucleation, whilst the H_2S pathway is the controlling mechanism for pyrite crystal growth.

7.1.3. Fe isotope fractionation during bulk pyrite formation

Bulk pyrite formation carried out at pH 6 through the reaction of FeS_m with H_2S is characterised by a large kinetic fractionation favouring the incorporation of lighter isotopes into the neoformed pyrite ($\Delta^{56}Fe_{FeSm\text{-}pyrite}$ ~ 2.2 ‰, chapter VI). It was assumed that under such experimental protocols, most of the observed Fe isotope fractionation reflects the crystal growth mechanism, since pyrite nucleation barrier is rapidly overcome with suitable FeS_m substrate (Rickard, 1997). However, batch experiments do not permit us to assess the relative contribution of both nucleation and crystal growth mechanisms in the final Fe isotope signature. Major disadvantages when performing batch experiments is the very little freedom with which experiments can be run. Large reactant concentrations used in chapter VI are not representative of natural conditions, in which Fe concentrations are nano- to millimolar, and FeS_m formation is restricted to Fe rich environments. Furthermore, the rates and concentrations are continuously changing in batch experiments, unlike in natural systems in which Fe(II) inputs are continuously provided by hydrothermal vents, river loads and dissimilatory iron reduction (chapter I, section 1.2.1.2). Finally, as the two pyrite forming mechanisms depend on pH, the use of large amounts of pH buffer can be required to examine one particular mechanism.

The aim of the study is to develop a protocol permitting the determination of the Fe isotope fractionation produced under stable conditions and reactant concentrations approximating those representative of natural sediments using a chemostatic reaction vessel. Such experiments permit us to assess a wider pH range (5 to 8) without using any pH buffer and also permit us to form pyrite from less concentrated conditions. We

used pyrite seeds as a nucleation surface (Harmandas *et al.*, 1998), and millimolar $Fe(II)_{aq}$ and $S(-II)_{aq}$ were introduced continuously into the chemostatic reaction vessel to grow pyrite from saturation with respect to FeS_m (Wilkin and Barnes, 1996; Wolthers *et al.*, 2005).

7.2. Experimental Methods

7.2.1. Reactants

All reagents and acids were analytical grade and solutions were prepared using 18.2 MΩ cm deionised water and made up in O_2 free grade N_2 sparged (Butler *et al.*, 1994) 0.2 M NaCl. Iron(II) solution was made by dissolution of Mohr's salt $Fe(NH_4)_2(SO_4)_2.6H_2O$ (Sigma Aldrich™) in N_2 sparged 0.2 M NaCl. Mohr's salt was used for its ability to resist oxidation in solution. Sulphide solution was made by dissolution of $Na_2S.9H_2O$ (Sigma Aldrich™) in N_2 sparged 0.2 M NaCl. 0.005 M H^+ solution was prepared by dilution of concentrated HCl in N_2 sparged 0.2 M NaCl. 0.005 M OH^- solution was prepared by dissolution of NaOH in N_2 sparged 0.2 M NaCl.

7.2.2. Procedure

Two pyrite seeds were encapsulated in an epoxy resin, allowing one pyrite surface to be in contact with the media. The pyrite surface was cleaned with 0.01 M HCl, rinsed with deionised water and freeze-dried to prevent oxidation. Before the experiment, the pyrite seeds were introduced into the chemostat reaction vessel whose capacity is set at 1.4 L with a float. The chemostat reactor (Fig. 7.1) was filled with the 0.2 M NaCl media for the benefit of the pH electrode, sealed and the reaction was stirred with a magnetic stirrer (Fig. 2.3 in chapter II). All reagent solutions (*i.e.* 2 L 0.5 x 10^{-3} M $Fe(II)_{aq}$ and 2 L 10^{-3} M $S(-II)_{aq}$), the pH adjusting solutions (*i.e.* 0.005 M HCl and 0.005 M NaOH), and the reaction vessel were N_2-sparged for 30 min. Trace amounts of oxygen in the oxygen-free grade N_2 supply was removed through a Supelco® gas carrier purifier which uses zirconium turnings to remove oxygen at temperatures > 400°C.

Reactants (*i.e.* $Fe(II)_{aq}$ and $S(-II)_{aq}$) were continuously introduced into a sealed 2 L glass reaction vessel *via* a Masterflex® peristaltic pump. The pH was measured, monitored and controlled with a Eutech Instruments pH 190® pH/ORP controller adjusting the reaction at pH 7 ± 0.1 with 0.005 M HCl and NaOH. The volume was

maintained at a constant level with a float control and excess solution was pumped out to a Pb(II) acetate containing waste. Pb(II) acetate ensured quantitative H_2S precipitation as PbS.

After one week reaction, 150 mL of the solution were sampled and filtered under flowing N_2 on a 0.45 µm membrane Millipore™ filter to collect the suspending solids. The filter was treated with 1.2 M cold HCl to quantitatively dissolve FeS_m. After HCl treatment, the filter was clear, indicating that pyrite suspensions were limited or nonexistent. The Fe solution was evaporated to almost dryness to remove excess acid and re-taken in 5 % HNO_3. The solution was essentially $Fe(III)_{aq}$ in nitric acid and was stored, pending [Fe] determination and Fe isotope analysis. The pyrite seeds were collected, rinsed and dried with absorbing paper and stored in a N_2-filled re-circulating Saffron alpha® anoxic chamber pending secondary electron microscope (SEM) and reflected light microscope analyses. After microscopic analysis, the pyrite surface was scraped with a scalpel to collect pyrite overgrowths. Solids were dissolved in concentrated HNO_3, and remaining carbon from the SEM coating was removed by vacuum filtration. The Fe solution was evaporated to almost dryness to remove excess acid and re-taken in 5 % HNO_3. The solution was essentially $Fe(III)_{aq}$ in nitric acid, and was stored, pending for [Fe] determination and Fe isotope analysis.

Figure 7.1: A: Overview on the chemostatic reaction vessel. The black colour of the reaction reflects the presence of mackinawite in the system. B: Zoom on the pH electrode and the float controlling the constant volume of solution in the chemostat.

7.3. Analytical methods

7.3.1. Microscopy

Pyrite seeds were taken out of the anoxic chamber and carbon coated for immediate SEM analysis. Surface imaging, mineral products determination and texture description were performed *via* backscatter detector on a Philips XL30CP® Scanning Electron Microscope (SEM) at 20 kV. Qualitative chemical analysis on the material surface was carried out with PGT® Spirit X-ray analysis as a mineral check. The pyrite overgrowth removal by scalpel scraping was checked with reflected light on a Leica DM250 microscope.

7.3.2. Spectrophotometric determination of [Fe(III)]

We used the thiocyanate method (Vogel, 1951) to determine [Fe(III)] in the solution by comparison with a calibration curve. Fe solutions were acidified with 2 mL 1:5 HNO_3, oxidised with a few drops of 0.2 M potassium permanganate, reacted with 4 M potassium thiocyanate and analysed at a wavelength of 480 μm. The Beer-Lambert's law is followed for a 0 to 5 ppm [Fe(III)] range with a precision 2σ of ± 0.1 ppm.

7.4. Results and discussion

7.4.1. The presence of pyrite overgrowths

SEM imaging shows that for both pyrite seeds, the surface is characterised by two topographic zones: higher relief zones separated linearly by depressions (Fig. 7.2.A). The linearity of the covering material could reflect the overgrowth alignment along the crystallographic axis of the original pyrite surface. There is evidence supporting that the upper zones are authigenic pyrite overgrowths covering the original pyrite surface, which is still observable in the linear depressions. First, the upper material is characterised by the presence of hemispherical depressions spread all over its surface (Fig. 7.2.A,B,C,F), but these depressions are not present on the original surface. Furthermore, this material does not cover silicate inclusions (Fig. 7.2.B,C,D,E,F), which is consistent with pyrite overgrowth mechanism. Initial evidence supporting pyrite as the neoformed product is that PGT analysis indicates that these overgrowths have a typical FeS_2 signature. Analysis of the edges of inclusion minerals also confirms FeS_2 signatures. There is no evidence of oxidation since no S(0) or Fe(III) phase is detected. Fig. 7.2.E,F shows the effect of the physical removal of the carbon

coated authigenic phase by scalpel scraping. Finally, [Fe] determination indicates that ~ 0.6 mg Fe was collected from the surface, which further indicates that pyrite has been formed on the surface of the pyrite seeds.

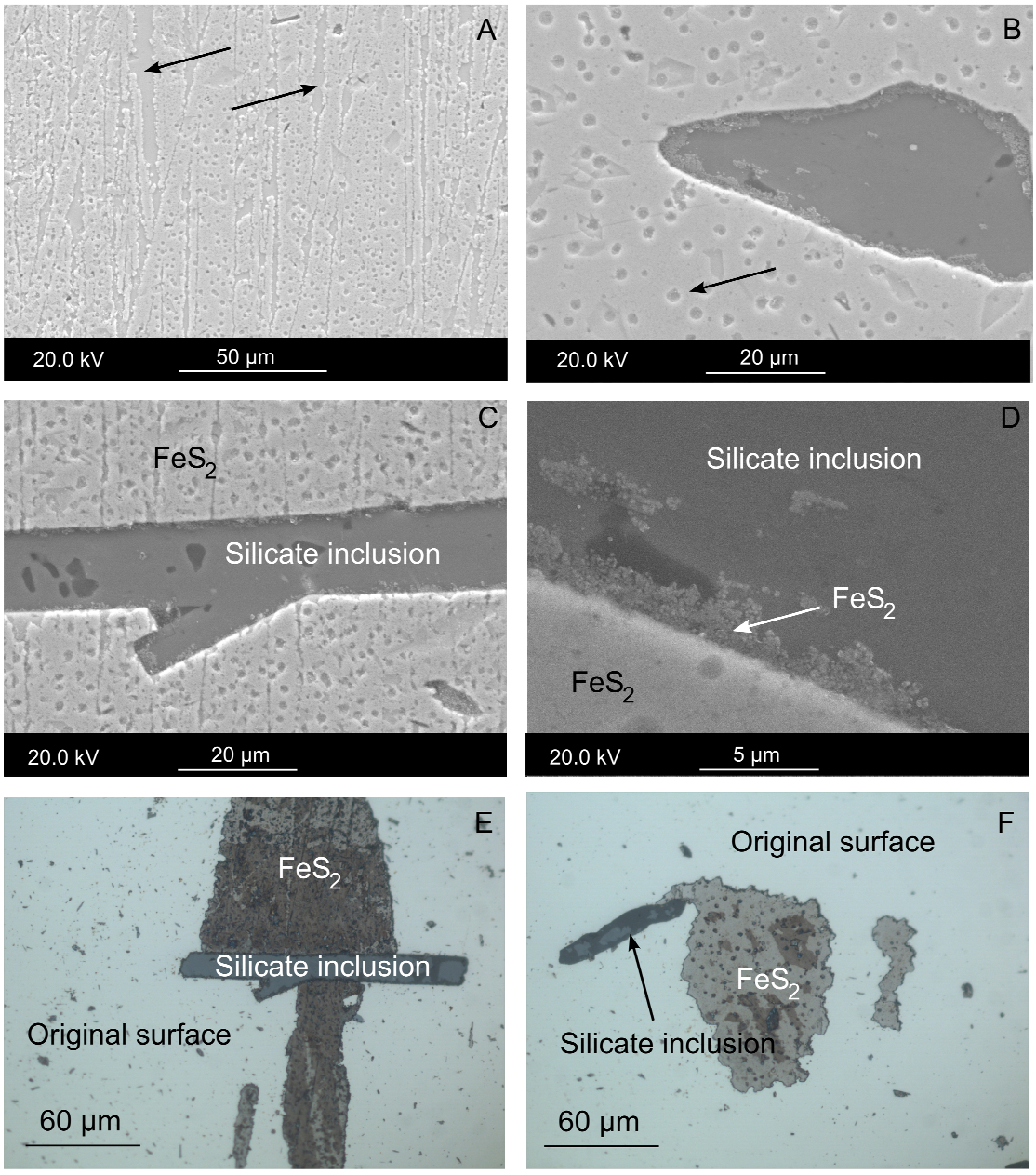

Figure 7.2: Secondary electron and reflected light microscopy of the reacted pyrite seeds surface. A: arrows show the linear depressions scattering the overgrowths. B: the arrow shows the hemispherical depressions within the overgrowths. C: A silicate inclusion free from pyrite cover. D: Pyrite overgrowths are present at the edges of the inclusion. E and F: Reflected light imaging of the pyrite surface after partial removal of the overgrowths.

The micrometric size of pyrite overgrowths produced within this experiment is consistent with results from other laboratory-grown pyrite overgrowths, which never reproduced coarse-size pyrite as widely found in nature, as noted by Grimes *et al.* (2002). This indicates that laboratory experiments tend to work with concentrations far above the pyrite supersaturation limit, favouring the development of numerous nucleation sites rather than pyrite crystal growth. The geochemistry, including isotope geochemistry, of pyrite formation at FeS undersaturation, and consequently at conditions more favourable to pyrite growth, is a comparatively under-explored topic in experimental research into the iron sulphide system.

7.4.2. Pyrite forming mechanism

The pH of the $Fe(II)_{aq}$ solution was ~ 4, and at this pH the dominant Fe bearing species is the hexaqua $Fe[H_2O]_6^{2+}$ (normally referred as Fe^{2+}). Up to ~ 12% of the total dissolved Fe(II) was constituted by the weak outer-sphere SO_4^{2-} ligand complex, $Fe[H_2O]_6SO_4^0{}_{aq}$ (calculated in Visual MINTEQ 3.0®). In the alkaline sulphide solution, S(-II) speciation is dominated by HS^- (Fig. 1.5 in chapter I). Reagent solutions were pumped into the reaction vessel at a rate of 0.4 mL min^{-1}. The pH of the reaction was set at pH 7.00 ± 0.1. Fig. 2.4 in chapter II shows that the reaction pH was constant through time.

Rickard (2006) showed that log $K_{1,sp}(FeS_m) = 3.5 \pm 0.25$ for the solubility reaction under acidic conditions (Eq. 7.9):

$$FeS_m + 2H^+ = Fe^{2+} + H_2S \qquad (7.9)$$

For neutral to alkaline regions, where $S(-II)_{aq}$ speciation is dominated by HS^-, Eq. 7.9 can be extended to Eq. 7.10:

$$FeS_m + H^+ = Fe^{2+} + HS^- \qquad (7.10)$$

As p$K_1(H_2S)$ is 6.98 (Suleimenov and Seward, 1997), log$K_{2,sp}(FeS_m)$ for reaction 10 is ~ -3.5. Under neutral to alkaline conditions, the equilibrium solubility of FeS_m is dominated by FeS^0_{aq}, with log$K_0(FeS_m)$ = -5.7 (Rickard, 2006). This means that at pH 7, when mixing Fe^{2+}_{aq} and HS^- at low concentrations, FeS^0_{aq} forms when $\log\{Fe^{2+}\} + \log\{HS^-\} + pH \geq 2.2$. When $\log\{FeS^0_{aq}\} \geq -5.7$, mackinawite starts precipitating from solution. At pH 7 and for $\Sigma[S(-II)] = 10^{-3}$ M, equilibrium solubility of FeS_m is dominated by FeS^0_{aq} (Rickard, 2006), which reacts with H_2S to form pyrite (Eq. 7.8, Fig. 7.3).

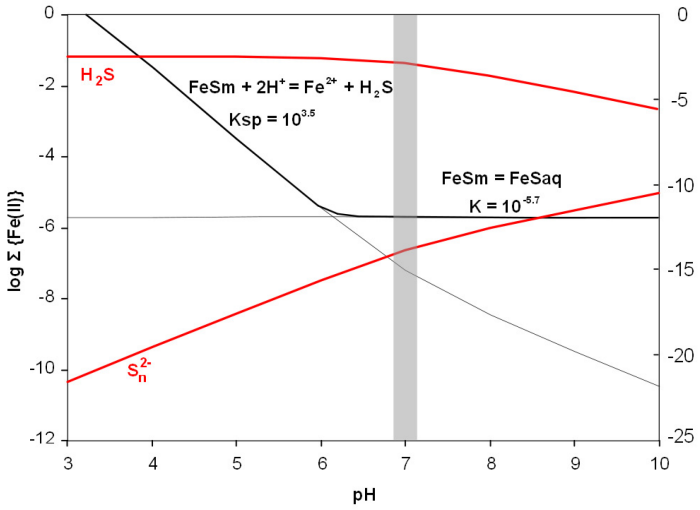

Figure 7.3: $S(-II)_{aq}$ speciation as H_2S and polysulphides (red curves) and total activity of dissolved Fe(II) in equilibrium with FeS_m (black curves) for $\Sigma\{S(-II)\} = 10^{-3}$ M as a function of pH. The grey area represents the experimental pH conditions, for which FeS^0_{aq} is the dominant $Fe(II)_{aq}$ species and H_2S the dominant $S(-II)_{aq}$ species relevant for pyrite formation.

The fact that H_2S_{aq} is the dominant $S(-II)_{aq}$ species in the system does not exclude potential pyrite supersaturation with respect to S_2^{2-} and Fe^{2+} only. Harmandas *et al.* (1998) showed that the pyrite supersaturation limit, Ω_{pyrite}, for the reaction (Eq. 7.11):

$$FeS_2 = Fe^{2+} + S_2^{2-} \qquad (7.11)$$

is given by Eq. 7.12:

$$\Omega_{pyrite} = \frac{(Fe^{2+})(S_2^{2-})}{K_{sp}(FeS_2)} \qquad (7.12)$$

where $K_{sp}(FeS_2)$ is the solubility product of pyrite for reaction 7.11, and $K_{sp}(FeS_2) = 10^{-24}$ for reaction 7.11 (Rickard and Luther, 2007). Harmandas *et al.* (1998) showed that $\Omega_{pyrite} \sim 10^{14}$ for reaction 7.11. Rickard and Luther (2007) suggested that for pH 7, pyrite supersaturation limit in terms of $\{Fe^{2+}\}$ and $\{H_2S\}$ in the presence of FeS_m is $\Omega_{pyrite} = 10^{10.7}$. For the experimental data illustrated in Fig. 7.3, $\Omega_{pyrite} \sim 3 \times 10^2$ on the basis of $\{Fe^{2+}\}$ and $\{S_2^{2-}\}$. Therefore, the polysulphide pathway in pyrite formation is unlikely to be of importance since pyrite is undersaturated with respect to polysulphides.

7.5. Conclusions and implications for natural systems

Pyrite overgrowths were formed at the surface of pyrite seeds in a continuous flow reactor from the reaction of FeS^0_{aq} with H_2S. Fe isotope analysis has not been

performed yet, but the Fe isotopic compositions of the pyrite overgrowths and the Fe(II) source should provide the isotope fractionation recorded during the mechanism involving pyrite growth. Experimental conditions were representative of environments with near marine pH and continuous input of ≤ millimolar $[Fe(-II)]_{total}$ and $[S(-II)]_{total}$. These preliminary results are pertinent for potential future research on the Fe isotope fractionations produced with varying reactant concentrations and pH. They provide the experimental basis to examine the behaviour of Fe isotopes during pyrite nucleation and growth at conditions approaching those of the natural environment and therefore to explore the details of Fe isotope distribution in modern sedimentary environmental conditions.

7.6. References

Anbar, A., Rouxel, O., 2007. Metal Stable Isotopes in Paleoceanography. Annu. Rev. Earth Planet. Sci. 35, 717–746.

Archer, C., Vance, D., 2006. Coupled Fe and S isotope evidence for Archean microbial Fe(III) and sulfate reduction. Geology 34, 153-156.

Balci, N., Bullen, T.D., Witte-Lien, K., Shanks, W.C., Motelica, M., Mandernack, K.W., 2006. Iron isotope fractionation during microbially stimulated Fe(II) oxidation and Fe(III) precipitation. Geochimica et Cosmochimica Acta 70, 622-639.

Butler, I., Schoonen, M., Rickard, D., 1994. Removal of dissolved oxygen from water: A comparison of four common techniques. Talanta 41, 211-215.

Croal, L., Johnson, C., Beard, B., Newman, D., 2004. Iron isotope fractionation by Fe(II)-oxidizing photoautotrophic bacteria. Geochim Cosmochim Acta 68, 1127-1242.

Crosby, H., Roden, E., Johnson, C., Beard, B., 2007. The mechanisms of iron isotope fractionation produced during dissimilatory Fe(III) reduction by Shewanella putrefaciens and Geobacter sulfurreducens. Geobiology 5, 169-189.

Czaja, A., Johnson, C., Beard, B., Eigenbrode, J., Freeman, K., Yamaguchi, K., 2010. Iron and carbon isotope evidence for ecosystem and environmental diversity in the ~ 2.7 to 2.5 Ga Hamersley Province, Western Australia. Earth and Planetary Science Letters 292, 170-180.

Grimes, S.T., Davies, K.L., Butler, I.B., Brock, F., Edwards, D., Rickard, D., Briggs, D.*E.G.*, Parkes, R.J., 2002. Fossil plants from the Eocene London Clay: the

use of pyrite textures to determine the mechanism of pyritization. Journal of the Geological Society 159, 493-501.

Harmandas, N., Navarro Fernandez, E., Koutsoukos, P., 1998. Crystal Growth of Pyrite in Aqueous Solutions. Inhibition by Organophosphorus Compounds. Langmuir, American Chemical Society 14, 1250-1255.

Icopini, G., Anbar, A., Ruebush, S., Tien, M., Brantley, S., 2004. Iron isotope fractionation during microbial reduction of iron: The importance of adsorption. Geology 32, 205-208.

Johnson, C., Beard, B., Klein, C., Beukes, N., Roden, E., 2008. Iron isotopes constrain biologic and abiologic processes in banded iron formation genesis. Geochim Cosmochim Acta 72, 151-169.

Johnson, C., Beard, B., Roden, E., 2008. The Iron Isotope Fingerprints of Redox and Biogeochemical Cycling in Modern and Ancient Earth. Annual Review of Earth and Planetary Sciences 36, 457-493.

Johnson, C., Beard, B., Welch, S., Croal, L., Newman, D., Nealson, K., 2005. Experimental constraints on Fe isotope fractionations during biogeochemical cycling of Fe. Geochim. Cosmochim. Acta 66, A371.

Johnson, C., Skulan, J., Beard, B., Sun, H., Nealson, K., Braterman, P., 2002. Isotopic fractionation between Fe(III) and Fe(II) in aqueous solutions. Earth and Planetary Science Letters 195, 141-153.

Luther, G., 1991. Pyrite synthesis via polysulfide compounds. Geochim. Cosmochim. Acta 55, 2839– 2849.

Matthews, A., Morgans-Bell, H., Emmanuel, S., Jenkyns, H., Erel, Y., Halicz, L., 2004. Controls on iron-isotope fractionation in organic-rich sediments (Kimmeridge Clay, Upper Jurassic, Southern England). Geochimica et Cosmochimica Acta 68, 3107-3123.

Rickard, D., 1997. Kinetics of pyrite formation by the H2S oxidation of iron (II) monosulfide in aqueous solutions between 25oC and 125oC: the rate equation. Geochim. Cosmochim. Acta 61, 115– 134.

Rickard, D., 2006. The solubility of FeS. Geochimica et Cosmochimica Acta 70, 5779-5789.

Rickard, D., Luther, G., 1997. Kinetics of pyrite formation by the H2S oxidation of iron (II) monosulfide in aqueous solutions between 25 8C and 125 8C: the mechanism. Geochim. Cosmochim. Acta 61, 135–147.

Rickard, D., Luther, G., 2007. Chemistry of Iron Sulfides. Chem. Rev. 107, 514-562.

Rickard, D., Butler, I.B., Oldroyd, A., 2001. A novel iron sulphide mineral switch and its implications for Earth and planetary science. Earth and Planetary Science Letters 189, 85-91.

Rickard, D., Grimes, S., Butler, I., Oldroyd, A., Davies, K.L., 2007. Botanical constraints on pyrite formation. Chemical Geology 236, 228-246.

Rouxel, O., Bekker, A., Edwards, K., 2005. Iron isotope constraints on the Archean and Paleoproterozoic ocean redox state. Science 307, 1088-1090.

Severmann, S., Johnson, C., Beard, B., McManus, J., 2006. The effect of early diagenesis on the Fe isotope compositions of porewaters and authigenic minerals in continental margin sediments. Geochim Cosmochim Acta 70, 2006–2022.

Skulan, J., Beard, B., Johnson, C., 2002. Kinetic and equilibrium Fe isotope fractionation between aqueous Fe(III) and hematite. Geochim. Cosmochim. Acta 66, 2995-3015.

Suleimenov, O., Seward, T., 1997. A spectrophotometric study of hydrogen sulphide ionisation in aqueous solutions to 350dC. Geochim. Cosmochim. Acta 61, 5187.

Vogel, A., 1951. A text-book of Quantitative Inorganic Analysis, Therory and practice, second edition. Longmans, Green and Co.

Welch, S., Beard, B., Johnson, C., Baterman, P., 2003. Kinetic and equilibrium Fe isotope fractionation between aqueous Fe(II) and Fe(III). Geochim. Cosmochim. Acta 67, 4231-4250.

Wilkin, R., Barnes, H., 1996. Pyrite formation by reactions of iron monosulfides with dissolved inorganic and organic sulfur species. Geochim. Cosmochim. Acta 60, 41267– 44179.

Wolthers, M., Charlet, L., van Der Weijden, C., van der Linde, P., Rickard, D., 2005. Arsenic mobility in the ambient sulfidic environment: Sorption of arsenic(V) and arsenic(III) onto disordered mackinawite. Geochimica et Cosmochimica Acta 69, 3483-3492.

Yamaguchi, K., Johnson, C., Beard, B., Ohmoto, H., 2005. Biogeochemical cycling of iron in the Archean-Paleoproterozoic Earth: Constraints from iron isotope variations in sedimentary rocks from the Kaapvaal and Pilbara Cratons. Chem. Geol. 218, 135-169.

Chapter VIII

Summary and Future work

The careful analysis of Fe isotopes in various synthetic iron sulphides (*e.g.* Guilbaud, Ellam, *et al.*, 2010; Guilbaud, Butler, *et al.*, 2010) has demonstrated the usefulness of Fe isotopes in tracing the chemical behaviour of Fe atoms within the diagenetic Fe-S system. The aim of this PhD project was to evaluate potential Fe isotope fractionations occurring during the abiological formation of iron sulphides and ultimately pyrite. Fig. 8.1 summarises the abiotic Fe isotope fractionations observed for major iron sulphide forming mechanisms.

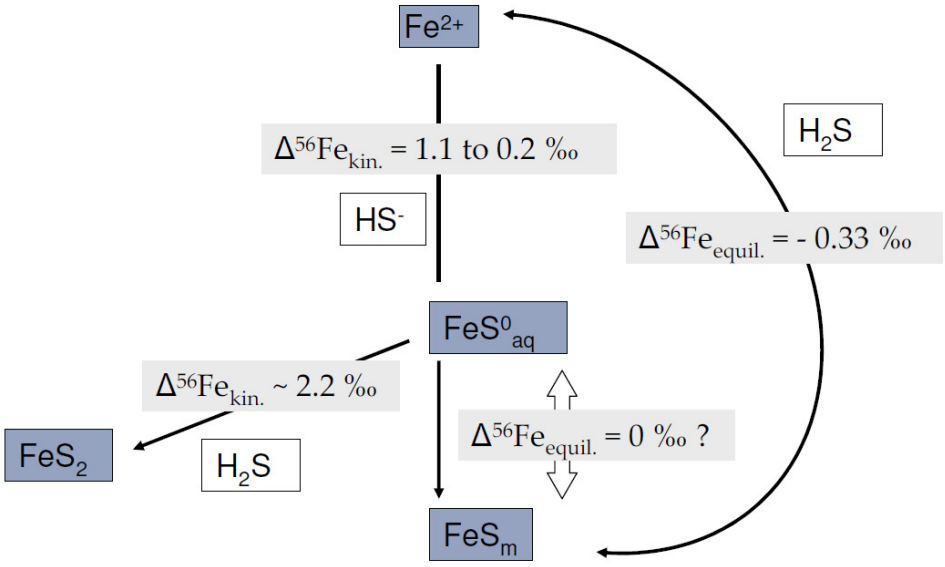

Figure 8.1: Experimentally determined Fe isotope fractionations occurring abiotically in the diagenetic Fe-S system. Note that the fractionation between FeS^0_{aq} and FeS_m is assumed to be ~ 0 ‰ but has not been directly measured. The major Fe-S phases investigated in this PhD are in blue, and the corresponding fractionations in grey.

8.1. The mobility of Fe isotopes in the nanoparticulate Fe^{2+}_{aq}-FeS^0_{aq}-FeS_m system (Chapters IV and V)

The precipitation of FeS_m from the reaction of $Fe(II)_{aq}$ with HS^-_{aq} incorporates kinetically lighter isotopes into solid FeS_m nanoparticles, which is consistent with previously published work (Butler *et al.*, 2005). Isotopic exchange between FeS_m and $Fe(II)_{aq}$ is controlled by the nanoparticle growth mechanism and rapidly asymptotes when ~ 75 % of Fe atoms have exchanged between the $Fe(II)_{aq}$ and FeS_m nanoparticles. The rates of isotopic exchange between FeS_m and $Fe(II)_{aq}$ are consistent with FeS_m nanoparticles that i) have a core-shell structure that restricts Fe mobility to

the surface shell, and ii) grow by aggregation-growth rather than Ostwald ripening (Chapter IV) (Guilbaud, Butler, *et al.*, 2010). Such core-shell structures have been observed in other transition metal sulphide nanoparticles such as NiS (Huang *et al.*, 2009) and ZnS (Zhang *et al.*, 2003). Due to the platy shape of FeS_m nanoparticles, it is difficult to confirm the core-shell structure of FeS_m by HRTEM imaging (Ohfuji and Rickard, 2006), although FeS_m edges are diffuse, which may indicate a disordered surface. Aggregation crystal growth has been observed for other nanoparticulate systems such as goethite nanoparticles (*e.g.* Waychunas *et al.*, 2005), with consequent implications for environmental investigations of contaminant metal trapping during nanoparticle growth.

Results suggest that the $Fe(II)_{aq}$-FeS_m couple in low temperature environments is kinetically inhibited from achieving isotopic equilibrium, at which FeS_m is predicted to incorporate heavier isotopes with respect to Fe^{2+}_{aq} (Chapter V, Guilbaud *et al.*, *submitted to Geochimica et Cosmochimica Acta*). It is important to note that ^{56}Fe depletion in FeS_m with respect to $Fe(II)_{aq}$ is due to kinetic effects (Butler *et al.*, 2005) and does not represent isotopic equilibrium as has been proposed (*e.g.* Johnson *et al.*, 2008). Therefore in modern anoxic sedimentary environments (*e.g.* Severmann *et al.*, 2006), in which FeS_m is a reactive Fe phase, the isotopic composition of FeS_m is not in equilibrium with porewater $Fe(II)_{aq}$. The idea that low temperature nanoparticles should be in equilibrium with the media is disproved for the Fe-S system.

8.2. The mobility of Fe isotopes during the formation of sedimentary pyrite (Chapter VI and VII)

Pyrite formation from the reaction of FeS^0_{aq} with H_2S_{aq} is accompanied by a large abiotic kinetic fractionation where the pyrite product is ^{56}Fe depleted with respect to the Fe(II) pool from which it forms (Chapter VI, Guilbaud *et al.*, *submitted to Nature Communications*). Pyrite formation is a unidirectional reaction, and atomic exchange between pyrite and the media after Fe sequestration into pyrite is strictly limited by the very low solubility of pyrite at low temperatures. This confirms that the pyrite forming mechanism itself can produce fractionations larger than 1 ‰, without the intervention of any biologically mediated reaction, or any redox change occurring to the Fe chemistry. Results highlight that contrary to previously proposed models (*e.g.* Rouxel *et al.*, 2005; Johnson *et al.*, 2008), pyrite is not a passive recorder of the Fe(II) pool from which it forms. The full range of Fe isotope signatures recorded in modern

and ancient sedimentary sulphides can be produced abiotically combining the fractionation factors between Fe^{2+}_{aq}, FeS_m and pyrite. The secular variations in Fe isotope compositions of pyrite reflect various extents of $Fe(II)_{aq}$ utilisation and degrees of pyritisation, as well as variations in source composition.

Using the experimentally determined $\Delta^{56}Fe_{FeS\text{-}pyrite}$ of ~ 2‰, most Archean sedimentary pyrite signatures indicate that the Fe isotope composition of the $Fe(II)_{aq}$ reservoir was ~ 0 ‰, which is consistent with the supposed composition of Archean hydrothermal fluxes (*e.g.* Yamaguchi *et al.*, 2005). There is no need for a large ^{56}Fe depleted $Fe(II)_{aq}$ pool to be produced prior to pyrite formation, and therefore no need for a large mass-balancing ^{56}Fe enriched reservoir $Fe(II)_{aq}$ to remain after pyrite formation. This is particularly true for an environment in which $Fe(II)_{aq}$ with $\delta^{56}Fe$ ~ 0 ‰ is continually injected into the system by hydrothermal vents as it is the case in the Archean, because the ^{56}Fe enriched Fe(II) produced during pyrite formation is then diluted in the large $Fe(II)_{aq}$ pool. Certainly, both DIR and the removal of $Fe(II)_{aq}$ as BIFs in ferruginous regions would promote the production of ^{56}Fe depleted fluids enabling the formation of light sedimentary pyrite. We suggest that low $\delta^{56}Fe$ signatures in Archean sedimentary pyrite indicate that the portion of Fe removed as pyrite was relatively small in respect with the portion of reactive Fe remaining in the Fe(II) pool (*e.g.* Canfield, 2005).

Pyrite grows when reactant concentrations approach those of natural environments and are continuously introduced into the system (chapter VII). The mechanism involves the reaction of FeS^0_{aq} with H_2S. Isotopic analysis for this experiment has not been performed yet but should provide the basis for the development of future work in exploring Fe isotope fractionations from natural conditions.

8.3. Some ideas for future work

Some fundamental answers have been provided by the results of the experiments carried out through this PhD, opening up a range of new questions for Fe isotopes in the Fe-S system, and offering a strong basis to approach experimentally this field of stable isotope geochemistry. The subsequent section reviews some ideas of further research that could be studied in continuity of the work presented in this thesis.

8.3.1. Kinetic Fe isotope fractionation between Fe^{2+}_{aq} and FeS_m via the H_2S pathway

The precipitation of FeS_m by addition of $Na_2S.9H_2O$ into $Fe(II)_{aq}$ follows the HS^- formation pathway (Eq. 1.5 in chapter I) as $Na_2S.9H_2O$ is strongly alkaline. However, this mechanism may not be representative of Archean seawater conditions in which pH is expected to be acidic (*e.g.* Grotzinger and Kasting, 1993), and H_2S to dominate $S(-II)_{aq}$ speciation. As the H_2S pathway involves a different FeS_m forming mechanism, the resulting Fe isotope fractionation between $Fe(II)_{aq}$ and FeS_m may be also different. Preliminary results (Pękala, *pers. comm.*) suggest that a fractionation significantly different from the one involved in the HS^- pathway occurs with the H_2S pathway. Experimental design would involve the use of buffered $Fe(II)_{aq}$ and $S(-II)_{aq}$ solutions by non-complexing buffers. The difficulty with such a design is to buffer a H_2S_{aq} solution at ~ pH 4 without H_2S to be removed as a gas or forming S(0). Alternatively, to avoid the use of any buffer, $H_2S_{(g)}$ can be transferred into a non-buffered $Fe(II)_{aq}$ solution *via* a gas transfer manifold (Chapter II, section 2.2.2.3).

8.3.2. Determination of kinetic and equilibrium Fe isotope fractionations between FeS_m and FeS^0_{aq}

The results presented in chapter V suggest that at equilibrium, a significant Fe isotope fractionation between Fe^{2+}_{aq} and FeS_m records ^{56}Fe enrichment in the solid FeS_m. In chapter VI, we made the assumption that the dissolution of FeS_m into FeS^0_{aq} under neutral to alkaline conditions should experience little or insignificant fractionation since FeS_m and FeS^0_{aq} are structurally congruent (Luther and Rickard, 2005). In order to verify this assumption, it is essential to determine experimentally both kinetic and equilibrium fractionations between FeS_m and FeS^0_{aq}. FeS_m solubility indicates that FeS^0_{aq} dominates the $Fe(II)_{aq}$ speciation for neutral to alkaline pH (Rickard, 2006). Experimentally, it is not trivial to work with stable FeS^0_{aq} solutions in large amounts. Furthermore, when FeS_m is in equilibrium with FeS^0_{aq}, the FeS^0_{aq} reservoir is orders of magnitude smaller than the FeS_m reservoir, making its collection difficult for isotope analysis. Those issues can be overcome with a chemostatic reaction vessel which allows the use of large volumes to concentrate the reactants. Several floating dialysis membranes containing FeS_m would be placed in the reaction solution buffered at pH 8 (MOPS), to guarantee that FeS^0_{aq} dominates $Fe(II)_{aq}$ speciation at equilibrium. FeS_m nanoparticles would be contained within the membranes unlike FeS^0_{aq}, although Buffle *et al.* (1988) showed that the smallest FeS_m

nanoparticles may display a diffusion behaviour. The H_2S or purified O_2-free N_2 sparged buffered solution would be continuously introduced into the chemostat, and the excess volume collected and evaporated to concentrate Fe from FeS^0_{aq}. Time series Fe isotope analysis would be possible by sampling one dialysis membrane and its $Fe_{FeS(0)aq}$ equivalent through time.

Similar experimental design can be done for the determination of the Fe isotope fractionation between FeS^0_{aq} and FeS_m at equilibrium starting with labelled FeS^0_{aq} and "normal" FeS_m for the three isotope method. Because the size of both reservoirs is disproportionate, the exchange curves will be asymmetric, and therefore a large isotopic enrichment (*e.g.* > 100 ‰) would be necessary in the FeS^0_{aq} phase to ensure a significant drift in the Fe isotope composition of FeS_m during isotope exchange. In the case where the FeS^0_{aq} reservoir is too small for Fe isotope analysis, the equilibrium fractionation can still be predicted using the extent of isotopic exchange calculated from the FeS_m isotopic composition.

8.3.3. Determination of the Fe isotope fractionation during pyrite formation involving polysulphides as a S(-II)$_{aq}$ reactant

Chapter VI presented the Fe isotope fractionation resulting from the formation of pyrite when FeS_m dissolves and reacts with H_2S. Butler *et al.* (2004) confirmed that the polysulphide pathway (Eq. 1.9 in chapter I) may involve more Fe-S bond breaking than the H_2S pathway. As a result, the Fe fractionation recorded during this pyrite forming pathway could be consequently different to those recorded for the H_2S pathway. The experimental procedure would involve the use of tetrasulphide, Na_2S_4 rather than H_2S to react with FeS^0_{aq}. The reaction pH would be adjusted by the non-complexing MOPS buffer at pH 8. The experimental and extraction protocols would then follow those described in chapter II.

8.3.4. Determination of the equilibrium Fe fractionation between Fe^{2+}_{aq} and pyrite

Results from chapter VI show that the formation of sedimentary pyrite is a unidirectional reaction recording kinetic isotope effects. Theoretically derived equilibrium numbers between Fe^{2+}_{aq} and pyrite (*e.g.* Polyakov *et al.*, 2007) can therefore not be compared with the results in chapter VI. However such comparison would be useful to assess Fe isotopic equilibrium in hydrothermal systems or during Fe mobilisation by burial diagenetic fluids. The three isotope method could be applied

to the Fe^{2+}_{aq}-pyrite system at 100-150°C. ^{56}Fe enriched pyrite microcubes could be formed as described in chapter V and VI, and left in contact with a $Fe(II)_{aq}$ solution of natural isotopic composition at 100°C to allow Fe isotopes to exchange between both phases. If the assumption that $\Delta^{56}Fe_{FeSm\text{-}FeS(0)aq} = 0$ ‰ is true, the result from this experiment (*i.e.* $\Delta^{56}Fe_{Fe2+\text{-}pyrite}$) would also provide indirectly the equilibrium fractionation between FeS^0_{aq} and pyrite.

8.3.5. Pyrite crystal growth from undersaturated and saturated conditions with respect to FeS_m

If the assumption that $\Delta^{56}Fe_{FeSm\text{-}FeS(0)aq} = 0$ ‰ is not true, it becomes quite clear that the measured fractionation in chapter VI represents $\Delta^{56}Fe_{FeSm\text{-}pyrite}$ and not $\Delta^{56}Fe_{FeS(0)aq\text{-}pyrite}$. The range of variables accessible using a chemostatic reactor open up a variety of possible research, including pyrite formation from conditions undersaturated with respect to FeS_m (Harmandas *et al.*, 1998), which would directly assess $\Delta^{56}Fe_{FeS(0)aq\text{-}pyrite}$.

8.3.6. The role of microorganisms for the Fe isotope signatures of pyrite

Pyrite forming reactions conducted in microbiological experiments have documented rates of pyrite formation substantially larger than those from abiotic systems (*e.g.* Canfield *et al.*, 1998). Whether or not biologically mediated reactions have also an influence on the Fe isotope signature recorded in pyrite is not known. Again, the chemostatic approach described above could assess this question by investigating the rates of pyrite formation when microorganisms are present and the subsequent Fe isotope composition of pyrite.

8.4. References

Buffle, J., de Vitre, R., Perret, D., Leppard, G., 1988. Combining field measurements for speciation in non perturbable waters, in: Metal Speciation: Theory, Analysis and Application. Lewis Publishers Inc., London, pp. 99-124.

Butler, I., Archer, C., Vance, D., Oldroyd, A., Rickard, D., 2005. Fe isotope fractionation on FeS formation in ambient aqueous solution. Earth and Planet. Science Letters 236.

Butler, I., Bottcher, M., Rickard, D., Oldroyd, A., 2004. Sulfur isotope partitioning during experimental formation of pyrite via the polysulfide and hydrogen

sulfide pathways: implications for the interpretation of sedimentary and hydrothermal pyrite isotope records. Earth and Planet. Science Letters 228, 495-509.

Canfield, D.E., Thamdrup, B., Fleischer, S., 1998. Isotope Fractionation and Sulfur Metabolism by Pure and Enrichment Cultures of Elemental Sulfur-Disproportionating Bacteria. Limnology and Oceanography 43, 253-264.

Canfield, D., 2005. The early history of atmospheric oxygen: Homage to Robert M. Garrels. Annual Review of Earth and Planetary Sciences 33, 1-36.

Grotzinger, J., Kasting, J., 1993. New constaints on Precambrian ocean composition. J. Geol. 101, 235-243.

Guilbaud, R., Ellam, R., Butler, I., Gallagher, V., Keefe, K., 2010. A procedural development for the analysis of 56/54Fe and 57/54Fe isotope ratios with new generation IsoProbe MC-ICP-MS. J. Anal. At. Spectrom 25, 1598-1604.

Guilbaud, R., Butler, I.B., Ellam, R.M., Rickard, D., 2010. Fe isotope exchange between Fe(II)aq and nanoparticulate mackinawite (FeSm) during nanoparticle growth. Earth and Planetary Science Letters 300, 174-183.

Harmandas, N., Navarro Fernandez, E., Koutsoukos, P., 1998. Crystal Growth of Pyrite in Aqueous Solutions. Inhibition by Organophosphorus Compounds. Langmuir, American Chemical Society 14, 1250-1255.

Huang, S., Harris, K., Lopez-Capel, E., Manning, D., Rickard, D., 2009. "Amorphous Nickel Sulfide" Is Hydrated Nanocrystalline NiS with a Core-Shell Structure. Inorganic Chemistry 48, 11486-11488.

Johnson, C., Beard, B., Roden, E., 2008. The Iron Isotope Fingerprints of Redox and Biogeochemical Cycling in Modern and Ancient Earth. Annual Review of Earth and Planetary Sciences 36, 457-493.

Luther, G., Rickard, D., 2005. Metal Sulfide Cluster Complexes and their Biogeochemical Importance in the Environment. Journal of Nanoparticle Research 7, 389-407.

Ohfuji, H., Rickard, D., 2006. High resolution transmission electron microscopic study of synthetic nanocrystalline mackinawite. Earth and Planet. Science Letters 241, 227.

Polyakov, V., Clayton, R., Horita, J., Mineev, S., 2007. Equilibrium iron isotope fractionation factors of minerals: Reevaluation from the data of nuclear inelastic resonant X-ray scattering and Mössbauer spectroscopy. Geochimica

et Cosmochimica Acta 71, 3833-3846.

Rickard, D., 2006. The solubility of FeS. Geochimica et Cosmochimica Acta 70, 5779-5789.

Rouxel, O., Bekker, A., Edwards, K., 2005. Iron isotope constraints on the Archean and Paleoproterozoic ocean redox state. Science 307, 1088-1090.

Severmann, S., Johnson, C., Beard, B., McManus, J., 2006. The effect of early diagenesis on the Fe isotope compositions of porewaters and authigenic minerals in continental margin sediments. Geochim Cosmochim Acta 70, 2006–2022.

Waychunas, G., Kim, C., Banfield, J., 2005. Nanoparticulate Iron Oxide Minerals in Soils and Sediments: Unique Properties and Contaminant Scavenging Mechanisms. Journal of Nanoparticle Research 7, 409-433.

Yamaguchi, K., Johnson, C., Beard, B., Ohmoto, H., 2005. Biogeochemical cycling of iron in the Archean-Paleoproterozoic Earth: Constraints from iron isotope variations in sedimentary rocks from the Kaapvaal and Pilbara Cratons. Chem. Geol. 218, 135-169.

Zhang, H., Huang, F., Gilbert, B., Banfield, J., 2003. Molecular Dynamics Simulations, Thermodynamic Analysis, and Experimental Study of Phase Stability of Zinc Sulfide Nanoparticles. The Journal of Physical Chemistry B 107, 13051-13060.